Imaging of Myelin proteins during injury and differentiation

by

Sayed Muhammed Rassul

A thesis submitted to

the University of Birmingham

for the degree of

DOCTOR OF PHILOSOPHY

Institute of Inflammation and Ageing

College of Medical and Dental Sciences

University of Birmingham

September 2018

Abstract

Myelin injury plays a role in many devastating conditions, including multiple sclerosis, and neuromyelitis optica. Previous work in understanding myelin injury has utilised a combination of high-resolution static imaging modalities, such as electron microscopy, and ensemble-averaged imaging, such as immunohistochemistry. Within the work presented in this thesis the behaviour of myelin basic protein was addressed, during various stages of differentiation and injury.

In order to explore this several reporters for myelin basic protein were designed and encoded within Semliki forest constructs in order to induce protein transduction in oligodendroglial cells. Reporters utilised several fluorescent tags including Dendra2, mCherry, and GFP. These viral vectors were characterised to determine the expression kinetics and toxicity within cells.

Following the production of the MBP reporters, a complement injury modality was optimised to induce myelin/oligodendrocyte specific injury with little injury within axons/neurones. This myelin injury was utilised for live imaging of myelin using the MBP reporters produced previously.

The reporters produced were utilised to explore the change in particle dynamics following myelin injury, using single molecule TIRF imaging. Responses to injury were compared over various stages of oligodendrocyte differentiation, where it was found that MBP dynamics following injury varied most when mature oligodendrocytes were injured.

Acknowledgements

I am thankful to all the people who have supported and guided me throughout my time within Birmingham.

I would first like to thank my supervisors, Daniel Fulton, Robert Neely, and Iain Styles, for allowing me to pursue this scientific adventure, and for providing insightful comments and guidance to develop me as a scientist. And also my collaborator Professor Pranab Das, who provided me with the materials and support for the immunology segments of my work.

Next, I would like to thank my colleagues within the PSIBS and Sci-Phy doctoral training centre. They have provided me with a range of different outlooks on my work, and have been instrumental in encouraging me. Of particular mention is my year of the course; Nat Wand, Suzie Mason, Siobhan King, Sophie Glinton, Iggy Partarrieu, Emma Meeus and Rich Young who have provided me with some great experiences and friendship. In addition to this I have also met some wonderful people in the centre who have provided me insights to expand the reaches of my work, such as Zoe Schofield, Kamlesh Patel, Emma, and Vicky.

I have been lucky to work within two amazing groups who have developed me as a scientist and helped me grow as a person. The first of which is the Neely group, both past and present, who gave me somewhere to work when needed, joined me for the highs and lows of my work, and treated me like an amazing member of the family. Special thanks go to Ashleigh Rushton and Darren Smith for being some of the best people to talk to, whether it was about science, or when I needed to escape the science. Also, I would like to thank to Pippa Tucker for her support in her short but useful project with me.

I would like to thank the Neuroscience and Ophthalmology group, including Simon, Adam Thomson, Chloe Thomas, Andrea Halsey, Gibran, Callum Watson, Rachel Vincent, Caryl, Maryam Esmaeili, Masa Otsu, and Patrick. Although I may have aided in their onsets into diabetes they have provided me with great comradery within my time, always willing to help when needed, and just generally chat to help me feel less isolated. Of particular mention is Maryam Esmaeili for all her advice on the way; and Masa Otsu who provided me with primary cells to work on, and supported me in directing my PhD to where it went.

I have been blessed to have met amazing friends along the way, including; my fellow warrior in arms María Ceprián who has provided me with the energy and sometimes not so gentle prompts to finish; Bram Geron and Eva Reindl who were the most amazing people to just bump into one day, and end up long-time friends; Emily Guggenheim, Mike Clancy, Mohab Elfaref, and Kam Patel, who not only provided me with a means to relax after the science, but always there to help me deal with my problems; and my group of friends who refer to themselves as “the future doctors”, Justyna Czarnocka, Ryan Huo, Sarah Lastackhi, Pavel Hofman, Dennis Vansoest, Gabor, Elena, Selina, Neval and Marina.

Finally, I am exceptionally grateful to my siblings, Sakina Rassul, and Aliabbas Rassul who have provided support along the way.

Contents

Table of figures

Table of tables

Abbreviations

DAPI	4',6-diamidino-2-phenylindole
BHK	Baby Hamster Kidney
bp	Base Pairs
BBB	Blood brain barrier
BSCB	Blood spinal cord barrier
CNS	Central Nervous system
CNP	Cyclic-nucleotide-phosphodiesterase
DIV	Days in Vitro
DNA	Deoxyribonucleic acid
dbcAMP	Dibutyl adenosine 3',5'-cyclic monophosphate
emOL	Early myelinating oligodendrocyte
EAE	Experimental autoimmune encephalomyelitis
EBV	Epstein Barr Virus
EBV	Epstein Barr virus
ECM	Extracellular matrix
FBS	Fetal Bovine Serum
FP	Fluorescent protein
Gal C	Galactocerebroside C
Golli	Genes of Oligodendrocyte lineage
GFP	Green Fluorescent protein
HILO	Highly inclined and laminated optical sheet
LD50	Lethal dose 50%
LSM	Light Sheet Microscopy
LB	Luria-Bertani
LPC	Lysophosphatidylcholine

MSD	Mean Square displacement
MHT	Multiple hypothesis linking
MS	Multiple Sclerosis
MAG	Myelin Associated Glycoprotein
MBP	Myelin Basic Protein
MOG	Myelin Oligodendrocyte Glycoprotein
NF200	Neurofilament 200 dA isomer
NG2	Neurone/glial antigen 2
nsP	Non-structural Protein
OL	Oligodendrocyte
OPC	Oligodendrocyte Precursor cell
Opalin	Oligodendrocytic Myelin Paranodal And Inner Loop Protein
PFA	Paraformaldehyde
PRR	Pattern Recognition receptors
PNS	Peripheral Nervous system
PBS	Phosphate Buffered Saline
PIP2	Phosphatidylinositol 4,5-bisphosphate
PALM	Photoactivated light microscopy
PDGFαR	Platelet Derived Growth Factor Receptor α
PCR	Polymerase Chain Reaction
pmOL	Premyelinating oligodendrocyte
pOL	Preoligodendrocyte
PPMS	Primary Progressive Multiple Sclerosis
PRMS	Progressive Relapsing Multiple sclerosis
PLP	Proteolipid Protein
RRMS	Relapsing remitting multiple sclerosis
RNA	Ribonucleic acid

SPMS	Secondary Progressive multiple Sclerosis
SFV	SemLiki Forest Virus
SNR	Signal to noise ratio
SMI	Single molecule imaging
STORM	Stochastic optical reconstruction microscopy
SOC Media	Super Optimal broth with Catabolite repression media
TIRF	Total internal reflexion fluorescence
TAE	Tris/Acetate/EDTA

Chapter 1

Introduction and literature review

"Magic is just science that we don't understand yet"

- Arthur C Clarke

1.1 Overview of the Central nervous system

The nervous system encodes and regulates all the body's functions, and consists of two elements, the central nervous system (CNS), and the peripheral nervous system (PNS)[1,2]. The key processing centre within the nervous system is the CNS, which itself consists of two key elements, the brain and the spinal cord. This is the part of the nervous system which is responsible for cognition, emotions, reflexes, and sensory processing[1]. This contrasts with the PNS which possesses most of the sensory receptors, to provide information on both the internal and external environment[1]. The key function of the PNS is to relay information to the CNS for processing, and to initiate a response in effectors such as glands and skeletal muscle in regards to this information[1,2]. Due to the differences in functions within the CNS and PNS, these environments have different physiologies and use different transmitters to convey information. In order to maintain the environmental differences which characterise the CNS, as well as protect the CNS from inhomogeneity and pathogens, the central and peripheral systems are separated by a layer of tight-junctioning epithelial cells, known as ependymal cells[3,4].

1.1.1 The Brain

The brain is one of the most complicated and important organs within the human body. Forming the higher centres of the CNS, it is responsible for higher processing and coordinating all the functions of an individual[1,5]. A brain exists within the nervous system of all vertebrates and most invertebrates, and rests within the cranial cavity in the skull. It consists of many different regions, all of which are specialised in their functions. The main categories within the brain consists of the cerebrum, brain stem, and the cerebellum[1,2,5].

The cerebrum is the largest part of the brain consisting of two hemispheres, here is where "higher functions" are processed, including personality, emotion, and memory[5,6]. The outer part of the cerebrum is known as the cerebral cortex, mainly consisting of grey matter. The morphology of the cortex varies with smaller mammals having a smoother cortex, whereas large mammals have sulci and gyri which form a more folded morphology, allowing a greater volume of tissues and hence greater capacity of functions[7]. The cortex consists of 5 main lobes, all of which have specialised structure and function. These lobes are the frontal, occipital, parietal, temporal and insular lobes[5,8]. Each lobe specialises in the information it processes, with the frontal working on higher cognitive functions, such as risk taking behaviour, reasoning, problem solving, the parietal lobe processing sensory information such as auditory information, taste, and touch, the occipital lobe involved processing of optic information, as well as recognition of faces, temporal lobe dealing with language, and the insula involved in motivation, interoception and subjectivity[1,9,10]. Deeper within the cerebrum many structures exist consisting of structures such as the thalamus, amygdala, hippocampus, and basal ganglia[1]. These have roles in many functions such as memory, motor planning, pleasure, satiety, disgust, and attention[1,11].

Below the cerebrum is the brain stem which is heavily involved in the regulation of cardiac and respiratory function[2,5]. This area consists of the medulla oblongata, Pons, and mesencephalon. The medulla oblongata, commonly referred to as the medulla, is the lowest part of the brain connecting with the spinal cord[12]. The medulla plays a role within many reflexes, such as swallowing and the gag reflex, as well as thermal homeostasis, heart rate, and digestion[2,5]. Laying rostrally from the medulla is the pons[1,2,5]. The pons is the point of origin of four of the cranial nerves, and connects the medulla to the cerebellum. The pons

contains the pontine nuclei which relays information from the cerebral cortex to the cerebellum. Rostrally from the pons is the mesencephalon, also referred to as the midbrain, which play a role within the oculomotor system, and motor planning[13]. The midbrain contains many important structures, such as the red nucleus, which receives most of the output of the cerebellum, the substantia nigra, which is heavily involved in motor regulation and implicated in Parkinson's disease, and the superior & inferior colliculi which are heavily involved in gaze regulation and attention shifting[14–16].

The cerebellum exists posteriorly to the cerebrum, and forms a key part of the hind brain, consisting of the cerebellum and the brain stem[17,18]. The cerebellum, like the cerebrum, is divided into 2 hemispheres, divided by a structure referred to as the vermis, and has sulci and gyri, referred to as fissures and fossa[17,18]. The cerebellum has a more regular pattern of fissures and fossa than the cerebrum[17,18]. The cerebellum plays a role in motor coordination, precision and timing of movements. With damage causing impaired gait, equilibrium, and motor learning[17]. The cerebellum consists of 3 lobes, the anterior, posterior and flocculonodular lobes, which contain 4 deep nuclei which connect with other regions within the brain, the dentate, globose, emboliform and fastigial nuclei[5,17].

1.1.2 The Spinal cord

The spinal cord in addition to the lower part of the brain, known as the brain stem, make up the lower processing centres within the CNS[5,11]. These centres are responsible for most of the reflexive activities, in addition to the homeostatic actions, of the body. The spinal cord itself carries all impulses from the brain to the PNS, in addition to signals to the brain from the PNS, other than those conveyed by cranial nerves[1,11]. These impulses from the brain are carried by nerves that descend through the spinal cord till it reaches the spinal nerve at the appropriate

level, where the impulse is transmitted out of the spinal cord and is eventually conveyed to its effector by elements of the PNS. The spine has approximately 31 pairs of spinal nerves that either enter or exit the spinal cord at each vertebral level, these are 8 cervical nerves, 12 thoracic nerves, 5 lumbar nerves, 5 sacral nerves, and 1 coccygeal nerve[1,5,11,12]. A high concentration of spinal nerves are in the narrowing at the end of the spinal cord, conus medullaris, which produces the structure referred to as the cauda equina[11,12].

The spinal cord is a long tubular structure encased in a membrane known as the thecal sac within the vertebral canal[12,19]. It consists of 2 enlargements to this shape, known as the cervical and lumbar enlargements[11,12]. The cervical enlargement extends from the fourth cervical vertebra to the first thoracic vertebra, and is responsible for the nerves extending to and from the upper limbs. Inferior to the cervical enlargement is the lumbar enlargement, which extends from the ninth to the twelfth thoracic vertebra[11,12]. This enlargement is responsible for housing the nerves to and from the lower limbs. Inferior to this enlargement is the conus medullaris where the spinal cord terminates, which within adults arises between the first and second lumbar vertebra[11,12]. The spinal cord itself consists of grey matter, which exists within the centre within a butterfly shape, and white matter which surrounds it[1,5,11,12]. The grey matter receives and transmits information from the body, and is split into 2, the dorsal grey horn which receives sensory information and ventral grey horn which transmits motor information to the skeletal muscles[5,11,12]. The white matter within the spinal cord contains the spinal tracks, which transmits information up and down the spinal cord, examples of which are the ascending spinothalamic tracks for thermal and nociceptive information, and the descending corticospinal tracks conveying voluntary motor information[1,5,11,12].

1.1.3 The Blood Brain Barrier

The blood brain barrier (BBB) is a group of physiological occurrences which occur within the CNS in order to tightly regulate the movement of molecules, ions, and cells between blood and the CNS[20]. The microvasculature which effects the CNS is non-fenestrated, in order to maintain CNS homeostasis and allow efficient neural function[21,22]. This function mainly lies within the endothelial cells of the vasculature, but also is influenced by the pericytes surrounding them, the glial cells within the CNS, the neurones, and the immune system itself[23–25]. The composition of this structure also varies slightly between the brain and the spinal cord[19].

CNS endothelial cells are exceptionally thin compared to their analogues within the periphery[26]. These cells are held together by tight junctions to restrict large molecular movements[27–29], with a number of transporters for lipophilic, and nutrient molecules[30–33]. Endothelial cells within the BBB contain many more mitochondria than seen in other endothelial cells in the body, as maintenance of conditions within the CNS requires movement of molecules against their diffusion gradients[34].

Above endothelial cells lay the pericytes, which rarely contact the endothelial cells[35]. These cells are embedded within the basement membrane surrounding them[20,35]. Pericytes are essential for control of the diameter of the vasculature, as well as being involved within wound healing, and immunoregulation[20,36,37]. The interaction of pericytes with the endothelial cells prevent the expression of leukocyte adhesion molecules within the cells, as well as inhibiting molecule movement through transcytosis[38,39]. Pericytes also contact with astrocytes in order to receive information on neuronal actions to regulate blood flow[40]. Astrocytes themselves have also been shown to be important in the formation of the blood brain barrier[40,41].

The pericytes are embedded in an extracellular matrix referred to as the basement membrane, secreted by the pericytes, endothelial cells, and astrocytes within the system[42,43]. The basement membrane is composed of many secreted molecules such as laminins, glycoproteins, and collagen[20]. This provides processes which are signalling the vasculature an anchor as well as providing an extra filter for molecules being transported[20].

1.2 Cerebellum

The cerebellum is a key part of the hind brain[1,11]. Its name is derived from latin meaning little brain, due to its appearance as a smaller version of the brain[44]. The cerebellum plays a role in motor control and the control of cognitive functions, like attention, however, it should be noted that it does not initiate motor activity but plays a role in the coordination, precision and timing of movements[17,44,45]. Damage to the Cerebellum results in a variety of impairments including the inability to perform fine movements, impaired gait and posture, poor equilibrium, and impaired motor learning[18,46,47]. Unlike the cerebrum, where damage would cause impairments contralaterally, when cerebellar damage causes motor impairments they tend to occur ipsilaterally[48]. As well as motor and balance impairments, cerebellar injury can also induce cerebellar affective syndrome, where the symptoms are more emotional and behavioural[49]. The spectrum of cerebellar affective syndrome symptoms include distractibility, impulsiveness, anxiety, inability to understand social boundaries, aggression, dysphoria, and ritualistic behaviours[49].

1.2.1 Anatomy of the cerebellum

The cerebellum is located in the posterior cranial fossa, behind the pons and medulla, with all connections to and from the cerebellum travelling through the pons[11,17,18]. Like the Cerebrum the cerebellum consists of 2 hemispheres, with gyri, referred to as folia, and a midline, referred to as the vermis[11,18,45]. Unlike the cerebrum which has an irregular pattern to its sulci and gyri, the folia in the cerebellum are arranged in parallel[11,17,18]. The cerebellum is covered in the Tentorium Cerebelli, which is the layer of dura mater which separates the cerebellum from the cerebrum[50]. The surface of the cerebellum is exclusively grey matter, with the white matter within the cerebellum forming the structure referred to as the arbor vitea, due to the

similarity of its structure with a branching tree[51]. The arbor vitae conceals 4 cerebellar nuclei, the dentate, globose, emboliform, and fastigial (Figure 1.2 A)[17]. The globose and emboliform nuclei are referred together as the interposed nuclei, and with the fastigial nuclei are a component of the spinocerebellum[11,17]. Connecting the cerebellum to the rest of the nervous system are the 3 cerebellar peduncles[11,17]. The superior peduncle is mainly used to output information to the cerebral cortex, the middle peduncle receive inputs from the pontine nuclei which relay information from the cortex, the inferior peduncle receives inputs from the vestibular nuclei, spine and tegmentum, and output to the vestibular nuclei and reticular formation[11,17]. The cerebellum has 3 main arteries which supply it, the superior cerebellar, anterior inferior cerebellar, and posterior inferior cerebellar[11,52]. The superior cerebellar artery supplies the upper region of the cerebellum, the anterior inferior supplies the front of the under surface of the cerebellum, and the posterior inferior serves the cerebellar notch and the rest of the under surface. All the arteries anastomose within the pia matter[52].

The cerebellum is subdivided into 3 lobes the anterior lobe, the posterior lobe, and the flocculonodular lobe (Figure 1.1)[17,18]. The flocculonodular lobe, also known as the vestibulocerebellum or archicerebellum, is the oldest part of the cerebellum[17]. Its main connection is the vestibular nuclei, as well as sensory inputs. It is involved in balance and spatial orientation, as seen when damage occurs, as it leads to gait and equilibrium issues[17]. The medial areas of the anterior and posterior lobes form the paleocerebellum, also known as the spinocerebellum, this region fine tunes limb and body movememnts[17,44,51]. The spinocerebellum receives mainly proprioceptive and cranial trigeminal inputs, as well as visual and auditory[17,44,51]. Fibres from this region project mainly to cerebellar nuclei to modulate descending motor signals in the cerebrum and brain stem. The lateral zone consists of the

lateral regions of the anterior and posterior lobes, and is the largest part of the cerebellum, also known as the cerebrocerebellum or neocerebellum[17,44]. This region receives inputs from the cerebral cortex, mainly the parietal lobe, through the pontine nuclei, and out puts are mainly to the red nucleus and thalamus. It is suggested that this region plays a role in movement and cognitive planning. Damage to this region leads to dysarthria, dysmetria, intention tremors, as wells as errors in speed force and direction of movements[11,53].

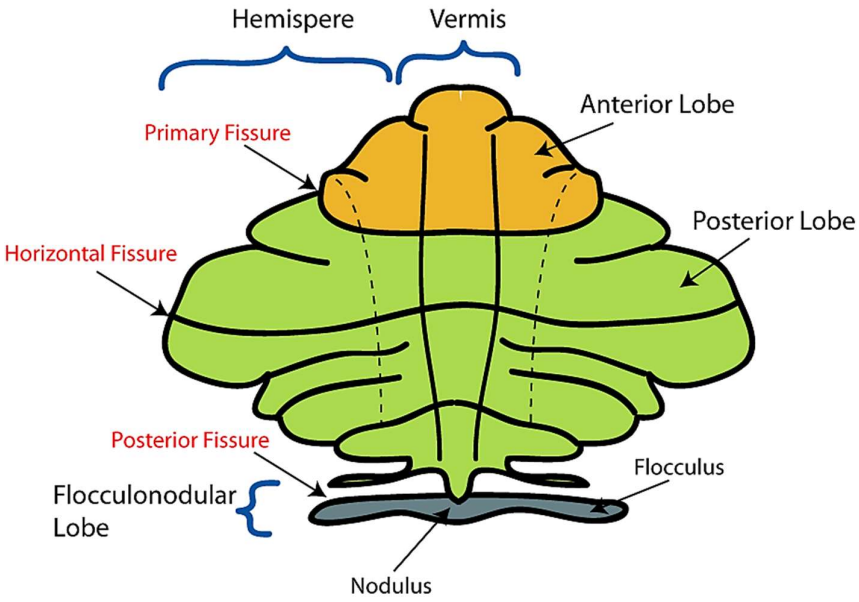

Figure 1.1: Cerebellar anatomy, showing its lobular structures, where they are, and how they are bounded. The anterior lobe ends at the primary fissure where the posterior lobe starts, the posterior fissure separates this from the flocculonodular lobe. This figure was extracted from O'Brien and Hill 2016. [18]

1.2.2 Cell types and circuitry of the cerebellum

The cerebellum has more neurones than the rest of the brain, with the total being more than 3 times that of the neocortex[54]. These neurones produce 3 types of axonal projections mossy fibres, climbing fibres, and parallel fibres[11,17]. Mossy fibre projections originate from the pontine nuclei and project excitatory synapses onto the granule cells in the granule layer of the cerebellum, which project to Purkinji cells through parallel fibres, which ultimately signal

the deep nuclei, some mossy fibres may also project directly to the deep nuclei as well[11,17]. Within the granule layer the ends of mossy fibres form enlargements known as rosettes, which can contact up to 20 granule cells at a time[55,56]. The contacts between granule cells and mossy fibres are referred to as glomeruli[56]. Climbing fibres project to Purkinji cells, and form collaterals to deep nuclei[55,56]. Climbing fibres transfer signals from inferior olivary nuclei to Purkinji cells, each climbing fibre inputs into 1 Purkinji cell, but makes many synapses with it[11,17,55,56]. Climbing fibres have a low fire rate, however, they induce multiple action potentials due to the multiple synapses[11,17,55,56]. The third type of projection is the parallel fibre connections, which originate from bifurcations of granule cell projection and project onto Purkinji cells, Golgi cells, basket cells and stellate cells[11,17,55,56]. The signal of each parallel fibre is weak, and projects onto multiple Purkinji cells[17]. In order to excite the Purkinji cells multiple parallel fibres must be active. Many of the larger projections within the cerebellum tend to project to the deep cerebellar nuclei and use glutamate as a neurotransmitter, producing excitatory synapses[11,17,55,56]. On the other hand, smaller cells tend to be GABAergic, and tend to project to the inferior olivary nucleus[17,55].

The Cerebellum consists of 3 cellular layers, the granular layer, Purkinji layer, and the molecular layer (Figure 1.2 C)[11,17,55,56]. Deepest layer is the granule layer which is densely packed with granule cells and interneurons. Granule cells are some of the smallest neurones within the brain, but amount to about ¾ of the neurones in the brain[11,17,55,56]. Granule cells project between 4 and 5 dendrites, ending with a dendritic enlargement, known as a dendritic claw[11,17,55]. These dendritic claws receive excitatory inputs from mossy fibres, and inhibitory inputs from Golgi cells[11,17,55]. Granule cell projections tend to be thin and unmyelinated, and project to Purkinji cells. Granule fibres project up to the molecular layer, where they bifurcate

and form parallel fibres, making the characteristic T shape[11,17,55]. The next layer along is the Purkinji layer where the cell bodies of the Purkinji cells lie[11,17,55,56]. Purkinji cells are distinguished by their flattened profusely branching dendritic trees. All the dendrites form in the plane perpendicular to the cerebellar folds[17,55]. Purkinji cells have many dendritic spines to receive inputs from multiple parallel fibres, as their signals are weak and many are needed to induce an action potential[17,55]. Purkinji cells have spherical cell bodies, which express the marker calbindin, and use GABA as their neurotransmitter[11,17,55,56]. The outer most layer within the cerebellum is the molecular layer where the dendritic trees of the Purkinji cells project. The parallel fibres cross this layer and synapse with the Purkinji cells and interneurons such as stellate and basket cells also form inhibitory synapses with Purkinji cells here[11,17,55,56].

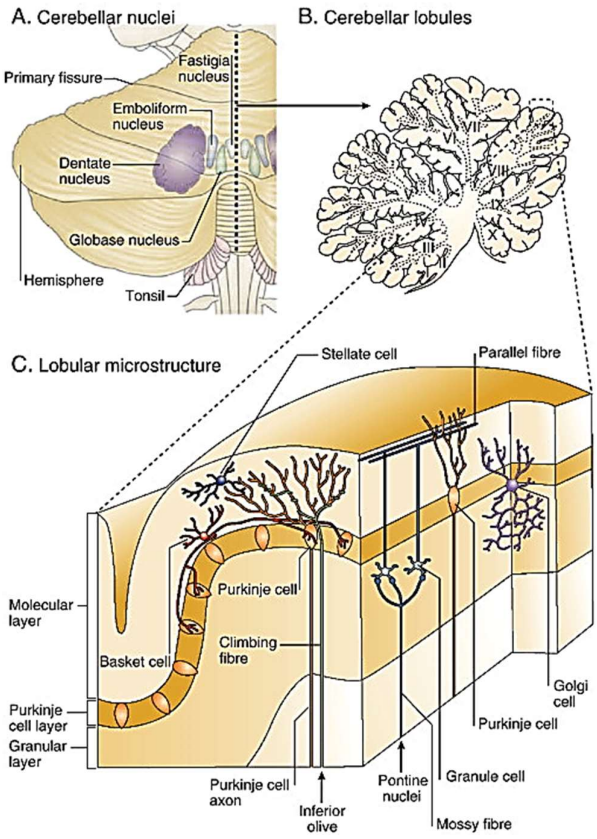

Figure 1.2: Structure of the Cerebellum. A) Depiction of a singular hemisphere of the cerebellum, showing location of cerebellar nuclei. B) Cross sectional image of the cerebellum showing the structure, with the arbor vitae in the centre. C) Depiction of the cellular structure of the cerebellum, showing the location of the various layers and the organisation within the layer. These images have been extracted from Moulton et al 2010.[57]

1.3 Neurones

The nervous system is divided into the CNS, which consists of the brain and spinal cord, and the PNS, which consists of the rest of the nervous system elements[1,58]. There are two key cell types within the nervous system, the neurones and the glial cells[11].

Neurones are seen as the main cells of the nervous system, as they are essential to produce the observed activity of the brain[11,59,60]. The human brain has approximately 86 million neurones, most of which are within the cerebellum[61,62]. The general structure of a neurone consists of dendrites to receive incoming information, this information is transmitted to the cell body which contains the nucleus and intracellular organelles, and an axon, which relays the information away from the cell body, and transfers signals to other cells[1,11,51]. Although many cells contain all these structures they are not present in all neurones, such as retinal amacrine cells which do not have axons or photoreceptors which have no dendrites[1,11,63]. Clusters of neurones working on similar functions are known as ganglia outside of the brain, and within the brain as nuclei[11].

The role of neurones is to transfer and integrate information to produce a response to a stimuli. These signals are normally conducted through changes in the electrochemical gradient of the cell, known as action potentials[64] (Figure 1.3). At rest neurones have a net negative membrane potential of about -70mV, which is maintained by the ion channels within the cells and the presence of large anions which are too large to cross the membrane[1,11]. This is the state of the neurone until it receives an input. These inputs are normally received by the dendrites, through a variety of ways. One example is the dendrites of skin stretch receptors, where stretch in the ruffini corpuscle causes the dendrites of the sensory neurone to become

discharged[1,11]. This can also be achieved by inputs from other dendrites, in this case there can be a number of dendrites, or a number of synapses involved[1,11]. These signals are then conducted to the cell body, where the signals from all the dendrites are processed, and summated, if the resulting signals are large enough an action potential is initiated within the axon[1,11]. Action potential generation occurs when a large enough depolarising signal is received that pushes the membrane potential past the threshold, causing voltage-gated sodium ion channels to open, as the sodium concentration intracellularly is low, and the electrochemical gradients favour influx, it diffuses in, causing further depolarisation[1,11,64]. Activated sodium channels enter an inactive state within 1-2 ms of activation terminating the depolarising influx. The membrane potential is then restored to the resting potential by the delayed opening of voltage gated potassium channels, which allow potassium ion efflux along the electrochemical gradients created by the action potential and pre-existing high levels of potassium ions inside the neuron, hyperpolarising the cell below resting potential. The potassium channels then close, and the sodium potassium pumps within the neuronal plasma membrane re-establish the resting potential by importing potassium and exporting sodium at a 3:2 ratio[1,11,64]. The depolarisation is unidirectional as the parts of the preceding region of the axon will remain unresponsive to further depolarisation as the voltage gated sodium channels will be in their refractory periods and the region will be in a hyperpolarised state[1,11,64]. An important feature of the action potential as a signalling mechanism is that the process is time exhaustive as it requires channel opening, and the restoration of ion gradients by slow active transporter pumps, so for the nervous system to work efficiently some of its neurones acquire an insulating material, known as myelin[65], to allow the signal to travel further distances without need for signal boosts from action potential generation, this process is known as

saltatory conduction[1,11,64,66–68]. Gaps occur between segments of myelination known as nodes of Ranvier, these exist to modulate the signal allowing interactions with ligands, other processes and allows the signal to be amplified[1,11,64].

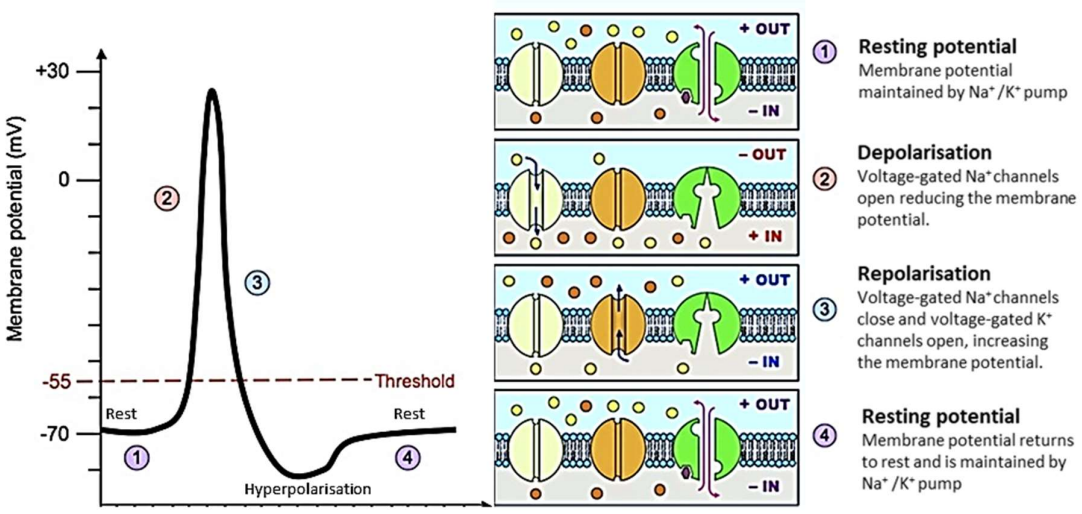

Figure 1.3: Depiction of an action potential, showing the ion movements during each phase of the action potential. 1 shows the membrane at rest where the sodium potassium pump maintains the membrane potential at approximately -70mV. 2 shows depolarisation of the membrane following stimulation beyond threshold. Here the membrane potential is reduced to approximately 30mV as sodium diffuses in as the voltage-gated sodium channels open. 3 voltage-gated sodium channels close due to refractory, and voltage-gated potassium channels open. This repolarises the membrane beyond resting potential. 4 the membrane potential returns to rest, achieved by the sodium potassium pump.

Based on their functions neurones are split into 3 groups, sensory neurones, motor neurones, and interneurons[58,69]. Sensory neurones receive information from sensory receptors on the state of either the environment (exteroceptive), the state of the body (interoceptive) or body position (proprioceptive)[58]. These cells tend to be pseudounipolar, as they have axons which branch into 2, one of which take on the function of a dendrite whilst the other is used for transmission, in the case of primary sensory neurones this allows their cell bodies to be in the dorsal root ganglia or the cranial sensory ganglia[5,58,69,70]. The next group of neurones are the motor neurones, these carry information to effectors such as muscles, organs, and glands[5].

Motor neurones are much larger than sensory neurones and tend to be multiple polar cells[58,70]. There are 3 classifications of motor neurones, somatic motor neurones, special visceral, and general visceral[58,71]. Somatic neurones innervate skeletal muscles and tend to be involved in locomotion, special visceral which innervates muscles involved with facial expression, phonation, chewing and swallowing[1,11,58,71]. The third classification is the general visceral neurones, which innervates smooth muscle, glands, and indirectly signals cardiac muscle[1,11,58,71]. Interneurones may receive information and send information from other neurones[1,11,58,71]. These neurones play a role in signal integration, and learning. These cells can make many contacts, like in the hippocampus where interneurones make about 1000 synapses with other cells[58].

The structure of neurones are divided into about 4 groups, depending on their numbers of projections from the cell body, and the position of their cell bodies (Figure 1.4). Unipolar neurones are not normally seen in vertebrates, as cells which present as unipolar, such as photoreceptor cells, start of life as bipolar cells and therefore are termed pseudounipolar[72]. Bipolar cells have 2 projections from the cell body, an example of which within the body would be retinal bipolar cells which receive inputs from photoreceptors and transmits them to the retinal ganglion cells[5,58,69,70]. Intermediately between the unipolar and bipolar cells is the pseudounipolar cells, these cells have one projection from the cell body, however, this branches into 2 fibres[5,58,69,70]. These cells are commonly utilised as sensory fibres. Beyond bipolar cells are multipolar cells, which have numerous projections from the cell body, this is the structure more commonly associated with neurones, as many motor and interneurones use this structure, an example of which are the purkinji cells within the cerebellum[5,58,69,70].

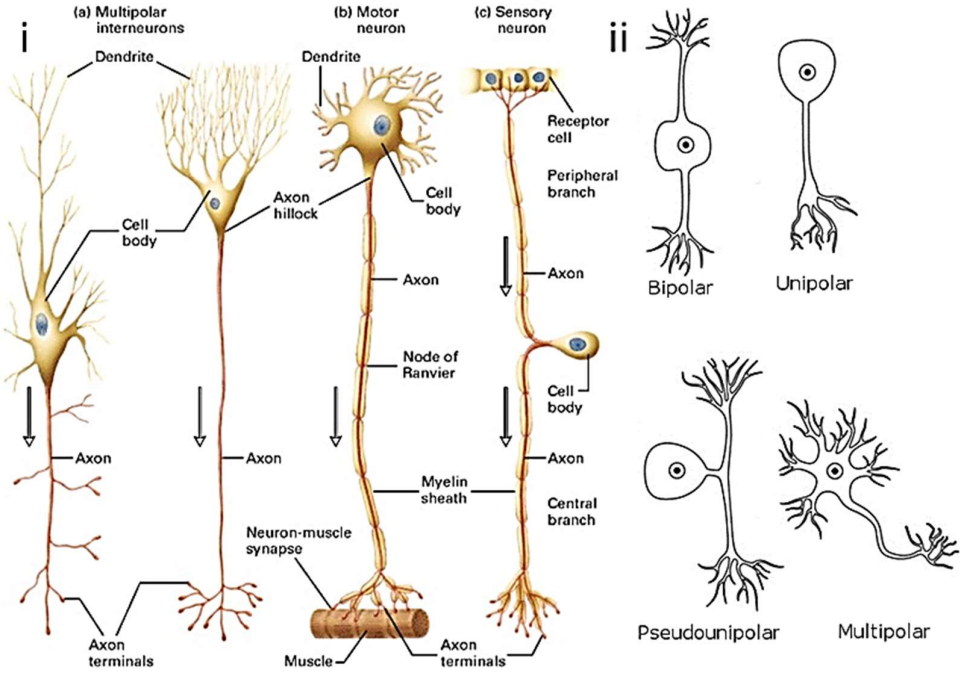

Figure 1.4: Classifications of neurones. i) Depiction of the different types of neurones, showing their variations in sizes, and number, of projections, and location of the cell body. ii) The different categorisations of neurone morphologies, based on the number of projections from the soma existent, unipolar cells are not exceptionally common within the human body, but can exist with cells like amacrine cells[58]. Figures were extracted from Concepts of Biology—1st Canadian Edition[73].

1.3.1 Markers of neurones

Different neurones within the body express a number of unique molecules which can be used to identify them as neurones. Within this work only two of these were addressed for use with CNS neurones.

Neurofilament (NF) is the name given to the intermediate filaments found the cytoplasm of neurones. These form the cytoskeleton of the neurones with the microtubules and microfilaments. There are up to 5 proteins which neurofilament is composed of, which can co-assemble in different formations for different neuronal subtypes. Of key interest in myelinating cells is neurofilament H, which exists as a 200kDa band in SDS page, also referred to neurofilament-200 (NF200)[46]. Expression of this neurofilament is low in developing

neurones, but increases postnatally during myelination[74,75]. Another interesting Neurofilament is vimentin, which is up regulated for neurite outgrowth in the CNS[74,76].

Calbindin is a marker for projecting neurones, such as purkinji cells and neocortical interneurones. Calbindin is a calcium binding protein, with some cross reactivity with magnesium, however, it has a greater affinity to calcium[77]. For this reason calbindin is suggested to be a calcium sensor rather than a buffer[78–80]. This is also supported as calbindin undergoes a conformational change upon calcium binding but not upon magnesium binding, which could aid in its role within calcium transport[81]. In addition to this calbindin is known to play a role in the prevention of apoptosis within osteoblast cells, through the inhibition caspase-3[77].

1.4 Glial Cells

The second main component of the CNS, working alongside the neurones, are the glial cells. Glial cells first were described by Virchow who referred to them as nervenkitt, which was German for nerve glue[82]. The name was later translated to Greek leading to the name neuroglia. These cells are smaller than neurones, and exist within both the CNS and PNS, however, as these cells were referred to as nerve glue the role of these cells were neglected for a number of years[60,82]. Glia constitute to between 33% to 66% of the brain mass depending on the organism, therefore there must be more to their roles than to fill the space neurones don't occupy[54,59,83]. Glial cells do not participate directly within the nervous signally within the human brain, however glia are believed to outnumber the neurones 3 to 1. Although the exact numbers of glia in relation to neurones is a source of contention[61,84,85]. The discovery of this phenomenon has led to a resurgence of research into glial cells in the recent years, showing that these cells have numerous important roles within the nervous system. Their known roles include maintaining the cellular environment and ionic milieu within the CNS, providing tropic support to neurones, guiding neural development both through signalling and as scaffolds in early development, controlling the uptake of neurotransmitters, and protecting the brain from pathogenic attack[60,86–92]. Glial cells have been characterised into 3 categories, the macroglia, consisting of the astrocytes and oligodendrocytes, and microglia. These different type of glia each display unique morphological and functional properties[11] (Figure 1.5).

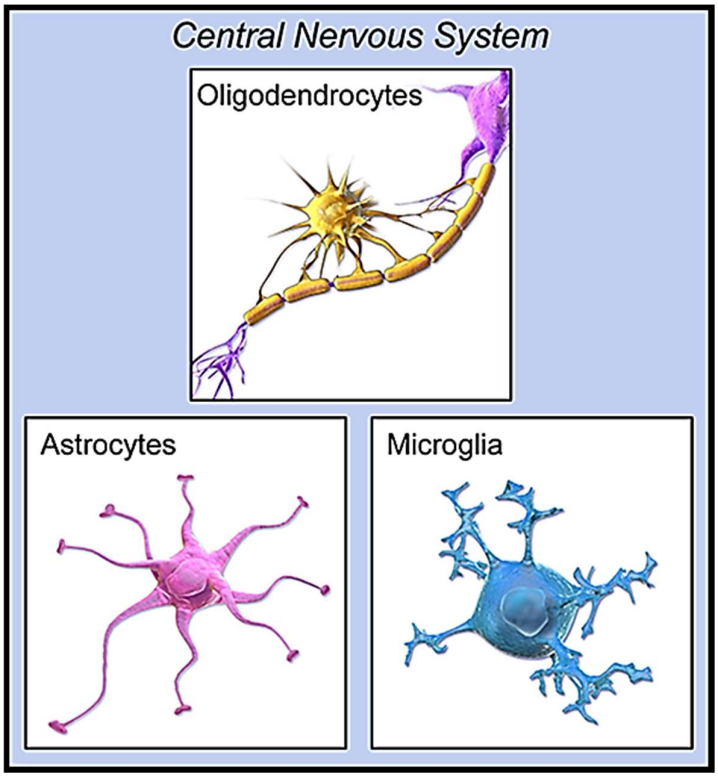

Figure 1.5: Types of Neuroglia, not to scale. Figure depicts an Oligodendrocyte myelinating an axon, Astrocyte, and a microglial cell. Image is modified from Blausen Medical 2014[93].

1.4.1 Microglia

Microglia are seen as important for producing an immune response within the CNS. They are commonly referred to as the macrophages of the nervous system, as they have share many properties with peripheral macrophages[60]. Microglia are small highly ramified cells, which patrol the CNS at rest, and when a pathogen is detected or the blood brain barrier is compromised, are known to change into an active state to perform a phagocytic role[91]. They exist in similar numbers in the CNS to neurones, and have highly dynamic, active processes at rest. Microglia don't originate from the ectoderm like other glia, and the majority of microglial cells are made postnatally[94,95]. This could be related to the role of microglia in synaptic pruning, which would be in higher demand postnatally[96,97].

1.4.2 Astrocytes

Astrocytes are seen as mainly support cells within the CNS[60]. This is mainly due to its role in maintaining the extracellular environment[59]. However, astrocytes have been observed to have a number of different functions within the CNS. The first role is its role in producing elements of the extracellular matrix (ECM) to support neurones, as well as controlling the volume of ECM [98,99]. In addition to controlling the ECM composition the astrocytes play a role in controlling the environment within the synapse, astrocytes are known to wrap around the pre- and post- synaptic termini to form a tripartite synapse[100–102] . This allows the astrocyte to control the signalling within the synapse, through the control of the movement of ions, the uptake of neurotransmitters, or the release of gliotransmitters[103,104]. These functions can be facilitated as astrocytes possess receptors for various neurotransmitters[59]. In addition to this signalling it is suggested that astrocytes may also signal other neurones[59,105], this may be achieved through gliotransmitters, but also through the control of metabolites as astrocytes contact both neurones and capillaries to shuttle nutrients and metabolites between them[106,107].

Astrocytes also play a role in the protection of the CNS from pathogenic material, it has been shown astrocytes play a role in the formation and control of the blood brain barrier, which prevents pathogenic material from the periphery from entering the CNS[25,59]. In addition to this, it has also been observed that astrocytes play a role in the immune response to pathogens, and are known to be the main source of reactive oxygen species scavengers, and to be involved in the formation of neural scars[59,86,108–115].

1.4.3 Oligodendrocytes

Oligodendrocytes (OLs) are the myelinating glial cells of the CNS (Figure 1.6). This insulation provides the neurones with a lipid rich coating, known as the myelin sheath, which has a low water content making it well suited to provide the cells with electrical insulation, and is not universal, with OLs only selecting axons with diameters greater than 0.2 µm to myelinate[90]. In order to ensure correct myelination, OLs have receptors which detect neuronal activation, which plays a role in OL differentiation, and myelination[116,117]. Part of this signalling between myelin and neurones also plays a role in channel positioning, with myelination causing sodium channels to cluster at nodes of ranvier[118–120]. Myelin is known to also play a role in trophic support for axons, and is needed to maintain long axons[68,121,122]. Conditions where myelination is impaired, such as leukodystrophies and multiple sclerosis, lead to reduced cognitive and neurological function, and loss of various abilities.

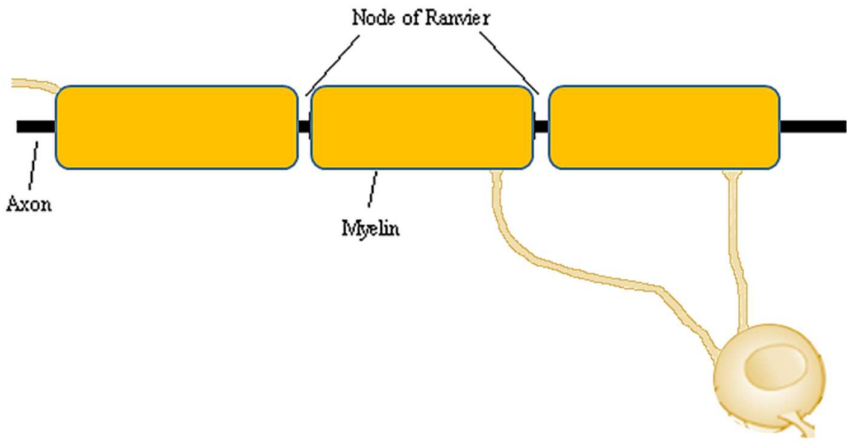

Figure 1.6: Myelination from an oligodendrocyte. Figure shows the organisation of myelin with nodes of Ranvier between myelin segments to allow signal propagation. The figure also shows that an axon may have many myelin sheaths from a singular oligodendrocyte, and may also have sheaths from a number of oligodendrocytes.

1.4.4 Myelin

One of the key functions of OLs is the production of myelin. Myelin was first described by Antoni Van Leeuwenhoek in 1717 who identified nerves consisting of vessels (myelin) and canals (neurones)[67]. Unfortunately as the secrets of Leeuwenhoek's lenses died with him, this was not corroborated until Ehrenberg who showed that nerves consist of a marrow sheath (myelin) and brain tube (neurones)[123]. Following this re-discovery numerous researchers looked into the marrow sheath, and many different names were produced. This led to Virchow coining the word myelin to identify these sheaths as well as some other entities with the same colour, based on the word myelos which refers to the bone marrow like colour[124]. The function of this sheath and how it was produced was not understood, with the dominating theory of the time being that the myelin sheath was produced by the axon itself. It was not till the discovery of the osmium stain, which allowed myelin to further be understood, that myelin was able to be defined as fibres rather than globules[67,125]. These fibres of myelin were discovered to form concentric layers of 170-186Å thickness in the PNS and approximately 160 Å thickness in the CNS. The Bunge lab found that within the CNS these layers are produced by OLs, whose processes can extend as far as 12µm, and that individual OLs can produce multiple regions of myelination (internodes) on multiple axons[67,126–129]. Myelin was discovered to be 70-85% lipid, and 15-30% protein with differences in these ratios arising between the CNS and PNS[130].

Virchow rightfully identified that the role of the myelin sheath was to insulate the axon (Virchow 1858), which was later supported by Ranvier[125]. This insulation was later understood to be key for salutatory conduction [66,131–133]. Saltatory conduction refers to the ability to

propagate an action potential along myelinated fibres, providing a faster conduction velocity. This works as the axon only needs to depolarise at nodes of Ranvier. Ranvier and Saious suggested that myelin plays a role in nutrition and energetic support within the axon, this was supported by the work of Funfschilling and Lee[125,134–136].

The myelin sheath is a multilamellar structure composed of flattened myelin membrane, the integrity of which determines the speed of transmission (Figure 1.7)[137]. The sheath contains 2 regions which can be identified by electron microscopy, the major dense line, which is formed by the adherence of the cytosolic surfaces of the plasma membrane, and the intraperiod line, which is formed by the extracellular surfaces[88,137].

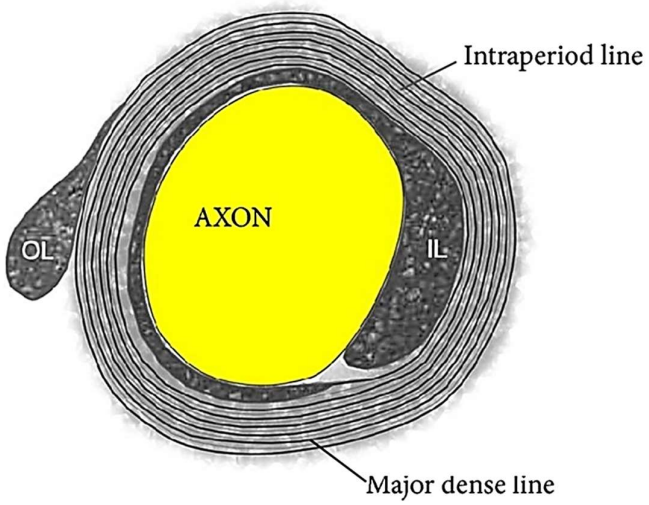

Figure 1.7: Myelin sheath surrounding an axon. The oligodendrocyte extends its flattened process to make concentric layers of myelin. The major dense line is produced where 2 cytosolic regions of membrane adhere, whereas the intraperiod is produced by the extracellular surfaces of the membrane. The cytoplasmic content of the process is compacted and accumulates in small pockets, the pockets that are near the axon form the inner loop (IL), whereas pockets closer to the periphery produce the outer loop (OL). Image from Greer 2013[138]

1.4.5 Myelin Damage

Damage to existing myelin (Demyelination) has profound effects on neurological function, and can lead to symptoms such as neuropathic pain, myasthenia, and spasms[139]. Traumatic spinal cord injury causes a disruption within the communication between glia and axons, leading to demyelination and loss of function. The primary trauma causes physical damage to the myelin, and compaction of the neurone. This leads to a disruption in ion dynamics in the CNS, which affects the conductivity within the trauma site[140]. Although the mechanical injury from the primary trauma causes damage, the secondary trauma which occurs a number of hours after this causes the most damage[141]. The secondary damage can occur due to a variety of reasons including ischemia, haemorrhaging, free radical production, and immune system activity, the result of which is more necrosis. Here the cascade of events causes the damage to spread from the original site of injury to adjacent sites, this forms an environment which is not accommodating to regeneration within the spinal cord, which ultimately leads to irreversible loss of function. This damage is self-propagating within and around the injury site[142]. For this reason the repair of myelin (remyelination) is key to pave the way for DNA regeneration[143]. This works via two mechanisms, firstly myelin restores impulse conduction by preventing signal loss, and secondly myelin reduces the vulnerability of axons by acting as both a physical barrier for the noxious signals within the tissue, and a source of trophic support.

CNS inflammation itself is one of the most common causes of myelin damage; a prominent example of which is multiple sclerosis (MS). Multiple sclerosis is one of the most extensively researched demyelinating diseases, whose cause is still unclear[142]. It has previously been

found that patients suffering from MS exhibit lesions within the CNS, which lack myelinating OLs, and possess an immune response within these lesions against the myelin[47,144,145]. Both of these symptoms impede successful re-myelination within these patients. B cells and T cells have been shown to be involved in the pathogenicity of MS, with these cells entering the CNS by permeabilising the blood brain barrier, and producing an autoimmune response to myelin antigens[24,146,147].Other immune cells are recruited through the release of pro-inflammatory cytokines which exacerbates the demyelination and OL death[139].

1.4.6 Remyelination

Remyelination occurs in several stages, and is a response to demyelination[143]. Progenitor cells migrate into areas where demyelination has occurred, and differentiate into mature OLs, which are used to myelinate the exposed regions of the axon. The mature OLs extend processes towards the injured axon, using signals from the extracellular matrix. These processes produce myelin proteins and synthesise myelin membrane, which wraps itself in several layers around the axon. The myelin proteins are synthesised within the processes near the site of remyelination, rather than within the cell body, this is believed to occur in this manner to support the efficiency of the process of re-myelination[90]. Although remyelination does occur spontaneously, the quantity of this is inadequate to cause functional sensory and motor recovery in conditions such as traumatic spinal cord injury or MS[142]. This remyelination has also been shown to produce myelin which is not structurally the same as the original myelin sheath, with remyelination producing shorter and thinner internodes compared to those on normal axons[148]. These shorter myelin structures have a detrimental effect on the conduction speeds of the axon, as there are more nodes of Ranvier and therefore more of a

need for signal propagation (Figure 1.8). These myelin sheaths are adequate in restoring near normal function to the axons, however, a mild loss of ability is still apparent[149].

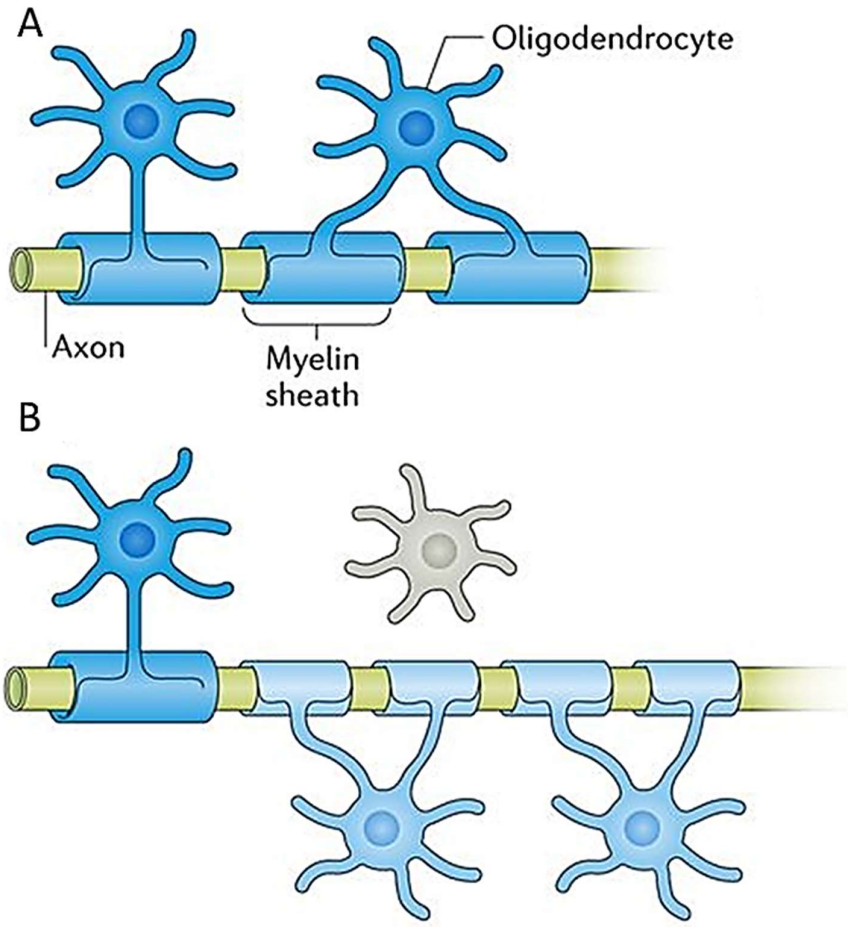

Figure 1.8: Depiction of axon myelination before and after remyelination. A) Depiction of myelination within an axon. As can be seen axons can be myelinated multiple times from a single oligodendrocyte and contain segments of myelination from multiple oligodendrocytes B) Depiction of remyelination of an axon. It can be seen that segments of remyelination (light Blue) form shorter than the original myelination (Dark Blue). Image was modified Franklin & ffrench-Constant 2017[150].

1.4.7 Myelin Proteins

Although the majority of the composition of myelin is lipids, proteins make up approximately a third of myelin[88,130]. These proteins play a key roles in the structure and function of myelin.

Cyclic-nucleotide-phosphodiesterase (CNP) constitutes 4% of the total myelin protein. It is known as a Wolfgram protein as its existence was suspected by Wolfgram when a group of proteins were found to be insoluble in a mix of chloroform and methanol[88]. CNP is found at a high concentration in immature myelin, however, it is not found in mature compact myelin when immunocytochemically stained for[88]. It has been suggested CNP has a role in the formation of myelin through membrane expansion as overexpression of CNP has been shown to cause irregular membrane expansion in OLs[151].

Myelin Associated Glycoprotein (MAG) is a membrane spanning protein from the immunoglobin superfamily[88]. Within the adult rat CNS MAG is limited to the periaxonal collar of the myelin sheath, where as in the PNS it is largely distributed in the intermodal regions of myelin. Knockouts of MAG have been shown to allow normal functioning myelin, however, abnormal formation of a periaxonal cytoplasmic collar, and has organelles within the lamellae [152]. Over expression of MAG has been shown in the PNS to cause over myelination, suggesting it has a role in surface detection, which is confirmed by studies using anti-MAG antibodies where it has been shown MAG plays a role in neurone, glia interactions[153,154].

Myelin Oligodendrocyte Glycoprotein (MOG) was first identified as an antigen for inducing demyelination[88]. MOG is a myelin protein which is only present in mammalian species, and is highly conserved. MOG is localised to the outer lamellae of compact myelin, and tends to be used as a marker for OL maturation[88].

Myelin proteolipid protein (PLP) corresponds to approximately 50% of myelin proteins[88]. PLPs are located on the major dense line and intraperiodic line of myelin. PLP knock out in mice

does not affect the competency of OLs to myelinate, however, the myelin formed is less stable shown with condensation in the intraperiodic lines[155]. PLP knock out also causes axonal swelling in the neurone suggesting that subtle alterations in myelin structure may affect axonal viability[88]. Over expression of PLP perturbs the formation of myelin and the viability of OLs[156]. It has also been shown that over expression of PLP reduces the quantity of other myelin proteins such as myelin basic protein MBP, which could account for the effects on OL viability[157].

The **Myelin Basic Protein (MBP)** content of myelin constitutes approximately 30% of the total protein[88], and has been found to be expressed in mice as early as embryonic day 14[158] . Deletion of the MBP gene in mice, such as that which occurs in shiverer mutant mice, results in a lack of a major dense line in the myelin structure due to its incorrect compaction [159]. Post-translational modification of MBP through methylation is believed to be important for the compaction role of MBP[160]. Recent findings have suggested that MBP drives myelin biogenesis using phase interactions[161]. These phase interactions are mediated by hydrophobic interactions from the phenylalanine residues in MBP, and have been implicated in forming a structural mesh within myelin to cause compaction[161]. This mesh is suggested to play a role in the extrusion of other myelin proteins to the periphery of the myelin leaflet, by making the myelin leaflet less permeable to molecules above a certain size[161]. MBP thus far is the only myelin protein known to be required for generating compact myelin sheaths[162].

1.4.8 Oligodendrocyte Markers

Antigenic markers are used to identify OLs, their phase of maturity and the cells leading up to mature OLs. There are several markers which can be identified for OLs, and their precursor cells (Figure 1.9). A few key myelin markers are addressed here.

The OL transcription factors, Olig1/2, are useful in determining an OL lineage, as they are present from OL precursor stage throughout to mature OL stage[163,164]. Olig1/2 are both members of the basic helix loop helix family, with Olig2 producing a 323 amino acid long peptide, and olig1 producing one of 271 amino acids[165–167]. Both proteins are highly associated with chromosome 21, this has led Olig2 to be implicated with a role within Down syndrome, due to its actions to regions close to the Down syndrome critical region[166,168]. At this region transcription factors have been shown to have actions in the production of reactive astrocytes, neural repair, and OL precursor differentiation[164,169–172].

Prior to committing to an OL path, oligodendrocyte precursor cells (OPCs) express Neurone/glial antigen 2 (NG2). NG2 is a chrondroitin sulphate proteoglycan, a class of proteins known to be upregulated in neural regeneration, and cell adhesion[173–175]. NG2 itself has been shown to be involved in cell adhesion, motility, cytoskeletal organisation, and outgrowth, as well as repulsive to neurones[174,176–184]. It is first expressed at embryonic day 14, and can be seen throughout the hindbrain following embryonic day 16[185]. At embryonic day 17 NG2 expression is concurrent with that of platelet derived growth factor α receptor (PDGFαR)[185,186]. Expression of NG2 reaches its maximum density at postnatal day 10, and then is lost from maturing OLs a few days later[186–188]. NG2 is not only expressed within OPCs but also within pericytes so PDGFαR tends to be used when immunopanning for mice OPCs[189–191].

Platelet derived growth factor receptor α (PDGFαR) is a tyrosine kinase receptor with a high affinity to all isoforms of platelet derived growth factor[192]. Platelet derived growth factors are abundant throughout different parts of the body, such as smooth muscles, fibroblasts[193], and within the CNS platelet derived growth factor A is expressed by neurones and astrocytes[194]. They play a role in processes such as angiogenesis, gastrulation, and alveolar development, and more specifically within OPCs they are involved in proliferation, migration, and maturation[192,193]. PDGFαR is expressed from embryonic day 15, and is expressed concurrently with NG2 at embryonic day 17[185,186,192].

A2B5 is a marker for gangliosides within OL lineage cells, in particular the GQ ganglioside, and used to mark the OPC phase. Gangliosides exist in large quantities within the CNS[195]. They have many intercellular roles including intercellular trafficking and cell signalling[196–198]. It is a commonly used OPC marker *in vitro*, but is also useful to mark neuronal progenitors, therefore A2B5 is not useful as a specific *in vivo* marker for OPC[199–201].

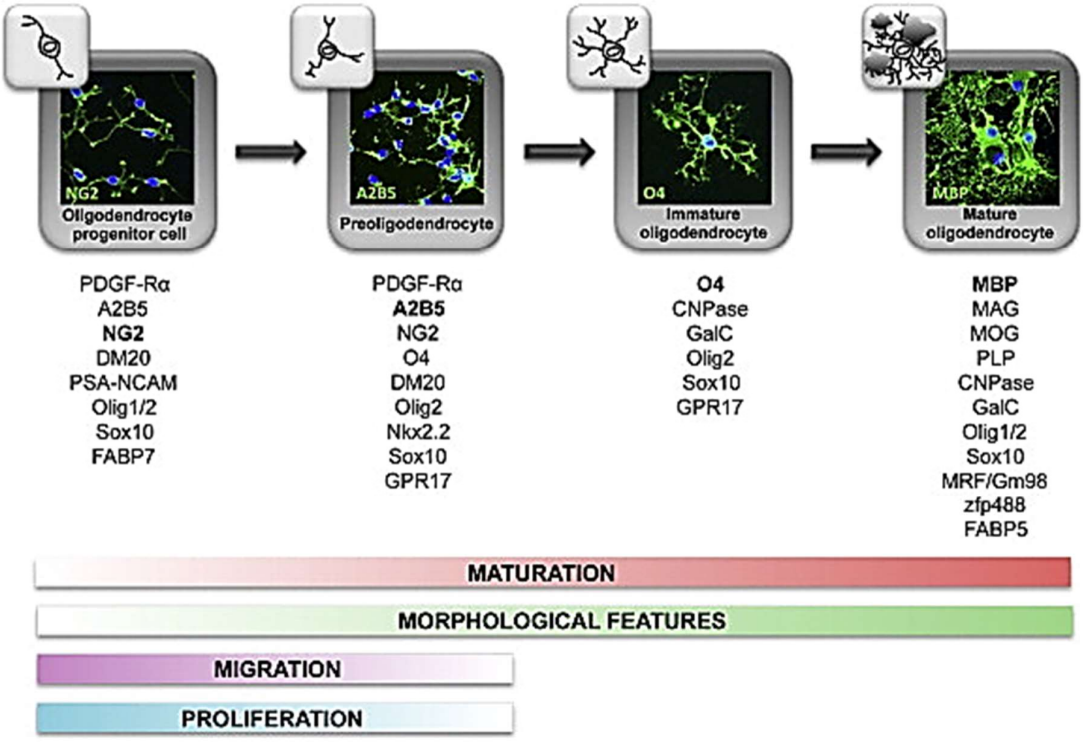

Figure 1.9: Marker timeline for cells in the oligodendrocyte lineage. Common markers utilised for detection are shown in bold, with the scale of maturity and proliferation shown at the bottom. Image was extracted from Barateiro et al 2014[202]

1.5 Multiple Sclerosis

Multiple Sclerosis (MS) is a chronic demyelinating autoimmune disorder that affects the nervous system impairing a variety of functions. There are various different clinical pathologies accounting for the extent and progression of MS in patients. MS affects more than two million people worldwide, with no known cure[203].

1.5.1 Risk

There is no know etiological trigger of MS identified, and the causes are still unknown. However, there are a number of risk factors which have been identified to increase chances of patients progressing to MS. Many proposed risk factors include Serum vitamins, vaccinations, surgical trauma, and environmental agents[204–208]. Trauma has been implicated in the development of MS, with premorbid injuries being associated with diagnosis of MS[209]. Surgery has also been implicated with MS, especially in surgeries involving lymphatic tissue at a young age[206]. However, the part of trauma and surgery in the development of MS is controversial, with most studies suggesting if it plays a part it is small[203,206,209]. Another risk factor which is suggested of MS is vitamin D levels, with vitamin D intake being inversely related to MS onset, relapse rate, and clinical severity[203,210,211]. However, a number of these studies show that dietary vitamin D levels don't exhibit an association with MS incidence[210]. This relationship of vitamin D may also play a role in the discrepancy of MS rates in different climates, with more temperate climates, like north America and northern Europe, showing a marked increase compared to more hotter climates, such as Asia and Africa[212]. Infection with viruses have been implicated, especially the Epstein Barr virus (EBV) [213,214]. Patients with clinically active MS have a tendency to express antibodies against the EBV[215–217]. This seropositivity was found to be higher than individuals without MS who have been in contact

with the EBV, this was found to be the only virus seropositivity out of those tested which differs between those effected with MS and those not[215,216]. From Belbasis's meta-analysis of risk factors for MS only three environmental causes were shown to be highly related with MS[218]. Two of these were linked to EBV, seropositivity to EBV and infectious MONO, the other factor being smoking.

One key risk factor is sex, as females are almost twice as likely to develop MS than men[212,219–223]. The exact reason of this yet to be determined, however, it has been suggested to be linked to testosterone levels, and in preliminary results by Chitnis testosterone replacement therapy has beneficial effects[222]. However it must be noted that the prevalence of MS is enhanced due to the premature mortality of men[212,224]. It has also been suggested this is due to the willingness of women to consult on health problems, as more benign cases are seen in women, however, from the work of Orton it is seen that the interval between onset and diagnosis on average is the same between sexes and therefore not due to male reluctance to consult[212,221].

Most of the genes implicated with MS susceptibility are associated with immune processes, and are genes related to other autoimmune diseases[225]. Approximately 200 genes have been identified which may play a role, with the HLADRB1*1501 haplotype being identified as the most significant genetic indicator for MS[203,223].

1.5.2 Presentation

MS consists of two distinct occurrences, firstly there is diminishing neurological function, and reductions in cognitive processing ability[203,226,227]. The second occurrence is the episodes of disability, referred to as relapses, which may last anywhere between days to weeks. The

amounts of both these occurrences vary depending on the phase, and presentation of MS the patient exhibits.

There are 4 types of presentation of MS, the most common of which is relapsing-remitting. Diagnostically there is no clinical test to distinguish between the different presentations, the only way to distinguish is through the clinical course from onset. Relapsing remitting MS (RRMS) constitutes about 85% of patients with MS[228–231]. This presentation is characterised by temporary relapses where new symptoms present, patients are normally otherwise able to progress within their lives as normal. This may develop into secondary-progressive MS (SPMS) over time, this is normally between 20-25 years from onset. With SPMS symptoms worsen, with a reduction in the amount of remission, or even an absence of remission. In addition to this 10% of patients presenting with MS have symptoms classifying them with primary progressive MS (PPMS)[203]. This is characterised by slowly worsening symptoms from the beginning without recovery[228–231]. The final presentation is progressive relapsing MS (PRMS), which is the rarest form effecting up to 5% of patients[203,232]. This is characterised by progressive neurological dysfunction, with acute relapses, and no remission.

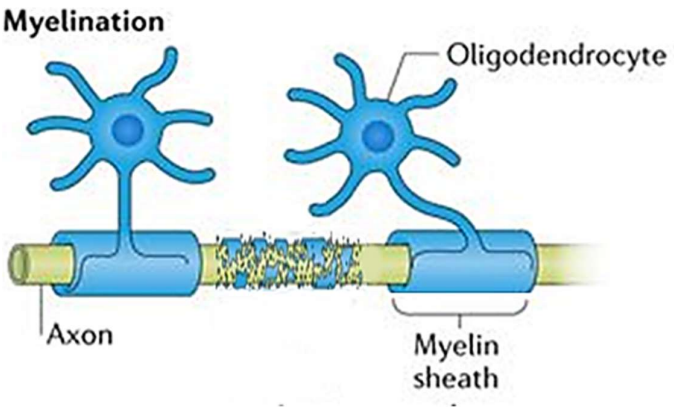

Figure 1.10: Myelination during multiple sclerosis. The figure shows patches of myelination from OLs with some cell debris from demyelination. This area of demyelination does not benefit from myelination, but remyelination can't occur due to the existance of the cell debris. Image was modified Franklin & Ffrench-Constant 2017[150].

MS consists of 2 phases, the early phase which is defined by a focal inflammatory response, and a later phase which is independent of inflammation[212]. The median time from onset to death within patients varies from 24 years to 45 years depending on a range of factors, however, all studies suggest that life expectancy of patients is reduced by at least about 14 years compared to the general population[203,233–242]. Within the first 20 years of the disease is it believed that survival rates are the same as with the general population, and that risk of death increases due to increase disability, and an increase in suicide rates[203,233,238,239,241,243,244].

Pathologically, MS presents with focal areas where demyelination, inflammation, and gliosis occur, referred to as lesions[203] (Figure 1.10). Lesions present throughout the CNS, but vary in frequency. The most common location for lesions are perivascular areas within the brain, although subpial lesions, associated with leptomeningeal inflammation, and spinal lesions, associated with clinical disability, are also key in understanding the condition[203,245–249]. These lesions are more capable of repair within younger patients, corresponding to the increased severity of symptoms causing the progression of patients from RRMS to SPMS[250–252].

Within these lesions both macrophages and microglia are abundant, in addition to astrocytes, all of which promote an immune response through the complement system, through the expression of complement C1q, as well as recruiting more immune cells through the expression of opsonising agents, such as complement C3[23,253–256]. The blood brain barrier becomes leakier, allowing more macrophages to invade the plaques, exasperating the plaques and producing a self-propagating injury[257,258]. In addition to this the adaptive immune system also plays a role, as CD4+ and CD8+ cells have also been observed within the lesions[259]. Drugs which reduce T cell and B cell invasion into the plaque, have been shown to limit the formation of plaques within MS patients, however, it should be noted all disease modifying drugs thus far limit white matter lesions but do not seem to delay clinical progression[203,260].

1.6 The Immune System

The emergence of multicellular organisms posed a requirement to protect the organism from foreign material which could potentially disrupt the ability of the organism to work efficiently, and maintain homeostasis[261]. This foreign material, known collectively as pathogens, disrupt normal cell function in order to redirect resources to fuel the pathogen's own replication and spreading. This not only aids the pathogen's survival but also allows the pathogen to spread to other cells and possibly other organisms[261–263]. As the pathogens redirect the cellular resources to their own processes, the cells have less resources for their own functions, which has an effect on its functions within a multicellular system. Also by-products from pathogen-related processes, known as toxins, can be harmful to the organism[261,264]. In order to combat this a set of cellular and molecular defences, known as the immune system, exists with the aim to eliminate these pathogens from the organism. This system is required to destroy the pathogens, and any toxins they may produce, with minimal damage to the host tissues[261,265]. It must also be able to tolerate normal tissue from the host (self tolerance) and commensal organisms[262,265,266]. In order to achieve the recognition of the vast array of pathogens, and combat their array of mechanisms the immune system has developed a range of complex tools. The mechanisms to recognise these pathogenic materials can be categorised within 2 categories, the innate responses which are genetically inherited and non-specific, and the adaptive responses which are clonally unique, highly specific, and change during the organism's life span (Figure 1.11)[261,262,267].

1.6.1 Innate Immune system

The innate immune system is encoded by genes which are existent within the host's germ line[265]. The innate immune system consists of various components, including physical

defences such as the skin, cilia, tight junctions, and mucosal layers, chemical defences such as small protein and bioactive molecules, and cellular defences such as immune cells[261,265]. The physical defences are the first line of defence, they non-specifically restrict what may enter the body, and also play a role in preventing pathogens establishing themselves outside of the body[261]. When the physical defences fail to prevent pathogen entry the other defences are required[261,265]. The chemical defences include various small molecules, such as complement, defensins, cytokines, and enzymes, all of which play different roles in collaboration with the cellular defences[265,268,269]. The chemical defences can be categorised as the constitutively active molecules such as complement, defensins, and ficolins; and the molecules which must be activated, such as cytokines, chemokines, and enzymes[265,268,269]. All molecules play a key role in either attacking the pathogens, recruiting other immune entities to dispose of the pathogens. One of the key innate immune elements which are recruited by this are entities utilised in cellular defence such as the immune cells[261,265]. The immune cells at this level recognise and target structural features which are not common within mammalian cells [267]. The receptors involved, referred to as pattern recognition receptors (PRR), help control not only pathogens, but also help control the levels of commissural organisms, and clear host cells which have died or are injured[261,265,270]. These receptors exist in all cell types, but the combinations vary between different cell types.

1.6.2 Adaptive Immune system

The adaptive immune system is the next line of defence for an organism. This is form developed by exposure of the organism to various pathogens[261,265]. The adaptive immune system is only utilised if a pathogen has been present for an extended amount of time, and is only evident in vertebrates[271]. Adaptive immune responses take a matter of days to mount a

defence as cells need to be proliferated to respond to the pathogen, whereas the innate immune system activates on the order of hours[261,265]. The response of the adaptive immune system is long lived, as immune cells which are formed for the pathogen may lay dormant following the eradication of the initial exposure, and can form an immune memory[261,262,265,271]. The adaptive immune system is more specific than the innate system, with many cells encoding a response to a single pathogen[261,262,265,271]. This is the stage where identification of the hosts own cells, self-identity, must occur. Responses here can either be mediated by an antibody or by the cell. Antibody mediated responses are occur when B cells are activated and secrete antibodies, which bind to a target on the pathogen referred to as an antigen[261,271]. This prevents the pathogen from binding to receptors to initiate its response, as well as marking pathogens to allow phagocytes to find and ingest them. These antibodies are highly specific and can distinguish antigens which differ by one amino acid or are optical isomers of each other[271]. Cell mediated responses occur when T cells react to a foreign antibody directly, the T cells then either recruit macrophages to dispose of the pathogen or kills the cells itself. This stage of the immune system is specific and allows immune memory, which is an advantage in dealing with more devastating viruses as it allows immune priming using immunisation. Immunisation involves exposure to inactivated pathogenic components, which activates the immune system, and allows the body to produce adaptive immune memory cells to response to the pathogen[272,273]. This system may also be detrimental if dysregulated as is the case with various allergies such as hay fever, and asthma[265,274,275]

Both the innate and adaptive systems are required to combat the full plethora of pathogens encountered by the organism.

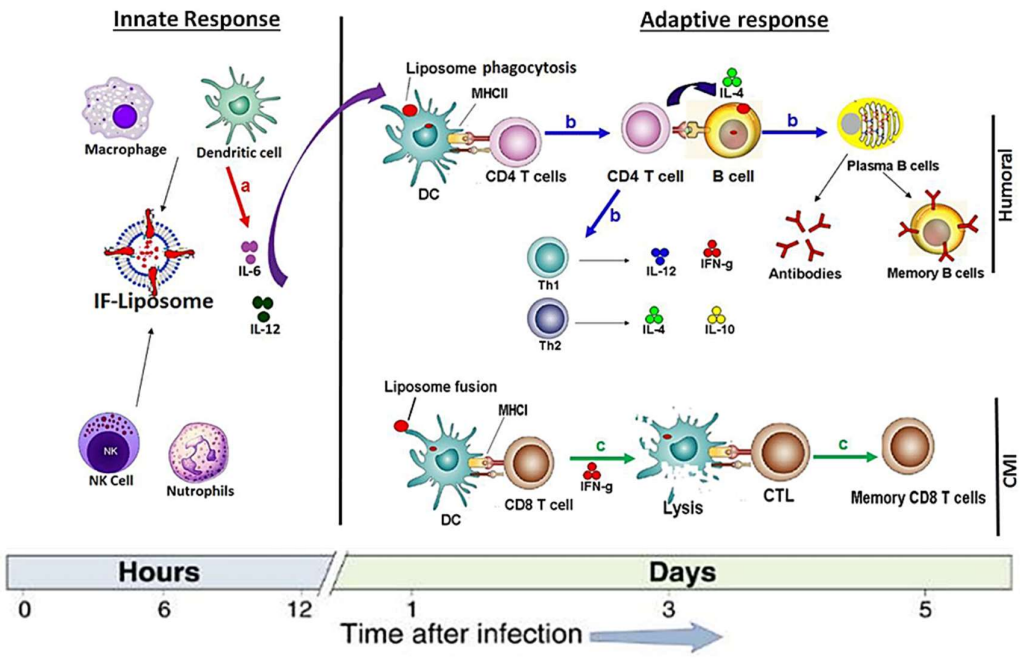

Figure 1.11: Depiction of the innate immune system and the adaptive immune system. The innate immune system comprises of many different element including the dendritic cell (DC), macrophages, neutrophils, and natural killer (NK) cells. These all signal the adaptive immune system, whether it is the production of products like immunostimulatory liposomes (IF-liposomes), or production of secondary messengers such as interleukins (IL). These elements activate the adaptive immune elements such as the T cells. T cells may differentiate to form other cell types, such as T helper cells (Th1/2), or may signal the activation of other cells such as B cells. B cells when activated produce antibodies against the pathogen as well as producing memory cells to help combat the pathogen in the future. This figure was adapted from Faisal 2015[276].

1.7 Complement system

The complement system is a key element of the innate immune system, comprising of an array of molecules ranging from membrane proteins and receptors, to plasma molecules, all of which form a self-propagating cascade to attack pathogens[268]. Complement comprises of over 30 molecules, which account for up to 10% of the total amount of proteins within serum. These molecules serve many functions within in the body including within tissue regeneration, synaptic pruning, homeostasis, and the adaptive immune response[256,266,277–286]. The term complement was originally coined by Paul Ehrlich in 1899, in reference to heat inactivatable substances in serum which were found to improve the antimicrobial immune response of antibodies[275]. Complement proteins generally are synthesised by hepatocytes within the liver, however , they may also be made locally, as seen in the CNS where astrocytes, microglia and neurones produce complement[281,287–292]. Inactive complement precursors circulate the body normally, and activates in response to a pathogen[293]. In addition to this expression of complement also increases during periods of infection and ischemia[281]. Alterations in the levels of complement proteins can lead to various pathologies, such as tissue/ organ damage in over activation[294], and conditions such as lupus erythematosus when deficient[295–297].

Activation of the complement system can occur from 3 distinct pathways, the classical, lectin and the alternate pathway. All these pathways converge at the production of a factor C3 convertase[293].

The classical pathway utilises complement protein C1q which binds to the Fragment crystallisable (Fc) binding site of the immunoglobulin (Ig), normally Ig M/Ig C, and C-reactive protein following antigen binding[274,275,293,298]. This forms a complex with complement C1r to

activate C1s, the activated C1s is used to cleave complement factors C2 and C4, Figure 1.12[275,293]. The Lectin pathway has a number of recognition molecules, such as mannose binding lectin, collectins and ficolins. The recognition molecule forms a complex with a serine protease to form a C1-like complex, cleaving factors C2 and C4. Both the classical and lectin pathway lead to the conversion of factor C4 to factor C4a and C4b, and factor C2 conversion to C2a and C2b. The factors C4b and C2a then form the C3 convertase[274,275,293,298].

The alternative pathway activates spontaneously using complement factors B,D,H and properdin, in a process referred to as antibody independent hydrolysis, this is achieved by hydrolysis of factor C3 using factor B to form C3(H_2O)FB, which is then further matured using factor D to form a C3 convertase, C3bBb[275,293,298].

The C3 convertases formed cleave factor C3 to factor C3a and C3b. The factor C3a is utilised as a chemoattractant to recruit more inflammatory cells, whereas the C3b is utilised as a tag for apoptotic debris clearance, and bind to the C3 convertase to form factor C5 convertase[299,300]. The C5 convertase cleaves factor C5 forming C5a and C5b, C5a attracts more inflammatory cells, and triggers granule release[299]. Whereas, C5b initiates the membrane attack complex by binding to factors C6, C7, C8, and up to 18 molecules of C9[264] (Figure 1.12).

This complement cascade results in the formation of a membrane attack complex to kill cells, inflammation to attract phagocytes, macrophages and neutrophils to the area and the activation of the phagocytes to clear the foreign and damaged material produced[256,301,302]. C3b is a key opsonising agent, tagging pathogens for clearance and recruiting various macrophage cells to clear pathogens[256,299].

Aberrant complement activity is associated with a number of autoimmune conditions such as glomerulonephritis, Sjögren's syndrome, and rheumatoid arthritis[268,274,295,303]. Showing that complement cascade is important in fundamental immune processes.

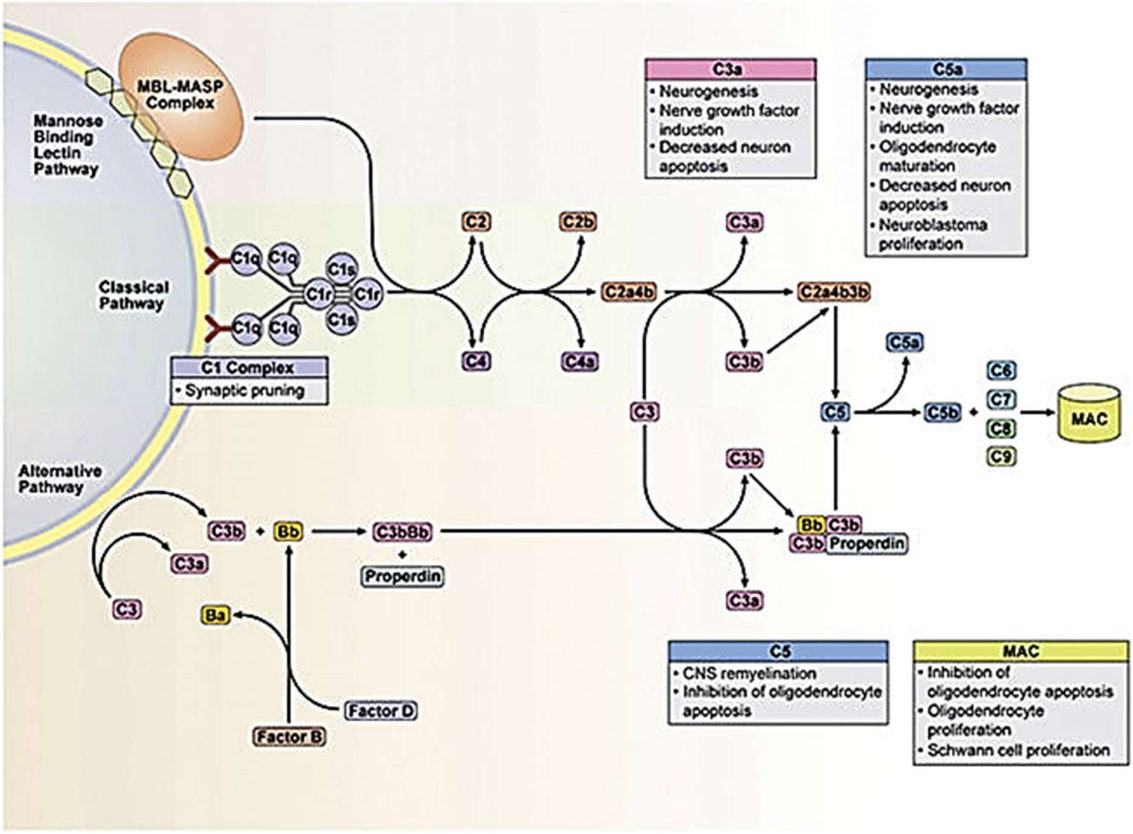

Figure 1.12: Depiction of the complement Pathways. This shows the Mannose binding lectin pathway, the classical pathway, and the alternate pathway. All these pathways converge at the formation of complement C4, which is used to form C5 and so on till the MAC complex is produced. This Figure was extracted from Rutkowski et al 2010 [293]

As complement proteins are well conserved, viruses have also adapted in order to combat this crude system and to utilise it in infection[304,305]. Viruses such as the vaccinia, cowpox, and variola viruses have developed means to evade complement by mimicry of its regulatory proteins, for example the vaccinia virus produces a factor I like protein to cleave C4b and C3b, whereas some other viruses like human immunodeficiency virus incorporate complement proteins into their viral envelopes to evade immune response, or use

complement proteins as receptors for infection, an example of which is the Epstein–Barr virus which uses complement protein CD21 to infect B cells[268,303,305,306].

One of the other interesting functions of complement is its functions in neuroprotection and synaptic pruning (Figure 1.13)[281–283]. It has previously been shown that mice injured with kainic acid exhibit a greater injury if the mice were deficient in complement protein C5[307,308]. This role of complement is also supported by results in experimental autoimmune encephalomyelitis where C5 seems to provide an anti-apoptotic function[309]. To further these results, it has been shown that the MAC complex inhibits apoptosis in Schwann cells and OLs (Figure 1.12) [310,311].

It has been suggested that the classical complement pathway plays a key role within synaptic pruning (Figure 1.13)[281]. Complement protein C3a has been suggested to play a role within neurogenesis, with blocking of C3a following ischemia inhibiting neuroblast migration and neurogenesis[312]. In addition to this, stimulation of complement protein receptor C5aR has been shown to inhibit caspase-9 driven apoptosis within granule cells in the cerebellum[313]. This is supported by the downregulation of C5aR mRNA in terminally differentiated cells, as occurs when OPCs mature into OLs[314]. Complement protein C1q has also been suggested to have a role in synaptic pruning, as C1q levels are upregulated in neurones and microglia in CNS diseases such as Alzheimer's disease, Huntington's disease, glaucoma and amyotrophic lateral sclerosis, when synaptic terminals are being lost[282,311,315–318].

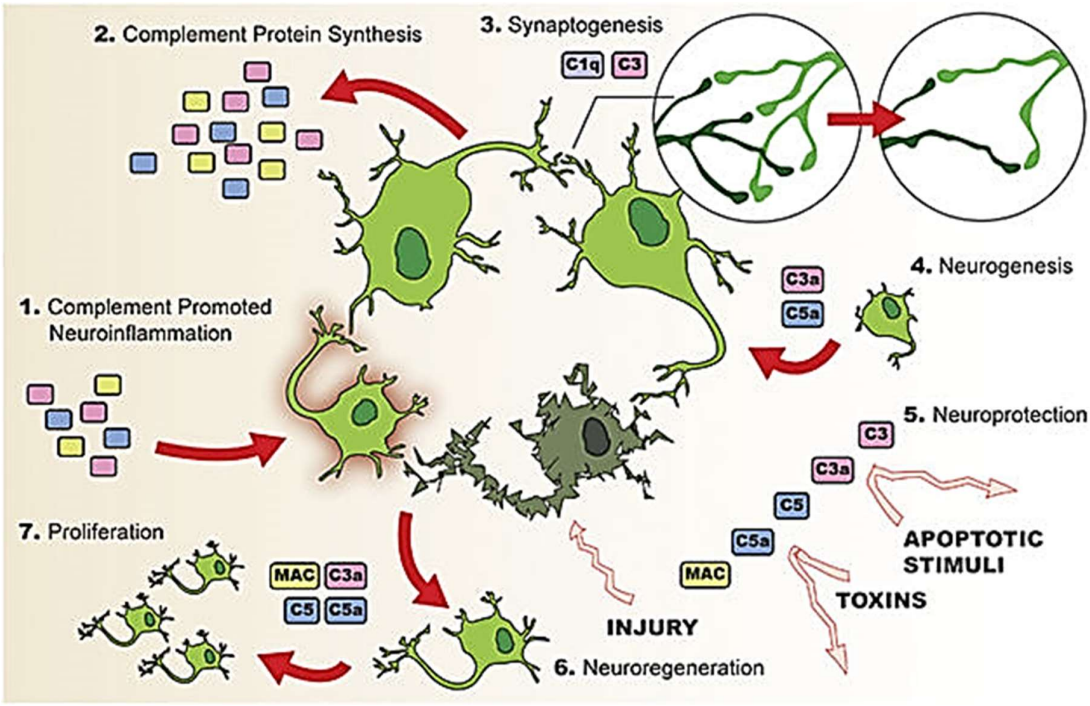

Figure 1.13: Functions of the complement cascade on various phases of the glial and neuronal life cycle. Complement promotes neuroinflammation in addition to supporting cellular development, cellular regeneration and viability following injury. Both neurones and glia produce a complete set of complement proteins which interact with a range of receptors to induce many functions. C1q exhibits a role in synaptogenesis by causing synaptic pruning in mice. Binding of complement C3a and C5a to their receptors in progenitor cells exhibits a role in maturation, and differentiation. Complement proteins have also been shown to play a neuroprotective role in cellular injury conditions, by inhibition of apoptosis and stimulation of growth. This stimulation of growth has also been seen within remyelination studies within the CNS. This Figure was extracted from Rutkowski et al 2010 [293]

1.8 Fluorescence

In order to observe the effect of biological components, such as complement, there must be a means to tag the components. Fluorescence provides a means to do so.

The term fluorescence was first used in Sir George Gabriel Stokes' paper titled "On the change of refrangibility of light", as a means to describe the property of the mineral fluorite which he observed[319]. Fluorescence is brought about by electrons within the singlet ground state absorbing energy, normally through photons, which causes a molecular transition that promotes electrons to raise to a higher energy state, referred to as the highest vibrational state[320,321]. From this point the electron falls through vibrational states, releasing vibrational energy, until it reaches the excited state. From here the electron releases the energy required to return to ground state. This energy manifests itself as light (Figure 1.14). This emitted light is of a higher wavelength and lower energy than the light utilised to excite the electrons. This difference in wavelength has underpinned fluorescence microscopy as the excitation and emission light can readily be separated[320,321].

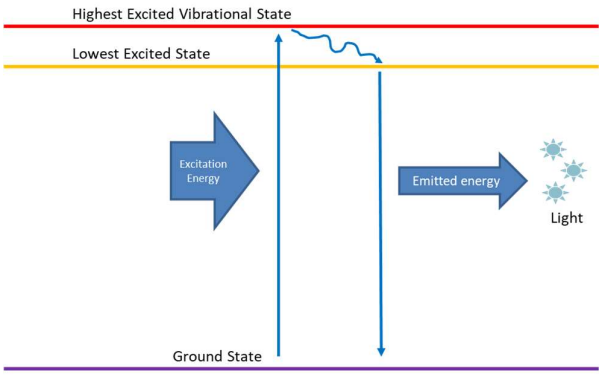

Figure 1.14: Jablonski diagram of fluorescent protein activity. The excitation energy is normally provided by a photon of high energy, or multiple photons simultaneously to provide enough energy to reach the higher vibrational state. Some of this energy is lost, such that the electron enters the excited state, where the electron releases energy as light in order to return to ground state. Due to the energy loss between the higher vibrational state and excited state, the wavelength of emitted light is different to that of the excitation light.

1.8.1 Fluorescent protein (FP)

Fluorescent proteins (FPs) have provided an important tool for use within biological imaging[322]. This has been useful as FPs are genetically encodable so can be introduced into cells without fixation of premiabilisation, this has allowed information on protein expression, and localisation to be performed with more reliability[323].

The first fluorescent protein which was studied was green fluorescent protein (GFP), which was first isolated from Jelly fish, *Aequorea victoria* , in the 1960s[324]. Prior to this work the only bioluminescent molecule identified was luciferin[325], as all other cases of fluorescence observed were seen in mineral states such as fluorite. From *Aequorea Victoria* two proteins were identified, aequorin and GFP, both of which showed interesting properties[324]. Aequorin when purified was shown to emanate a blue glow, which was later found to work in a Forster energy transfer with GFP to make the jelly fish emit green light. It was not till 1992 that the chromophore for GFP was discovered[326–328], which was later found to autocatylse[329]. Although the original attempts to synthesise GFP from its genes were not successful[330], it was eventually achieved by the work of Chalfie in 1993 where GFP was established as a staple lab tool[331]. Following that many other fluorescent proteins have been generated through point mutations or discovered, such as monomeric cherry FP[332], blue fluorescent protein[329], and yellow fluorescent protein[333]. It was found that GFP does not affect function when fused to other proteins (fusions), allowing FP fusions to become useful in exploration in structure and function of proteins[325,334–337]

1.8.1.1 Photoswitchable FPs

Since the discovery of GFP many unique and peculiar fluorescent proteins have been produced with interesting spectral properties[338]. Some mutants of GFP such as citrine,

enhanced yellow fluorescent protein, and cyan fluorescent protein, showed the property of photoswitching, where following irradiation with certain wavelengths, the molecule undergoes a change in structure which allows the fluorescent signal to be diminished or salvaged reversibly[339], as shown with mIRIS FP (Figure 1.15). However, these original mutants of GFP showed poor contrast, as they did not photoswitch efficiently[339]. The discovery of kindling fluorescent protein provided the first utilisable signal for a photoswitchable protein within research. However, due to its existence as a tetramer it proved impractical for many research uses[339,340]. Following this the monomeric FP Dronpa was discovered[341], which was a photoswitchable green protein with a baseline 'on' phenotype[341]. This allowed the discovery of other photoswitchable proteins through mutation such as Padron FP, where methionine at position 159 is converted to a tyrosine, which has a baseline 'off' phenotype[342]. Further understanding of the chromophore allowed new photoswitchable versions of previous FPs to be produced such as mApple[322] and rsCherry[343]. Photoswitchable proteins tend to be 11 strand β-barrel structures, with an alpha helix in the centre[344]. The 4-(p-hydroxybenzylidene)-5-imidazole chromophore is generated auto-catalytically, and a cis/trans isomerization of the methylene bridge between these 2 rings determines the state[339]. Dronpa FP is in the cis conformation at rest which is stabilised by hydrogen bonding between serine in position 142 and hydroxybenzylidene, providing it with a baseline 'on' state[339]. Padron FP, on the other hand, exists in a Trans geometry at rest as the tyrosine in position 159 interacts with the p-hydroxyphenyl ring stabilising the chromophore.

1.8.1.2 Photoconvertible FPs

In addition to photoswitchable fluorophores, another key variety of FP exist, known as photoconvertible fluorophores[338], which undergo an irreversible change in structure triggered by light. This is illustrated with mIRIS FP in Figure 1.15, where UV light induces the incorporation of a side chain into the π-bond system of the chromophore[345], causing the chromophore to change from a 2 ring system into a 3 ring system[346]. One of the first examples of a photoconvertible was kaede FP, which upon ultraviolet irradiation irreversibly converts from its native green emission to a red emission[347]. Following this a number of photoconvertible proteins were produced such as mKIKGR[348], Dendra2[349], and mEOS2[350], all with slightly modified spectral properties[351]. In addition to this, a number of jointly photoconvertible and photoswitchable FPs have been produced, such as Iris FP[352], and Niji FP[353] (and as also shown in Figure 1.15). This allow finer experimentation than either photoconvertible proteins, or photoswitchable proteins alone, as it allows control over both the emission wavelength, and the ability to activate the FP.

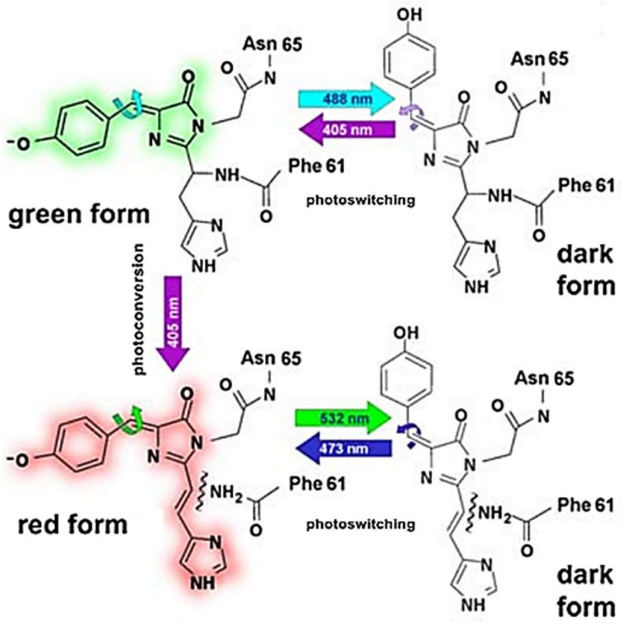

Figure 1.15: Diagram of the photomanipulation of mIRIS FP. It can be seen that photoswitching occurs in both the red and green forms of the FP, causing a switch between the fluorescent form and the dark form. Photoconversion also occurs within mIRIS with 405 nm light, causing a conversion between the green and red form. This occurs as the photo conversion extends the π electron system of the chromophore to the third ring of the structure, effectively acting as a 2 ring to 3 ring conversion of the chromophore[354]. This image was adapted from Wiedenmann et al 2011[355].

1.9 Single molecule Imaging

Traditional fluorescent imaging in the life sciences utilises imaging on the "ensemble average" level, which looks at the population as a whole. This has allowed a "break-neck pace of growth" within the life sciences as it has allowed us to make discoveries on the average behaviour of molecules quickly, helping smooth out any anomalous data[356]. However, the molecules in living cells undergo more dynamic behaviours and movements, with each molecule experiencing the behaviours at different time scales[357]. Ensemble techniques do not allow these kinetics, dynamics, and behaviours of molecules to be teased out. These behaviours are important in understanding the true interactions and consequences of molecular fluctuations in a sample[358]. Of exceptional importance is the understanding that genetically identical cell cultures, may show identical results on an ensemble level, however, the population is intrinsically heterogeneous with different cells showing variations in physical, chemical, and biological properties[356]. This intrinsic heterogeneity is valuable in the adaption of the cells to the environment, and therefore key to survival[359–361]. Also many of the conventional modalities require cells to be fixed which causes distortions on the true structure of proteins[362]. This is where the emergence of single molecule imaging has allowed further understanding in the field.

Single molecule imaging (SMI) techniques allow the observation of the stochastic and probabilistic behaviours which drive biological reactions, and the interplay of molecular interactions and random collisions[363]. The pivotal point of SMI is the ability to identify individual molecules within the population, observe their precise location, and follow them in the cellular environment, which is not possible or necessary within ensemble averaged imaging[323]. Single molecule techniques can be split into 2 categories, Single molecule

localisation, and single molecule tracking[364–366]. Single molecule localisation techniques utilise single molecule information to quantify and locate molecules within a sample[334,367]. This requires high resolution imaging, such as super resolution techniques, and normally is performed at the cost of temporal resolution, as many higher resolution modalities are slower, or require fixed samples[367]. Localisation experimentations allow information on the number of the labelled particle, structure of the system, particle interactions in terms of co-localisations, and distribution of particles within the system to be derived from the experiments. Single molecule tracking on the other hand focuses on the dynamic behaviour of a system, by following a particles point spread function[368]. As samples are being tracked, faster imaging modalities are required, and live samples must be imaged. With tracking experiments information on the molecular dynamics, interactions in terms of dwell times, and movement of the particle can be derived [369].

When designing single molecule experiments there are several considerations which must be addressed, such as the choice of probe, the labelling methods, and the microscope setup. The biggest challenge for SMI is the generation of a signal which must be detected above any biological background luminescence[364]. The choice of probe is instrumental to producing viable results within single molecule modalities. The probes composes of 2 elements, the specificity molecule, for targeting the molecule of interest, and the label. In order to reduce the labels effect on the target molecule, a 1 to 1 ratio of reporter to target is normally utilised. The targeting molecule and reporter are normally conjugated to ensure the target can't be lost. In terms of photophysical characteristics, inorganic fluorophores (such as Quantum Dots) provide stronger reporter signals, which bleach less and can be smaller reducing their effect on the target. However, these probes need to be applied exogenously, and require many

additional steps to conjugate them to the molecule of interest and ensure that they do not alter the behaviour of the molecule being studied. On the other hand organic fluorophores, such as fluorescent proteins, can be expressed by the cell of interest, conjugated to the protein of interest, with little effect on the function of the proteins they are conjugated to, these tend to be larger which allows a greater signal to noise ratio, however, they are easily photobleached relative to quantum dots[325,334–337].

The next key consideration is the imaging modality being utilised. Here the resolution of the images both spatially and temporally must be assessed. Imaging with high spatial resolution require high signal to noise ratios, which can be gained using longer exposures, and normally require stationary particles[370]. Whereas modalities with high temporal resolution tend to sacrifice spatial resolution to do so, as more sensitive detectors are required[371]. Next the penetration distance of incident light must be assessed, in terms of membrane proteins or single cells lower penetration imaging like total internal reflection fluorescence, may be utilised. On the other hand for thicker samples, like tissue slices, require techniques such as light sheet microscopy, or confocal microscopy[372]. In addition to this, the level of photobleaching and toxicity must be assessed, as techniques requiring higher laser powers, or longer exposures, will lead to more rapid photobleaching of samples and even damage to the sample, especially if imaging is needed for extended time periods[373]. Here the level of signal must also be assessed. Imaging techniques such as confocal microscopy allow greater penetration of the excitation beam into the sample. However, this will lead to greater background as fluorophores in layers above and below the plane of imaging will be activated[374,375]. This can be remedied using planar imaging such as light sheet microscopy, however, particles outside of your field of view will also be activated[376].

Following imaging analysis of the images is the next concern. Particles within the images must be detected to allow downstream processing[323]. There are a number of detection algorithms each with their own advantages and disadvantages. Otsu thresholding utilises a cluster based thresholding, assuming the system is bimodal, consisting of background and foreground[377,378]. This is computationally efficient, however, deals poorly with photobleaching, poor contrast, or halo effects. The watershed method for particle detection deals with the image as a topographic map, with the intensity of each point being a height[378,379]. Although this deals better with poor contrast images than the Otsu method, it tends to over segment the image. Wavelet spot detector utilises wavelets to remove high frequency noise from the images, and identifies particles through local maxima[380,381]. However, it deals poorly with non-circular objects. The choice of the correct particle detection method of the images obtained is key to ensure downstream processing is reliable.

The next step for single molecule experiments is post processing. This ranges from tasks such as observing the level of co-localisation within the sample, or clustering, or linking particles for track formation. In terms of tracking there are a number of algorithms which can be utilised for particle tracking, depending on the amount of prior information, the properties of the particles being tracked, and the amount of computational power available. Global optimisation linking is a robust method, which requires a large computational power[382,383]. It relies on the ability to link all detected particles in all frames with each other, to determine the most likely particles track for each particle energetically, determined using a global scoring system. This is computationally intensive, and requires high performance systems for large data sets. The multiple hypothesis linking technique (MHT) utilises deferred logic to reduce the computational power required compared to the global optimisation technique[384,385]. The

MHT utilises data from subsequent frames to reduce the number of possibilities which exist, producing a likelihood ratio to assess the viability of a track. Although this reduces the amount of computation power compared to the global optimisation technique, it is still a computationally heavy technique. The nearest neighbour technique reduces the amount of computational power further as it tracks particles based on a unique feature, this requires each particle to have a unique feature, whether it is the intensity, shape, or colour[386]. This works well if particles are well separated and have a unique feature which can be used to identify the particle easily. The least computationally heavy tracking technique is the probabilistic data association technique, this utilised prior knowledge on the dynamics of the particle to refine particle tracking results, however, this requires some knowledge on the particle dynamics to be known[386,387].

1.10 Single Molecule Microscopy techniques

SMI can utilise many different types of imaging modalities, to provide different levels of resolution, sample penetration, bleaching/phototoxicity, and signal[388]. When choosing an imaging modality consideration needs to be placed into selecting the right modality, as different modalities preferentially enhance one or two of these aspects at the cost of the others[374].

1.10.1 Confocal Microscopy

Confocal microscopy is one of the key microscopy techniques within biology, which utilises apertures to remove out of focus signal[389] (Figure 1.16). Within confocal microscopy two apertures are utilised, one to spatially reject the excitation beam focusing the light path, and another to filter out the emitted light to reduce any stray signals from planes, other than that being imaged[364]. Confocal microscopy requires either the stage or the laser beam to move in vertical and horizontal directions to scan the sample[389]. Confocal microscopy has a higher signal to noise ratio than a wide-field fluorescent microscope, as out of focus light is rejected by the apertures, improving the contrast within the image, allowing finer activities to be imaged, such as DNA repair [390], and viral activities[391]. However, classical confocal microscopy is known to rapidly induce photobleaching and phototoxicity within samples[391], and due to the precision of the pinholes and mirrors it is known to have slow imaging speeds[374]. In order to circumvent these issues other implementations have been utilised, such as Spinning disk confocal microscopy[392] and Airyscan[364]. Spinning disk confocal microscopes utilise a pattern of apertures in order to filter out of focus light, this allows faster acquisition rates than classical confocal microscopy as multiple points are recorded in parallel, this also allows each point to be illuminated for longer, allowing lower intensity light to be used, and thus reducing the

phototoxicity and photobleaching[392]. However, spinning disk modalities suffer from lower spatial resolution than classical confocal, meaning the depth at which images can be taken is lower[364,392]. Airyscanners utilise an array of small detectors to collect all the emitted light from the sample, each detector behaves like a small pin hole in the confocal microscope[393]. This provides greater resolution images, with lower signal to noise ratios than seen with confocal microscopes[394].

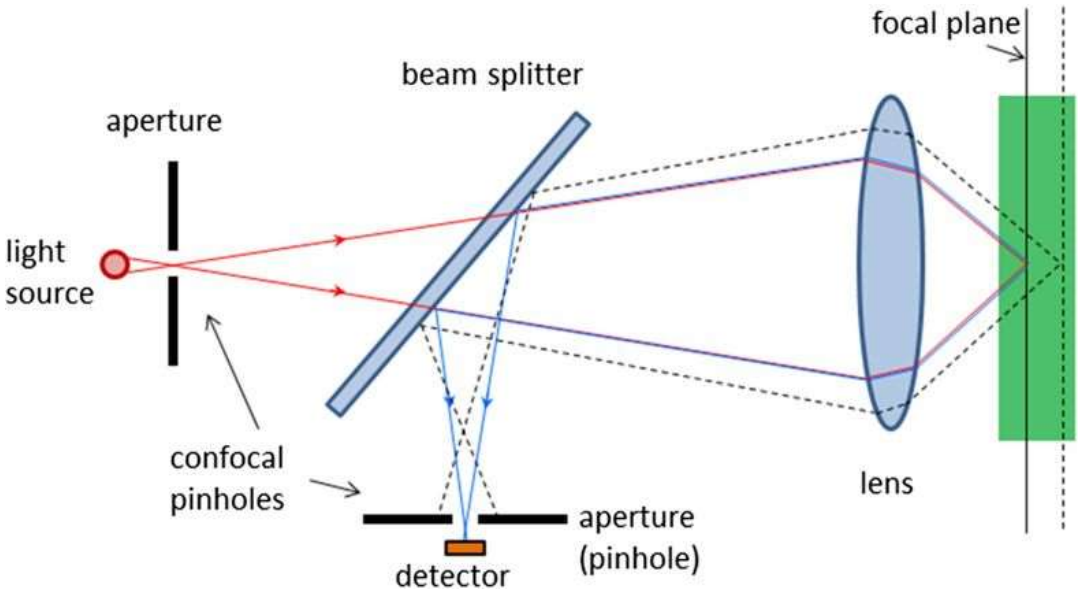

Figure 1.16: Diagram illustrating the principle of confocal microscopy. The light source is focused by the aperture to filter out any stray excitation light. This passes through a dichroic mirror, which allows the light from the source to pass through but to reflect the emitted wavelength, this may also be a beam splitter in order to allow observation from an eye piece and detection using the detector. The light before the detector is filtered using an aperture to remove out of plane signal. This figure has been extracted from Gramatikov 2014[395]

1.10.2 TIRF Microscopy

Total internal reflection Fluorescence (TIRF) microscopy utilises an excitation beam at a narrow incident angle to the sample. This angle is finely tuned to produce an evanescent wave[396]. If the angle is too large, the period of refraction is too long leading to reflection of the light, whereas if the angle is too shallow the period of refraction is too short so the light is transmitted[396]. When the beam of light is correctly tuned the light produces an evanescent

field in a region of interface between the two surfaces have different refractive indices, such as the cell membrane, the angles utilised are directly related to the refractive indices of the two surfaces, and can be determined through Snells law[323]. The evanescent field produced can extend as far as 100 nm before it is lost, this allows illumination of a small section of the surface, and only activates probes on the surface of the sample as the wave only penetrates as far as 150nm into the sample, providing a high signal to noise ratio as little background is produced[323,396]. Although TIRF produces great axial resolution, ~50 nm, it has poor sample penetration, which has led to the production of highly inclined laminated optical light sheet microscopy[397].

1.10.3 HiLo Microscopy

Highly inclined laminated optical light sheet (HiLo) microscopy, often referred to as "near TIRF" microscopy utilises a thin optical sheet of illumination with a sharp imaging angle[398]. The sharp angle of HiLo microscopy allows penetration of up to 300 nm into the sample, double that which is possible with TIRF microscopy, with the light sheet compensating for the loss of light arising due to the lack of the correct angle to produce an evanescent field[398]. HiLo microscopy has a slightly lower signal to noise ratio compared to TIRF[398,399]. The image produced is constructed from two components, which are recorded separately: the in focus high-frequency imaging components, derived from a high pass filter with uniform illumination, and the low frequency components, obtained through local contrasting with grid illumination[399].

1.10.4 Light Sheet Microscopy

Light sheet microscopy, like HiLo microscopy, utilises a low power light sheet, however, the illumination plane is orthogonal to the imaging plane[365,376]. The light sheet tends to be thin,

and the samples need to be either optically clear or close to optically clear[365,376,388]. The sample is illuminated one plane at a time, which leads to a high signal to noise ratio, as little background is produced from out of focus planes. A low power illumination is used, which leads to a low phototoxicity, and little photobleaching, this is especially advantageous with thicker samples as unlike HiLo or confocal microscopy the path of the illumination beam does not pass through other layers of sample[376]. Resolution of light sheet microscopy depends greatly on the set up used, with the resolution being highly dependent on the numerical aperture of the lenses[374,376].

1.10.5 Super resolution techniques

Normal light imaging is limited in the resolution it can achieve by the diffraction limit, which is a limit of microscopy caused by the diffraction of light, meaning that when two objects which are being imaged are less than 200 nm apart they can't be distinguished as two separate objects. This limit is a big challenge within SMI where there could be a requirement to image objects on this scale, or smaller. In order to combat this a number of imaging paradigms have been established in order to overcome this limit, these techniques are referred to as super resolution techniques. These techniques utilise the discrepancies between particles in terms of their blinking, bleaching, emission and excitation spectra to localise individual fluorescent probes and construct images in a pointillistic manner.

1.10.5.1 STORM

Stochastic optical reconstruction microscopy (STORM) is a super resolution technique which utilises the blinking properties of fluorophores[400]. Reporters are made to switch on and off using a UV laser, occasionally fluorophores will stochastically enter a triplelet state which is non-fluorescent[401]. In order to return from this state the fluorophore utilises oxidation from

the buffer it is in. This occurs at different rates for each molecule, allowing them to be separated such that the locations of the molecules can be reconstructed. STORM can provide a spatial resolution up to 20 nm[400,402]. As imaging requires observation of single molecules over extended periods of time, live imaging is not possible, and it deals poorly with non-stationary samples[388,403].

1.10.5.2 PALM

Photoactivated light microscopy (PALM) utilises photoswitchable fluorophores to provide a sparse signal. Fluorescent probes are subjected to a low power of the activation light, which stochastically causes molecules to convert to their on state[404]. These molecules are subjected to a high intensity illumination beam to photobleach them. This process is cycled thousands of times in order to get a representation of all the molecules within the sample. This allows PALM to provide resolution of particles up to 20 nm apart[367,398,404].

1.11 Semliki Forest Virus

In order to express the fluorescent tags within cells, a vector is required. Viruses are a useful vector as they are designed to bypass the cells natural defences to pass their genetic material to the cell.

The Semliki forest virus (SFV) is an Alpha virus of the togaviridae family. It was first isolated from mosquitoes originating from the Semliki forest, Uganda, in 1942 [263,405]. Its symptoms are similar to that of malaria or the flu, with individuals suffering from headaches, fever, joint pain, abdominal pain, and diarrhoea[263,405]. All alpha viruses are arboviruses, so are spread by arthropods, most surviving in nature by replicating alternatively within vertebrate hosts and hematophagous arthropods, like mosquitoes[405]. For this reason these viruses thrive in tropical regions where many appropriate transmission vectors like mosquitoes exist. For SFV this vector is more commonly mosquitoes of the Aedes genus[263,405,406].

The alphavirus genome is composed of single positive stranded RNA, enclosed by a capsid structure, and a lipid bilayer derived from the host, seen in Figure 1.17.[405,407] Alphaviruses are small viruses, consisting of 4 structural proteins; known as E1-3, and capsid protein; and 4 non-structural proteins (nsP), known as nsP 1-4[272,405]. The virus particle identifies the cell through the use of its transmembrane proteins, such as the E1/E2 proteins which identify surface proteins on the cell, such as laminin and heparin, causing cell entry and fusion, allowing the RNA genome to be delivered into cells for immediate RNA replication, as seen in Figure 1.18[272,405]. Upon translation the virus shuts down host transcription through the use of non-structural protein 2, which inhibits RNA polymerase II by inducing degradation of the

RNAPII complex, Rpb1[408]. Alpha viruses typically contain two initiation sites, one of which tends to be inactive[409].

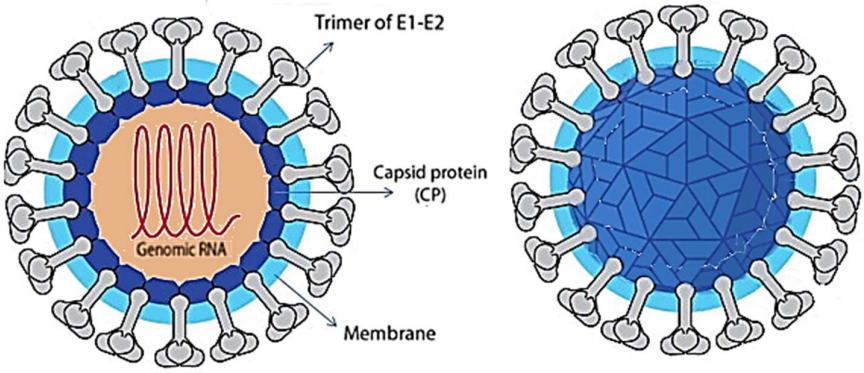

Figure 1.17: The structure of an alpha virus. This shows the RNA genome, the icosahedral structure composed of capsid protein, host membrane, and E1/E2 transmembrane structural proteins for cell fusion, receptor binding, and cell entry. Figure was adapted from Carossino et al 2014[272].

The alpha viruses SFV and Sindbis have both demonstrate the ability to induce encephalitis within mice[406,410,411]. Avirulent versions of SFV exhibit the ability to induce demyelination within mice, and foetal death within pregnant mice, this is believed to be due to the ability of SFV to preferentially infect glial cells[406,410,411]. The SFV genome consists of approximately 1300 base pairs (bp)[405,406,412]. The most commonly used strands of SFV used in research are the A7(74) strain derived from the avirulent A7 stain produced by Bradish, or the prototype strain derived from the L10 strain produced by Glasgow 1991, an example of which is pSP6 SFV4[413–415]. Although the L10 strain consists of a longer genome, both strains amplify equally well within baby hamster kidney (BHK) cells, however they vary in their ability to multiply in neurones[416]. The SFV itself shows a gender discrepancy in sensitivity, with male mice being more sensitive to SFV than female[417].

Although most work on SFV concentrates on mice, as it mainly effects small mammals, it has been shown to also effect humans, leading to outbreaks of mild febrile illness, for this reason SFV is classified as a biosafety level 2 virus, with a Lethal dose (LD50) of 1-2 plaque forming unit of the virulent strain[418,419].

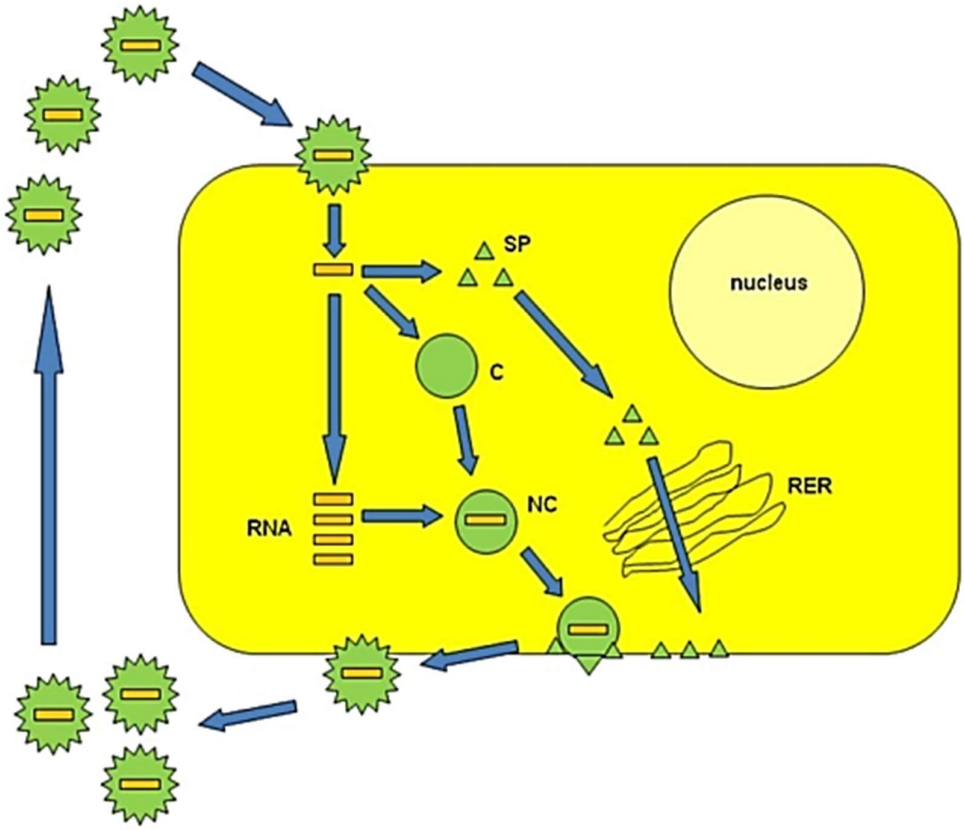

Figure 1.18: The life cycle of Alphaviruses. The virus enters the host cell using the spike proteins, allowing fusion to the plasma membrane. RNA is released from the viral particle into the cytoplasm, this allows the expression of new spike protein (SP), caspid protein (C), and the replication of the viral RNA. New viral RNA and caspid protein form the nucleocaspid. The spike proteins undergo modifications within the rough endoplasmic reticulum (RER) and are transported to the membrane. At the membrane the nucleocaspid assembles with the spike proteins, and the plasmid is released through membrane budding. Figure was extracted from Lundstrom 2015[405]

1.12 Aims and hypothesis

The work presented in this thesis addresses the behaviour of MBP during oligodendrocyte differentiation and following myelin injury. These behaviours will be probed by imaging of a chimeric protein, containing a photoconvertible fluorescent protein (dendra2) attached to the MBP molecule. SFV was chosen as the vehicle to deliver the protein into cells, rather than methods such as lipid transfection, as infection with SFV allows efficient transgene expression, in both cells and tissue samples. The dendra2 MBP fusion protein will also be used to explore myelin injury, both induced by complement mediated methods in brain slices, and through a chemically induced injury in dissociated cell cultures. These injuries were selected as early presentations of MS have been found to possess complement-mediated myelin injury, while chemically induced injury was utilised as these models provide a fast acting, efficient injury suitable for SMI studies[420]. These studies will provide information on the behaviour of MBP following various types of myelin injuries, and may provide insight into the earliest stages of myelin disruption during oligodendrocyte and myelin injury.

1.12.1 Hypothesis

It is believed that the response of MBP to injury will vary according to the level of differentiation of the cells. These believes are as follows;

MBP within mature OLs will show less mobile behaviours than MBP within immature cells

When observing MBP on a single molecule level it is believed that MBP within mature myelin would be highly confined with little to no particle diffusion, as MBP would be interacting with other elements of the cell and other MBP molecules as observed in the literature[161,421,422]. This will be contrasted with the OPCs, where it is believed MBP will be highly mobile with its actions

being defined by Brownian motion, as these cells should not express the mature proteins which MBP would interact with.

The behaviour of MBP within mature OLs will be more mobile following injury, but immature cells will not show a change in behaviour

Following injury to mature myelin it is believed that the MBP interactions will be broken, leaving MBP more mobile such that it will closely resemble the particle behaviour of immature cells. This is believed as following injury and remyelination myelin is shown to change morphology[148], suggesting the MBP interactions may change[161,421,422]. In the case of immature cells it is hypothesised that the behaviour of MBP will not change following injury, as there are little to no interactions to be broken.

Complement injury will produce demyelination in OLs

It is hypothesised that the complement induced injury will produce a myelin injury analogous to that seen within MS, with a strong myelin injury and little to no injury to neurones. It is believed that this injury will be achievable with a lower concentration of complement and antibody than used in previous work. It is believed that this injury would induce a reorganisation of MBP, which would cause an alteration in the shape of the cell.

1.12.2 Aims

The aim of this research is to investigate the behaviour of MBP during oligodendrocyte differentiation and injury, which may further the understanding of the processes which occur within demyelinating conditions such as MS, and neuromyelitis optica. To achieve this the following aims must be achieved;

Establish protocol to label MBP

A protocol to label MBP had to be established, which may be extended to other myelin proteins at a later point. This labelling approach should be achieved such that individual molecules can be observed, and in a way that allows presentation of MBP in mainly oligodendroglial cells. To achieve this MBP will be fused with dendra2, and this fusion protein will be encoded within an SFV vector for delivery to oligodendrocytes in brain slice cultures, immortalised cell lines, and primary cultures of OLs.

Establish and characterise a model of myelin injury

A myelin injury model shall be established, which represents one of the immune initiated components seen within demyelinating conditions, such as MS, and optimised such that a neuronal injury does not present in response to the treatment. This model shall be supplied by the use of complement induced injury, which can be made to target myelin through the use of the classical pathway, where antibodies against myelin proteins induce the formation of a complement complex.

Observe the behaviour of MBP in response to injury and differentiation.

The SFV based vector established previously will be used to observe the behaviour of MBP following myelin injury, and at various stages of differentiation in cultured OLs to see how differentiation status and injury alters these behaviours at the level of single MBP molecules. The understanding of these behaviours, and how they change, may provide new information on the molecular interactions of MBP during OL differentiation, and a new model in which to analyse the effects of OL injury on myelin integrity.

1.12.3 Chapter outline

The work performed within this thesis is divided into three parts.

The first section (Chapter 2) will outline some of the general methods utilised across all results chapters within this work. This includes the culture techniques for the cells used, the compositions of cell culture media used, and other general protocols used in multiple studies within this thesis.

Chapter 3 explains the design and characterisation of the SFV vector used to observe the actions of MBP. The design of the chimeric protein, the infection rate, the expression behaviour, and the viral timeline will be addressed within this chapter.

Chapter 4 will explore the use of an immunological myelin injury utilising the complement system. This chapter will address the concentrations to be used, the treatment time, the mechanism of action, as well as utilising the treatment in collaboration with the SFV vectors, described in Chapter 3, to observe myelin injury within cultured brain slices.

Chapter 5 describes the single molecule studies, which explore the behaviour of MBP in cultured OL cells. Utilising the SFV vector this chapter will look at the effects of OL differentiation, and injury on the behaviour of MBP by looking at protein diffusion, and confinement within various cells.

The final section (Chapter 6) will address the work in this thesis as a whole, in order to produce conclusions, identify work that could be performed to further the presented results, and identify how this work fits in within the field.

Chapter 2

General Methods

"Research is what I'm doing when I don't know what I'm doing"

- Wernher Von Braun

2.1 Overview of methods

The experiments described within this thesis utilised both *in vitro* tissue and cell culture techniques. Specific details on individual experimental groups and specific methods for the work performed will be addressed within the experimental chapters 3-5. Within the work presented the majority of the cell based work was performed on Oli-neu and baby hamster kidney (BHK-21) cell lines. These cell lines were maintained throughout the duration of study, and utilised to test imaging conditions, staining conditions, and injury conditions when deemed necessary. A number of culture solutions were produced to maintain the cell and tissue samples, these were composed of different components, optimised for the samples being studied. Many studies throughout the work utilised SFV vectors, of various concentrations, both within tissue and cell samples. While cell samples could be transduced with SFV by addition of the vector to the culture media, tissue cultures had to be injected with the vectors to ensure cells within the deeper layers of the slice were infected. In order to test for certain phenotypes immunostaining was performed in both tissue and cell samples. This is a method underpinning a large amount of the work within chapter 4.

2.2 Oli-neu culture

Oli-neu cells were cultured for use within various experiments within this work, these cells were kindly supplied by Prof Jacqueline Trotter (University of Mainz). These cells were cultured as follows. Sato media was developed as outlined in Trotter et al[423]. This media contained all the agents required to cultivate Oli-neu cells, formula of which is shown in Table 2.1 . Cell stocks were defrosted and diluted using an excess of SATO media, to remove the DMSO used as a cyroprotectant, and centrifuged at 150 x g for 5 minutes at 4^{o}C, to pellet out the cells, following this the solution was aspirated out leaving the cell pellet. The resulting cell

pellet was resuspended in 4 ml SATO media and seeded into a T25 plate (430639, Corning). After 2 days the cells were passaged, the media was removed from the cells, and the cells were submerged in 3ml 1x trypsin. The cells were left to trypsinise for 5 minutes at 37°C and then the trypsin was inactivated by addition of 3 ml SATO media, following this the cell solution was collected and centrifuged at 150 x g for 5 minutes at 4°C. The cells were resuspended in 10ml fresh SATO media and plated into a T75 plate (3276, Corning). The cells were passaged every 3rd day following that, and split at a 1:3 ratio into T75 flasks. Oli-neu cells were maintained like this until used for experiments.

2.3 Baby Hamster Kidney (BHK-21) cell culture

BHK-21 cells were cultured for use within the production of SFV, the optimisation of imaging conditions within the SMI experiments, and for the confirmation of immunofluorescent staining. BHK-21 cells were procured from the University of Warwick, School of life sciences, and were cultured as follows: BHK media was produced as outlined in Basic Concept of Biotechnology 2015[424]. Cell stocks were defrosted and diluted using an excess of warmed BHK medium, and centrifuged at 150 x g for 5 minutes at 4°C, following this the solution was aspirated to isolate the cell pellet. The cell pellet was resuspended in 8 ml BHK media and seeded into a T75 plate. After 2 days the cells were passaged, the media was removed from the cells, the cells were washed in sterile PBS (P4417, Sigma) and then were submerged in 3ml 1x trypsin (15400054, Thermofisher). The cells were left to trypsinise for 5 minutes at 37°C and then the trypsin was inactivated by addition of 3 ml BHK media, following this the cell solution was collected and centrifuged at 150 x g for 5 minutes at 4°C. The cells were resuspended in 24ml fresh BHK media and plated into a three T75 flasks. The cells were passaged every 3rd day following that, and split at a 1:3 ratio into T75 flasks. These cells were

maintained like this until used for experiments. Any excess cells were pelleted out as described previously, then resuspended in 1ml of freezing media, and stored at -70^{O}C.

2.4 Sacrificing Mice

Within the work C57 black 6 mice (C57BL/6) were sacrificed for the procurement of primary cells, and cerebellar brain slices. All mice were bred by the Biomedical Services Unit at the University of Birmingham. All animals were killed according to home office approved methods listed in the schedule one methods prescribed within chapter 14 of the Animals (Scientific Procedures) Act 1986.

2.5 Infection with SFV

In order to infect OLs within cultured brain slices with the SFV construct, the viral solutions had to be injected into white matter tracks. To achieve this the brain slice was transferred to a shallow tissue bath mounted to an upright microscope (Zeiss Axioscope 1), and submerged in approximately 1 ml pre-warmed injection media. The slice was surveyed at 20x to locate white matter tracks. The viral solution was diluted 1 in 10 in pre-warmed injection medium, and 10 to 20 µl of this was loaded into a glass micropipette which was then attached to a micromanipulator. The micropipette was lowered into the tissue bath and positive pressure was applied via a 1 ml syringe connected to the pipette to ensure a clear flow of injection solution. The micropipette was then lowered into the white matter track under visual guidance so that the tip penetrated the tissue by approximately 10 to 50 µm. The syringe was depressed for approximately 2 seconds to release virus (approximately 2-10 nl) into the sample, with successful injection signalled by a slight expansion of the tissue upon solution ejection. Multiple injections were made to provide an even distribution of injections along each white matter track in the slice. Following injection of the white matter tracks the slice

was washed in warmed injection wash media and returned to incubate at 37°C. Samples were observed 6-12 hours following injection to ensure expression of the chimeric protein.

2.6 Immunostaining

In order to test samples for expression of various markers, such as NG2 within the single molecules samples, or MBP within cultured brain slices, immunostaining was performed. This was performed with a standardised protocol with minor modifications to incubation times to allow staining of both cells and tissues. Samples were fixed using 4% paraformaldehyde (PFA) (F003, TAAB) for up to 16 hours at 4°C, following which the samples were gently washed with PBS three times to ensure any excess PFA is removed. Samples were then permeablised with a solution containing 0.2% triton (X100, Sigma) and 10% goat serum (S1000, Vector Laboratories) diluted in PBS, at room temperature for 4 hours for tissue samples, and 1 hour for cells. These samples were then stained with a primary antibody against the target marker, with the antibody diluted to appropriate levels in carrier solution containing 10% goat serum and 0.05% triton. Samples were left to incubate with the primary antibody at 4°C for approximately 16 hours. Following this the samples were washed in PBS 4 to 5 times to remove all unbound primary antibody. The samples were then treated with secondary antibody diluted 1 to 400 in antibody carrier solution as detailed above. The cells were left to incubate for 2 hours at room temperature, whereas the slice cultures were incubated for 5 hours. The samples were then washed in PBS 4 to 5 times and stained with a 300 nM DAPI solution (D9542, Sigma) at room temperature for 20 minutes. All incubation steps were conducted in dark conditions to minimise the amount of photobleaching which may occur during the protocol.

2.7 Media Compositions

Table 2.1: Compositions of media used within these studies performed.

SATO/ Imaging Sato	DMEM (Phenol red free for imaging) (10569/21063, Thermofisher) Apo-Transferrin 10ug/ml (T2252, Sigma) Insulin 10 µg/ml (I5500, Sigma) Putrecine 100 µM (P5780, Sigma) TIT 500 nM (T6397, Sigma) Sodium Selenite 220 nM (S5261, Sigma) L-Thyroxin 520 nM (T1775,Sigma) Horse serum 1% (H1270, Sigma) Progesterone 6 µg/ml (P8783, Sigma)
BHK Media	GMEM (11570576, Gibco) FBS 10% (F7524, Sigma)
Freezing media	DMEM (10569, Thermofisher) Horse Serum 20% (H1270, Sigma) DMSO 10% (D2650, Sigma)
OPC media	DMEM:F12 (D6421, Sigma) N2 1% (17502001, Thermofisher) B27 1% (17504, Thermofisher) Penicillin-Streptomycin 50 units/ml (15070, Thermofisher) FGF2 20 ng/ml (PHG0266, Thermofisher) IGF1 100 ng/ml (PHG0078, Thermofisher) PDGF-AA 20 ng/ml (PHG0035, Thermofisher) Hydrocortisone 360 ng/ml (H0888, Sigma) Glutamax 2 mM (35050061, Thermofisher)

Differentiation media	DMEM:F12 (D6421, Sigma) N2 1% (17502001, Thermofisher) B27 1% (17504, Thermofisher) Penicillin-Streptomycin 50 units/ml (15070, Thermofisher) TIT 500 nM (T6397, Sigma) Hydrocortisone 360 ng/ml (H0888, Sigma) Glutamax 2 mM (35050061, Thermofisher)
Dissection media	DMEM:F12 (D6421, Sigma) Glutamax 2 mM (35050061, Thermofisher) Penicillin-Streptomycin 50 units/ml (15070, Thermofisher)
Injection media	DMEM (10569, Thermofisher) MgCl2 10 mM (M8266, Sigma) Penicillin-Streptomycin 125 units/ml (15070, Thermofisher) Tetrodotoxin 500 nM (AB120054, Abcam)
Injection wash media	DMEM (10569, Thermofisher) Penicillin-Streptomycin 125 units/ml (15070, Thermofisher)
Slice culture media/ Imaging Slice Culture media	MEM 50% (Phenol red free for imaging) (42360/51200, Thermofisher) EBSS 20% (Phenol red free for imaging) (24010/14155, Thermofisher) Glucose 36.46 mM (G7528, Sigma) Penicillin-Streptomycin 50 units/ml (15070, Thermofisher) Horse Serum 25% (H1270, Sigma)

All serums utilised within these studies were heat inactivated to reduce native complement activation. This was performed by incubating the media in a water bath at 56^{O}C for 30 minutes,

with occasional inversion to ensure mixing within the serum. This serum was placed on ice for approximately 10 minutes in order to allow any precipitating material to settle, then was filtered sterilised using a 0.2 µm filter. These stocks were stored at -20^{O}C until needed.

Chapter 3

Development of Semliki Forest viral Constructs

“we only see easily the facts on which one's attention is already attracted. ”

- Louis-Antoine Ranvier

3.1 Introduction

All the work in subsequent chapters required the use of fluorescent myelin protein constructs in order to understand responses of myelin proteins. This construct must contain a suitable fluorescent protein for the required experiments and must be associated with a myelin protein, whose analysis may provide insight into the dynamics of myelin proteins during myelin development and injury. It was decided that a photoswitchable or photoconvertable protein would be used as they allow more information to be derived on protein dynamics such as diffusion, or local protein tracking. The choice of myelin protein used was driven by the available literature, for which there is just a single report describing SMI of the myelin protein MBP. Finally, the construct would be delivered to OLs in brain slices using a SFV based vector. The concentration of this viral construct must be quantified, its expression properties must be understood and its toxicity must be explored, to ensure the resultant construct will be viable for the experiments performed in subsequent chapters.

3.2 Fluorescent protein development

pRSET B expression Plasmids encoding several fluorescent proteins (FP) were obtained from Katholieke Universiteit Leuven (KU Leuven). These proteins consisted of various enhanced or photoconvertable/switchable FPs, including eGFP, Dendra2, mEOS, Dreiklang, rsGFP, NIJI, and Dronpa, the characteristics of which are summarised in Table 3.1. All the plasmids were amplified using the K12 E.coli Stain, NEB® Turbo Competent E. coli (High Efficiency) (New England Biosciences) and extracted using a miniprep format, QIAprep Spin Miniprep Kit (Qiagen), to produce DNA stock solutions of 300 ng/µl. These FPs were then sequenced using Sanger sequencing, within the Functional Genomics, Proteomics and Metabolomics Facility (University of Birmingham).

Table 3.1: Summery for the photo physical characteristics of obtained Fluorescent proteins. Within the cohort is a mix of photoswitching FPs, such as Dreiklang, which has wavelengths to convert between the on and off states, and photoconverting FPs, such as Dendra2, which has a wavelength to change the emission profile from Green to red. The protein NIJI possesses both traits.

Protein	Excitation Wavelength	Emission Wavelength	Photoconversion Wavelength	Excitation Wavelength	Emission Wavelength	Stop
Dendra2	486	505	405	558	578	N/a
mEOS	482	516	390	571	581	N/a
Dreiklang	500	529	N/A	N/a	N/a	On 365 Off 405
RS GFP	493	510	405			
NIJI	469	507	405	526	569	Green Off 488 on 405 red off 561 on 440
Dronpa	503	518				On 400[425,339,341] Off 490
eGFP	488	509	N/A	N/a	N/a	N/a

From the photophysical data shown in Table 3.1 it was deemed that from the photoswitchable FPs only Dreiklang was suitable, as the others would undergo photoswitching at wavelengths close to their excitation wavelength. In addition, from the spectra of the photoconverting FPs, Dendra2 was the most compatible with the filters and lasers available in the microscopes which were planned to be used. Although NIJI possessed both traits, it was deemed unsuitable as, at the wavelengths available within the imaging systems which were to be used, the excitation beam line would induce photoswitching making imaging over an extended period in both channels difficult.

In regards to the myelin protein incorporated into the construct, the aim was to analyse the dynamics of a myelin in OL cells at different stages of differentiation, and during injury. Human

and Murine myelin consist of approximately 30% protein, and to understand the mechanisms within myelin one of the key proteins should be explored[65]. The key proteins which could be explored are MBP, PLP, and CNP[88]. MBP and PLP constitute 80% of the proteins within myelin[65,88] so these proteins would be good candidates for use within the construct. PLP is the most abundant myelin protein, constituting 50% of the proteins within myelin. It is a membrane protein coded on the X chromosome, and well conserved between human and murine species. Gene deletion and transgenic studies in mice have revealed important roles for PLP and MBP in myelin function. Knock out of the gene encoding PLP in mice does not prevent the formation of compact myelin, however, the myelin is less stable[88,426]. PLP knockdown also resulted in axonal swelling and degeneration suggesting that PLP plays a key role in the maintenance of myelin. Overexpression of PLP is linked to Pelizaeus-Merzbacher disease an X linked disorder which is associated with diffuse hypomyelination within the CNS and a reduction of mature OLs[88,427,428]. MBP constitutes approximately 30% of the protein within CNS myelin. Its role within the myelin is related to myelin folding and compaction. The importance of MBP function within myelin is seen in an MBP deficient mouse strain, the shiverer mouse strain, which exhibits hypomyelination and presents with a generalised tremor [429,430]. In contrast to MBP knock out, overexpression of MBP results in immature OLs, and so has been suggested to impede maturation and myelination[431]. The work of the Simons lab[161] has revealed that homotypic interactions between MBP proteins play a role in the structuring of myelin. Based on these findings we hypothesised that MBP molecules may undergo a change in behaviour, for example decreased confinement, following injury. PLP is a transmembrane protein and thus its dynamics are likely to be greatly confined[88]. On the other hand, while MBP exhibits interactions with membrane bound molecules such as

Phosphatidylinositol 4,5-bisphosphate, PIP2, it is not physically integrated into the plasma membrane. MBP is therefore likely to exhibit a greater range of dynamic behaviours and so is more suitable as a target for these novel imaging studies. MBP was therefore chosen for incorporation into the construct.

3.3 Generation of FP-MBP vector cDNAs

3.3.1 FP selection and Modelling

Dendra2 was chosen as the fluorescent reporter for MBP. This was mainly due to its compatibility with the microscopes being used, as well as its ability to be photoconverted, which could be utilised to obtain a sparse signal for tracking within a different channel. Previous work from the Simons lab[161] using MBP-FP fusion proteins reported that it was necessary to introduce a spacer sequence between MBP and the FP to maintain the native function of MBP in the modelling of compacting myelin. Constructs containing MBP directly fused to an FP fail to exclude MAG and MOG from compacting myelin, a known function of MBP[161]. However, when MBP is separated from the FP by a spacer sequence it retains the ability to exclude these proteins[161]. Based on these findings we decided to follow the construct design described by the Simon's group (see Figure 3.1). The Simons group used a spacer fragment containing either Oligodendrocytic Myelin Paranodal And Inner Loop Protein (OPALIN) or Proteolipid protein (PLP) within their studies on MBP[161], with the choice of spacer sequence depending on the FP used. Both OPALIN and PLP are transmembrane proteins and the Simons group utilised the intracellular regions of these proteins to act as a spacer. We designed two chimeric protein constructs containing the PLP fragment (PLP_{FRAG}): (1) mCherry (mCherry-PLP_{FRAG}-MBP); (2) GFP (GFP-PLP_{FRAG}-MBP); and one construct containing the OPALIN transmembrane fragment (TM); Dendra2-TM-MBP).

Following experimentation with the Dendra2-TM-MBP construct it was found aberrant cell death occurred within infected cell cultures. It was determined that this cell death was related to the presence of the OPALIN fragment, which appeared to increase the toxicity of the MBP fusion protein, making infected cells exhibit signs of reduced viability (rounding up, retraction of processes) much earlier than seen with other FP constructs. Typically cells infected with SFV exhibit signs of reduced viability after approximately 48 hours as the vector effectively takes over the host cells protein synthesis machinery limiting production of essential native proteins. In the case of Dendra2-TM-MBP cell viability was impaired as early as 6 h. This severely limited the window for experimentation and imaging, and provided doubt within the single molecule experiments as to whether observed changes in MBP dynamics were physiological or pathological. Another consideration was whether the OPALIN fragment, as a transmembrane protein, may exert additional influences on the behaviour of MBP (e.g. localisation, confinement), that may confuse the analysis of MBP dynamics. Based on these considerations the construct was deemed unacceptable for use within the single molecule work discussed in chapter 4. The effect of the transmembrane region on the observed behaviour of MBP may not have been as important to the Simons group, as many of their experiments were observing proteins on an ensemble level, where the effect of a small fragment of membrane protein would not be so apparent. It was therefore decided that a new construct where MBP was directly conjugated to Dendra2 (Dendra MBP) would be adequate for the single molecule work, where the focus was on monitoring MBP behaviours such as confinement / diffusion, rather than its functions in the modelling of compacting myelin as investigated previously[161].

The choice of producing a directly fused Dendra2-MBP protein is supported by other work from the Simons lab where directly conjugated FP MBP constructs were used to investigate the role of PIP2 in the formation of associations between MBP and the cell membrane[432,433].

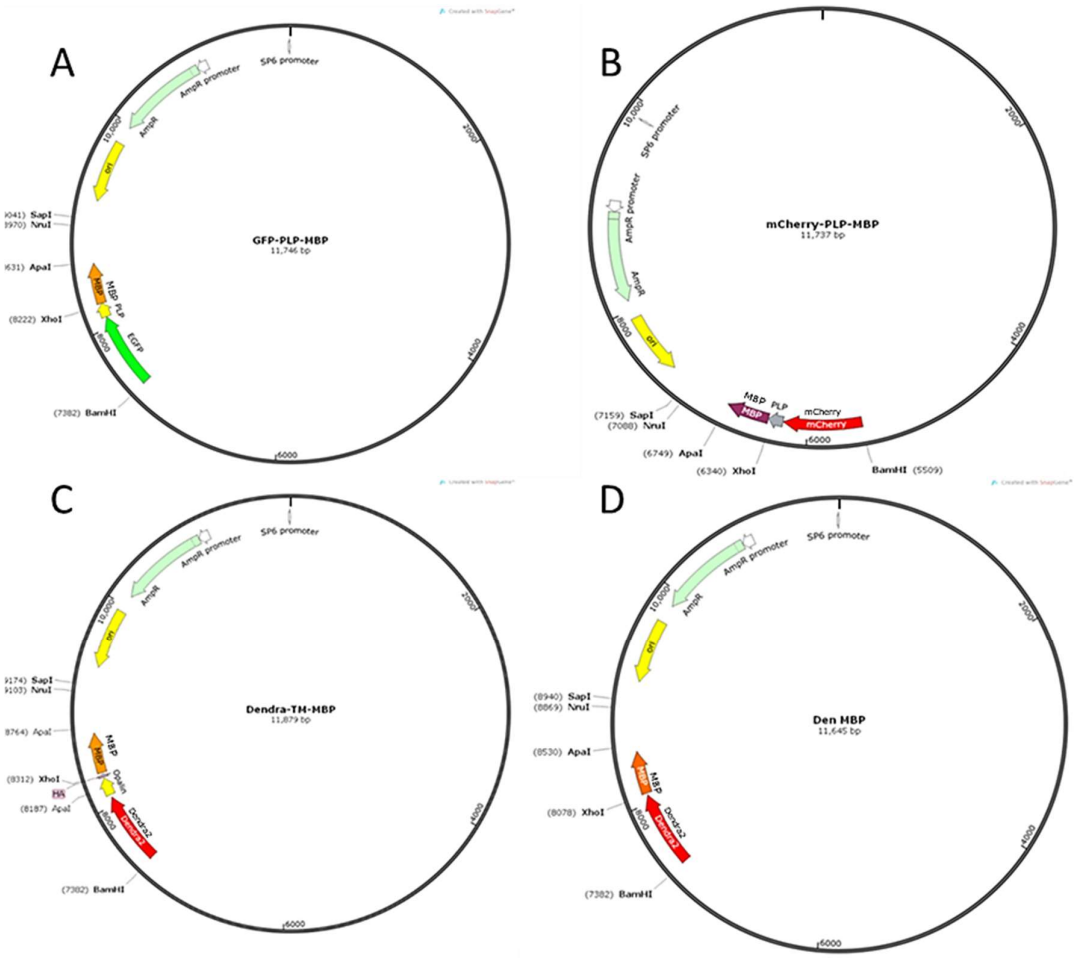

Figure 3.1: DNA maps of FP MBP Constructs in A7(74). (A) GFP construct containing PLP and MBP fragments. Enhanced GFP (eGFP) was used instead of GFP due to increased quantum emission, increasing the signal to background ratio. (B) mCherry construct containing PLP and MBP. (C) Dendra2 construct containing OPALIN and MBP. (D) Dendra2 construct containing MBP. Key enzyme restriction sites are shown: XhoI, ApaI, BamHI represent the cloning sites used in the generation of all of the fusion constructs. During subsequent SFV production, either SapI or NruI were used to linearize the recombinant vector cDNAs to enable their use as templates in *in vitro* RNA synthesis reactions.

3.3.2 Template cDNA preparation

Production of the MBP-FP constructs required well defined DNA templates of the individual components including the fluorescent proteins and MBP. The original DNA templates for the

fluorescent proteins were obtained from Dr Peter Dedecker (Ku Leven, Leuven, Belgium), and templates for MBP bound to either the transmembrane proteins, OPALIN or PLP, were kindly provided by Prof Mikael Simons (Max Planck Institute for Experimental Medicine, Göttingen, Germany). All of these cDNA plasmids were provided as dried stocks on filter paper. These were eluted in 10µl nuclease free water, enough to submerge the paper, and left overnight to produce low concentration stocks of DNA. These DNA stocks were then used to transform chemically competent E.coli (NEB Turbo) to allow amplification of the cDNAs. Aliquots of E.coli in 1.5 mL Eppendorf tubes were incubated with 1-2 µl of eluted DNA, depending on the elution volume, and left to stabilise for 30 minutes, this allows the calcium chloride in the solution to neutralise the negative DNA backbone. In order to get the DNA inside, the cells are stressed through heat shocking in a water bath at 42^{o}C for 30 seconds, this makes the membranes permeable allowing DNA to enter the cell. Transformed E. coli were then allowed to recover by placing tubes on ice for 5 minutes. E. coli were then incubated in Super Optimal broth with Catabolite repression (SOC) medium (S1797, Sigma) at 37^{o}C in a shaking incubator for 1 hour. This step is necessary to promote cell growth and allow time for cells to express the resistance proteins encoded by the cDNA plasmids (required for subsequent clone selection steps). Following this incubation this solution was used to inoculate culture plates by spreading a range of dilutions (25 µl, 50 µl and 300 µl) of solution on to Luria-Bertani (LB) plates. LB plates were produced using LB agar (L2897, Sigma) with 100 µg/mL ampicillin to enable selection of clones expressing the desired cDNAs. Preparation and inoculation of the LB plates were performed within a laminar flow hood to maintain sterility. Inoculated plates were incubated overnight at 37^{o}C, in order to provide optimal conditions for the E.coli to produce bacterial colonies. The next day plates were inspected for colonies and well isolated colonies were

picked using a sterile 200 µL pipette tip. Selected colonies were then used to inoculate 5 mL preparations of LB broth (L3022, Sigma) containing 100 µg/mL ampicillin. These 5 mL preparations were then shaken to encourage mixing, then left to incubate at 37^{o}C on a shaking incubator for 16-20 hours. The duration of this incubation varies depending on when the solution reaches an optical density at 600nm of about 0.6, indicating optimal E.Coli growth. Glycerol stocks were made from a small proportion of the E. coli stocks using 50% glycerol (50% glycerol, 50% PBS) and stored at -80^{o}C, to ensure that samples from the same colony could be used to re-produce DNA in the future. The remainder of the cell solution was pelleted by centrifugation at 3500 rpm for 12 minutes to collect the cells. The media supernatant was aspirated out and cDNA isolated from the pellet using a GeneJET Plasmid Miniprep Kit (K0502, Thermofisher) as per the kit instructions. The Pellet was suspended in the supplied resuspension solution and the pellet dissociated thoroughly by trituration and vortexing to ensure efficient mixing. The cells were then lysed using the cell lysis solution to release the cell contents, and the samples then treated with the neutralisation solution, to neutralise the solution, and bind any nuclear DNA or free proteins. This produced a white precipitate containing bound material. This precipitate was pelleted using centrifugation and the supernatant was added to the purification column, which was then washed using the supplied wash solution to remove any free floating material which had not passed through the column, and dried to remove any excess ethanol from the wash solutions. At this stage the desired plasmid DNA should be adhered to the column and be free of the ethanol present in the wash solution. The bound cDNA was then eluted from the column using 30 µL of nuclease free water to produce a high concentration stock of template DNA. The exact concentration of the

resulting cDNA was then determined using a nano-spectrometer (Figure 3.2) and adjusted to 300 ng/µL using nuclease free water.

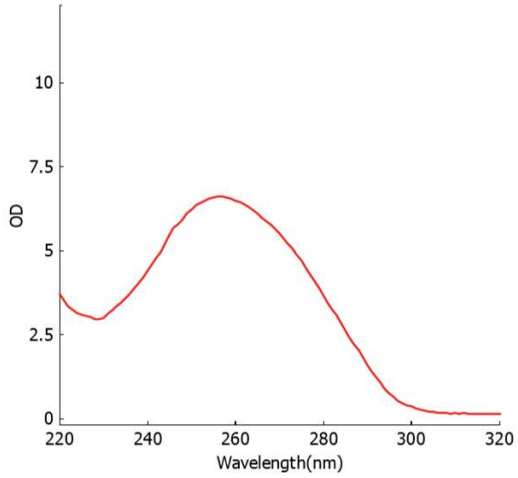

Figure 3.2: Nano spectrum of template DNA amplification. The spectrograph shows the DNA has a good purity.

3.3.3 Preparation of FP cloning inserts

3.3.3.1 PCR synthesis of FP inserts

Oligonucleotide primers were designed to synthesize new versions of the FP constructs containing enzymatic restriction sites suitable for the subsequent cloning steps. The DNA sequences of the expression vectors, the coding DNA for the protein, and the final vector were taken into account to identify the possible restriction enzymes to use. Three unique restriction endonucleases were found to be ideal for use with the protein and the final SFV A7(74) vector: Bam HI , Xho I, and Apa I (Figure 3.1) as they did not exist in the coding sequences, and were present as unique sites within the multiple cloning region of the vector. These sites were also chosen as they produce sticky ends following restriction, which are typically more convenient, and provide good specificity, in ligation reactions.

Having identified the restriction enzymes to be used, the primers were designed. These primers must overlap with the sequence of interest enough to be specific without having an

exceptionally large melting temperature. Based on literature[434] it was decided that primers of between 14-28 bases would be ideal. These sequences were carefully chosen to have GC contents between 45-60% to ensure the primer binds well to the template, but is not too difficult to remove, and that no hair pin structures or self-annealing regions would be present[435,436]. In accordance with advice from an established supplier of restriction enzymes (NEB), a sequence of bases was added to the 5' end of the primer to provide the enzymes an overhang to bind to and ensure optimal restriction enzyme activity[434,437]. This sequence was carefully selected to ensure that it did not increase the GC content too much, or induce annealing, and that the new sequence did not induce new restriction sites for any of the enzymes to be used in the work.

The structure of the primers (Figure 3.3) consisted of, from the 5' end, the enzyme support sequence, the restriction site, and the overlapping sequence of at least 14 bases. The forward primer and the reverse primer consisted of different restriction sites to allow a unique site to be at each end of the sequence. The primers for the fluorophores had Bam HI within the forward primer and Xho I on the reverse primer, whereas for the MBP and TM-MBP fragments, primers were designed such that the forward primer contained Xho I, while the reverse primer contained Apa I. This design would allow the FP and MBP fragment to join, to produce a fusion construct that could subsequently be cloned into other vectors containing these Bam HI, and Apa I. The Xho I site, also allows the FP or MBP fragments to be interchanged with other FPs or myelin proteins if required in the future using either Xho I and Apa I or Bam HI.

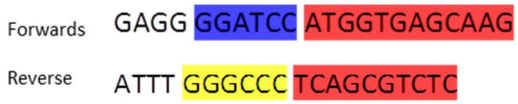

Figure 3.3: PCR Primer sequences. These primers were used for the addition of Bam HI (top) to the front of the sequence, and Apa I (bottom) to the end of the sequence. These sequences have a 4 base overhang to ensure optimal restriction. Coding sequence (Red) is handled in the reverse complement configuration for the second primer to allow it to bind to the complementary strand. Bam HI (blue) is attached to the forwards primer, whereas Apa I (yellow) is bound to the reverse primer

New DNA sequences were synthesized from these primers by using the polymerase chain reaction (PCR). Template DNA was mixed with reagents for the hot start Q5 polymerase kit (M0493, NEB) for PCR amplification, on ice to prevent enzyme and primer degradation as well as to prevent non-specific polymerase binding, as shown in Table 3.2 A. This solution was mixed and placed in a thermocycler programmed with the settings in Table 3.2 B. The program starts with a prolonged initial denaturation step to induce a single stranded morphology within the template DNA, and to activate the polymerase. Subsequent denaturation steps are shorter as they only aim to make the DNA single stranded. The temperature is then reduced to the annealing temperature, which is the temperature at which the PCR primers bind loosely to the template strands, thus determining the specific loci at which PCR will occur. The temperature is then increased to the extension temperature where the polymerase works most efficiently. This pattern of denaturation, annealing and extension steps were cycled 34 times (see Table 3.2 B for justification of cycle times). Further cycles would likely be sub-optimal due to exhaustion of enzymes, degradation of the primers, and an increased chance of producing non-specific DNA strands.

Table 3.2: PCR reaction conditions. A) PCR reaction recipe, all components were added in order on ice, to reduce the amount of non-specific binding of the enzyme. B) Thermocycling conditions for the PCR reaction. 34 cycles were chosen as this produced the most beneficial results in previous PCR reactions using Q5 polymerase within the lab, in terms of sequence accuracy and amount of product

A

Reagent	Volume
NEB Q5 Reaction Buffer	10 µl
dNTP	1 µl
Forward Primer (10 µM)	2.5 µl
Reverse Primer (10 µM)	2.5 µl
Q5 Enzyme	0.5 µl
Template DNA	0.5 µl (1ng)
Nuclease Free Water	33 µl

B

	Temperature	Time
Initial Denature	98	45 Seconds
Cycle Denature Annealing Extension (34 Cycles)	98	15 Seconds
	62	45 Seconds
	72	45 Seconds
Final extension	72	4 minutes

3.3.3.2 Purification of PCR FP inserts

In order to remove free nucleotides and the DNA template from the PCR mix, the Sigma GenElute PCR Clean-Up Kit (NA1020, Sigma) was used. The columns were prepared by the addition of Sigma GenElute Column preparation solution, which was run through the column by centrifugation at 14000x g for 30 seconds. The DNA to be purified was then mixed with DNA binding solution, which contains guanidine chloride to reduce the hydrogen bonding, helping the DNA elute out of solution and bind to the silica column. This solution was added to the centrifuge tube and spun for 1 minute at 14000x g. The silica columns were then washed twice with GenElute wash solution, which is ethanol based, to prevent the DNA from eluting off the column. The columns were then centrifuged without any contents to ensure all the ethanol from the wash solution was removed, as this interferes with the UV spectra of the DNA, and with any enzyme activities required in subsequent cloning steps. Next, the DNA was eluted in approximately 50 µl nuclease free water, which was incubated with the columns for approximately 2 minutes prior to centrifugation to maximise the recovery of isolated DNA.

Finally the DNA solution was thoroughly mixed, and quantified using a nano-spectrometer (BioSpec-nano, Shimadzu).

3.3.3.3 Agarose gel electrophoresis

Having produced purified DNA the size of the DNA had to be determined to provide initial validation that the correct sequence was synthesized. In order to do this agarose gel electrophoresis was performed, where DNA is separated by size within an electric gradient, with the agarose providing physical hindrance on the DNA movement, so larger molecules will not move as far as smaller molecules, and non-linear molecules would move differently to linear molecules of the same size. In this case the agarose was made at 1% in Tris/Acetate/EDTA (TAE) buffer (B49, Thermofisher). The agarose was heated in the microwave and swirled occasionally, to dissolve the agarose, this solution was then allowed to cool in a water bath set at 60^{o}C (a temperature where agarose remains in solution), and Gelgreen nucleic acid stain (41005, Biotum) was added to the solution and mixed. The gel mould was then assembled and levelled to ensure the gel produced would be homogenous in thickness. The gel solution was poured into the gel mould with a comb providing either 14 or 20 wells (depending on the number of samples being tested), foil covered to protect the green DNA probe, and left for 20 minutes to set completely. The comb was then removed from the mould and the gel submerged in the electrophoresis tank filled with TAE (1X). DNA was then prepared by mixing approximately 300 ng of DNA, with gel loading buffer (B7024, NEB). Importantly, this buffer contains a dye which migrates within a 1% gel at the same rate as a 1 kB linear DNA fragment, thus enabling easy assessment of protein migration during electrophoresis. The DNA was then loaded into the wells with a 2-log DNA ladder (N0550, NEB)

in the first and last lane of the gel, and the gel run at 90 v for 1 ½ hours in the dark. The gel was then removed and imaged on a trans-illuminator (Figure 3.4).

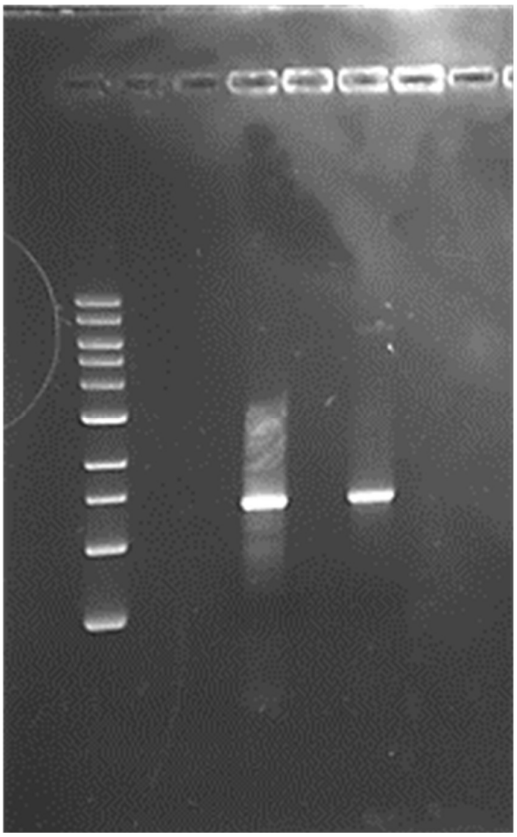

Figure 3.4: Agarose electrophoresis gel of PCR products. Left is the ladder, followed by the crude PCR product, and right the PCR product following clean up. Smears in the band for the crude product are believed to be a mixture of enzymes, dNTPs and primers.

Following electrophoresis, the PCR amplified DNA solutions were restricted with either Fast digest Bam HI and Xho I, or Xho I and Apa I depending on the restriction sites added to the DNA, for 1 hour to produce DNA fragments with sticky ends (all digestions were performed with Fermentas Fast Digest enzymes (Thermofisher). The digested PCR products were then subjected to further PCR clean up, using a Genelute PCR clean up kit as previously described to remove the overhang fragments which were excised from the DNA, and concentration was confirmed on a nano-spectrometer (Figure 3.5).

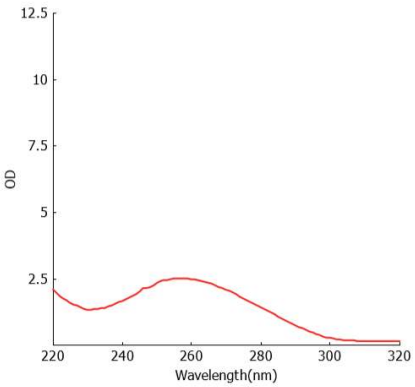

Figure 3.5: Spectrum of DNA insert following digestion with restriction enzymes to produce sticky ends.

3.3.4 Construction of vector cDNA

In order to prepare the SFV A7(74) vector DNA for insertion of FPs, the multiple cloning site was digested using Bam HI and Apa I, leaving a DNA backbone with sticky ends complementary to the FP inserts. After enzymatic digestion the vector DNA was purified by gel electrophoresis. Specifically, the DNA was run within an agarose gel to separate the DNA fragments by size, and the resulting bands visualised using a blue light trans-illuminator to reduce the possibility of DNA damage from the visualisation. To further protect the DNA the trans-illuminator was used as briefly as possible, whilst the DNA band of interest was excised from the gel using a scalpel. The excised band was weighed in an Eppendorf, with the derived weight used to identify the volume of binding buffer to be used during the gel extraction process. Gel extraction was performed using the GeneJET Gel Extraction Kit (K0691, Thermofisher) as directed by the manufacturer's protocol. As the extracted DNA was larger than 10kb the solubilised gel solution was diluted as directed in the manual, and an additional binding step was performed. The final elution step was also performed at 65^{o}C to aid elution. The eluted DNA was then cooled on ice before being quantified using a nano-spectrometer (Figure 3.6).

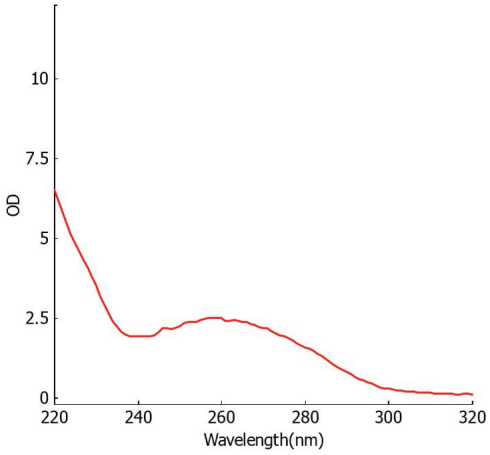

Figure 3.6: Spectrum of DNA Vector following Digestion, and gel excision and purification.

DNA Fragments were ligated together using a T4 DNA Ligase (M1801, Promega). The reaction solution, Table 3.3, was incubated at room temperature for 2 hours, or in the case of some more troublesome constructs, overnight at 4°C. The quantity of insert and vector to use for the reaction was determined by one of two equations depending on the number of inserts used and the vector. The first of these equations determines the concentration of DNA in picomoles for both the insert and the vector. From this the ratio of vector to insert must be considered as recommended by New England Biolabs, these normally provide an excess of insert to bind to the vector. The second of the equations was a simplified equation to determine the nanograms of insert DNA to be used if 30 ng of SFV A7(74) vector DNA was used within the reaction. Both equations were used depending on the reaction being performed. When the ligation involved a single insert, for example Dendra2-MBP, where the A7(74) vector used already contained a MBP sequence (one of the previous FP-MBP vectors being used as a vector), Equation 3.2 was used. However, when the reaction involved two inserts, as was the case for Dendra2-TM-MBP where sequences for both Dendra2 and TM-MBP were ligated simultaneously, then Equation 3.1 was used. In this example

recommendations from New England Biolabs suggested that a molar ratio of 1:5:5 (vector : insert : insert) would provide the greatest probability of successfully producing the required construct, so the equation was used to determine the amount of insert required to heed the advice.

$$pMole = \frac{1000}{No.Base\ pairs\ x\ 650Daltons}$$

Equation 3.1: Equation to calculate the moles of DNA produced. Used for multiple inserts or experiments where a different vector was used

$$\boldsymbol{Amount\ of\ insert\ needed\ (ng) = 3\ x\ (30\ x\ \frac{insert\ Base\ Pairs}{Vector\ Base\ Pairs})}$$

Equation 3.2: Equation to determine the amount of insert required in a reaction with 30 ng SFV A7(74) vector and only 1 insert, requiring only a 1:3 ratio.

Table 3.3: Composition of ligation reactions, all produced on ice, before reaction at room temperature. V+I indicates a reaction with both vector and insert, V+ indicates a reaction with vector and ligase but no insert, V- indicates a reaction with vector but no insert or ligase.

Dendra TM	V+I	V+	V-
V	0.67	0.67	0.67
I	0.79	0	0
Buffer 2X	5	5	5
H2O	2.54	3.33	4.33
T7	1	1	0
Total	10	10	10

3.3.5 Transformation

As with the original vectors the ligated DNA had to be amplified to a usable quantity, as the quanitity produced would be too low to detect the correct construct. In order to amplify the amount of plasmid DNA, the DNA was transformed in to competent E. Coli. 1 µl of ligated DNA solution was added to 25 µl of NEB Turbo Competent E. coli (C2984) on ice, mixed by light trituration. The same was done with the vector only controls. The DNA was then amplified as previously mentioned in the DNA amplification section. The plasmid DNA generated from ligations would be compared to controls to ensure no/little growth, showing that there are no contaminates that cause the plasmid to reform, or that intact DNA is not within the vector solution. Following this verification, 10-15 colonies presenting with differing morphologies

were selected out to be grown (Figure 3.7). Part of these colonies were tested with colony PCR to ensure it contained the gene of interest, whilst the rest were inoculated into 5ml of LB Broth with Ampicillin for growth, and placed in a shaking incubator. The colonies which yielded positive confirmation from the colony PCRs were left to incubate for 10-18 hours, depending on the turbidity of the solution measured using the optical density at 600nm, whilst the other colonies were abandoned. The cell solutions were then pelleted out by centrifugation at 5400g at 4°C, these pellets were then minipreped using a GeneJET Plasmid Miniprep Kit (K0503, Thermofisher) to extract the DNA as per the kit instructions. The DNA was quantified using the nano-spectrometer (Figure 3.8), and verified using restriction digest and sequencing

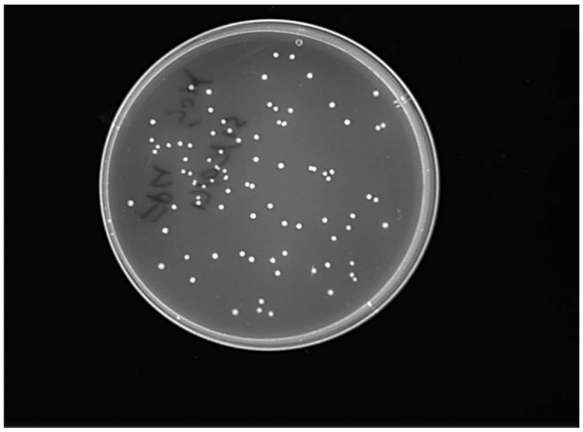

Figure 3.7: Colonies of Ligated product, utilised for amplification, showing optimal colony spacing for selection.

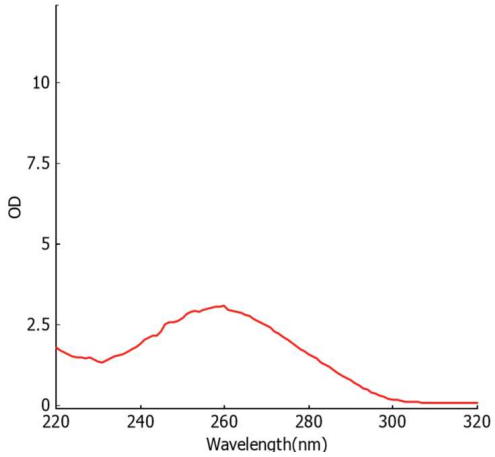

Figure 3.8: Nano-spectrum of construct DNA following transformation.

3.3.6 DNA verification

3.3.6.1 Colony PCR

Following transformation of the ligated plasmid into E. Coli, the plates were checked for colonies, summarised in Figure 3.10. Some of these colonies were selected out for further growth in LB amplicilin. Part of each of the colonies selected were used to verify the DNA produced in the ligation. These colonies were selected out using a pipette tip. The tip was swirled within a PCR solution, prepared on ice, as described in Table 3.4, this is similar to the mix used for the PCRs performed previously, however, more water was added as the template DNA is provided here from the colony. The mixture was thoroughly mixed, then placed in the thermocycler with the thermocycling conditions in Table 3.4. The thermocycling conditions have an extended denaturation step compared to PCRs performed previously, this is to promote plasmid release from cells. Following the thermocycling protocol, DNA was purified using Sigma PCR clean up kit as was performed previously, and electrophoresis was performed using an agarose gel (Figure 3.9). The results of this were compared to the expected size of the fragment generated, calculated by identifying where the plasmid would bind to the DNA. Colonies which produced fragments of the expected size were carried forward and purified.

Table 3.4: Colony PCR reaction conditions. (Left) colony PCR master mix composition. (right) Colony PCR thermocycling conditions with an extended initial denaturation step, to induce the expulsion of DNA from the cells.

Reagent	Volume
NEB Q5 Reaction Buffer	10 µl
dNTP	1 µl
Forward Primer (10uM)	2.5 µl
Reverse Primer (10uM)	2.5 µl
Q5 Enzyme	0.5 µl
Nuclease Free Water	33.5 µl

	Temperature	Time
Initial Denature	98°c	5 Minutes
Cycle Denature	98°c	15 Seconds
Annealing	62°c	45 Seconds
Extension (34 Cycles)	72°c	45 Seconds
Final extension	72°c	4 minutes

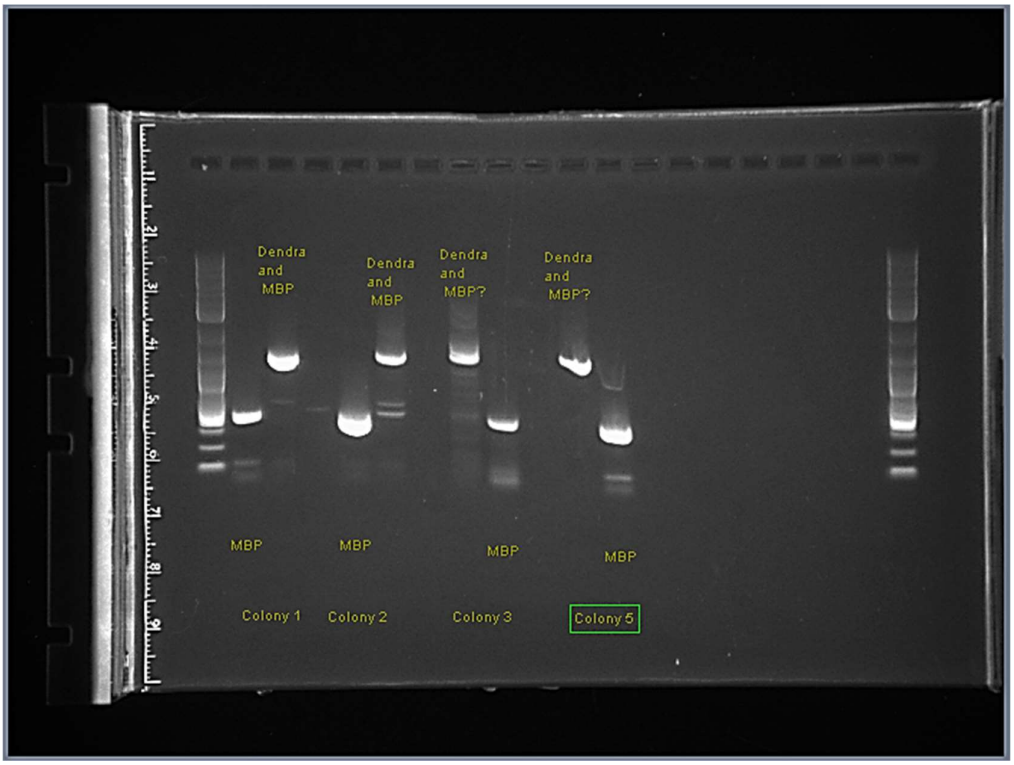

Figure 3.9: Agarose gel of colony PCR products. In this case all colonies were probed for both MBP alone, and MBP with Dendra2. All colonies tested here showed the results desired, except colony 2 which showed an additional product when tested with Dendra2 and MBP together,

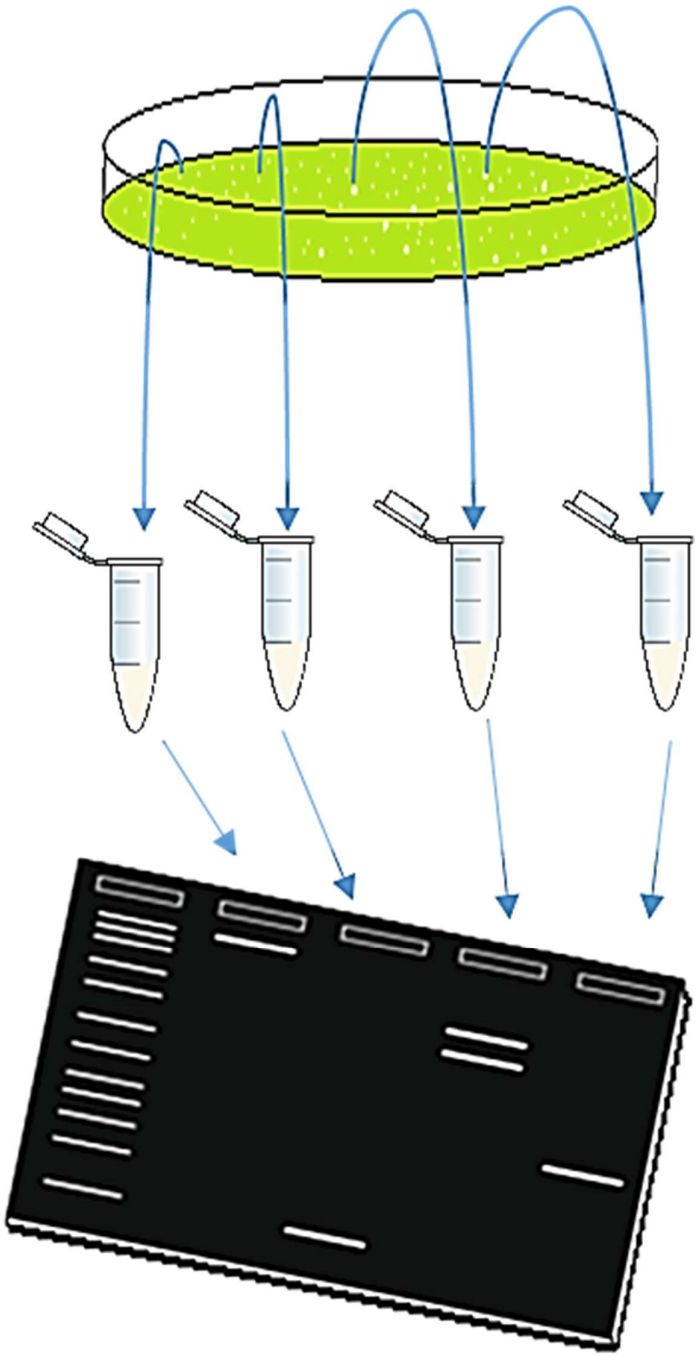

Figure 3.10: Schematic of colony PCR workflow, starting at bacterial colonies expressing the plasmids. These are transferred to PCR tubes with PCR master mix. The resultant product from PCR is run within a gel to identify the correct colonies from the profile seen.

3.3.6.2 Restriction Digestion

Following DNA purification the DNA was verified using restriction digest. Restriction sites were selected to probe different parts of the DNA, such as the whole insert, the FP coding part of the insert and the MBP part of the insert. In all cases 500ng of DNA was incubated with 0.5ul of enzyme (0.5 unit) for 1 hour. All the enzymes were also tested individually to ensure that the enzymes cleave the DNA leaving a linear product, this ensures that there are the sites within the DNA and the enzymes are still functioning. Electrophoresis was performed on the solutions to determine the restriction pattern, and the size of the DNA fragments (Figure 3.12).

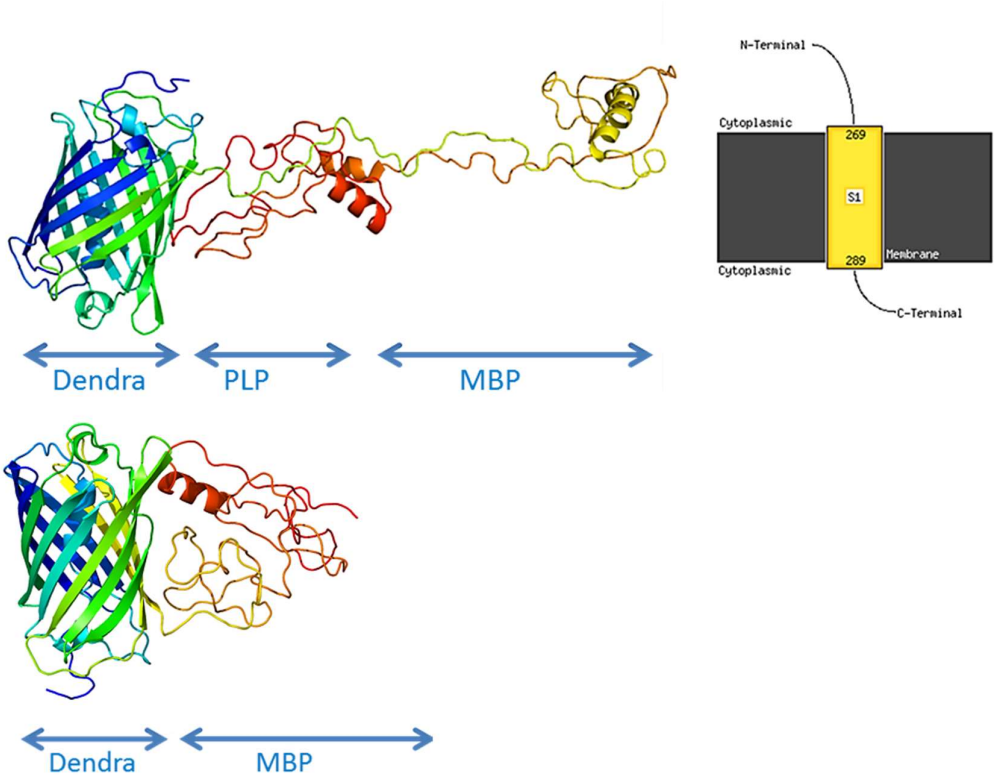

Figure 3.11 Molecular models of Dendra TM MBP and Dendra MBP. According to molecular modelling the transmembrane version has interactions with the membrane, although it is not completely anchored in the membrane. The Dendra MBP complex does not have this interaction due to the lack of the transmembrane element. For the structure of the molecule it should be noted that Phyre2 did not have sufficient reference material to be confident in the structure of MBP.

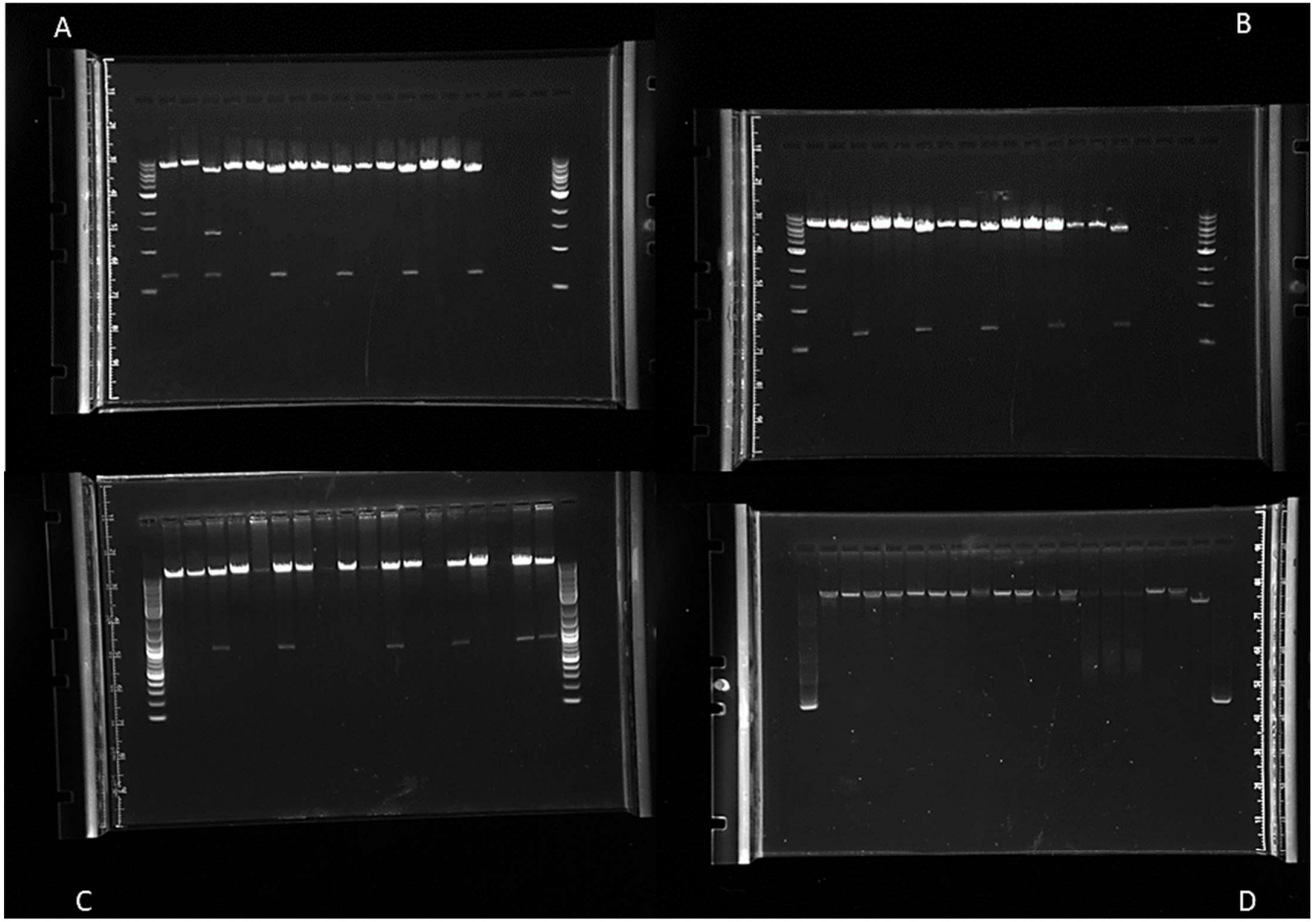

Figure 3.12: Restriction digest results. A) Double digests of all possible constructs with Bam HI and Xho I, wells are ordered from the Ladder on the left, Bam HI digest, Xho I digest, Double digest. B) Restrictions of all plasmids with Xho I and Apa I, again using the pattern Xho I single digest, Apa I single digest, double digest C) Restrictions of all plasmids with Bam HI and Apa I, again using the pattern Bam H I single digest, Apa I single digest, double digest. D) Signle digests utilising the linearization enzymes. Ordered Rru I, Lgu I, Bam HI.

3.3.7 Sequencing and Protein Modelling

DNA sequences for the chimeric proteins which were produced needed to have their sequences verified before they could be transferred to a virus. This was achieved through the use of Sanger sequencing. The samples were selected for sequencing from the results of the restriction digest, if the restriction pattern for the DNA was correct, both the right number of bands and the right size of the DNA fragments, the DNA would be sequenced. DNA was prepared by mixing 3.2 pmol of the primers with 400 ng DNA, and made to 10 µl using nuclease free water. Sample solutions were submitted for Sanger sequencing performed by the Functional genomics services, University of Birmingham. Following retrieval of the sequencing results, the data was imported into Snapgene® viewer to visualise the spectra (Figure 3.13), the corresponding sequence was also compared to the predicted DNA sequence using the comparison software, Jalview2 (Figure 3.14)[438]. From the Jalview results it can be seen that the predicted sequence of the construct matches the sequencing results very well, with 800-1000bp of alignment for both the forwards and reverse primers, the loss of alignment after this could be attributed to the loss of accuracy in sequencing for long fragments[439]. Between the 2 fragments enough overlap exists to determine the full sequence the construct, and show that the sequenced DNA matches the predicted sequence. Following this the DNA sequences were also submitted for Blastx[440] analysis, to ensure the MBP and FP sequences map well with their recognised peptide sequences (Figure 3.15). From the blast results it can be seen that the peptide sequences match well with both the GFP superfamily, which corresponds to GFP and all its mutants, and MBP superfamily, this is further supported as the top matches from the blast library were Dendra, and an mouse MBP isoform, confirming the correct construct was

designed and that the final protein was not lost through the DNA formation. Once the DNA sequences were confirmed, the DNA was prepared to produce the viral genome.

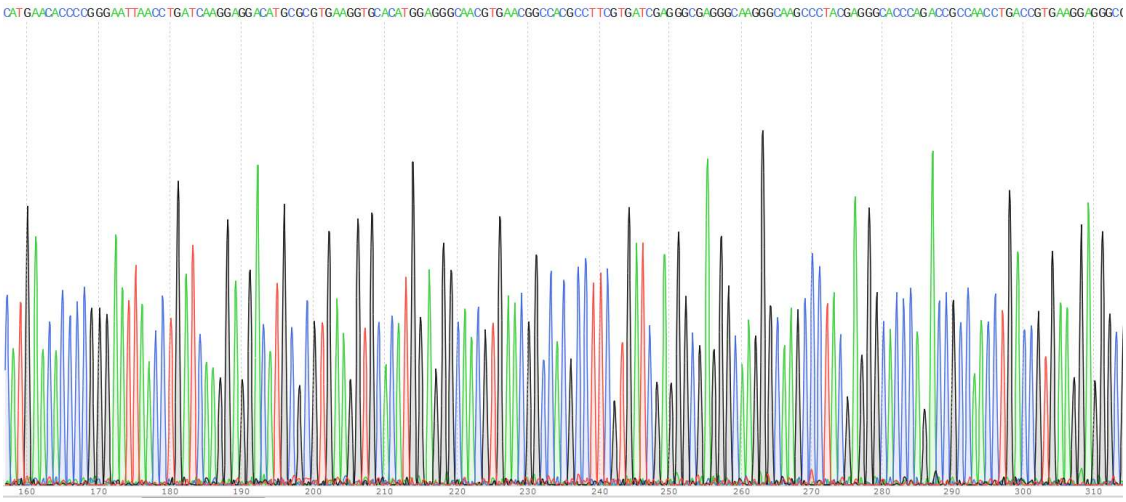

Figure 3.13: Sequencing results

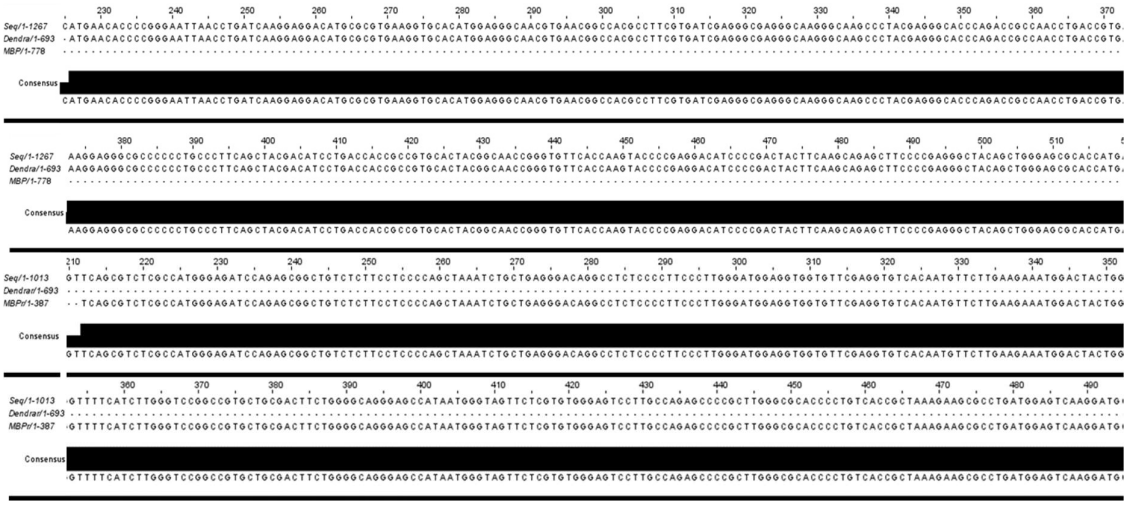

Figure 3.14: Sequencing comparison using Jalview. The top 2 rows refer to the forward sequence, with high consensus between the sequenced data and the predicted sequence of dendra. The bottom 2 rows refer to the reverse sequence, showing a high consensus with the predicted reserve MBP sequence.

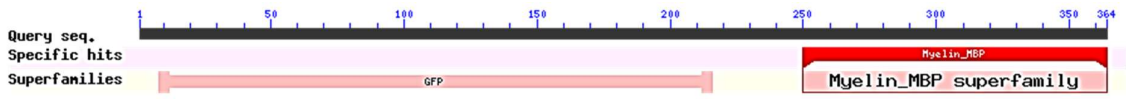

Figure 3.15: Blast results confirming the presence of Dendra2 from the GFP superfamily, and the presence of a MBP isoform.

Having confirmed the DNA sequences of the chimeric proteins the protein sequences were inputted into the protein modelling software, Phyre2[441], to provide an approximation of the conformation of the protein. The Phyre2 modelling showed, that the existence of the FP does not obstruct MBP in either the Dendra2-TM-MBP or the Dendra2-MBP construct, however, it should be noted due to the lack of reference material, within the Phyre2 library, it could not confidently identify the structure of MBP (Figure 3.11). However, this could also be due to MBPs unstructured organisation[137,442]The Phyre2 platform identified that Dendra2-TM-MBP has an interaction with the cytoplasmic surface of the plasma membrane which corresponds with the position of the transmembrane region within the sequence, this interaction was not discovered in Dendra2-MBP, supporting the suggestion that the interaction was due to the transmembrane fragment, as it is not apparent when it is removed.

3.4 Generation of infectious recombinant SFV particles

SFV particles were generated from SFVA7(74)-FP-MBP vector cDNAs according to methods described by Ehrengruber et al[412]. Detailed steps are described in the following sections and summarised in Figure 3.17.

3.4.1 Plasmid linearization

Following sequencing of the DNA, the plasmid was linearized to prepare the DNA for *in vitro* transcription to make the RNA genome of the virus. Linearization is required as transcription proceeds to the end of the DNA template, so linearizing the DNA serves to define the length of the transcript. SFV vector cDNAs contain unique restrictions sites (Nru I and Sap I) located close to the SP6 promoter whose activity drives *in vitro* transcription[443]. To linearize the plasmids the restriction enzymes Nru I, and Sap I were identified, as these left the gene of interest intact as well as leaving the chimeric protein in frame with the SP6 promoter[412]. To

produce sufficient DNA 15 µg of plasmid DNA was mixed with fast digest buffer (1x) and 10 µl (10 units) of enzyme, this was incubated at 37^{o}C for 40 minutes. Following this an additional 5 µl of enzyme was added to ensure the DNA was restricted, and left for 20 minutes. The DNA was then tested using gel electrophoresis to ensure the plasmid was linearized (Figure 3.16).

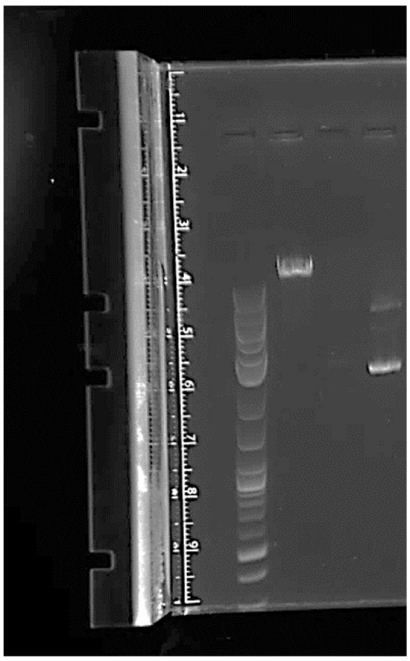

Figure 3.16: Gel showing linearized cDNA (middle) compared to intact plasmid (Right). The intact plasmid has multiple bands reflecting the multiple conformations common to plasmid cDNA such as coiled, and nicked.

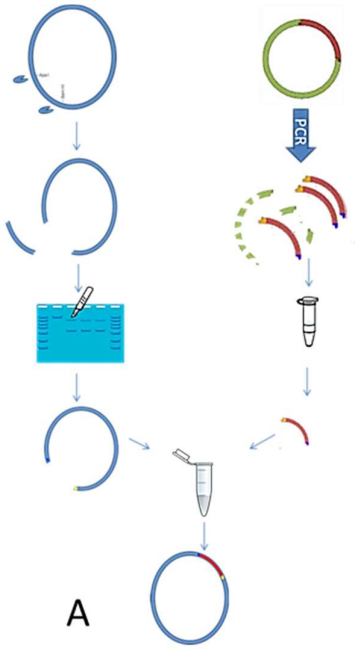

Figure 3.17: Schematic of the construct formation workflow. The vector (Left) is digested and gel extracted to produce a linear vector molecule with sticky ends, the insert (right) undergoes PCR to produce sticky ends and isolate it from its vector. This is cleaned up to remove any fragments of vector and dNTPs, and mixed with the linear vector. These are ligated to make the next construct.

3.4.2 Phenol Chloroform precipitation

Following linearization digested cDNA should be purified for downstream processes. In addition, the subsequent *in vitro* transcription step requires a high concentration of DNA, as half the reaction volume required is provided by the transcription buffer (2x buffer). Phenol chloroform precipitation provides a useful method to remove impurities such as restriction enzymes and concentrate the cDNA. First, the DNA of interest was mixed in a 1 to 1 manner with the phenol chloroform mixture (phenol / chloroform / isoamyl aclohol (25:24:1)). This solution was then mixed well by vortexing to facilitate dissociation of proteins and DNA in the respective solutions, before centrifugation at 24,000g for 5 minutes at room temperature. This caused the formation of 2 layers, the aqueous phase on top containing the nucleic acids, and the organic phase at the bottom containing proteins, and hydrophobic lipids. The top layer

was the transferred into a new tube and mixed in a 1 to 1 ratio with 100% chloroform to remove the remaining phenol, and increase the purity of the resultant solution. The top layer of this was removed and mixed with an excess of ethanol (2.5x) as well as sodium acetate (1/10) to reduce the hydrophilicity of the DNA, making it easier to precipitate out. This mixture was stored at -80°C for 20 min (or -20°C overnight), to reduce the activity of nucleases which are potentially existent, as well as increasing the yield of DNA by precipitation. The DNA is then spun at 4°C for 30 minutes at maximum speed. The tube was then inverted carefully to remove the ethanol ensuring the pellet was not disturbed, the tubes were then filled with 75% ethanol to remove any residual salts existent with the DNA. The tubes were centrifuged and the ethanol was removed by inversion. The pellet was left at room temperature for 2 hours to remove any residual ethanol, then resuspended in 11µl nuclease free water, 1µl of which was used to determine the DNA concentration using a nano-spectrometer (Figure 3.18).

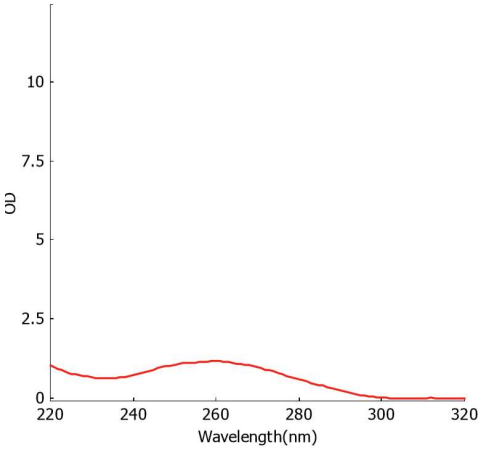

Figure 3.18: Spectrum of precipitated DNA following ethanol precipitation.

3.4.3 *In vitro* transcription of SFV vector cDNA

SFVs possess RNA genomes, thus the genetic material produced thus far (e.g. cDNA) were incompatible with viral production. To enable the generation of infectious SFV particles from the vector cDNA, this must be converted into RNA *via* an *in vitro* transcription reaction. The *in*

vitro transcription was performed using the Ambion mMESSAGE mMACHINE® SP6 transcription kit (AM1340, Thermofisher) and was performed as directed in the instructions. Reactions were performed using 1 µg of the template cDNA. The reaction mixture was prepared, as shown in Table 3.5, at room temperature to prevent precipitation of the supplied buffer. Once the reaction was assembled it was mixed thoroughly and incubated at 37°C for 2 hours. Following this the RNA was kept on ice to reduce any possible nuclease activity. The resulting RNA was verified using both the nano-spectrometer, where the 260/280 absorption ratio was observed as pure RNA solutions would produce a ratio close to 2[444], and gel electrophoresis where RNA are found to run faster on the gel than the linearised template cDNA (Figure 3.19 A). Following these checks the RNA was stored at -80 until pending further use.

Table 3.5: Composition of the in vitro transcription reaction, added in order on ice.

Reagent	Quantity
NTP/CAP	10 µl
Reaction Buffer	2 µl
Nuclease free Water	to 20 µl total
DNA template	1 µg
GTP	2ul
Enzyme	2 µl

3.4.4 SFV generation

3.4.4.1 Packaging cell line electroporation

Baby hamster Kidney (BHK-21) cells are used as the packaging cell line for the protocol used in this thesis[412]. BHK-21 cells must be electroporated with solutions containing two distinct RNA molecules to initiate SFV production. The first RNA solution contains the newly cloned SFV vector encoding the SFV genes for replication and the inserted transgene. The second RNA solution contains Helper2 RNA which encodes the packaging information required to produce

infectious SFV particles. Division of replication and packaging genes into separate RNA molecules provides an important safety feature in this SFV system[412,443]. Prior to electroporation BHK-21 cells were grown in 75cm^2 tissue culture flasks (430725U, Corning) until reaching the late log-growth phase, approximately 1-day post inoculation, where the cells are at 80% cell confluency [406]. Electroporation was performed using Cell Line Nucleofector® Kit L (VCA-1005, Lonza) according to the manufacturer's instructions. Specifically, electroporation media was mixed consisting of 82% Special solution and 18% supplement from the Nucleofector® Kit L. These solutions were assembled on ice. The media from the BHK-21 cells was then aspirated, and the cells were washed in PBS to remove any residual media from the flask, to prevent inactivation of the trypsin enzymes required for cell detachment. The cells were then covered in 1x trypsin and incubated for up to 5 minutes to remove them from the surface of the flask. The cells were then resuspended in an excess of BHK media, (see Chapter 2 for recipe), to inactivate the trypsin. The cell solution was centrifuged at 150xg for 10 minutes, and the resulting supernatant aspirated. Cells were suspended in BHK media and counted on a haemocytometer. The solution was divided into units containing 1 million cells each and the cells were pelleted out by centrifugation as mentioned previously, and each unit was suspended in 100µl of special solution/supplement mixture. Immediately before electroporation 5ul of the SFV A7(74) construct RNA (1µg/µl) for the viral genome and 5ul of helper solution (1µg/µl) to provide the packaging information for the virus were added in, and the solution was transferred into the nucleofector cuvettes. These were electroporated in the Nucleofector device on program A-031 as suggested by Lonza[445]. Following electroporation cells were diluted with warmed BHK media and added to a T25 flask containing 4ml of pre-warmed media at 31ºC. Electroporated cells were then

incubated at 31°C 5% CO_2 for two days to allow the virus to be produced and packaged. Monitoring of the cells during this stage provided evidence of successful electroporation and SFV activity. First, expression of the FP-MBP transgenes was assessed by observing FP signals in the flasks using an inverted fluorescent microscope. Second, production of SFV particles leads to reduced cell viability as packaged particles are released from the cell leading to membrane budding and alterations in cell morphology (rounding up, detachment). Once these signs were confirmed the media was harvested, and the virus was activated as described below.

3.4.4.2 SFV particle activation

SFV A7(74) possesses a point mutation in the p62 precursor protein, which produces the E2 and E3 spike protein on the virus[412,443]. This renders the SFV replicons cleave deficient and therefore non-infectious. This provides an additional safety feature in protecting users from the virus. In order to activate the virus and make it infectious, the viral solution had to be incubated with 100 µL Alpha chymotrypsin (20 mg/mL) at room temperature for 30 minutes, which cleaves p62 at a leucine residue rending the viruses infectious[412,443]. This activates the virus by cleaving the p62 cleavage site of the virus[446]. The reaction was then stopped by the addition of 100µL aprotinin (10mg/ml). The activation reaction was stopped as it has been shown that the maximal infectivity is achieved when about only about 40% of the virus is cleaved[413,446,447]. The virus was aliquoted out to reduce the freeze thaw cycles of the virus during usage, and stored at -80°C.

3.4.4.3 Virus quantification

Once the virus was successfully produced, the viral titre had to be determined to ensure that similar amounts of viral units would be utilised between viruses. This was achieved by seeding

BHK-21s into 6 well plates, allowing them to achieve approximately 100% confluence, and then infecting BHK-21 cells with various dilutions of virus, 1 in 10, 1 in 50, 1 in 100, 1 in 500, 1 in 1000, 1 in 10000 all in 1ml of solution. Cells we incubated with viral solution at 37^{o}C for 1 hour, and then washed and placed in fresh media. Observations of transgene FP expression were performed 24 hours later to estimate the number of infectious units/mL. Dilutions where observed under the microscope to identify wells with expression which were neither too dense nor sparse to enable easy and accurate counting of infected cells. These wells were then sampled for 15-25 fields of view on the microscope to quantify the number of cells expressing the fluorescent protein construct (Figure 3.19). These numbers were averaged to give the mean count/field, and this number multiplied by the factor required to scale up the field size (μ^2) to the total number of fields possible given the surface area of the well (Equation 3.3). Using this calculation to provide the amount of infectious SFV units in 1 well it was then possible to determine the number of infectious SFV units/mL of viral solution by multiplying by the dilution factor used for that well (e.g. 1:10, 1:100 etc).

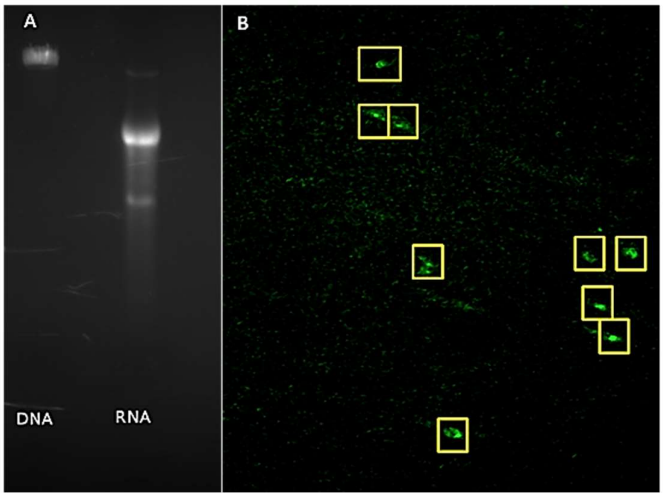

Figure 3.19: Quantification and verification of FP-MBP. (A) Agarose Gel to compare DNA and RNA for GFP-TM-MBP. The first lane (left) contains the linearised construct DNA, the final well contains RNA products from the *in vitro* transcription reaction. (B) Image of cells infected with a 1 in 10 dilution of the virus solution, taken with spinning disk confocal microscope. Imaging was performed with the following parameters: 10x objective, 800ms exposure time, excitation 485nm. Within the image, 9 cells were identified as infected. This count was utilised within Equation 3.3 , giving the concentration of 3.5x10^5 infectious particles/mL in the viral stock solution.

$$viral\ units/ml = \left(mean\ count\ per\ field \times \frac{area\ of\ the\ well\ (mm^2)}{field\ area\ (mm^2)}\right) \times dilution\ factor$$

Equation 3.3: Titre calculation to find the concentration of virus within solution .

3.4.5 Validation and characterisation of SFV vectors in oligodendroglial cell lines

Having produced SFV vectors expressing the chimeric proteins it was then necessary to confirm the ability of the vector stocks to infect an appropriate cell type. In order to achieve this Oli-neu cells were grown to about 70% confluency, after which they were infected with SFV A7(74) GFP-PLP-MBP at a 1 in 10 dilution (1 hour incubation at 37^{o}C). Oli-neu cells were used for this experiment as they are a well characterised model of OPCs[448–450]. In addition, large numbers of Oli-neu cells can be grown in the lab, thus they provide a more convenient model for this validation work than primary cells or brain tissue cultures, where there is a large burden of animal work and time involved. Infected cells were left for 24 hours at 37^{o}C to allow

expression of the chimeric proteins to reach maximum expression. These cells were then fixed overnight at 4°C using paraformaldehyde (PFA), then stained with the nuclear stain DAPI to provide an additional cell marker. The cells were then observed on a spinning disk confocal microscope, on widefield mode. Images of cells containing GFP-PLP-MBP were overlaid on the DAPI images to identify cells containing GFP-PLP-MBP (Figure 3.20). From the images produced it could be seen that the virus did not infect all the cells within the dish, and that the transgene is present throughout the entire cell except the nucleus. These are positive results for this work as it confirms that the vector produces fluorescent signals of an intensity suitable for imaging, and that it enables a level of infection that is sparse enough to allow proficient resolution and imaging of single cells.

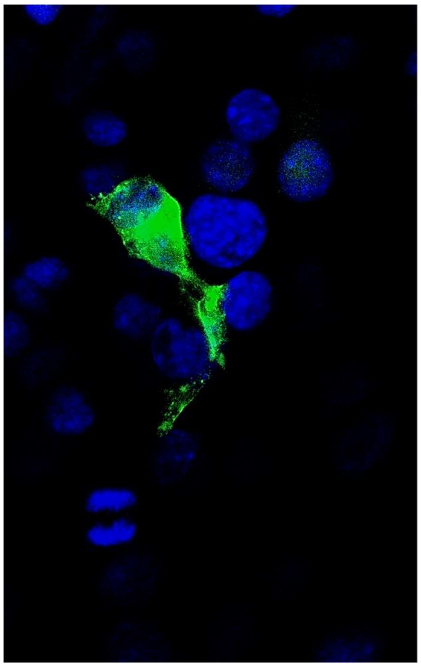

Figure 3.20: Preliminary images depicting Oli-Neu cells expressing the GFP chimeric protein (Green). Blue counterstain indicates cell nuclei as labelled with DAPI. Images taken at 20x, with excitation at 485nm and 351 nm. It can be seen that many cells are in frame but only one is expressing GFP.

Following this result, the infection rate of cells was investigated for the viral construct. For this work Oli-neu cells were grown until they reached approximately 80% confluency within a 35

mm imaging dish with a circular 14mm^2 glass bottom (P35GC-0-14-C, Mattek). The media within these dishes was then carefully aspirated, and A7(74) FP-MBP was added such that 7500 viral units were delivered to the well. These cells were left for 16-20 hours to allow the construct to be expressed and mature. The cells were then stained to identify the plasma membrane by incubating them briefly in CellMask Deep Red Plasma membrane Stain (C10046, ThermoFisher). Cells were then fixed and stored in PBS pending imaging. The cells were then imaged on the spinning disc confocal microscope, with 40 fields of view captured. Within these images the number of CellMask positive cells (red cells, providing the total number of cells), and transgene expressing cells (green cells) were quantified. Using this data it was possible to determine that the efficiency of infection with the Dendra2-MBP vector, when used under the current infection conditions, was 23%.

3.4.6 Kinetics of transgene expression in Oli-neu cells

The kinetics of transgene expression were explored to understand the length of time required for cells to express the fluorescent MBP construct, and the time it takes for the expression to reach its maximum. Cells were cultured in imaging dishes until they were approximately 70% confluent. The cell medium was then aspirated to remove the culture media and infected with 7500 units of A7(74) construct suspended in fresh imaging SATO media. These cells were incubated for 1 hour at 37^{o}C 5% CO_2, after which the virus solution was removed and the cells washed with fresh medium to ensure as much virus was removed as possible. Cells were then imaged on the spinning disc confocal microscope (either on Confocal or Widefield mode) to collect a baseline image where FP signals could not be observed. Images of the cells were taken for every 1.5 hours until the level of fluorescent signal could not be seen to change. One final image was also taken at 24 hours as a positive control to ensure cells were infected. From

the images it was observed that the SFV A7(74) construct is expressed at approximately 3 hours post infection with expression reaching a peak at 6 hours.

It should be noted that these times are approximate, as the timeline can be slightly quicker or slower depending on the resilience of the cells being infected.[451]

3.4.7 Viability of infected cells

Survival of the cells were a key point to explore when considering the utility of the new SFV vectors. If the construct is toxic to the cells this would alter the interpretation of any results obtained when imaging MBP in live cell experiments. In addition, the approximate length of time before activity of the SFV vector produces significant signs of reduced viability in cells (rounding up, process retraction) is important to know as it determines the maximum length of time available to image cells following infection. In order to investigate this, Oli-neu cells were infected with SFV A7(74) Dendra2-MBP. In the case of Dendra-TM-MBP, cells were imaged to collect a baseline image approximating the first detection of fluorescence (referred to as 0 hours in Figure 3.21). Images of the cells were then taken approximately every 3 hours using both bright field and fluorescent imaging. When no fluorescence was observed imaging was terminated. It was seen that upon expression of the construct cells began to appear injured (rounding up, retraction of processes), and this phenotype became more apparent up to 6 hours at which time all infected cells appeared to show this injured phenotype. By 9 hours, all infected cells had retracted their processes, and un-infected cells started to migrate into the field to occupy the newly vacated spaces. By 24 hours no fluorescent cells could be seen and the field was populated with uninfected cells only. These results suggested the Dendra2-TM-MBP virus possessed an additional level of toxicity compared to the other viruses. This was contrasted with results from the Dendra2-MBP virus (Figure 3.22), where following virus

expression up to 24 hours only a small number of infected cells show an injured phenotype, this number slowly increases until 36 hours, where many of the infected cells died and were replaced by other fluorescent cells which had migrated within the dish. By 48 hours many of the infected cells were lost with few fluorescent cell bodies visible within the dish, leaving only uninfected cells.

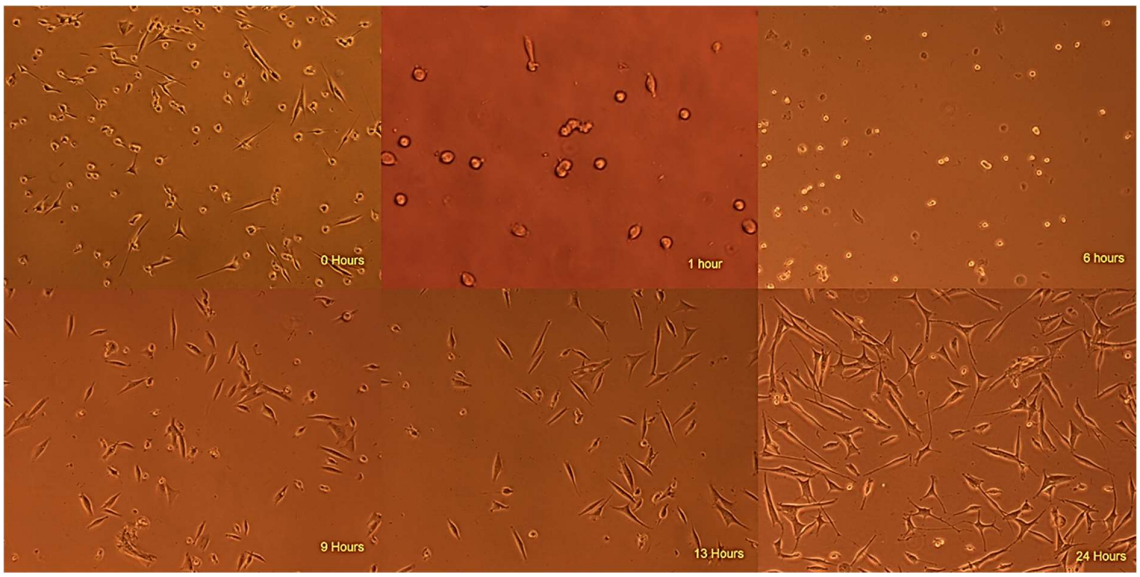

Figure 3.21: Viability assay of Dendra2 TM MBP. Cells are shown to possess an injured morphology with loss of processes and rounding up as early as 1 hour post expression. The infected cells die off within 9 hours and are replaced by uninfected cells.

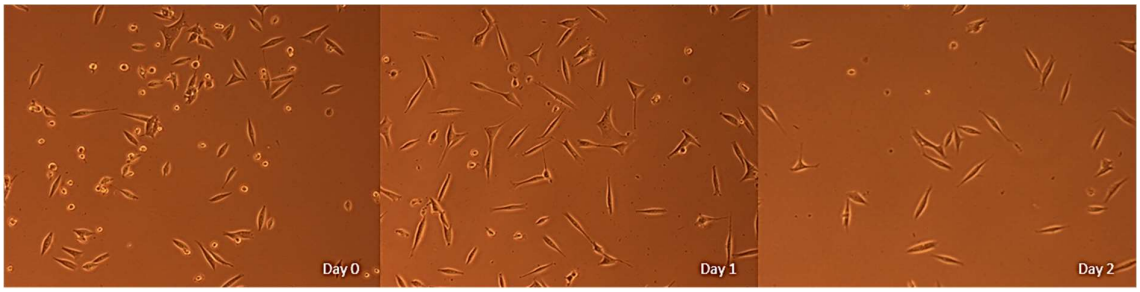

Figure 3.22: Viability assay of Dendra2 MBP. Here a small number of cells are shown to be injured from expression of the protein, however, cells are shown to be expressing the protein up to 2 days where all infected cells are shown to have died and been replaced by uninfected cells.

3.4.8 Virus expression profile

Previous work in the field found that MBP protein expression occurs mainly by free polysomal synthesis in OL processes, with MBP mRNA being transported to processes through granules

[452–454]. This expression profile was tested in the MBP constructs, to see if MBP shuttling is changed when expression is mediated by the SFV A7(74) vector. For these experiments the MBP-Dendra2 construct was used. MBP-Dendra2 expression started 3 hours following infection of cells (Figure 3.23). The expression started in small clusters within the perikaryon of the cells with little to no expression observed in the processes at this point. As time progressed the cells expressing MBP-Dendra2 started to change in morphology. This may reflect the normal migratory behaviour of cells of this type such as OPCs, where forward motion involves cell and process extension[455]. Another possibility is that these changes in morphology actively facilitate protein transport to the processes of Oli-neu cell, inducing the processes themselves to compact. The bulk of the fluorescence was still observed within the perikaryon of the cells following expression, suggesting that expression is driven by cell machinery within the cell body, and not *via* free polysomes within the processes. This result contradicts the results of previous studies within the field using MBP, where Nucleoside triphosphate labelling showed that MBP RNA is shuttled to the processes[452,453].

3.5 Conclusion

This chapter describes the creation of a number of new SFV vectors encoding various FP-MBP proteins designed for the exploration of the behaviours of MBP (Table 3.6). This construct was designed and created de novo from the DNA template, and made into viral particles. These viral particles were tested to see their expression properties, such as expression localisation, expression timeline, the infection rate, and the virulence. It was concluded that the new SFV vectors produce a pattern of infection with suitable efficiency to infect approximately one quarter of cells in a given culture, leading to FP-MBP expression lasting three hours to two days following infection.

Table 3.6: Summery of SFV A7(74) viruses produced. All viruses, other than the Dendra2-TM-MBP virus, showed viral expression up to 2 days following infection. The GFP-PLP$_{frag}$-MBP virus was shown to be the most tolerable construct out of all the construct produced.

Virus	Titre (Viral Units/ml)	Time till expression (Hours following infection)	Last observed expressing cell (Hours following infection)
Dendra2-TM-MBP	$3.66x10^5$	3	12
GFP-PLP$_{frag}$-MBP	$3.5x10^5$	3	60
mCherry-PLP$_{frag}$-MBP	$3.4x10^5$	3	39
Dendra2-MBP	$3.9x10^5$	3	39

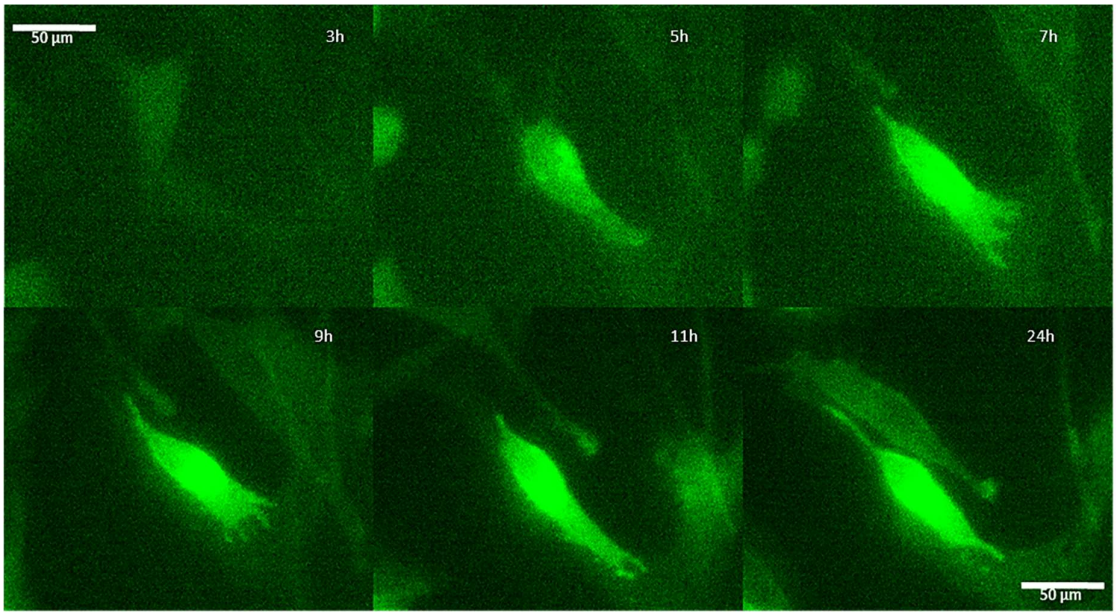

Figure 3.23: Virus expression over time. It can be seen that expression starts within the cell body at 3 hours, and that expression is accompanied by a change in morphology that appears over time with the cell, progrerssing from a triangular shape at 3 hours, to a bipolar shape (two processes) by 24 hours.

Chapter 4

Complement-mediated oligodendrocyte and myelin Injury experiments

"How can a three-pound mass of jelly that you can hold in your palm imagine angels, contemplate the meaning of infinity, and even question its own place in the cosmos?"

- Vilayanur Ramachandran

4.1 Introduction

Myelin plays an essential role within the brain, providing trophic support to neurones, protection to axons from pathological conditions within the environment, and by providing an insulation to the axons, allowing saltatory conduction[67,68,88,121,132]. Conditions where demyelination occurs, such as MS, neuromyelitis optica, and central pontine myelinolysis, can have detrimental effects on brain function, leading to a myriad of symptoms such as pain, visual deficiencies, poor homeostatic control, and loss of motor coordination[203,212,456–458]. When demyelination occurs the functional effect on the neurone is the same, with the loss of trophic, environmental, and signalling support. However, the mechanisms by which these injuries propagate may vary greatly. For example, demyelination in the CNS can be induced by a number of causes, including physical trauma, such as spinal cord injury, immune mediated attack, as is the case with MS, and excitotoxicity, like what happens within Stroke, to name a few.

Complement proteins have been shown to be implicated in the progression of MS, with complement activation being heavily localised to areas of active myelin destruction in MS patients[459]. Of key interest is complement C3 which has been linked with the progression to clinical disability within MS patients[460]. Complement C3 and C1q have also been found to be elevated in areas near demyelinating plaques in secondary progressive cases of MS, as well as complement C3 being present within the CSF of patients with relapsing remitting MS in association with an increase in Complement C4a [23,256,460–462]. Reduction of serum complement using cobra venom factor has been shown to reduce the severity of EAE, an experimental model of MS[463–466]. For this reason within this study we chose to focus upon immune-mediated damage involving the complement system. For this injury an anti-MOG antibody

was chosen to make the injury specific to myelin, as this is an injury which has previously been shown to produce demyelination similar to that seen in MS[467,468]. This gives us a chance to apply live-imaging approaches to determine how the myelin injury progresses at the level of myelin proteins. To date the analysis of myelin injury has relied on static methods, for example electron microscopy and immunofluorescence[469,470]. These methods do not provide detailed temporal resolution of myelin injury. In contrast, a live-imaging approach has the potential to provide greater insight into the temporal development of the injury, thus it could help to guide the development of pharmacological interventions for the protection of OLs and myelin in the face of ongoing demyelinating conditions.

First discovered in serum as a system which complemented the roles of antibodies, the complement system is a key element in the innate immune system[298]. The complement system has three key roles in the immune response, providing an early line of defence against pathogens via formation of the membrane attack complex on targeted cells, initiating the recruitment of the adaptive immune system in the form of various types of T-cells, and participating in mechanisms of cellular waste clearance[297,298]. In the case of these experiments the interest is in the early attack function, as this activity provides a means to induce external physical damage to OLs and myelin membranes (demyelination), and the generation of myelin debris that may trigger the recruitment of an adaptive auto-immune response that could set the stage for the development of a demyelinating disease state.

Antibody treatment with complement has previously been established as a means to induce demyelination in brain slices, which is considered to be reversible, e.g. remyelination is possible [467,468,471–473]. This injury was considered to be myelin specific leaving axons un-injured,

and when utilised with antibodies against MOG, presents a phenotype analogous to certain aspects of MS pathology[468,474–477]. The aim of this work is the development of an imaging system capable of resolving the earliest stages of myelin injury, thus it was important to characterise the kinetics of complement activation. In addition, to avoid studying secondary effects due to axonal injury it was also important to confirm that the model selectively induced myelin injury with minimal effects on axons.

Previous work on the complement injury modality utilised 7% complement and 100 µg of antibody, both utilised in excess.

4.2 Methods

4.2.1 Level of complement needed to induce injury

The first aspect of the complement injury which was considered for optimisation was the level of complement required to obtain a myelin injury within organotypic slice cultures. Previously it was shown that a treatment of 7% complement combined with 60 µg/mL of an anti-MOG antibody produced effective demyelination [467,471,473,478]. However, this work did not provide optimisation data to explain the choice of this concentration of complement and anti-MOG. It is therefore possible that lower concentrations of both compounds may provide an equally effective demyelination treatment. This is important for two reasons. First, as noted above, it was desirable to produce a selective myelin injury with minimal axonal injury. Second, anti-MOG is expensive, thus optimisation of the concentrations required to induce demyelination would provide a useful modification to the protocol. Previous work within the lab determined that concentrations as low as 20 µg/mL of antibody produced effective demyelination when combined with 7% complement. For this reason the effects of 20µg/mL anti-MOG was

investigated when combined with 7%, 3% and 1% complement to determine the level of complement necessary to facilitate myelin injury.

4.2.2 Cerebellar slice cultures

Cerebellar slice cultures were produced by Dr Daniel Fulton according to the methods described by Fannon et al 2015[120]. Six-well culture plates were prepared 1 day before the acquisition of cerebellar tissue slices. Millicell-CM organotypic culture inserts (PICMORG50, Millipore) were placed in the required wells containing 1ml of culture medium (Table 2.1). Sterile confetti membrane discs (FHLC01300, Millipore) were added on top of each culture insert (five to eight segments per insert) to provide a substrate for stable adherence, and to enable easy transfer of individual slices during experiments and subsequent staining procedures. The plates were then maintained in a humidified cell culture incubator (37°C, 5% CO_2) overnight[120]. To obtain brain tissues, postnatal 9-10 (P9-10) days old C57BL/6 mice were sacrificed by Home Office approved methods according to Schedule 1 of the Animals (Scientific Procedures) Act 1986. After this procedure brains collected and placed immediately in oxygenated ice-cold slicing solution. Cerebella were dissected out in slicing media and attached to the vibrotome stage using super glue. Cerebella were sectioned at 350 µm thick slices and then observed under a light microscope to detect and remove slices of uneven or irregular cuts, and to trim away unwanted pieces of brainstem. Slices were then transferred on to pieces of confetti membrane. The slices were cultured in this way for 7-14 days, with media changes every second day. Slices were regularly observed to monitor viability, through the observation of slice integrity and white matter tract continuity, preceding the initiation of an experiment slices were judged on quality, and viable slices were selected.

4.2.3 Slice Selection

Prior to experiments slices were surveyed and selected based on their viability. This was performed on a bright field microscope using the 4x objective to assess the slice quality and 10x objective to assess the white matter track quality (tracks being the central regions of folia white matter containing myelinated purkinje cell axons). Slices were classified by a 3-point system based on the quality of the white matter tracks as observed at 4 and 10x (Figure 4.1). +++ represented slices with clearly defined white matter with mainly continuous tracks. ++ represented slices with clearly defined white matter with some continuous tracks. + represented slices containing white matter which had lost some definition and contained few continuous tracks. – represented slices which had lost all traces of white matter structure. Typically only slices of +++ / ++ where used for experiments.

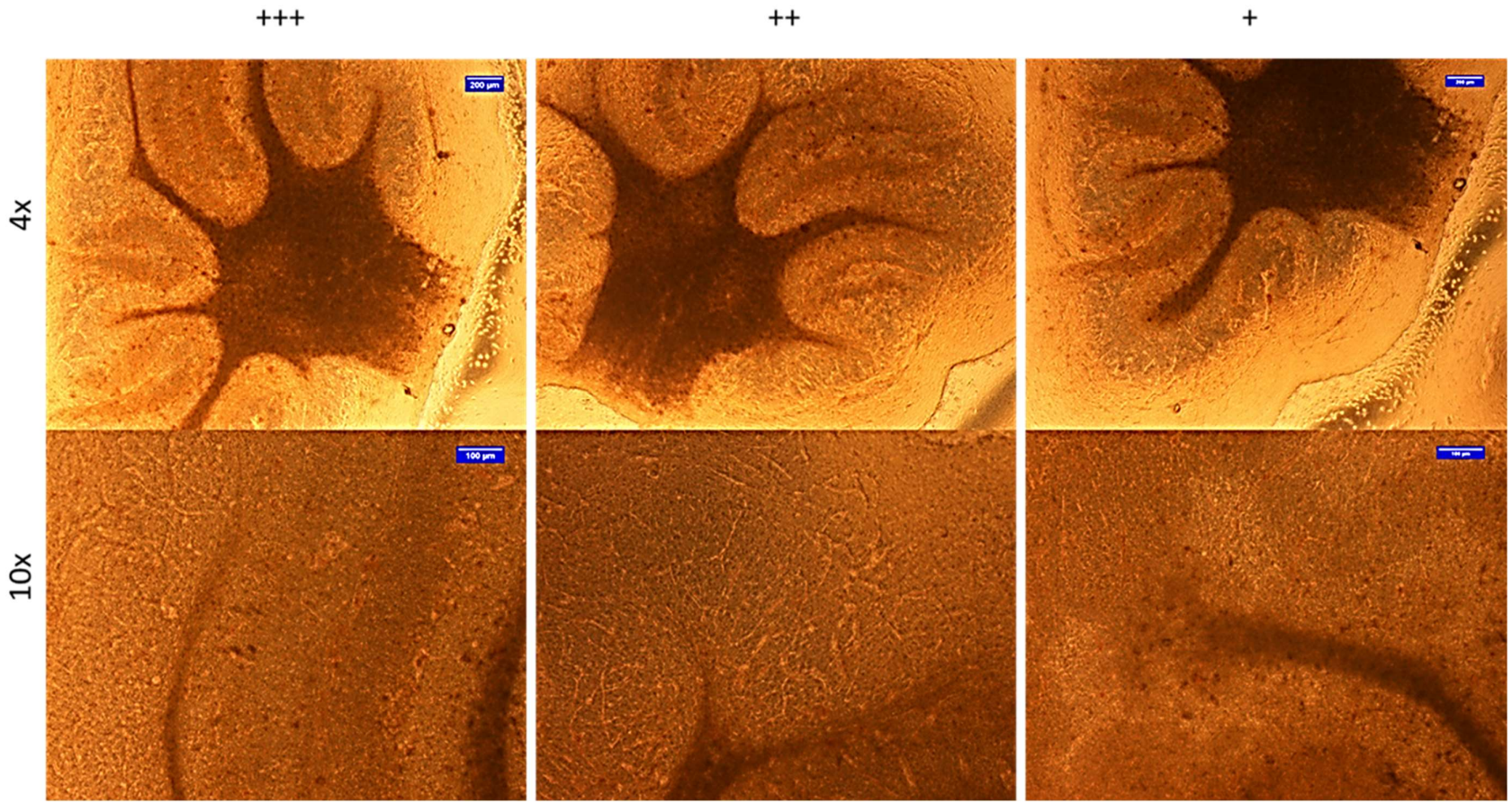

Figure 4.1: Brain Slice Ranking examples of slice conditions meeting each rank. It can be seen that slices with lower ranks (+/++) have a greater amount of granularization and are less continuous. Whereas the higher ranks are more continuous with less granularization

4.2.4 Complement concentration assay

Selected slices were arranged to ensure an equivalent number of slices of similar quality within each group. Typically experiments used a minimum of 3 slices per group. Wells within a 6 well plate were prepared with the treatment conditions outlined within Table 4.1. A stock of sterile filtered complement solution was prepared by dissolving lyophilised baby rabbit complement (CL3441, VH Bio) in 1 ml of ice cold culture medium, this was further diluted 1 in 10 in culture media to make a 10% stock to minimise variation through pipetting errors. 1ml of this solution was then added to each well, and culture inserts holding the slices were added to the wells to start the complement treatment. Treatments were performed at 37^{o}C for 24 hours, following which, the slices were fixed for 16 hours at 4^{o}C with 4% paraformaldehyde (PFA) solution. The fixed slices were stained with Rat anti-MBP (MAB386, Merck Millipore), with a secondary stain utilising a Goat anti-Rat antibody conjugated to alexafluor488 (A-11006, Thermofisher) to detect myelin, and 4',6-diamidino-2-phenylindole (DAPI) (D1306, Thermofisher) to visualise nuclei, then mounted on microscope slides with aquamount (18606, Polysciences). Slices were imaged on an inverted microscope (Zeiss) equipped with a spinning disk confocal module (Andor Technologies). Confocal images were collected with a 20x Air objective (N.A. 0.5) with an exposure time of 800ms. Z stacks containing the complete myelin track (as defined by anti-MBP staining) were produced with an image every 5µm. These images were then imported into FIJI for processing.

Table 4.1: Complement concentration assay injury conditions.

Condition		Media	Complement	Antibody	Antibody Concentration
Complement Injury 7% complement	IgG	Slice Culture media	5:7 dilution	Mouse IgG1 Isotype Control (M5284, Sigma)	20 µg/ml
	MOG			Anti-MOG (MAB5680, Merck Millipore)	
Complement Injury 3% complement	IgG	Slice Culture media	3:10 dilution	Mouse IgG1 Isotype Control (M5284, Sigma)	20 µg/ml
	MOG			Anti-MOG (MAB5680, Merck Millipore)	
Complement Injury 1% complement	IgG	Slice Culture media	1:10 dilution	Mouse IgG1 Isotype Control (M5284, Sigma)	20 µg/ml
	MOG			Anti-MOG (MAB5680, Merck Millipore)	

4.2.5 Neuronal Injury validation

Six slices were selected to evaluate the level of neuronal injury arising from treatment with 20 µg/mL anti-MOG plus 3% complement. Here 3 groups were analysed: two groups utilising 3% complement treatment with 20 ng/ml of an antibody (1) anti-MOG with 3% Complement (anti-MOG/Complement); (2) mouse IgG isotype control (m IgG control) plus 3% complement (IgG control/Complement); and one slice with no complement or antibody (3). Anti-MOG / complement treatments were initiated as previously described (4.2.4), after which slices were fixed and labelled against MBP, with a goat anti-rat antibody conjugated to Alexafluor 488 (A-11006, Thermofisher), to detect myelin, and against the 200 dA isomer of neurofilament (anti-NF200), with a goat anti-chicken antibody conjugated to Alexafluor 594 (A-11042, Thermofisher), to label axons. Slices were then mounted and imaged as described in section 4.2.4 before being imported into FIJI for processing and ranking.

Analysis of injury progression and repair

In order to see how the injury progressed over time, and whether remyelination was possible in this protocol, a time course examining myelin injury was performed. The aim of this experiment was to find the optimal time to observe the myelin injury. In order to achieve this slices were arranged in 3 groups: two groups utilising 3% complement treatment (1) anti-MOG/Complement treatment; (2) IgG control/Complement; (3) no anti-MOG / no complement. Time points for analysis were 1 day, 3 days, and 10 days after exposure to the treatment. Previous experiments (4.2.4, 4.2.5) had used a 1 day time-point for analysis, thus 3 days allowed time for a greater degree of myelin injury to occur, while 10 days represented the amount of time by which remyelination had previously been reported to occur[479]. 3 Slices were allocated to each group, with the quality of slices between groups adjusted to ensure homogeneity across the groups. Treatments were performed as described in 4.2.4 and allowed to continue for 24 hours, after which they were terminated by replacement of the media with fresh culture media. Slices were then incubated in culture medium for the required amount of time, with the 1 day time-point classified as 1 day after the removal of the treatment. Slices were then subjected to fixation, anti-MBP/anti-NF200 staining, imaging and analysis as described previously.

In order to understand whether the responses seen were due to the combination of the antibody with complement, and not the individual components, this experiment was repeated with the following additional groups: (1) m IgG isotype control only; (2) anti-MOG only; (3) complement alone. These additional groups were designed to probe the effect of each of the components in isolation. These samples were treated, stained and mounted as described previously.

4.2.6 C9 stain

To investigate whether the myelin injury produced by anti-MOG/complement treatment are a result of the formation of the membrane attack complex, slices were stained with anti-C9 which recognises complement complex. For this work we used a custom polycloncal anti-C9 raised in rabbit, provided by Prof Pranab Das (School of Immunity and Infection, University of Birmingham). Four groups of slices were studied: (1) no treatment (providing a background control for C9 levels in the slice system); and three groups using 3% complement, (2) complement alone; (3) m IgG control/complement; (4) anti-MOG/complement. Slices were treated for 24 hours, after which slices were labelled with anti-C9 and MBP, and with DAPI used as a counter stain against the nuclei. These samples were mounted and imaged as described previously.

4.2.7 C9 Time course

To determine how complement activation progresses following initiation of the treatment, a time course study was performed, looking at the levels of the C9 complex at each time point. Slices were treated as described previously (4.2.7) with either anti-MOG/complement, or m IgG control/complement. Slices were then fixed in PFA at the following time-points: 30 minutes, 3 hours, 6 hours, and 12 hours following exposure to the treatment. After fixation slices were labelled using antibodies against the C9 complex and MBP, plus DAPI as a nuclear counterstain. Samples were then mounted and imaged as previously described (4.2.4).

4.2.8 30 minutes injury condition

In order to see if the C9 complex activation observed following 30 minutes of anti-MOG/complement exposure would be sufficient to induce myelin injury within the brain slices, an injury condition was tested where exposure to anti-MOG/complement was

performed for only 30 minutes. 3% complement treatments were prepared as conducted in 4.2.8, with slices treated with either anti-MOG/complement, or m IgG control/complement. Following 30 minutes of exposure all slices were carefully washed in warm culture media to remove any residual complement or signalling molecules. Slices were then transferred into a well of fresh slice medium, and incubated for a further 24 hours at 37^{o}C. Following this slices were fixed using PFA, stained with anti-MBP and anti-NF200, and mounted as described above. Slices were then imaged and analysed as described in 4.2.4.

4.2.9 Live imaging

4.2.9.1 Evaluating the 'bubble' setup for live-imaging

The conditions required for live imaging of slices were investigated. Imaging could not be performed with slices on culture inserts, as although the inserts are optically clear, they place the slices in a position outside of the focal distance of the lenses on the microscope. For this reason 'bubble imaging' was performed, where slices were imaged in imaging dishes (Mattek) submerged in a small bubble of media, approximately 100 µL of imaging media. Bubbles were used to achieve a balance between the need to provide nutrients to the slices via the culture medium, and the requirement for adequate levels of dissolved gasses (O_2/CO_2), which would not be possible if slices were submerged in large volumes. To test the viability of OLs within slices maintained under these conditions we used a previously generated farnesylated mCherry (mCherry-f) virus, SFV A7(74) mCherry-f to label and image OLs, as fernesylation leads to membrane localisation making it easy to track changes in cell morphology[480,481]. First, slices were examined carefully to select slices with sections of viable white matter tracks. These slices then received intra-white matter injections with SFV A7(74) mCherry, after which they were left to incubate for 7 hours at 37^{o}C/5% CO_2 to allow expression of the reporter

proteins. Slices were surveyed for fluorescence, and live imaging was performed using the Andor spinning disk system. Confocal Z stacks were collected at 564nm (800 ms exposure) with a 20x Air Objective (0.5 N.A.) at 5µm intervals covering the entire range of the cells. Based on the appearance of imaged OLs under these 'bubble conditions' it was determined that slices could be imaged for periods of up to 6 hours (Supplementary Figure S4.1).

4.2.9.2 Live-imaging of anti-MOG/complement injury

Live imaging was performed using the 'bubble' setup tested previously (4.2.10.1). The slices were carefully selected such that slices with at least 1 highly continuous white matter track were selected. These slices received intra-white matter injections with the SFV A7(74) mCherry MBP virus after which they were incubated for approximately 7 hours to ensure expression of the reporter protein. These slices were then exposed to anti-MOG/complement and Z stacks of a selection of mCherry MBP positive OLs were collected every 1.5 hours between 3 and 12 hours after initiation of the treatment. Imaging parameters were as described in (4.2.10.1). In between imaging sessions slices were returned to the culture insert / culture well and maintained at 37^{o}C/5% CO_2. Target OLs were located in multiple imaging sessions based on their appearance within a map of the slice that was prepared prior to the start of the treatment. After the experiment images were exported and assessed in FIJI.

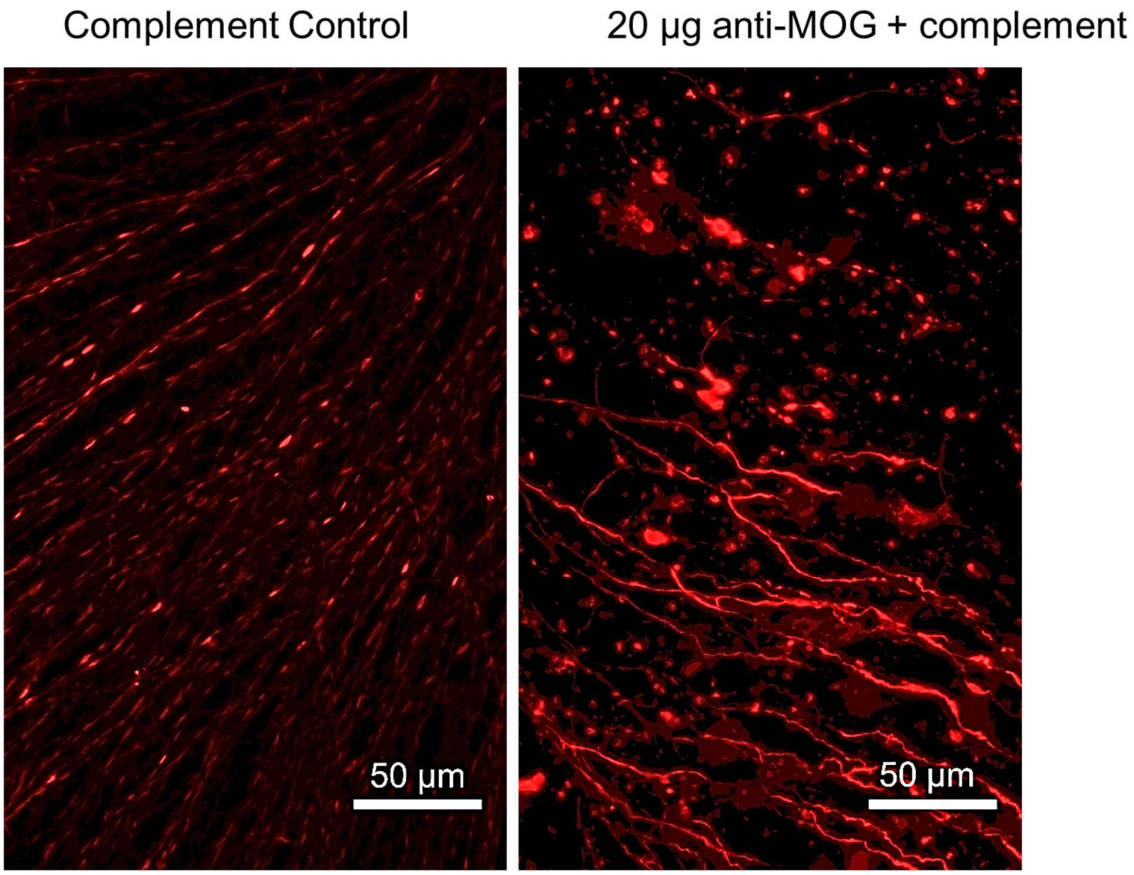

Figure 4.2: NF200 staining for 20 µg MOG with 7% complement. Clear neuronal degeneration is visible within the MOG treated sample compared to the complement control which is highly continuous with little blebbing. N=3

4.2.10 Image processing

A custom Image J macro (appendix), was used to load images in Fiji, perform contrasting, and produce maximum intensity projections from the z stacks. During the operation of this macro the Bio formats function was used to separate the imaging channels, which were then saved as individual tiffs to allow reference to an unmodified image if required at a later date. Images were contrasted using the Fiji brightness/contrast module, by setting the upper limit of the intensity histogram to the point of 35% saturation. Then the single channel image stacks were Z projected, using the maximum intensity within the stack, to produce a singular image for the analysis where all the OL processes were visible. Maximum projections were then saved in individual folders for each channel. To allow easy implementation of the macro all images

were taken with MBP in the first channel position of the stacks. DAPI images were not taken, but only used for initial focusing during imaging setup.

4.2.11 Ranking of Slice injury

To assess myelin and axonal injury in images taken from the brain slices a ranking scale (ranging from 1 to 4) was developed, where a score of 1 represented the greatest degree of injury, and 4 represented healthy / non-injured tissues (Figure 4.4). Rankings for myelin were performed by assessing the anti-MBP signal, whilst rankings of axonal injury were performed using the anti-NF200 signal (Figure 4.3). Both of these were chosen due to the morphology of the signals they produce, with both labelling the processes of either myelin or neurones in a continuous fashion, and thus providing an easy means to detect injury. In both cases ranking scores of 4 were assigned for processes which are continuous and show only a small amount of blebbing/ disruption. In contrast a ranking score of 1 was assigned where processes were barely evident and were mainly replaced by cell debris. Ranking scores of 3 and 2 were used where the processes were found to be partly discontinuous to highly discontinuous, with the amount of blebbing/ disruption and cell debris increasing.

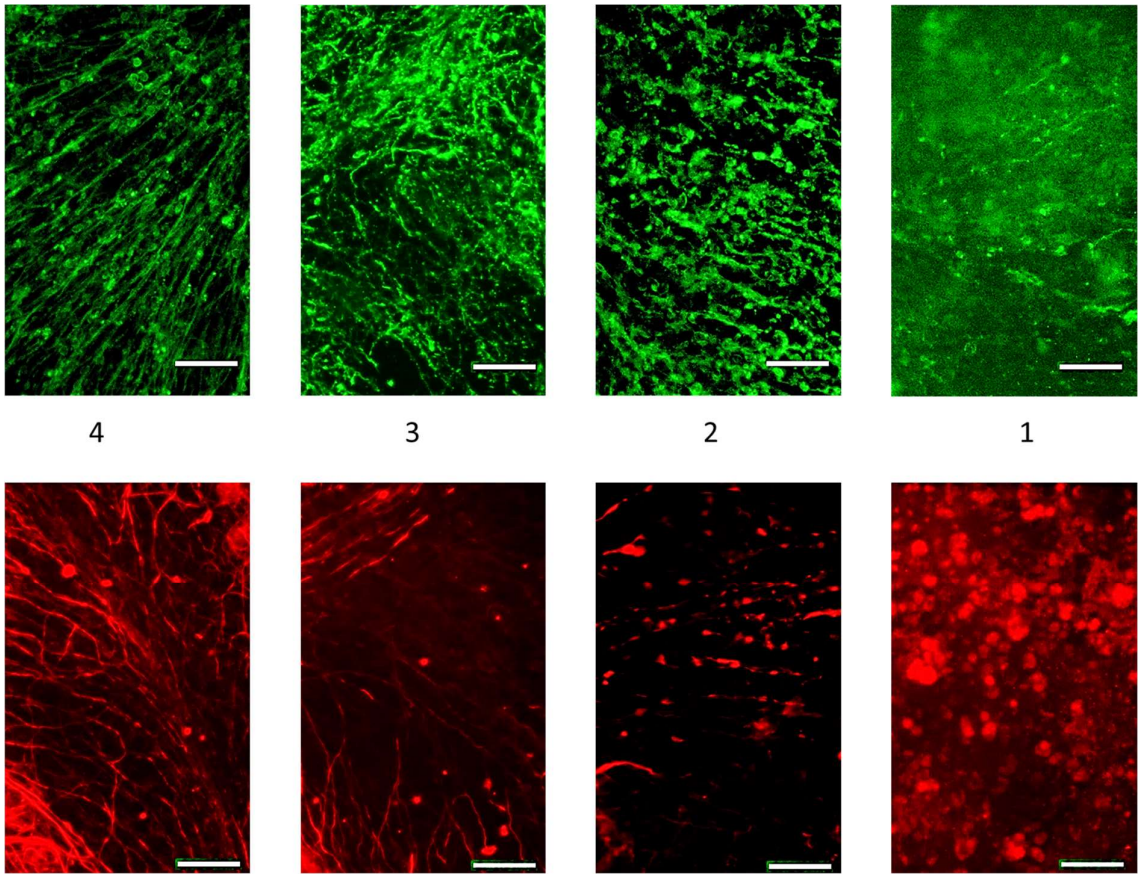

Figure 4.3: Scale for Injury rankings. The varying levels of discontinuity and blebbing can be seen with 1 having the most of both and 4 having the least.

4.2.12 Matlab blinding of Ranking

In order to ensure ranking of the images were done in a non-biased and a consistent manner, the images to be ranked were displayed to the ranker in a blinded manner. This was achieved through the use of a Matlab™ function (appendix). Following processing within Fiji, the Z projected images were fed into Matlab, where they were stripped of their names and displayed in a randomised order for the individual to rank. The order was then stored in a matrix with the original filenames, and ranking, for analysis at a later point. Once all of the images had been analysed the matrix was exported as an excel file. This blinded ranking was repeated 3 times, non-consecutively, to reduce bias to the rankings caused by the

confounding variables such as the state of the ranker, time of day, mood of the ranker, which may affect the rankers ability to rank images consistently.

Following ranking of the images, the images were separated out into experimental groups, and then assigned a label of either injured (rank scores 1 or 2), or uninjured (rank scores 3 or 4), based on the ranking scores they received. These data were then collated and graphed and a chi squared statistical test was performed to determine whether differences in the distribution of injured and non-injured images achieved a level of significance ($P<0.05$).

4.3 Results

4.3.1 Complement concentration assay

Analysis of the proportion of images exhibiting myelin injury revealed a dose-dependent effect of complement. Comparison of the proportion of images assigned as injured in m IgG and anti-MOG treated slices incubated with 1% complement did not reveal a statistical difference (p=0.06). However, the same comparison for slices treated with both 3% and 7% complement detected an increase in the proportion of images ranked as injured (3%: m IgG control 6%, anti-MOG 81%, p=0.000019; 7%: m IgG control 10%, anti-MOG 83%, p=0.0006) (Figure 4.4). This data indicates that 3% complement is the lowest usable concentration to produce a significant degree of myelin injury, thus 3% complement was selected for use in all subsequent experiments.

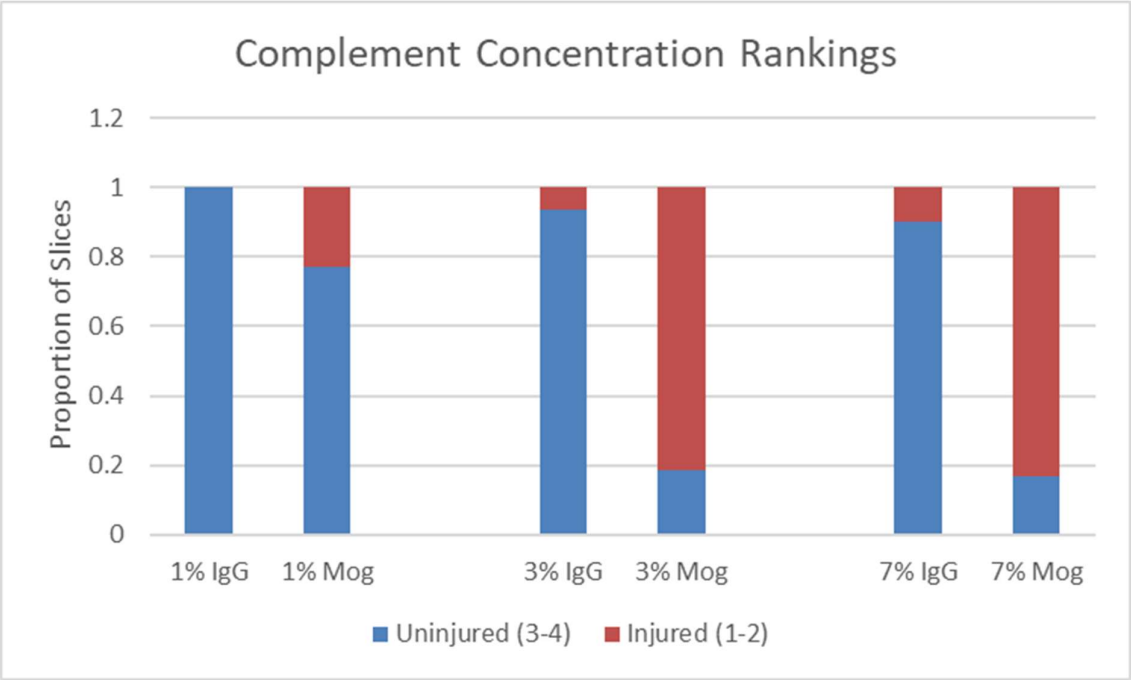

Figure 4.4: Complement concentration assay results. IgG show little injury to myelin within these experiment, whereas MOG with concentrations of complement greater than 3% showed significant injury. N=3

4.3.2 Investigation into the level of axonal injury

Having selected the combination of 3% complement with 20 µg/ml anti-MOG antibody as the optimal treatment to produce myelin injury by 24 hours, the effect of this treatment on axonal viability was then investigated. In agreement with the previous experiment (4.2.1) anti-MOG/Complement treatment resulted in a significantly greater proportion of myelin images ranked as injured when compared to the m IgG control/Complement treatment (m IgG control 9%, anti-MOG 50%, p=0.0267) (Figure 4.5 A). In contrast a similar comparison of axonal images did not reveal a difference in the proportion of images ranked as injured (m IgG control 90%, anti-MOG 89%, p=0.716) (Figure 4.5 B). This data shows that the level of axonal injury resulting from the 24 hour treatment with anti-MOG/3% complement is very low, thus providing confidence that this injury is myelin selective.

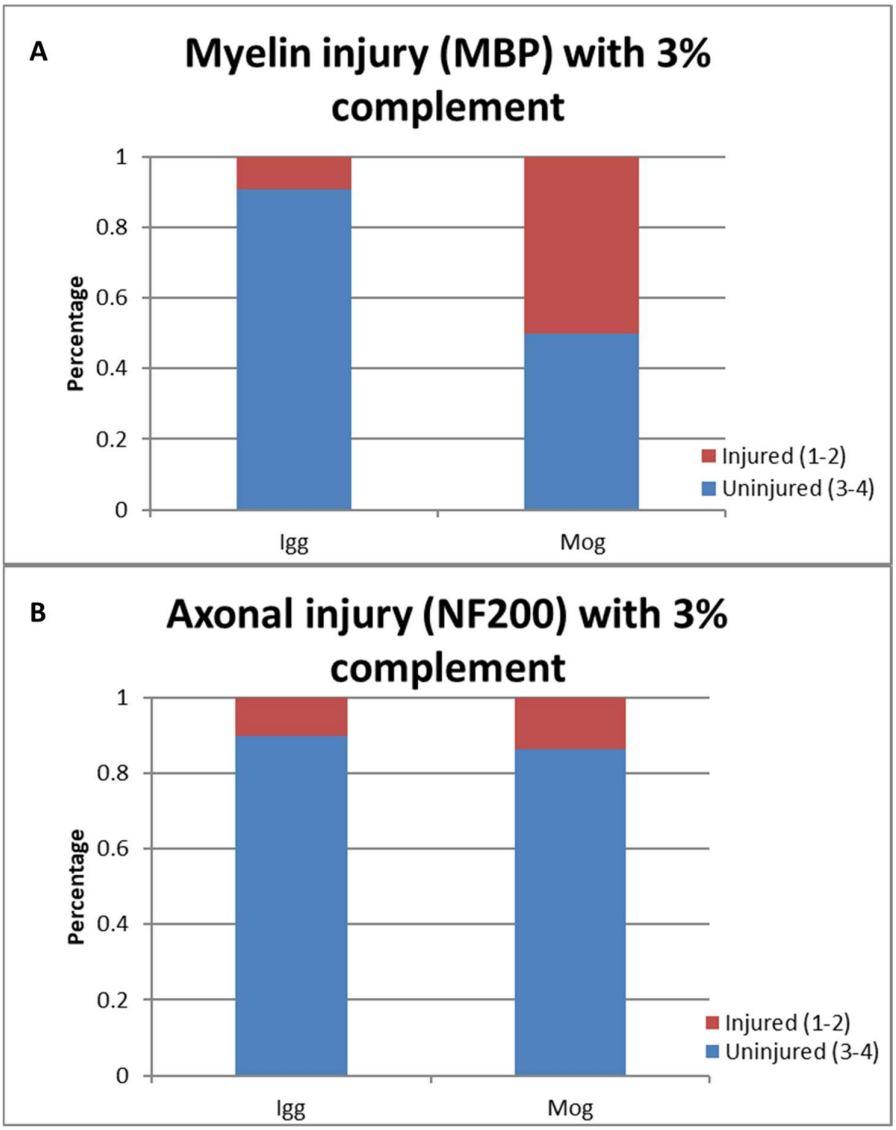

Figure 4.5: Rankings of Myelin and neuronal injury for 3% complement. From the tests with NF200 to look at neurone damage it was seen that 3% complement does not significantly injury axons (p=0.72 from chi^2) and does significantly affect myelin (p=0.03 from chi^2). N=3

4.3.3 Analysis of myelin and axonal injury progression

In order to determine the peak level of injury that would be observed with the conditions determined, a time course of injury was performed (Figure 4.6). The time points of 1 day, as performed in previous experiments, 3 days and 10 days, as it is suggested that remyelination should occur by this point, were used. From the results the injuries to the myelin between day

1 and day 3 were not seen as different (Day1 anti-MOG 66%, Day 3 anti-MOG 67%, p=0.941), this was supplemented with the results of the neurone injury, which showed that no difference (Day1 anti-MOG 17%, Day 3 anti-MOG 15%, p=0.912). However at day 10 it was observed that slices were significantly more injured in terms of the myelin (Day3 anti-MOG 67%, Day 10 anti-MOG 90%, p=0.018), this could also be seen when observing the signal from neurones which are notably more injured (Day3 anti-MOG 15%, Day 10 anti-MOG 100%, $p=1.46E^{-11}$). In terms of injuries within each group, day 1 and 3 both showed significant myelin injury when IgG control/complement and anti-MOG/complement were compared (Day1 IgG Control 13%, Day 1 anti-MOG 66%, $p=2.48E^{-5}$, and Day3 IgG Control 12%, Day3 anti-MOG 67%, $p=5.15E^{-7}$), whereas at day 10 no significant difference is seen between the treatments (Day10 IgG Control 80%, Day 10 anti-MOG 100%, p=0.201).

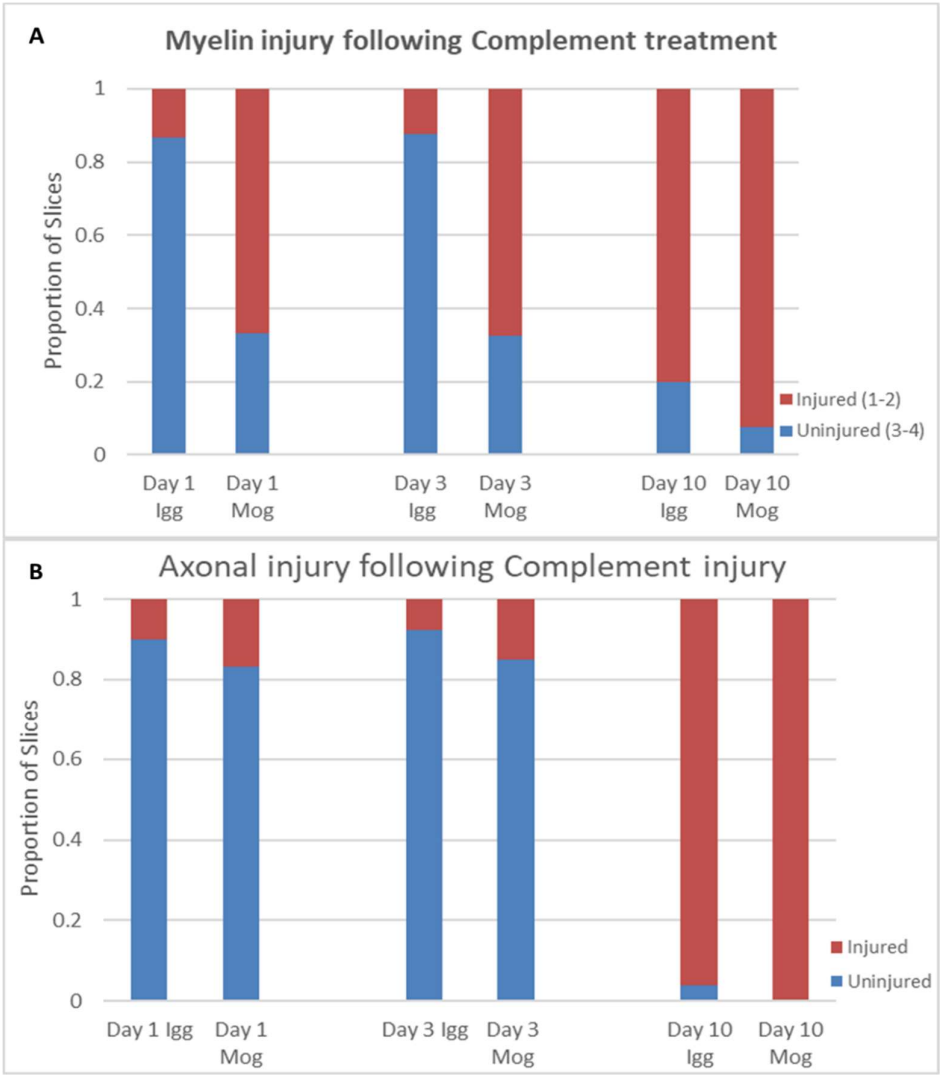

Figure 4.6: Rankings of injury following axonal and myelin injury progression. From these results it can be seen that myelin and axonal injury does not vary between days 1 and 3. Whereas after 10 days of injury myelin and axons both are severely injured in both injury conditions. N=3

4.3.4 C9 stain

To confirm that the complement system plays a role in the myelin injury produced by anti-MOG/complement treatment slices were stained with anti-C9 to label membrane attack complexes. From the anti-C9 staining it can be seen that untreated slices (no anti-MOG/no complement) and complement only slices showed a small amount of C9 labelling 24 hours after initiation of the experiment (Figure 4.7 A,B). This C9 signal likely reflects a basal level of

endogenous complement activity within the slices. In contrast, both m IgG control/complement and anti-MOG/complement treated slices showed a greater level of C9 Labelling at 24 hours. Interestingly, the m IgG control/complement condition showed strong levels of C9 activation with more pronounced cellular localisation when compared to the anti-MOG/complement condition (Figure 4.7 C), where the activation was more diffuse (Figure 4.7 D).The intense C9 activation seen at 24 hours in the m IgG control/complement group suggested non-specific binding of the m IgG, which is further supported by the stains shown in Supplementary Figure S4.1. To test this possibility slices exposed to a 24 hours treatment of m IgG control/complement were fixed and probed with anti-mouse secondary antibodies. These experiments revealed a low level of diffuse m IgG binding on slices that was not localised to specific regions (e.g. white matter / grey matter) (Supplementary Figure S4.1 A). This contrasted with signals from anti-MOG/complement treated slices where distinct immunosignals were apparent on cellular processes as expected for a myelin targeting IgG (Supplementary Figure S4.1 B).

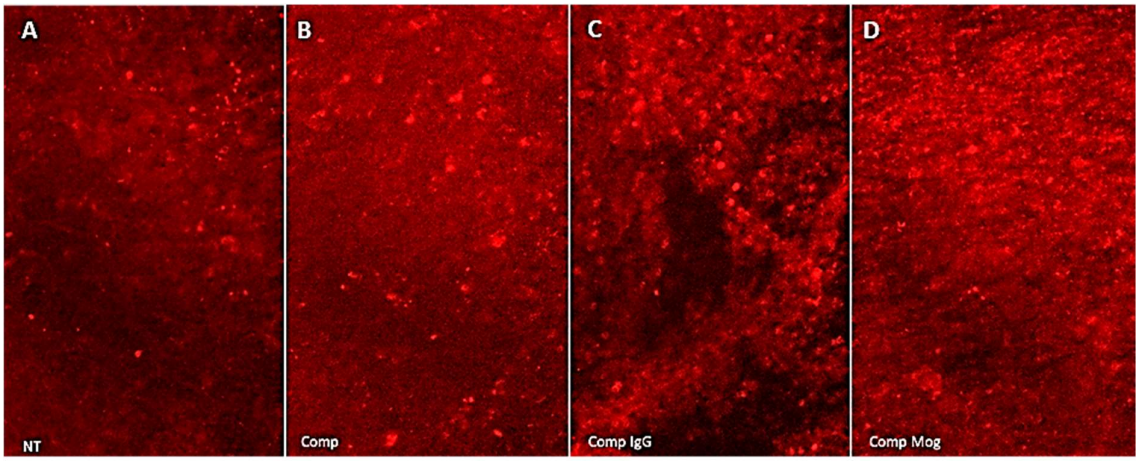

Figure 4.7: Complement C9 activation following treatment. No treatment (NT) shows a low level of residual activation, complement only treated slices (comp) show the same residual level activation as NT. complement with IgG (Comp IgG) shows localisation with cell bodies and processes, whereas MOG with complement (Comp Mog) shows localisation of C9 all across the slice. N=3

4.3.5 Analysis of C9 activation kinetics

Anti-MOG/complement treatment induced a more diffuse C9 signal at 24 hours when compared with m IgG control/complement (4.3.4, Figure 4.7 C-D). These observations appear to be at odds with the effects of these treatments on myelin viability, with anti-MOG/complement providing a significantly greater myelin injury (4.3.2, Figure 4.5). This discrepancy may be explained if anti-MOG induced a stronger and faster complement activation than the m IgG control treatment. In this scenario the peak of C9 activation may have occurred earlier than the 24 hour time-point, with diffuse levels at this time reflecting a loss of C9 from terminally damaged cells. To test this idea a time course was performed to analyse the progression of C9 activation following initiation of the anti-MOG/complement and m IgG control/complement treatments (Figure 4.8). For anti-MOG/complement it can be seen that C9 activation starts as early as 30 minutes after the injury had begun (Figure 4.8 A), while C9 levels remain low at this time within the m IgG control/complement treatment (Figure 4.8 B). C9 activation can be seen to progress across the sample in the anti-MOG/complement group as time passes, with the C9 signal localising to the white matter tracks, increasing to a peak intensity at 6 hours, before diminishing so that it is barely visible at 12 hours. In contrast, in the m IgG control/complement condition C9 complex formation is first seen at 3 hours, when it is present at a low levels, increasing over the subsequent time points, and remaining visible at 24 hours, as seen with the C9 staining done previously (4.2.4).

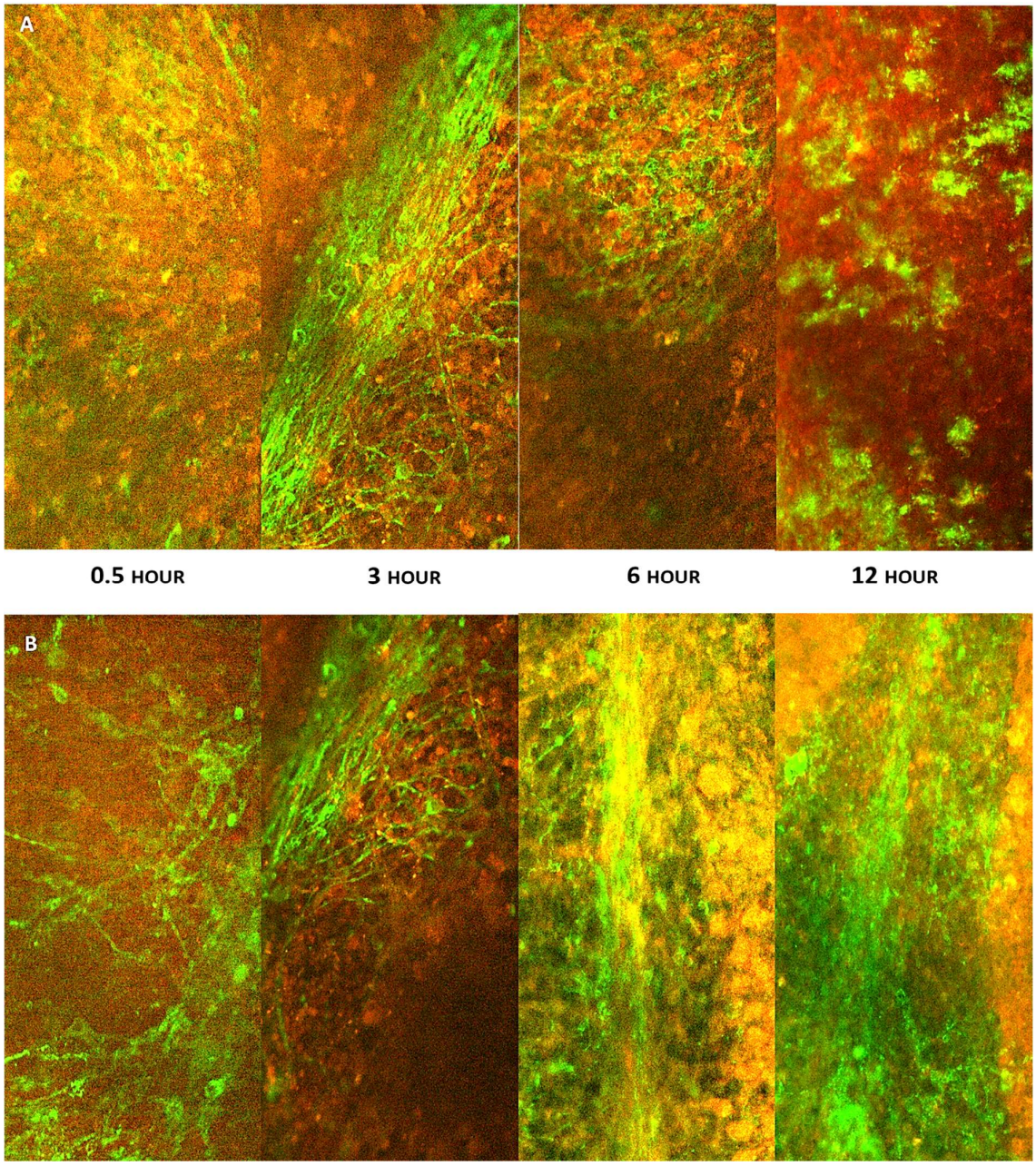

Figure 4.8: C9 activation during various treatment times of complement injuries. With the MOG/complement treatments (Row A) activation can be seen as early as 30 minutes (0.5 hours) can is seen to tail off around 12 hours of treatment. During this time C9 complex staining (Red) localises more around the myelin tracks (Green), until 12 hours where C9 complex activation dissipates and few myelin tracks are apparent. Whereas with the IgG control/complement treatments (Row B) activation is not seen till about 3 hours, with activation still being at high levels at 12 hours following treatment. N=2

4.3.6 30 minute injury experiment

Following the C9 time course experiment (4.2.5) it was questioned whether the degree of C9 complex formed after 30 minutes in the anti-MOG treated slices would be sufficient to induce a significant myelin injury within the slices. As shown in Figure 4.9 A, slices exposed to anti-MOG/complement for 30 minutes group showed a significantly greater proportion of images ranked as injured compared to those from the m IgG control/complement group (m IgG control /complement 12.5%, anti-MOG/complement 79.6%, $p=6.51E^{-21}$). Although a significant injury was seen for myelin, there was little to no injury to axons (Figure 4.9 B), with a similarly low level of images ranked as injured in the two groups (anti-MOG/complement 0%, m IgG control/complement 0%, p=1). This data indicates that a 30 min treatment with anti-MOG/complement induces a C9 activation of sufficient intensity to induce significant myelin injury without affecting axonal viability.

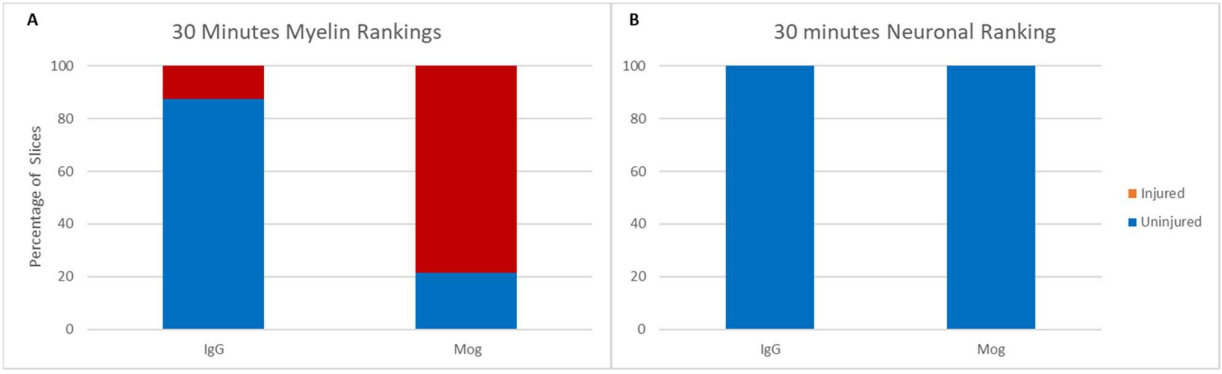

Figure 4.9: 30 minute complement injury. Left) Myelin injury, showing a significant injury between the MOG with complement group and the IgG with complement group. Right) Neuronal injury, showing that neurones were unaffected by the treatment. N=4

4.3.7 Live imaging

Live imaging of 28 OLs expressing A7(74) mCherry MBP provided insights into the kinetics of OL injury (Figure 4.10). OLs imaged from slices treated with anti-MOG/complement showed a loss of processes within 12 hours of treatment induction. The morphology of cells investigated did not show significant alterations at 6 hours, but between 6 to 7.5 hours of treatment OL morphology began to alter, with the loss of their thinner processes, and thickening / shortening of the remaining processes. By 9 hours

the cells had lost most of their processes, and by 11.5 hours all that remained were cell bodies and cellular debris.

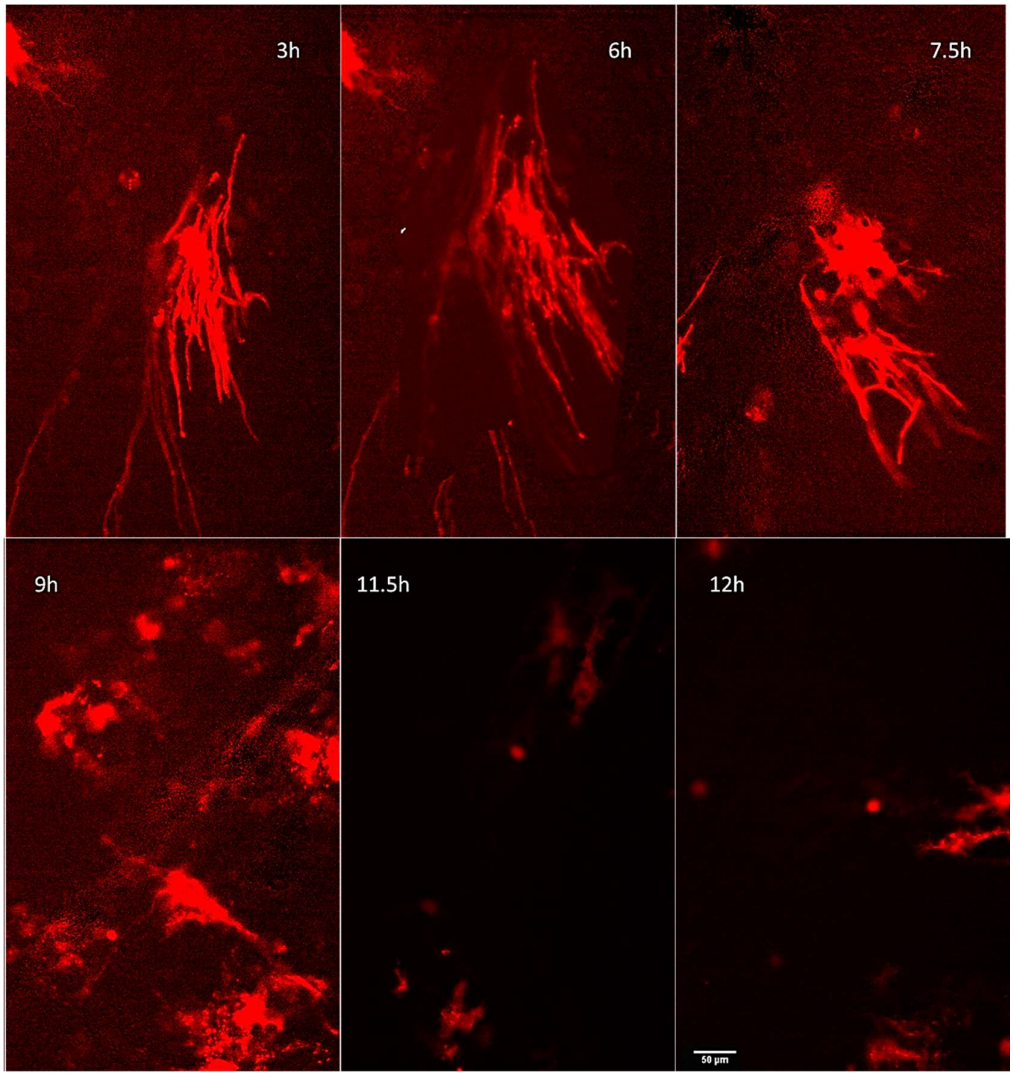

Figure 4.10: Live imaging study of MBP stained Oligodendrocytes. The process imaged here responds to the injury originally by trying to move away from the noxious stimulus, this is followed by cell injury, which by 9 hours leaves a lot of cell debris, as this cell debris is lost new cells migrate into field. N=3

4.4 Discussion

4.4.1 Brief summary

The work presented here was performed to identify a means to induce a myelin selective injury, which does not harm axons. This was in aim to have a model for demyelinating conditions, which could be comparable with conditions such as MS and central pontine myelinolysis where myelin damage is seen

long before neuronal damage is visible. In order to produce this injury a complement injury induced by immunoglobulins against a myelin protein, MOG, was utilised, and its injury was investigated. It was found that injuries can be performed using as little as 3% complement with 20 ng of immunoglobulin, and that this injury only needs 30 minutes treatment in order to produce an effect. This injury was found to preferentially injure myelin, and no recovery from the injury was observed within this work.

4.4.2 Optimisation of complement concentration

The aim of this work was to develop a myelin specific injury model which could be used within subsequent live imaging experiments. MOG complement injury has previously been utilised to induce myelin injury, with concentrations of complement of approximately 7% and 60 µg/ml of anti-MOG antibody with incubations of 2 days onwards[467,468,473,478]. These studies focused solely on the myelin injury induced and did not take into consideration the effect of these treatments on neurones. Although these studies suggested that only myelin injury is observed when using complement at 7%, this was a concern within the experiments presented in this chapter, as axonal injury would lead to myelin being falsely identified as injured as there are less neurones to myelinate, so this property of the treatment was explored within the work presented. Winter et al[467] suggested that concentrations of complement between 3 % and 12% can induce a similar injury to that seen in previous work with 7% complement, so the complement concentrations within this work were manipulated to reduce the potential risk to neurones. The quantity of complement was chosen to be manipulated rather than the quantity of antibody, as the antibody provides a key step in determining the targeting of complement to cells, but does not play a direct role in the injury itself. Reducing the level of complement reduces the amount of damage which can occur, as this reduces the level of spontaneous complement attack possible, this property of complement can be seen within

the C9 time course experiments (4.2.4), as well as reducing the amount of attack complexes which can form as a whole. It was important to maintain the concentration of antibodies at 20 µg/mL as this value had previously been validated as effective by our lab, and so represented an appropriate concentration for ensuring adequate complement/antibody interaction within the slice system. The experiments reported in 4.3.1 indicated 3% complement as the lowest concentration where a statistically significant injury was observed. Interestingly this value is within the bounds suggested by Winter et al[467]. 3% complement was selected for all subsequent experiments in this chapter.

4.4.3 Acute complement activation provides a selective myelin injury

Findings from experiment 4.3.2 showed that complement injury from anti-MOG/complement, when applied for 24 hours, did not induce a statistically detectable axonal injury. However, from the results of all the injury experiments taken together, it can be seen that axonal rankings are poorer only for the longest incubations with the MOG complement injury. This is highly apparent following the 30 minute injury experiments which show a reduced level of neurones with an injured phenotype compared to the other incubation times (0% injured with 30 min treatment, 10% with 24 hour treatment, and 15% with 3 day treatment). This may be a result from the formation of large quantities of the C9 complex, which may also interact with neurones if overly abundant within the experiment. The number of neurones with an injury phenotype did not show a significant disturbance for the time points compared within this chapter until the slices were left to incubate to about 10 days following complement treatment. This suggests that the injury either takes many days to induce an axonal injury phenotype, or further injury processes are engaged beyond the direct complement induced injuries. Whether these injuries are due to complement action or some other mechanism is

yet to be understood. However, from the 10 day time point both axons and myelin are observed to be severely injured, whereas before this time point injury to neurones is not seen as significant. Since no additional exposure to complement is seen by the slices after termination of the treatment this injury may be due to the loss of myelin, which is expected to be the main change occurring within the slice environment, as all complement proteins, and metabolites should be removed with the subsequent media changes. If this injury is due to a demyelination induced neuropathy it is an interesting phenomenon, which may be used to develop a greater understanding to how myelin and neuronal viability interact.

4.4.4 Involvement of the classical complement cascade in the myelin injury

Results from this chapter (4.3.4/4.3.5) clearly show that the myelin injury involves the complement pathway. The complement system involves 3 main pathways, the classical, the alternative, and the Lectin pathways all of which activate a cascade of events converging at the production of the C3 convertase[298,482]. The classical pathway involves the use of immunoglobulins, which induces the cascade ultimately resulting in the membrane attack complex. The lectin pathway recognition molecules, such as mannose binding lectin, collectins and ficolins, bind to mannose binding lectin associated serine proteases, which leads to activation of the complement cascade. The alternative pathway activates spontaneously causing the hydrolysis of the C3 thioester bond, which leads to the activation of the cascade and production of the attack complex[483]. In the case of these experiments myelin injury was associated with robust and early complement C9 activation, while a delayed C9 activation was associated with a non-specific IgG/complement treatment that did not induce myelin injury. Although, activation of complement was seen within the controls this was of low basal levels. The pattern of results seen with both treatment conditions is most consistent with the classical

complement pathway, as it was greater than basal activation, and the key difference between the experimental and control groups is the addition of antibody(e.g. myelin specific vs isotype control), and the classical pathway is the only antibody dependant pathway. This explains both the greater anti-C9 signals seen within the antibody conditions, and the different activation profiles between the anti-MOG and m IgG control antibody conditions.

4.4.5 Kinetics of C9 activation and myelin injury

Results from the C9 activation time course (4.3.5) and live-imaging experiment (4.3.7) indicate that the OL/myelin injury phenomenon develops in anti-MOG/complement treated slices several hours following the initial complement c9 activation. From the C9 activation experiments it is seen that levels of activated complement complexes steadily increase up to 6 hours following the treatment, while the live imaging experiments show that injury is not apparent until around 7.5 hours following the initial exposure. This suggests that there is a lag between C9 formation and injury presentation during which time the injury process is established. This lag time could be the time it takes for enough activated C9 to puncture the cells to induce an injured phenotype, or it could indicate that the injury to the cells is induced through an indirect means other than direct C9 induced membrane lysis[484–486]. The idea that an injury can't be seen until the complement complexes reach a critical threshold is supported by observations from the m IgG control/complement group, as although the levels of C9 elevate within the first 12 hours of treatment there is a clear lack of observable injury following 24 hours, up to 3 days. This effect could be due to the diffuse nature of m IgG control binding compared to the MOG binding, as shown in Supplementary Figure S4.1 as the IgG control injury may not provide enough localised damage to lead to an observable myelin response. This is because the C9 complexes within the IgG control/complement condition

show a level of cellular location, within the granule layer, although the cells this localises to has yet to be confirmed. The absence of an observable NF200 or MBP injury at 24 hours, although complement levels are high suggest either MBP and NF200 staining may not be sensitive enough to detect acute myelin injury, or that tolerance for the injury is high, such that the cells can resist showing an injured phenotype when the injury is not focused on it.

The findings from the 30 minute exposure experiments suggest that the critical threshold for C9 activation is lower than the peak threshold as observed a 6 hours (3.3.5). Certainly further complement activity is unnecessary for myelin injury as any messaging molecules and complement would be washed away during the washes that mark the end of the exposure. It should be noted that the live-imaging experiments involved only a few cells (28), thus further replications are required to confirm the kinetics of the injury. None the less, these observations provide strong evidence that the injury presentation at 7.5 hours is not directly related to the peak in complement C9 concentration. Instead this delay likely reflects the time it takes for the cells to respond to the damage induced by initial complement activation.

Chapter 5

Single Molecule Imaging

"There's as many atoms in a single molecule of your DNA as there are stars in the typical galaxy. We are, each of us, a little universe."

- Neil deGrasse Tyson, Cosmos

5.1 Introduction

Imaging of fluorescent signals in living cells and tissues is a key utility used to investigate the structure and function of biological machinery. Various fluorescence modalities allow efficient observation of numerous physiological activities within the cell, including cell death, using agents such as propidium iodide and Nucview™ [487], ion mobility, with agents such as Fura-2[488], to the distribution and trafficking of proteins via transgenic animal models[489,490], and lipid transfection and viral vector mediated delivery of FP tagged fusion proteins[172,401,491,492]. In the context of live-imaging fluorescence imaging is also advantageous since it enables greater spatial resolution than magnetic resonance or ultrasound techniques[493].

Fluorescent investigations can be divided into 2 groups, ensemble-averaged imaging and SMI, both of which have their uses in understanding biological systems. Ensemble-averaged experiments look at the sample as a whole, allowing analyses of cell to cell interactions, intracellular structures, and distributions of groups of molecules by considering the averaged behaviour of the molecules within the sample and not the full spread of molecular activities and their interactions with each other within the system[338]. Although averaging of these behaviours reduces the level of information available, it permits a rapid and relatively uncomplicated analysis that can be useful for many applications, for example the study of active C9 complement complexes seen in the previous chapter. However, as these methodologies look at the sample as a whole the results only depict the averaged behaviour of the molecules within the sample, and not the full spread of molecular activities and their interactions with each other within the system[338]. Single molecule studies, unlike ensemble imaging, look at individual molecules within the system allowing observation of less conventional behaviours within the system that would not be apparent when the averaged

behaviour of the systems is analysed. The main requirement of any SMI methodology is to resolve individual molecules within a population, and therefore see the full range of behaviours which occur within the sample. In order to understand a system, and define its activities, and structure, both ensemble-averaged imaging and SMI should be used. Within the field of glial biology much work has been done at the ensemble level, providing us with many useful insights[338,494]. To date few SMI methodologies have been utilised within the OL and myelin biology field, thus the ambition of the work presented within this chapter is to develop SMI methods for the analysis of myelin protein dynamics both during OL development and injury.

SMI methodologies can be divided into 2 categories, localisation and tracking, each with their own requirements and benefits, summarised in Table 5.1. Single molecule localisation utilises high resolution microscopy techniques, such as STORM or PALM, to provide precise spatial information on individual molecules within the system[364,400,495]. Due to this, and the algorithms used within localisation methodologies, samples tend to be fixed. This allows localisation experiments to derive information on the amount of molecules within the system, the structural organisation of the sample, and particle interactions through co-localisation. In contrast to this are the tracking methodologies which utilise live samples, and conventional optical imaging[323,388,496]. Super resolution imaging would be preferred within this modality, however, this provides a large level of complexity to imaging, which super resolution techniques have yet to address, so instead temporal resolution is prioritised over spatial resolution as this dimension is more important within tracking[497]. Tracking provides information on the molecular responses following an event, and allows observation of molecular movements and dynamics, and short-lived particle interactions. As much of the

ensemble-averaged work has been performed previously on the structure of myelin, and the role of MBP within it, single molecule tracking was chosen for the work within this chapter as little is known on the motility of MBP molecules, and therefore any reference to single molecule imaging hence forth within the chapter shall be a reference to single molecule tracking[338].

Table 5.1: Comparison of Single molecule tracking and Localisation methodologies

	Localisation	Tracking
Type of Resolution needed	Spatial	Temporal
Microscopy used	Super resolution/ Optical	Optical
Fixation	Yes	No
Information achieved	Quantification Structure Particle Interactions (Co-Localisation)	Molecular Dynamics Interactions (Dwell times) Movement

The most widespread single molecule techniques within biology are those which utilise fluorescent probes, which may be either inorganic or organic. Inorganic probes provide a high quantum yield and are normally more photostable than organic probes. A key disadvantage of these probes is that they must be applied ectopically, and can potentially be toxic to cells[321,498]. Organic fluorescent probes, e.g. FPs, on the other hand have the potential to be genetically encodable, and are generally well tolerated by cells, however, their quantum yields are lower than organic probes, providing them with poor signal to noise ratios in imaging[499].

One of the strategies to cope with poor signal to noise ratios is through an exceptional category of FPs, known as photoswitchable FPs[339,400]. These proteins may be converted between a fluorescent on-state, and a non-fluorescent off-state where fluorescent emission is prevented, thus allowing direct control over the fluorophore[351]. Photoswitching allows the

isolation of single molecules through the inactivation of the majority of fluorophores in the sample, leaving the remaining emitters as distinct point sources that can be resolved individually and tracked over time. This is also useful when performing super-resolution imaging, where fluctuations in the signal are used to improve the contrast of the image, as the protein signal can easily be manipulated, and therefore fluctuations can easily be controlled. Many photoswitchable proteins can also undergo photoconversion, where the protein enters an extra fluorescent state in which their emission converts from one wavelength to another[339]. These photoconvertible proteins increase the efficiency of SMI applications as they allow monitoring of multiple individual groups of molecules simultaneously.

For the work conducted within this chapter all SMI work was conducted on monocultures of adherent cells, rather than tissue explant samples such as the organotypic slice cultures as used in Chapter 4, as it allowed more flexibility, and reduced complexity for imaging the samples. Two types of cells were used within this work, the Oli-neu cell line, and primary extracted OPCs.

OPCs are an embryonically derived NG2 positive glial subtype, sometimes referred to as NG2 cells[177,500]. These cells are proliferative, migratory cells, unlike OLs, and are commonly identified antigenically by probing for the surface marker proteins NG2, A2B5, and PDGFαR[202,501]. The quantities of these markers vary within species, an example of such is the marker A2B5, which is key for cellular identity within rat OPCs, however, within mice OPCs the quantity of A2B5 is lower, so NG2 or PDGFαR are utilised instead[336,502]. *In vitro* studies have shown that OPCs are pluripotent cells with the potential to make OLs, type 2 astrocytes, and neuronal cells. Their lineage plasticity *in vivo* appears to be narrower, with astrocytes and

some neurons being generated in the embryonic CNS, but not in the postnatal or adult CNS[503]. *In vitro,* OPCs when exposed to high serum conditions produce type 2 astrocytes, referred to as such as they are produced from a different precursor cell origin than type 1 and show a neuron-like morphology, however, functionally they have not been observed to have different activities to type 1 astrocytes[202,336,504,505], while In low serum conditions OPCs produce OLs. Despite evidence for astrocytic fate in the embryonic CNS, and the generation of small numbers of neurons the majority of cells produced by OPCs *in vivo* are OLs[500]. Morphologically, OPCs have small soma compared to astrocytic and neuronal cell lineages, and are further characterised by the possession of fine processes.

Following differentiation of OPC cells, the cells progress through 3 different stages (Figure 5.1). The first stage is referred to in the literature as the late OPC/preoligodendrocyte stage ($_{p}$OL)[506–509]. At this stage the cells are still migratory, and proliferative, however, they have a multipolar morphology, with thicker processes, and larger soma than OPCs. $_{p}$OL cells start to express antigens recognised by the O4 antibody[510], suggesting a commitment to the OL lineage. Following this the processes of the cells start to become ramified and lengthen, these processes are normally compared to a spider's web. The cells stop expressing NG2 and A2B5 and start to express Gal C, at which point the cells are normally referred to as premyelinating oligodendrocytes ($_{PM}$OL). These cells then progress to extend the membranes of its processes to make flattened ensheathing sheets, while expression of classical myelin proteins, such as MBP, PLP, MAG and MOG begins, at which point these cells are referred to as myelinating oligodendrocytes ($_{M}$OL).

Oli-neu cells are a mouse immature OL cell line, which has been shown to be useful in looking at OL behaviours, and interactions[449,511–513]. The Oli-neu cell line was developed through the induction of the t-neu oncogene in OPC isolated from neonatal mouse cerebellum. The t-neu oncogene carries a point mutation causing tyrosine kinase to be constitutively active[450]. This causes Oli-neu cells to remains in an immature proliferative state where the expression of myelin proteins is suppressed. However, Oli-neu cells have the potential to differentiate to a more mature phenotype[449]. This differentiation is achieved through exposure to dibutyl adenosine 3',5'-cyclic monophosphate (dbcAMP)[449], and has been shown to induce a mature protein array within the Oli-neu cells, with myelin proteins such as PLP and MBP being expressed[450].

In order to understand MBP dynamics during various stages of OL maturation, SMI tracking of MBP was performed in Oli-neu cells, primary OPCs, and primary OPCs cultured under differentiating conditions. This allows further understanding on the behaviour of singular MBP molecules, and through the use of parameters such as confinement and diffusion, it allows inferences into MBPs interactions with itself as well as other OL proteins, such as PLP and CNP.

In order to understand how MBP behaviour changes during injury, the tracking data from healthy cells will also be compared to that obtained from Oli-neu cells subjected to a cellular injury involving exposure to a toxin that disrupts the lipid structure of the plasma membrane (lysolecithin). These conditions are expected to disturb the localisation of MBP producing a more mobile MBP phenotype, as MBP is known to interact with membrane proteins such as PLP and PIP2 with its behaviour well represented by Brownian motion[432,514].

It is also believed MBP would be more mobile in the immature cells, such as the OPC cells and Oli-neu cells, with little difference between the two, as both cell types will not be expressing the mature complement of proteins, which MBP interacts with.

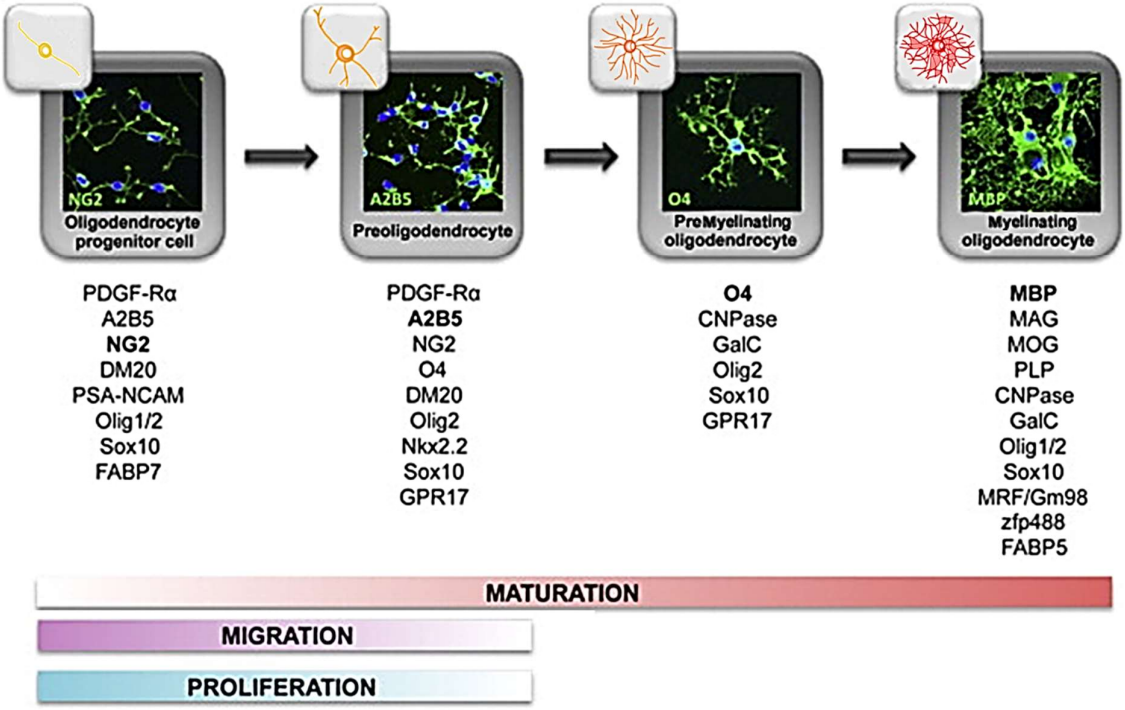

Figure 5.1: Depiction of markers expressed by OPC cells at different levels of maturity. The bars below the list of marks depict that as the maturity of cells increase the cells become less migratory and proliferative. This figure was adapted from Barateiro et al 2014[202]

5.2 Methods

In order to perform single molecule tracking an imaging modality with a high spatial resolution was required to reduce the amount of particle cross-over events observed within the images. This work was therefore conducted using cells rather than slices, as methodologies which can penetrate samples further tend to sacrifice spatial resolution to do so, and of the imaging systems available for this work it was seen as more feasible. Utilising cells also allowed more samples to be imaged, as they can easily be prepared and treated with the virus.

5.2.1 Oli-neu plating

Oli-neu cells were cultured as described in Chapter 3. Cells were then seeded into 3 imaging dishes (Mattek, P35GC-0-14-C) at a density of 30,000 cells per dish. The remainder of the cells were seeded into T75 flasks with approximately 500,000 cells per flask. The cells within imaging dishes were then submerged in 1ml SATO solution and gently swirled to ensure an even distribution. Cells were then incubated at 37°C for up to 2 days at which point they were assessed for infection with SFV vectors.

5.2.2 Oligodendrocyte precursor cell (OPC) culture

Neonatal mice (postnatal day 0 -2) were sacrificed using Home Office approved methods (described by the Animals Act, 1986). Brains were then dissected out and submerged in ice cold dissection medium. The cortices were separated from the midbrain and the meninges were removed using fine forceps. The cortices were then minced into 1mm^3 chunks and then incubated with trypsin and DNase for 20 minutes at 37°C, to liberate as many cells as possible, with agitation every 5 minutes to prevent aggregation. DMEM with 10% FBS was added to inactivate the trypsin, and the tissue was dissociated by trituration through a 10 mL serological pipette. This solution was then filtered using a cell strainer with mesh size of 70 µm, and centrifuged at 200 x g for 7 minutes at 10°C. The supernatant was removed and resuspended slowly, by trituration in 1 mL DMEM/10%FBS with a P1000 pipette, after which an additional 8.5 mL DMEM/FBS was added. 3 ml of this cell solution was transferred into a Poly-L Lysine coated T25 flasks pre-filled with 3 mL of pre-equilibrated DMEM/10%FBS, resulting in a total volume of 6 ml. The flasks were then incubated at 37°C for 16 hours. The next day a complete media exchange was performed to remove as much cell debris as possible, and the cells were left to culture for 9 days with ⅔ media changes being performed every third day, with insulin

supplementation to produce a final concentration of 2 µg/ml. Flasks were visualised each day to monitor cell growth. Positive signs include the steady formation of an astrocyte monolayer and the appearance and proliferation of putative OPC (small round cells with bright appearance) atop the astroglial cell layer. Once glial cell growth had reached an acceptable level, normally around 9 days, the flasks were shaken on an orbital shaker at 160 rpm for 30 minutes, following which the media was changed and the cells were placed on the shaker for a further 16 hours at 220 rpm. All shaking steps were performed within the culture incubator. Shaking in the second step detaches OPCs from the flasks. These suspended cells were then transferred into a non-coated 10 cm dish, and left to incubate at 37^{o}C for 30 min with gentle swirling every 10 min to prevent adhesion of OPCs. The cell suspension from these dishes were then collected and centrifuged at 1000 rpm for 5 minutes at 10^{o}C. The pellet was then resuspended in 1ml of fresh OPC media and 1-5 x10^{5} cells were seeded into imaging dishes (P35GC-0-14-C, Mattek).

OPC Differentiation

In order to differentiate the OPC cells, the cells were exposed to OPC media lacking fibroblast growth factor 2 (FGF2), PDGFαR, and Insulin-like growth factor 1 (IGF1), and supplemented with Triiodothyronine (T3), this media was referred to as differentiation media. The cells were maintained with media changes every other day for 1 week. This provided the cells with the conditions needed to induce differentiation of OPC into OL.

The maturity of these cells were examined through the use of immunocytochemistry for a marker for immature OPC cells, NG2. No signal was observed for NG2 from any of the differentiated cells, compared to undifferentiated cells where a strong NG2 signal can be observed (Figure 5.2). This confirms that cells observed progressed to a level of maturity

beyond the OPC phenotype. This also suggests that the $_{P}$OLs observed in this work were more mature than those within the literature, as expression of NG2 could not be observed within these cells[202,509].

Following the maturation process, 3 stages of cells were observed all of which were NG2 negative cells (Figure 5.2): (1) $_{P}$OL: multipolar cells with few ramifications which were analogous with $_{P}$OLs from the literature[202,506,509,515]; (2) $_{PM}$OL: multipolar cells which were heavily ramified and were analogous with $_{PM}$OLs from the literature; (3) $_{EM}$OL: Multipolar cells with regions of flattened membranes similar to the flattened myelin sheets observed for myelinating oligodendrocytes in vitro. Of note the flattened membrane areas observed in our cultures were not continuous like that seen in the literature, hence these regions will be referred to as myelinating bubbles[202,506,509,515]. In this thesis the 3rd type of cell is defined as early myelinating oligodendrocyte, as there are regions analogous with myelination, but the cells were not at the level of maturity where these regions are continuous. For imaging purposes only the myelinating bubbles were recorded from $_{EM}$OLs. Unfortunately, no cells presented with the mature myelinating phenotype presented in the literature after 1 week of differentiation[202,506,509,515].

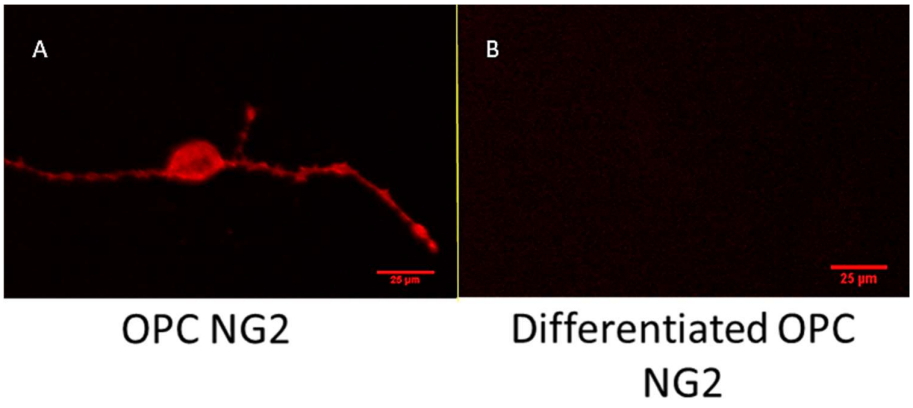

Figure 5.2: NG2 Staining of OPC cells, before and following differentiation. A) OPC before differentiation show robust staining for NG2. Following differentiation (B) NG2 staining is not detected within the dish indicating that OPC in the culture have differentiated beyond the OPC stage. NG2 staining was performed on a upright microscope at 100x magnification.

5.2.3 Infection with SFV

When the cultured cells were approximately 60% confluent, and more than 20% of cells possessed processes approximately 1.5 times the length of the soma, the dish was regarded as ready to image. An example of such a culture is shown in Figure 5.3. For OPC or differentiated OPC cells, it was decided that when the cells possessed processes that were 1.5 times the size of their soma they were ready to image. To prepare the dish for imaging, the cells were infected with the SFV A7(74) Dendra2 MBP virus to induce the production of fluorescent particles for tracking. This was achieved by removing all the media from outside the wells within the imaging dishes, and half of the media from within the well, leaving 100µl of media submerging the cells within the well. The residual media in the well was left to prevent both drying of the cells and reduce disruption to the cells, both of which could affect their viability. 25µl of virus solution was then added to produce a 1 in 5 dilution of the virus providing approximately 7500 infectious units of SFV to the dish. The media / SFV mixture was gently mixed, and left to incubate at 37^{o}C for 1 hour. Following the incubation the cells were promptly washed with fresh Imaging SATO media to remove any remaining viral units, and to

remove any metabolites existent in the media. This wash was performed 3 times to remove as much phenol red and virus from the dish as possible. These cells were left to acclimatise at 37ºC for 6 hours to allow sufficient protein expression, after which the cells were taken for imaging.

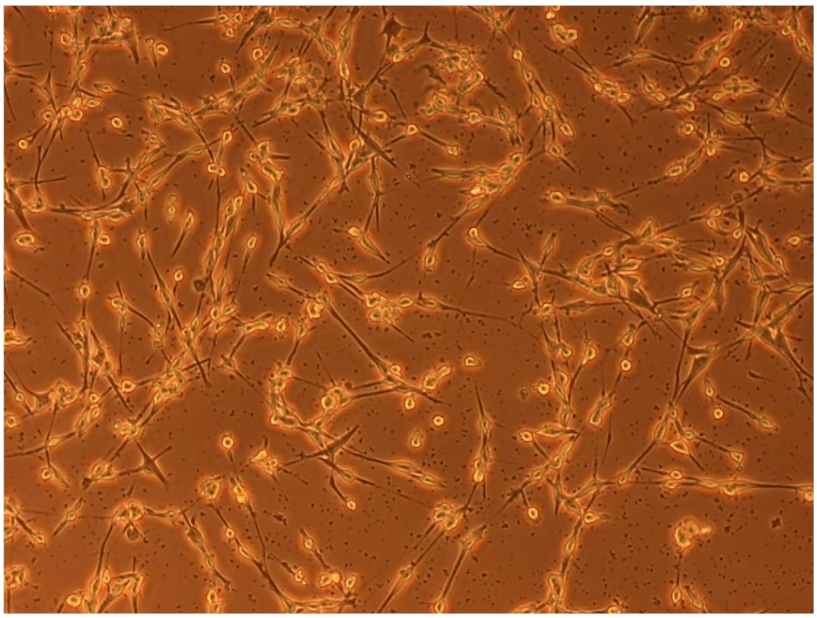

Figure 5.3: Oli-neu cells at stage of growth considered ready for imaging. The sample contained many cells with processes that are much larger than their soma, and a cell density of at least 60% confluent. These conditions were considered optimal for imaging of Oli-neu cells. Of note, many processes within this sample overlap which may be disadvantageous for imaging individual processes if overlapping cells are successfully infected.

5.2.4 Cellular imaging

For imaging, a focus was made on imaging processes of the cells examined, as this is the functional region in terms of MBP, and therefore where the most significant differences were most likely to occur. Also, as it had previously been observed MBP from the SFV vector is centrally expressed (Chapter 3), therefore a large amount of particles and movement would be seen, there would be a large amount of obstructive data to mask any real changes which may occur between samples if the soma were to be observed.

Imaging dishes containing the infected cells were imaged on an inverted widefield microscope, using a 100 x magnification with 1.4 numerical aperture. The cells were first surveyed under bright-field to find cells with processes, after which the microscope was converted to TIRF mode. Upon discovery of a process, the cells were viewed using 488 nm excitation to ensure the cells produced a fluorescent signal. The fluorescent cells were then primarily irradiated with 405 nm light for 5 seconds to induce dendra2 photoswitching from a 488nm excitation to 561nm, producing a spectrally sparse red signal, which could be tracked. Time-lapse imaging was performed on the selected region of interest with a 561nm excitation wavelength, and 30 ns camera exposure times for 2500 frames. In the case of exceptionally sparse signal, or rapidly photobleaching samples, an image was taken at 488nm to produce a reference image to compare the detected particles to, ensuring the particle tracks produced are existent within the processes of the cell, and are not likely to be due to free floating material within the dish. Following this, a new process was identified for imaging, till approximately 2 hours had passed. All resultant timelapsed-image stacks where processed following this using ICY bioanalysis [516].

5.2.5 Lysolecithin injury

Once baseline cellular images had been performed, the processes were injured using lysolecithin. This was achieved by first irradiating the imaged processes with 405 nm light for 30s each to promote further photoswitching from 488 nm to 561 nm. The cells were then treated with lysophosphatidylcholine (LPC) to produce an injury. For the Oli-neu cells 0.5 ng of LPC was used, and for the primary cells 0.5 pg was used as the primary cells were seen to be more sensitive to LPC. Unpublished data from the lab (S.Foale and D. Fulton unpublished) demonstrated concentrations which could be used to injure OL cells, which were used to

determine the concentrations used within this work. These processes where then reimaged using the time-lapse imaging parameters described above.

Table 5.2: Icy Tracking parameters. The parameters shown here were optimised utilising the Oli-neu cells, and were utilised for all the cells used within the analysis in this chapter.

Parameter	Setting
Expected number of False positives	30
Probability of detection	0.9
Expected number of new tracks per frame	20
Expected number of objects within the first frame	50
Expected track length	20
Average predicted displacement	5
Minimum probability of existance	0.5
Threshold of thermination	0.0001
Gate Factor	4
Depth of track trees	4
Number of new tracks per frame	15

5.2.6 Extraction of data

Images were imported into ICY bioanalysis for particle detection and tracking[516]. The images were opened and the contrast within the images adjusted to aid the detection of the processes by eye. Regions of interest were then constructed around the processes of the cell within the first image of the stack. The region of interest was verified with the other images within the stack to ensure it encompasses the process throughout the stack, and adjusted to ensure the region of interest was tightly confined to the process of the cell (Figure 5.4). In cases where the process moved within imaging, the longer segment was taken forward for imaging, or the images were excluded from analysis. This region of interest was then inputted into the Spot detector function, which utilises a wavelet particle detection protocol, and was set to expect detected particles to be approximately 3 pixels in diameter on a dark background, as previous imaging showed this to be an appropriate assumption[381]. Once particle detection was complete the detected particles were input into the particle tracker, utilising the parameters shown in Table 5.2, where the detected particles were compared to each other and the most

likely particle track was calculated for each detection[384]. This particle tracker utilises a multiple linkage hypothesis tracking algorithm to link the particles between each frame. These detected particle tracks were then filtered to remove any particle tracks which are exceptionally small, as these were deemed as tracks which would not provide useful data, and verified by eye to remove any tracks which were not bound within the confines of the cell[517]. Once the tracks were filtered, data was extracted using the motion profiler plugin, mean squared displacement plugin, and the export to XLS function within ICY bioanalysis. These operations provided outputs for the mean squared displacements for each track, the net displacement, gross displacement, the track lengths, and the raw track data[516,518]. These data were then utilised to produce comparative data for the different conditions.

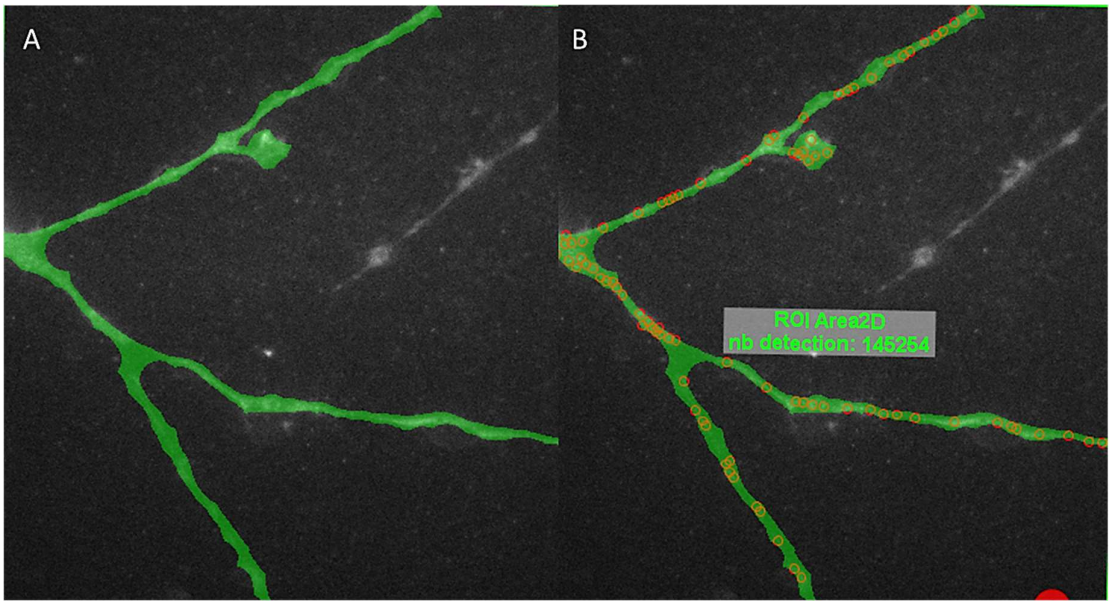

Figure 5.4: Selection of the region of interest within the image and spot tracking. Regions of interest (Green) were carefully drawn to cover the whole process (A). These regions were run through the spot detector function to find the particles within the image (B). These detections (Red) were then run through the particle tracker in order to produce particle tracks.

5.2.7 Data analysis

The outputted data was imported into Matlab, where the confinement ratio and diffusion coefficients were calculated from the displacement, and mean square displacement (MSD),

using both Equation 5.1 and Equation 5.3 respectively. The confinement ratio provides details on particle interactions, as particles which interact more with their environment show lower mobility, which suggests that there is either a structural interaction impeding its movement, or a functional relationship where the particle interacts with another molecule. This works well with the diffusion coefficient which provides the rate of diffusion of the particles within the region of interest. Thus, while the confinement ratio provides details on interactions, the diffusion coefficient provides data on movement. Histograms for the diffusion coefficient and the confinement ratio were produced to visualise the variation of behaviours within the system.

5.2.7.1 Confinements

The confinement ratio is defined as the amount of particle movement detected between the first frame of the track and the last frame, calculated by Equation 5.1. Confinement can be long lasting, or transient, such as the case with lipid rafts and brief molecular interactions[519]. It is also referred to in the literature as the Meandering index, or the chemotaxic index. As it is determined by the amount of net movement divided by the gross movement, the values produced are bound between 0 and 1, with lower values signifying constrained movement and high values signifying free movement[520]. If a particle being tracked constantly changes direction the confinement ratio will tend towards zero, as little net movement will be achieved, where as if the particle moves in a directed manner the ratio will tend to 1 as a large proportion of net movement will be achieved[521]. One key problem with the confinement ratio is that it tends towards zero with longer track lengths, as there are more possible regions of transient confinement, or movement back on itself. This is corrected for by the using the square root of the track duration as a correction factor, Equation 5.2[519,522] .

$$r_{con} = \frac{d_{net}}{d_{tot}}$$

Equation 5.1: Equation to calculate the confinement of a particle (r_{con}). The net diffusion of the particle d_{net} is divided by the path length/gross diffusion d_{tot}.

$$r_{con} = \frac{d_{net}}{d_{tot}} \, t_{(track)}$$

Equation 5.2: Equation to calculate the confinement ratio corrected utilising track length (t_{track}). This prevents short tracks from having larger ratios than longer tracks as the confinement of longer tracks tend to zero, however, this correction stops the ratios from lying between 0 and 1.

5.2.7.2 Diffusion coefficient

The diffusion coefficient is the amount of molecular movement through a surface over a unit of time, given by Fick's first law. This relies on the mass of the substance, the level of interaction of the solute with the solvent, the concentration, temperature and pressure. It can be calculated through Equation 5.3 or through the gradient of the root mean squared displacement graph. Freely diffusive molecules have a higher diffusion coefficient, freely diffusive rhodamine 6G and GFP have the coefficients of 2.8×10^{-10} m^2/s and 1.63×10^{-10} at 20°C respectively, where as highly restricted molecules tend to have a lower coefficients[523–525]. These numbers are dependent on factors such as the temperature, the size of the particles, and the concentration of particles existant[526]. This metric was chosen within this work as it provides a rate of movement for the particle tracks, allowing greater understanding of not only interactions, but also directionality of movement.

$$D = \frac{< x^2 >}{q_i t}$$

Equation 5.3: Equation to calculate the diffusion Coefficient from the MSD. The mean squared displacement in cm^2 ($<x^2>$) is divided by the dimensionality constant for the image (q_i) and the time interval in seconds being used. The q_i for the images used in this work was 4 as all recordings were made in only 2 dimensions.

5.3 Results

5.3.1 Qualitative view on Particle Movement

To provide a qualitative overview of particle movement prior to the quantitative description of particle diffusion and confinement representative motion profiles are presented from single regions of interest. Motion profiles illustrate the two-dimensional movement (X Y) of all particles from a region of interest with the origin of each particle set as 0, 0.

Oli-neu cells: From plotting the MBP particle displacements within each track it can be seen that particle tracks within Oli-neu cells do not show directionality. This can be seen as the distribution of displacements on the motion profile graph (Figure 5.5) is more elliptical, rather than linear, which is representative of random particle movements, and non-directed movement. It can also be seen from the displacement graph that movement within the sample is approximately equivalent in all directions with the graph being centred at 0, 0.

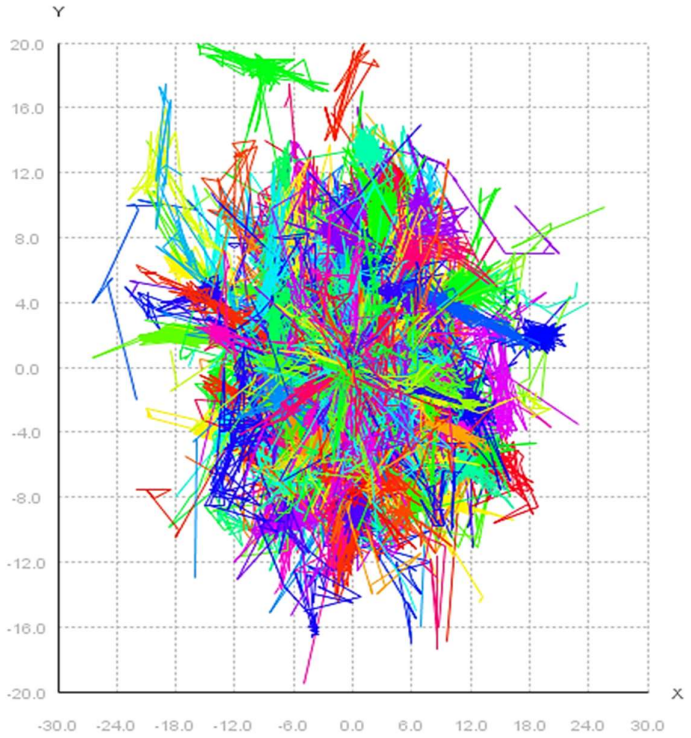

Figure 5.5: Oli-neu motion profile graph. Each coloured line within the graph represents the displacement of a particle in pixels, with 0, 0 being the position of the particle in frame 1. The graph is non-directional as the tracks extend in all directions in near equal proportions.

Primary OPC. From plotting the particle displacements of OPC cells a similar distribution can be seen within the graph as that seen with Oli-neu cells (Figure 5.6). The plot possesses an elliptical shape with particle tracks extending between both the positive and negative regions of the graph, showing movement in all directions. Compared to the displacement of the Oli-neu cells it can be seen that the graph has a less linear morphology, but movement extends to the same distances on average, and both morphologies are still quite elliptical. The particle tracks forming the displacement graph are more spread out, with particle tracks within the Oli-neu cells being seemingly clustered in direction and distance. However the OPC tracks seem to be more spread out, an example of which is the dark blue tracks within each, the tracks move in many directions both towards and away from its starting point in the OPC

graph, whereas a dark blue tracks in the Oli-neu graph originally moves away from its start point, but then is seen moving generally associated to its new point.

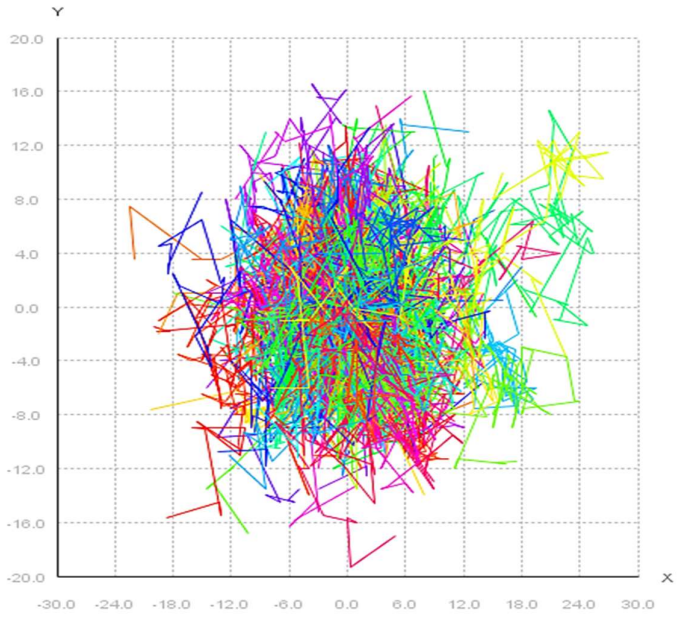

Figure 5.6: OPC motion profile. The graph is exceptionally elliptical in shape, demonstrating random movement in all directions.

Differentiated OPC: For differentiated OPC it can be seen that depending on the morphology of the cell the particle displacement varies, as seen in Figure 5.7 to Figure 5.9. When looking at the $_{P}$OLs it can be seen that like the Oli-neu and immature OPC cells particle displacement when graphed is elliptical (Figure 5.7) suggesting Brownian motion. For $_{PM}$OLs the morphology of the displacement graphs tended to be more elliptical (Figure 5.8) and dependant on the length of the processes. For $_{EM}$OL processes (Figure 5.9), it can be seen that the shape of the graph has a more linear presentation than that seen for the OPC cells and the Oli-neu cells. This varied depending on the size and the number of myelinating bubbles, with processes with numerous smaller bubbles producing graphs with a much more linear morphology.

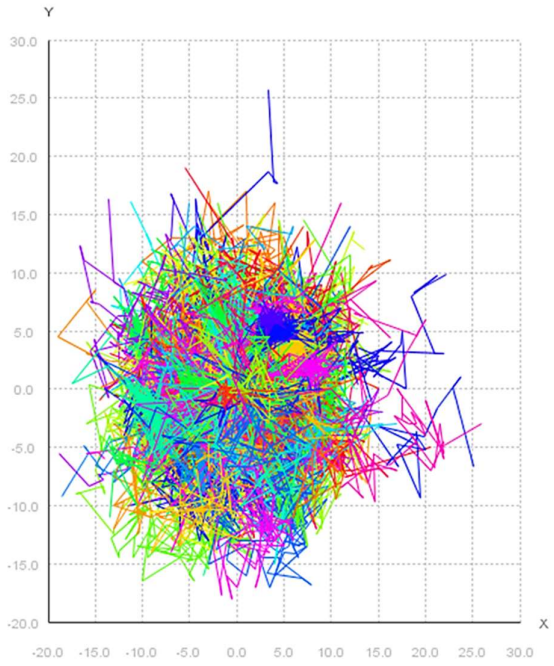

Figure 5.7: Motion Profile of $_{P}$OLs. The motion plot displays an elliptical phenotype suggesting that little to no directionality exists within the movement of particles.

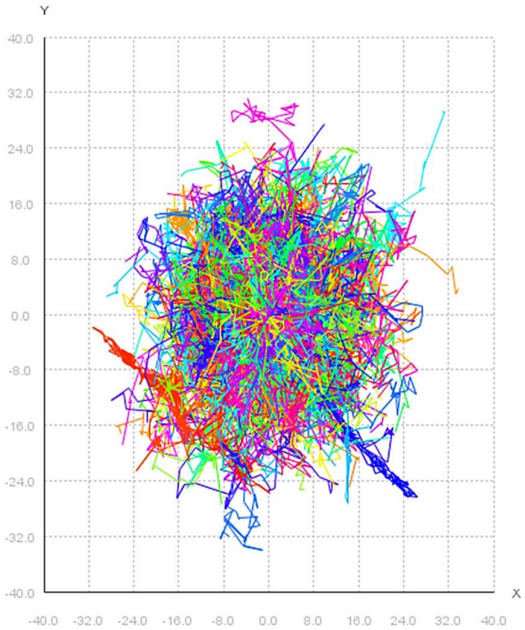

Figure 5.8: Motion profile of $_{PM}$OLs. The $_{PM}$OLs display an elliptical pattern in the plot of track motions, suggesting little to no directionality and random movement.

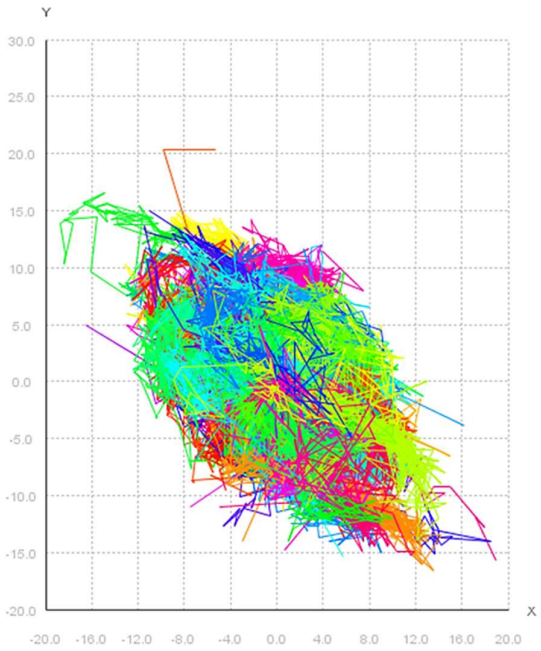

Figure 5.9: Motion Profile of $_{EM}$OLs. The graph is quite linear with many tracks displaying similar motion within the cells.

5.3.2 Diffusion Coefficients

It can be seen from the diffusion histograms that MBP particles in all of the cell types investigated have a range of diffusion profiles underlying their behaviours. The diffusive bodies can be divided into 3 groups, the slow moving populations, intermediate speed populations, and fast moving populations. Each cell type within this work is defined by different proportions of molecules classified within each group. For OPCs it can be seen that there is a broad range of particle movements (Figure 5.10) from the slow moving particles with coefficients less than $2.4e^{-3}$ mm^2/s which make up the majority of tracks, to the intermediary particles with diffusions between $2.4e^{-3}$ mm^2/s and $4.7e^{-3}$ mm^2/s, and faster moving particles with diffusion coefficients above $4.7e^{-3}$ mm^2/s which make up the smallest population within the tracks. Showing that particles within the OPCs still have the potential to be diffusive. When OPCs are differentiated this profile transforms into one which is more sedentary with slower moving particles still dominating the motion profile, and some

intermediately diffusive molecule tracks existing, but the faster moving particles being lost (Figure 5.11). These data suggest a reduced capacity for MBP diffusion within the OL phenotype. This phenotype is further enhanced when these cells are injured using LPC, with a loss of the intermediately diffusive particles, (Figure 5.12).

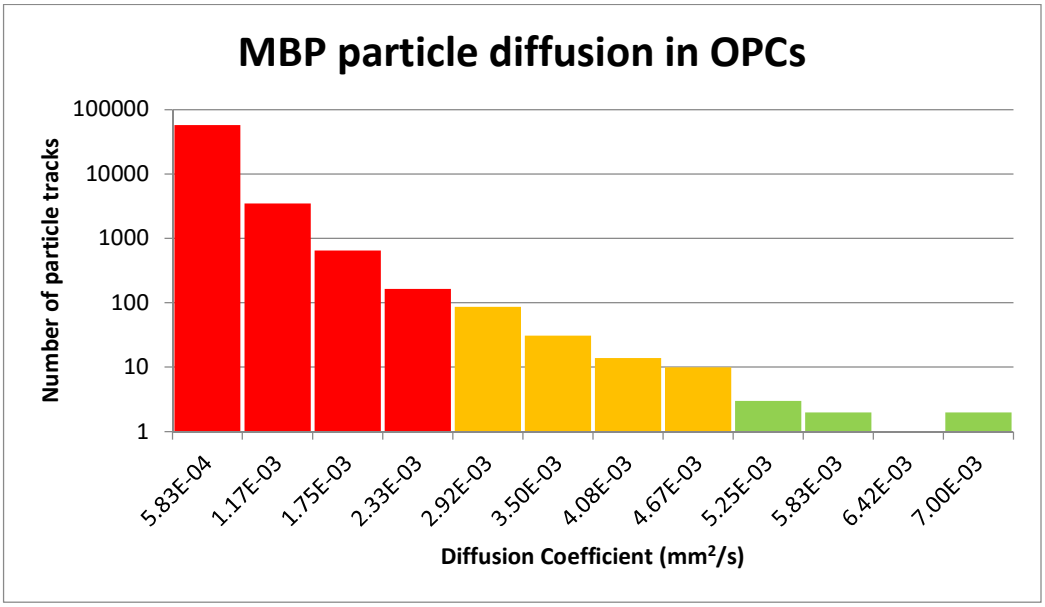

Figure 5.10: Histogram of OPC diffusion. It can be seen that although many of the particles would be classified as slow moving with diffusions less than $2.4e^{-3}$ mm²/s (Red), there is a range of diffusion profiles with fast moving particles with diffusions greater than $4.7e^{-3}$ mm²/s (Green), and particles of an intermediate profile between these boundaries (Yellow).

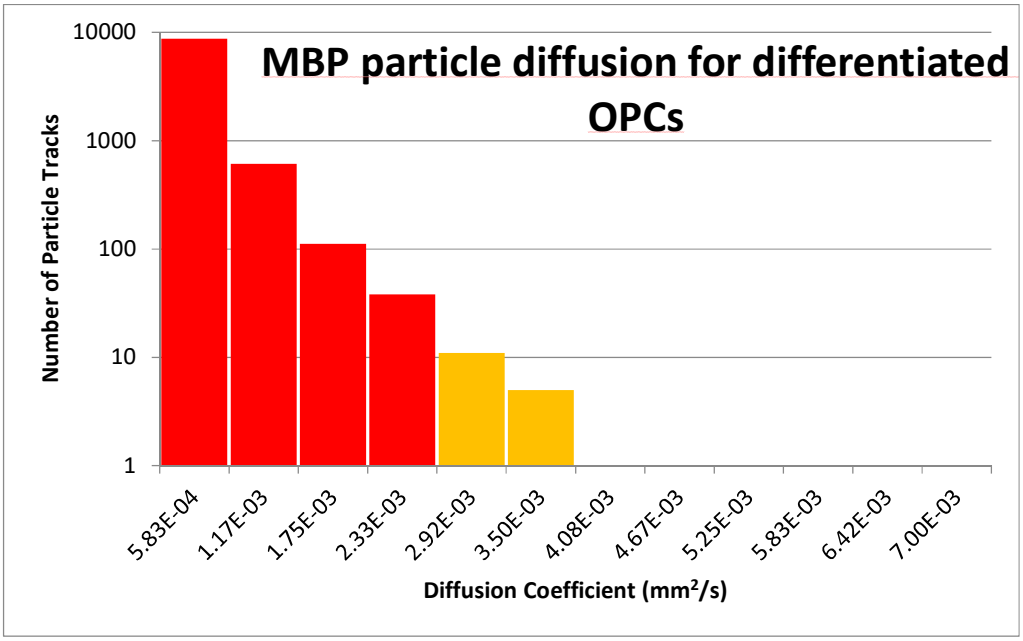

Figure 5.11: Histogram of particle diffusions for the differentiate OPCs. It can be seen that majority of the particles would be classified as slow moving with coefficients below $2.4e^{-3}$ mm²/s (Red), however, a number of particles do exist which would be classified within the intermediately moving category of between $2.4e^{-3}$ mm²/s and $4.7e^{-3}$ mm²/s (Yellow).

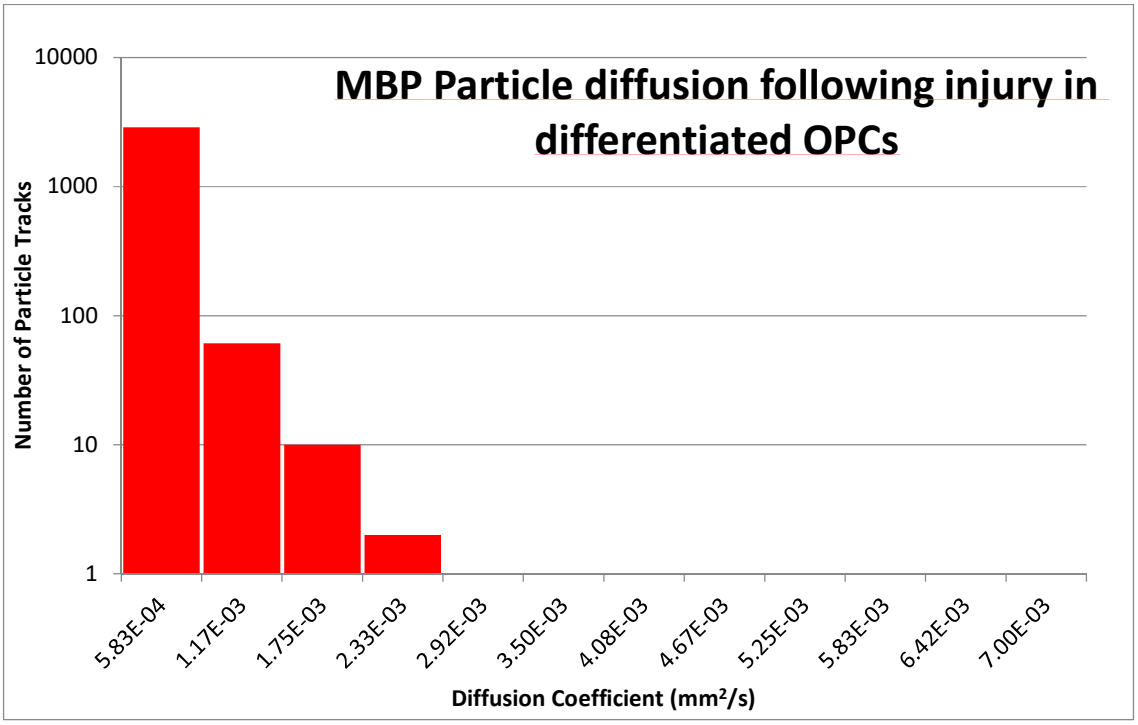

Figure 5.12: Histogram of particle diffusions within the injured differentiated OPCs. It can be seen many particles exist whose diffusion would be classified within the slow moving particle category (Red), with little to nothing within the other movement categories.

Oli-neu cells, being a cell line derived from OPCs, were expected to show a similar profile to that of the OPC cells. However, they show a similar profile to that seen with the differentiated cells (Figure 5.13). The Oli-neu MBP molecule tracks possess a small number of intermediately moving particles, with the majority of profiles falling within the slow moving group. The Oli-neu cells also show an absence of fast moving profiles seen in the OPC cells, which altogether suggests that Oli-neu cells possess a less diffusive environment compared to the OPCs.

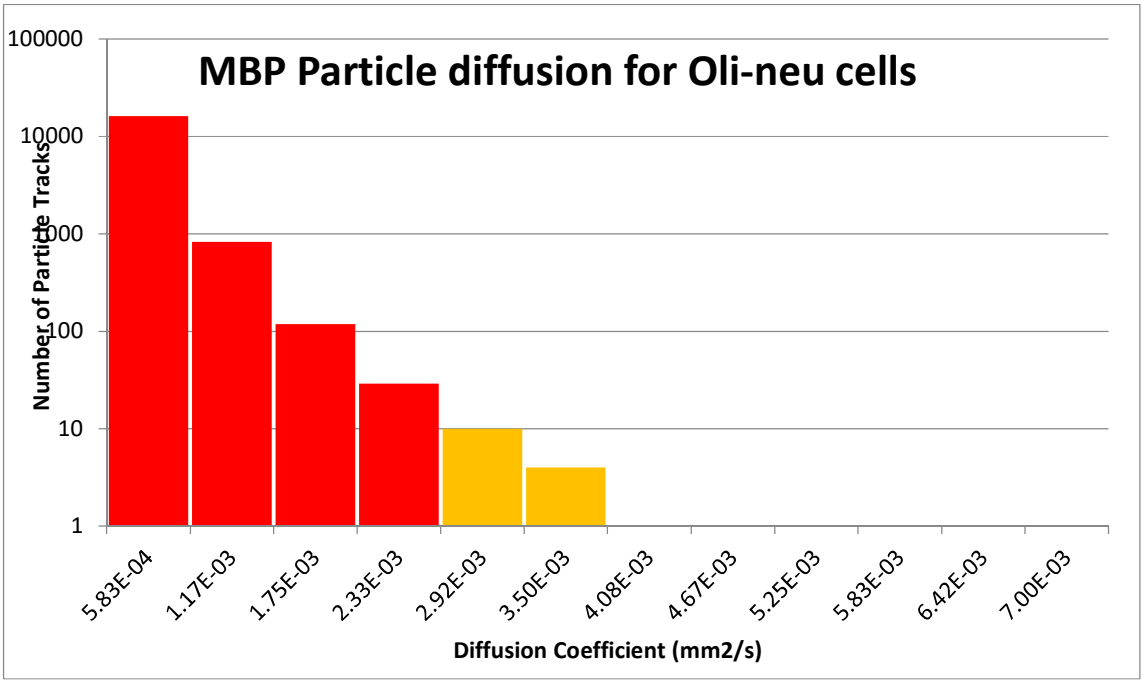

Figure 5.13: Histogram of Oli-neu diffusion coefficients. It can be seen that within Oli-neu cells particles are mainly slow moving (Red), but contains some potential for fast movement, with a number of particles being classified within the intermediate group (Yellow).

Overall it can be seen that the OPCs exhibit the most diffusive environment of the cell types tested, and that differentiation of OPCs leads to a hindrance in MBP particle movement suggesting a less diffusive environment arises following maturation.

5.3.3 Confinements

It can be seen that all the samples observed contain a mixture of molecule behaviours in terms of confinement, with some particles being exceptionally confined with values close to 0, and with some particles being freely mobile with values close to one. The distribution of these values is key when discussing the behaviour of MBP within the samples. The confinement data for OPC show that these cells show a distribution of confinement profiles centred approximately around 0.4, with some particles being highly mobile with ratios closer to 1, and some particles being highly immobile with ratios closer to 0 (Figure 5.14). This suggests that

while there may be some interactions within the samples, these influences do not affect all the particles equivalently.

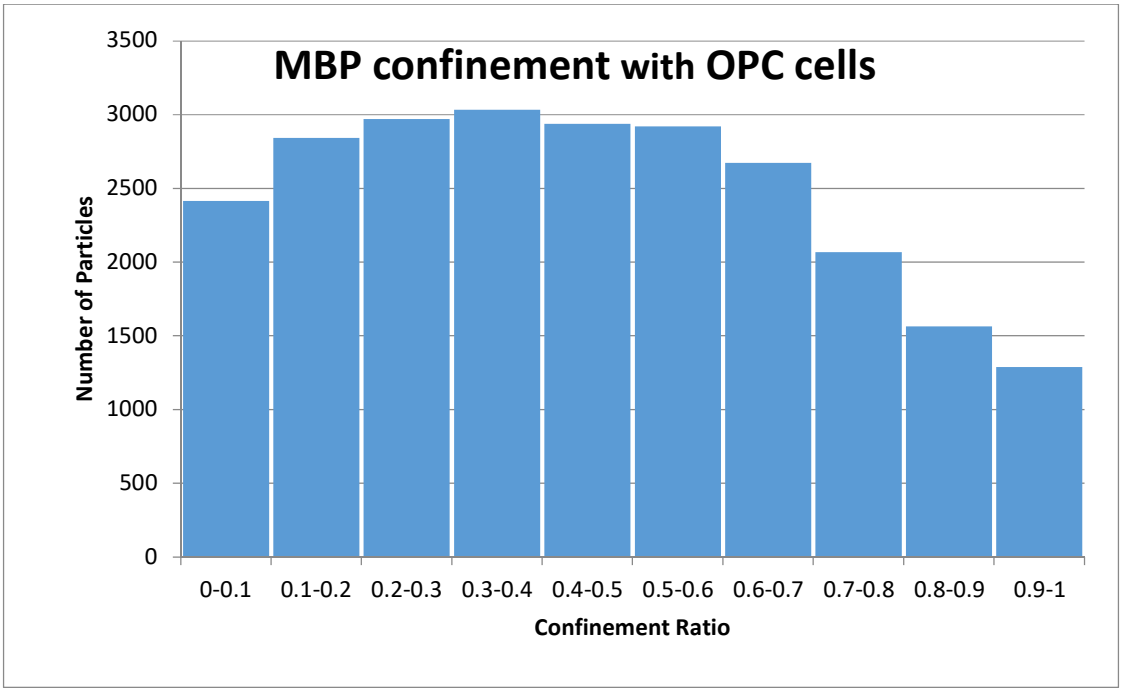

Figure 5.14: Histogram of OPC confinement ratios. It can be seen that there is a range of confinements within OPC cells with the peak of the histogram at 0.4.

Following differentiation of the OPC cells the distribution of the particle confinements as a whole shifts, with the distribution of particle confinements being shifted closer to 0, suggesting that as the cells differentiate MBP becomes more confined (Figure 5.15 A). When looking at the 3 different morphologies which are present within the differentiated cells, it can be seen all the cell morphologies show this shift, with the more confined particles contributing a greater proportion of the population. Within the $_{P}$OL cells the peak of the particle confinements exists at approximately 0.1 (Figure 5.15 B), with a distribution of all other confinements at a positive skew. This is the same as what is seen within the $_{EM}$OL (Figure 5.15 D). However, with the $_{PM}$OL cells this peak is sifted closer to 1 (Figure 5.15 C), suggesting

a more free phenotype, with the peak existing at approximately 0.4 and no strong skew seen, similar to what is seen with the injured OL cells (Figure 5.16).

Following the treatment of differentiated cells with LPC, the distribution of particle confinements shifts again, closer to 1, with the distribution resembling that of the undifferentiated OPC cells. This suggests that injuring the cells interferes with the molecular interactions that act to increase confinement in differentiated OL.

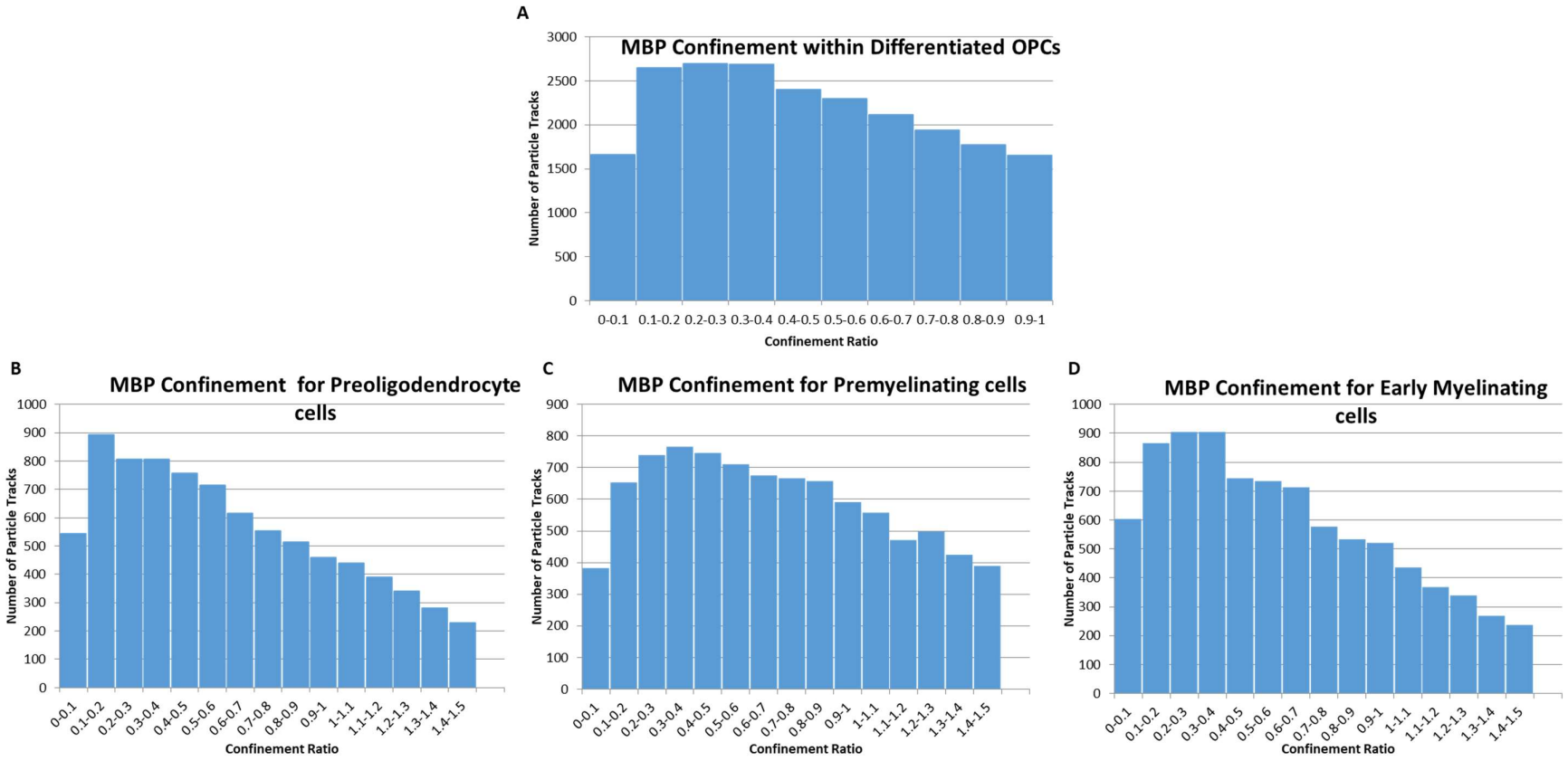

Figure 5.15: Histogram of differentiated OPC confinement ratios. It can be seen that a range of behaviours exist within all cell morphologies. When all three morphologies are together the histogram for the population is centred at 0.3, suggesting that the cells are weakly confined (A). However, when separated into the different morphologies it can be seen that the $_{P}$OLs (B) and the $_{EM}$OLs (D) possess stronger confinement, with the centres at approximately 0.2 and a positive skew, than the $_{PM}$OLs, which have their confinements centred at approximately 0.4 with near even distribution around it.

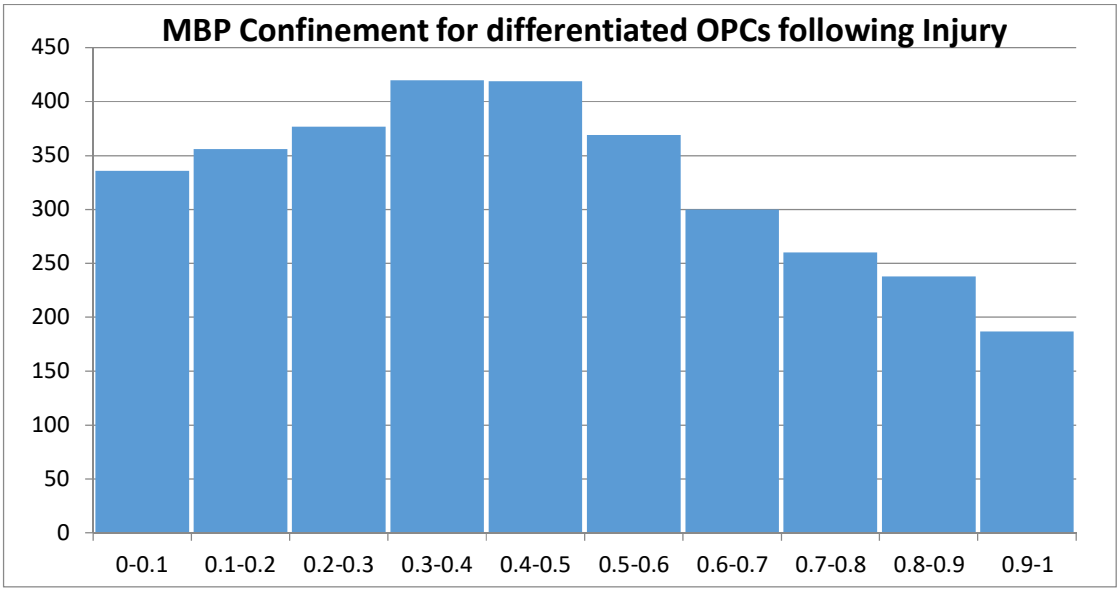

Figure 5.16: MBP confinement for differentiated OPCs following injury. The distribution of the confinements of particles from the injured OPCs showed an even distribution with a peaks at 0.4.

When exploring the distribution of the Oli-neu cells it can be seen that population contains more freely mobile particles than the OPC cells (Figure 5.17). Overall the distribution of the particle confinements itself is still approximately centred around 0.5, however, injured Oli-neu cells seem to show a slightly more even distribution, with a similar number of particles showing confinements greater than 0.5 and particles with confinements less than 0.5. Following injury to the Oli-neu cells the distribution of particle confinements show little change, with the profile of confinements still being approximately centred at 0.5, with a similar number of particles on each side, unlike with the differentiated OPC cells which showed a shift in the profile.

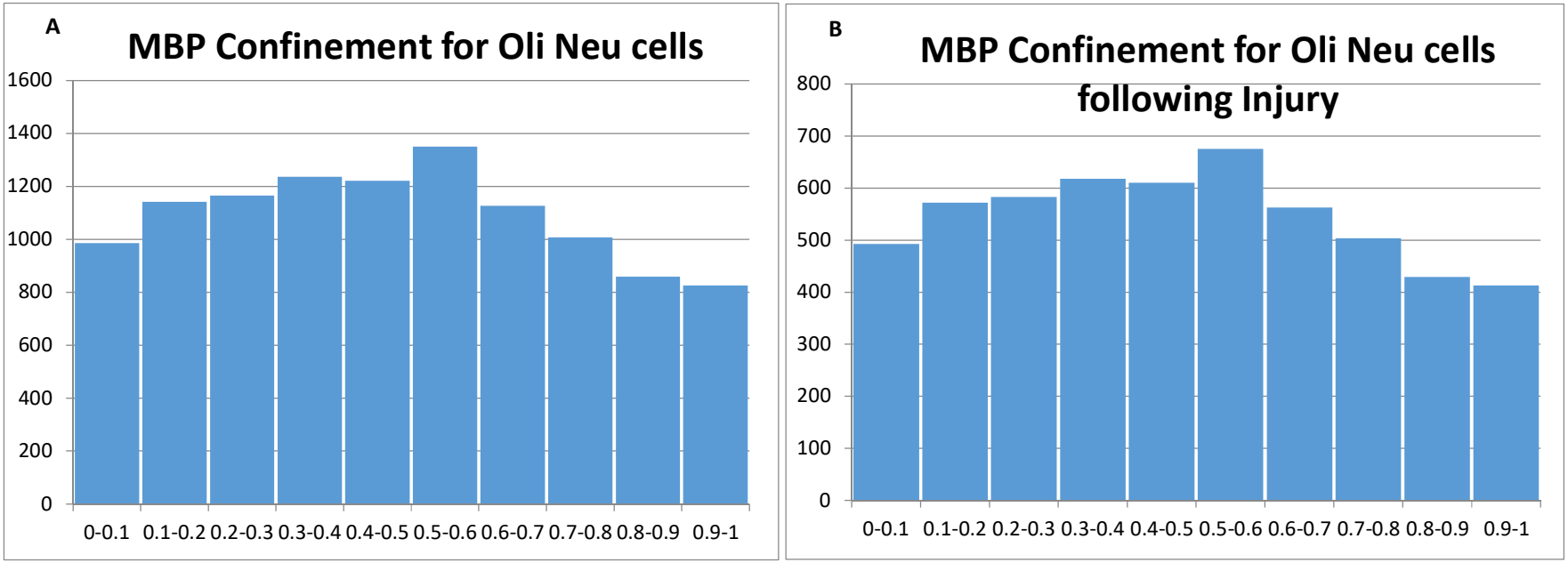

Figure 5.17: Oli-neu cell confinement. A) Oli-neu cells have an even distribution of confinements in baseline conditions. B) Following injury, the profile of Oli-neu cells does not change. It says evenly distributed with the peak of the histogram at approximately 0.4.

5.4 Discussion

The results of this chapter demonstrate that (1), the maturity of OLs alter the protein dynamics of MBP, with cells which are more mature possessing proteins showing more confinement, and less free movement; (2) Injury to OLs cause a more immature phenotype in terms of MBP protein dynamics, with proteins being more mobile and less confined; (3) The Oli-neu cell line, although an immature cell line, in terms of MBP protein dynamics is more complex in phenotype, with a mature phenotype for diffusion rates, but an immature phenotype for confinement (Figure 5.18).

5.4.1 The effect of OL maturity on MBP protein dynamics

Observation of MBP protein dynamics in OPC and differentiated OLs have shown that MBP becomes less mobile as cells progress down the OL lineage. This can be seen with both the confinement data, which shows that MBP increases in its confinement following maturation, and the diffusion rates which show that particles do not move as quickly following maturation. This change in mobility of MBP molecules, following maturation, may come about due to the expression of other mature myelin proteins, such as PLP and CNP, which have been shown to interact with MBP[137]. These interactions may also induce homotypic interactions between MBP molecules, leading to reduced MBP mobility within the samples[161]. However, this transition is not as marked as expected, as OPCs at the earliest stages of maturation still contain molecules which MBP interacts with such as lipids within the bilayer, actin, and the gangliosides[137,527,528].

In addition to its effect on the motility of the particles, maturity of the cells also effects the directionality of the molecules movements, as seen when looking at the plots of particle displacement. As the cells became more mature the particle displacement plots were found

to become more linear. This is quite evident at the point of $_{EM}$OL cells where the plot is more linear than elliptical, but difficult to see within the other conditions. The $_{EM}$OL cells show a level of directionality within their particle movements, this could be due to the presence of the bubbles which are assumed to contain nascent myelin structures which may provide an environment favouring greater directionality. The presence of presumed myelin with the bubble structures would also explain the observation that cells with multiple myelinating bubbles presented with more linear plots. This could suggest that myelin shuffles to the edges of the bubble to either facilitate bubble expansion, or to forms a meshwork for process flattening. However, MBP is known to perform an extrusion role on other proteins within myelin, such as CNP, MOG and MAG, which could also lead to a directional movement of MBP to the sides of the bubble, this could be confirmed by dual staining of MBP, and either MAG or MOG to explore whether extrusion of either of the proteins has occurred when this process occurs within the cells[161]. It may be difficult to detect directionality at earlier developmental stages, as for example the $_{PM}$OL cells possess highly branched processes in multiple directions, so if there is directionality within the molecular movements away/towards the cell body, or even from one membrane to another to form myelinating bubbles, this would be masked by the large amount of moving particles existent within the sample which will be moving in various directions. From the confinement histograms it can be seen that $_{PM}$OL cells present with less confinement than the other differentiated OPC types. The greater MBP particle mobility could be related to the expression of proteins which MBP interacts with, such as PLP, which could help induce MBP reorganisation, and therefore the formation of myelinating bubbles[137,156]. Alternatively it could simply reflect the absence of such interactions due to lower levels of these mature myelin components.

5.4.2 The effect of injury on protein dynamics

Injury with LPC effects the MBP protein molecular dynamics within differentiated OL precursor cells, causing them to be more mobile than uninjured cells. However, from the diffusion coefficients it can be seen that no fast moving molecules appear. The absence of faster moving elements within the injured cells suggests that MBP still has many particle interactions which are working on it despite the effects of the injury treatment, which hinder its movement. These interactions must be either transient to allow particles to move, explaining the increase motility, or the particles MBP is interacting with must be mobile and interact with other molecules within the sample. One explanation to the increased motility would be MBP particles leaking out of the cell following injury. However, particle movement is non-directional, and very few to no particles are seen extracellularly following injury, either in the environment or leaving the cells. Another explanation could be particle shuttling to the cell body for recycling, as part of process retraction. This is supported by the loss of processes following injury, with very little cell debris observed. However, if particles were being retracted to the cell body particle movement will yet again be directional which has not been observed. One final explanation is the formation of MBP aggregates following injury, which has been observed within demyelining conditions[529,530]. This explanation supports the data well, as individual MBP particles will be able to diffuse faster than the clusters, and following aggregation the aggregate may also be mobile, but with the larger size would be slower moving. However, the absence of this phenomenon within the Oli-neu cells suggests that the trigger for this MBP aggregation may not exist within the Oli-neu cells. This suggests the trigger for this response may lie within the profile of proteins existent within the differentiated cells, as this is the key difference between Oli-neu and the differentiated cells.

5.4.3 The Oli-neu cell type

The Oli-neu cell type is a well-established cell line model for OPC behaviour. From the work presented within this chapter, it can be seen that the Oli-neu cell line is peculiar in terms of its molecular dynamics. It presents with highly mobile particles, similar to that of the OPC cells, but, also lacks the fast moving populations present within the OPC cells, as was also apparent with the differentiated OPCs. This suggests that the OPCs used as a source for the Oli-neu cells may have been immortalised at a maturity level beyond that of the OPC cells but, one which is less developed than the $_{p}$OLs which display more confined molecular dynamics. This suggests that on a molecular level, Oli-neu cells do not provide a particularly faithful model for OPCs, whether mature or immature, but rather represent their own unique morphology. It should be noted however that the MBP characteristics observed here may be specific to the source of Oli-neu lines used in this work since additional sources of Oli-neu (e.g. cells not maintained in the Fulton laboratory) were not examined. The Oli-neu cells stocked in the lab have retained an OPC profile with the typical morphology and expression of NG2 expected of the line. However, stocks of the original donated line were not maintained thus experiments were performed on lines that had undergone multiple passages. There may then have been other molecular shifts in the phenotype that could account for the particular profile of MBP dynamics observed here. Further experiments with a fresh batch of cells with a known history could be useful for checking this possibility.

Unlike the differentiated OPC cells the Oli-neu cells do not change in molecular dynamics following injury, with cells treated with LPC showing similar dynamics to that seen in uninjured Oli-neu cells. This suggests that Oli-neu cells do not possess the mechanisms present in differentiated OPCs that cause slower moving particles with greater mobility. Oli-neu cells

show a MBP dynamics with a similar mobility, whether injured or uninjured, probably because Oli-neu cells do not possess the mature myelin proteins that would enable mobility reducing molecular interactions[449]. It has been suggested that MBP needs to interact with a number of molecules to induce aggregations[161]. Unpublished data from the lab confirms the expression of PLP, MOG, CNP and CD9 in the differentiated OPCs used in the present work (M. Otsu and D. Fulton, unpublished), which are known to be absent in Oli-neu cells. Therefore the number of interacting molecules such as CNP and PLP are limited leading to molecules being close to freely mobile with both the injured and uninjured systems[161].

5.5 Conclusions

The work within this chapter has explored the molecular dynamics of MBP within different levels of maturity. The results of this chapter support the hypothesis that mature oligodendrocyte cells will display a more confined molecular phenotype than immature cells. This was demonstrated by the observation of both the diffusion coefficient of the particles being tracked, as well as the confinement. Contrary to previous beliefs, Oli-neu cells did not display the same phenotype as immature OPC cells, but an intermediate phenotype on the molecular scale. This provides evidence against its use as a model for OL behaviour, at least on the molecular scale. Following injury to the cells a change of phenotype was observed in the mature cells, with MBP being less confined within the mature OLs, reverting to a confinement phenotype similar to that of the immature cells. With the immature cell types, such as the OPC and Oli-neu cells, a change of phenotype was not observed, suggesting that the change of phenotype seen in mature cells may be linked to the expression of mature markers.

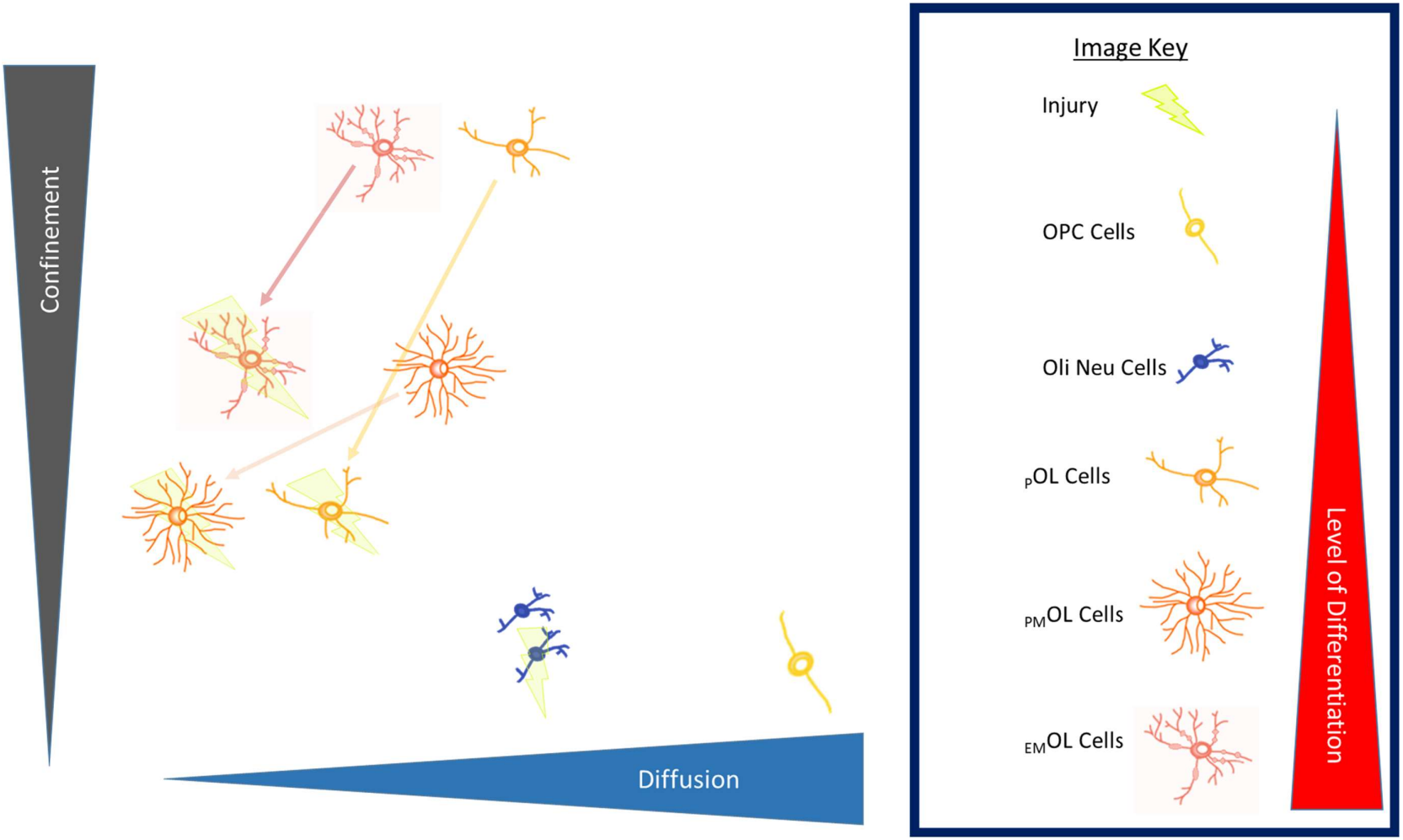

Figure 5.18: Summery of findings from single molecule analysis. It can be seen that the cells at a higher level of differentiation show more confined and less diffusive particle movement than those at lower levels.

Chapter 6

General Discussions

"We Live in a society exquisitely dependant on science and technology, in which hardly anyone knows anything about science and technology"

- Carl Sagan

6.1 Main Findings

This thesis aimed to develop tools and protocols to enable SMI analysis of MBP molecules during oligodendrocyte development and injury, and to apply these models of myelin injuries that are relevant to demyelinating conditions such as multiple sclerosis and neuromyelitis optica. It is hoped that these tools and protocols will provide new information on myelin injury that will support future pharmacological intervention for these conditions.

The work shown within this study has accomplished the following

1) The production of multiple viral constructs for the delivery of fluorescently tagged MBP, with a number of fluorescent proteins, for SMI observation of MBP behaviour. These proteins have been characterised according to their expression kinetics (onset and duration), and toxicity.
2) An immune based injury model was tested and optimised for the observation of myelin injury within brain slices. The models mechanism of action has been confirmed, and optimal treatment composition duration determined. This model was shown to produce a chronic injury which has minimal recovery.
3) The mobility of single MBP molecules has been characterised within immortalised and primary oligodendroglial cells of different maturities. This work shows that MBP becomes more immobilised (reduced diffusion / increased confinement) following maturation of the cells.
4) The mobility of single MBP molecules following chemical injury was characterised within both mature oligodendrocytes, and the Oli-neu cell line. This has shown that the mobility of MBP is altered following injury only in mature oligodendrocytes.

6.1.1 SFV Constructs for investigating protein function

The various SFV constructs produced were exploited in various ways within the work presented. The construct containing GFP proved useful for labelling oligodendrocytes, both in cell cultures and brain slices, as it allowed the development of the skills to morphologically identify oligodendrocytes within tissues, especially within transgenic animals. These skills were essential to develop for the work performed within this thesis, and the GFP chimera allowed these skills to be developed whilst the other chimera were being developed. The construct which contained mCherry was utilised for live imaging of OL in brain slices, where they were useful for identifying the kinetics of OL injury during complement-mediated injury. In addition mCherry labelled OLs could be identified using post-hoc immunohistochemistry. The Dendra2 virus was essential for the SMI work presented within Chapter 5, as the photoconversion allowed the isolation of the sparse signals required for SMI experimentation. These viral constructs showed useful characteristics for imaging as expression of the fluorescent chimeric proteins occurred within 6 hours of infection and was existent for a number of days. From the single molecule work it could be seen that the useful imaging window was between 6 and 9 hours of infection, this was determined as processes within the imaging dishes displayed characteristics suggestive of process retraction following 10 hours, such as intermittent process thickening and blebbing. This was followed by a slight level of process retraction. This imaging window (6 to 9 hours) allowed imaging of many processes, and allowed enough time to induce an oligodendrocyte injury, which could confidently be distinguished from potential cytotoxic effects resulting from the SFV vector at later time-points.

The expression pattern of MBP is different to that which is reported within the literature for MBP expression. The literature suggests that MBP is expressed locally from polysomes within the oligodendrocyte processes[452–454]. However, the results from the expression of MBP by the SFV virus suggest that MBP is actually expressed centrally within the cell body and transported to the process. This expression behaviour can be seen with all the SFV chimeric constructs. This may be related to the use of the SFV virus, as SFV contains a viral genome which is translated when the virus hijacks the host ribosomes. This may have led to MBP expression somatically, rather than locally like the literature suggests. This may also be the case as the MBP chimera lacks the regulatory elements that are contained within the normal golli-MBP gene, and which may contain targeting elements. One interesting finding from the MBP expression results is the bulk movement of MBP. Within the experiments performed it can be seen that MBP movement to the processes is accompanied by a change in oligodendrocyte morphology, this change in morphology usually progressed with a slight loss of processes following MBP expression, followed by the production of new processes arising from the perikaryal membrane containing MBP. These processes were of different thickness to that seen before MBP expression. These observations provide evidence for MBP producing strong interactions with the membrane, as no MBP expression is seen progressing within the pre-existing processes. Also, the production of thinner processes following the appearance of MBP supports the idea that MBP plays a compaction role even before the production of myelin sheets.

6.1.2 Immune model

The anti-MOG / complement myelin injury provides a useful model as it may replicate features of the early phases of injury within MS. Complement has been shown to be aberrantly activated in the early phases of MS, suggesting that the initiation of the myelin injury within MS occurs in a similar manner to the anti-MOG / complement model. Following this the injury progresses with or without complement activity, as can be seen within the 30 minute complement incubation experiments, and with the complement inhibition within patients suffering with MS[280,420]. The use of complement itself is well established for induction of injury within the CNS[467,468]. However, the conditions within the treatment needed to be optimised, to ensure injury is induced without over activation of the complement system, and with little to no axonal injury.

Within the work presented the m IgG control/complement treatment was treated as an experimental control condition. However, as seen from the work with the C9 time course, the m IgG control/complement condition produced extensive C9 activation, albeit on a slower time-course than that seen with in the anti-MOG/complement condition. This suggests that the m IgG control/ complement condition has the potential to induce an injury, which would be seen later than that resulting from anti-MOG/complement treatment. This was confirmed with the live imaging experiments, and the injury time course experiments, which showed that myelin injury is apparent in the IgG control/complement condition following 24 hours, and that, much like the anti-MOG/complement treatment, the myelin is completely devastated 10 days following treatment. These findings differ from those previously published by Harrer et al. 2009, where IgG control/complement treatment was used as a control for anti-MOG

induced injury[468]. Based on our observations the complement alone, or antibody alone conditions used in this thesis provide a more suitable control condition, as these conditions show little to no injury within the injury progression experiments.

6.1.3 Mobility of MBP following maturation

MBP is a myelin protein known to be heavily involved in myelin compaction[88]. This myelin compaction requires the existence of other mature myelin proteins, such as PLP and Gal C[531]. Interaction with these proteins initiates self-adhesion of MBP to other MBP molecules in order to form a framework for myelin compaction[161]. Although MBP is expressed within all experimental groups in these experiments, seeing as maturity of the cells varies within conditions, not all cells show the confined behaviour normally seen within mature oligodendrocytes. This is due to both the reduced number of proteins which develop as the cell matures, such as PLP which MBP interacts with, and also the reduced levels of MBP in the cells at the earlier stages of differentiation, compared to mature myelin, reducing the number of potential interacting molecules that any particular MBP molecule may form interactions with during self-propagation of the interactions.

6.1.4 Response of MBP following myelin injury

Within the work presented two key forms of myelin injury were performed. The first was a physical injury produced by complement proteins puncturing the membrane of cells. The second was a chemical injury to the myelin membrane induced by the myelin toxin LPC. Both injury modalities produced a dramatic response within oligodendrocytes involving the loss of processes. However, only cells injured with LPC revealed an increased mobility following injury. This may be related to the means of imaging, as different microscopy techniques were

utilised, however, within the live imaging experiments following complement induced injury, protein reorganisation should be noticeable on the ensemble level.

6.2 Future experiments

6.2.1 Determination of cell death mechanism in complement myelin injury

Although the work presented thus far has shown that the anti-MOG / complement injury utilises the classical pathway of complement injury, and that the observed injury involves production of the membrane attack complex, shown by the delay between the peak of C9 staining and the presentation of the injury, the mechanism of injury is still not fully characterised. Whether the membrane attack complex induces injury through membrane attack, or if the injury is seen through the triggering of an apoptotic pathway by high C9 levels has not been determined. In order to determine this a cell death assay must be performed, where cells are stained for apoptosis, and necrosis and the quantity of each type of cell death compared between injured and control slices. This approach would be helpful in confirming whether the observed myelin injury arises due to membrane attack complex induced necrosis, or whether the C9 complex induces a slower, intracellularly driven means for injury. One means to observe these pathways is through the dual use of the nucview apoptosis assay system and propidium iodide. Nucview provides a marker for caspase 3 activation which is highly prominent during apoptotic cell death, whereas propidium iodide labelling requires only an increase in cell membrane permeability which occurs during necrosis and the later stages of apoptosis.

6.2.2 Investigating excitotoxic injury

Within this work all the myelin injuries observed have actions which are believed to occur extracellularly, with complement making a membrane attack complex to permeabliise the membrane, and LPC disrupting the membrane[268,532]. In order to further understand the effect of myelin injury on MBP, injuries which originate intracellularly must also be investigated, as these can have pronounced effects on the function of MBP. One key form of injury which was not addressed within the work presented was excitotoxicity. Excitotoxicity has been associated with the injuries seen within MS, which means its molecular dynamics must be understood in order to understand injury within MS[485,533–536]. Excitotoxicity is a pathological process where over activation of receptors leads to cellular damage. This is most commonly associated with glutamate receptors. Blockage of the NMDA, and AMPA glutamate receptors has been shown to reduce damage to oligodendrocytes in the EAE model system from MS[535,537,538]. Although glutamate exicitotoxicity effects both axons and myelin, oligodendrocytes have been shown to be more susceptible than axons[539,540]. This susceptibility may be underpinned by the role of oligodendrocytes in glutamate homeostasis, the upregulation of glutamate receptors within MS, and the role of glutamate in oligodendrocyte precursor cell differentiation[448,541–543].

6.2.3 Investigating the interaction between MBP and other proteins

In this study it has been demonstrated using SMI methods that MBP interacts with other elements within oligodendroglia, which changes its protein dynamics. In order to elucidate on these findings further some of these interactions should be probed. In order to achieve this co-labelling of MBP and proteins such as PLP, Gal C, and calmodulin should be used for further

SMI studies. This would allow interaction times between MBP and these molecules to be observed, and could help to determine whether disturbances within these molecules during injury leads to the change in MBP dynamics observed. Of key interest is PLP, which is known to both be a membrane protein and to interact with MBP. PLP is a positively charged molecule, which is bound to the cytosolic surface of myelin[421]. It has been found to interact with MBP reversibly, in a non-electrostatic manner[422,544]. Within the work presented both injury modalities used (complement and LPC) involved damage to the myelin membrane, so to understand the increased mobility of MBP, following these myelin injuries, a membrane bound protein might provide a useful target for study. This approach may be especially relevant in understanding the lack of change in MBP dynamics following injury in early OPC cells since PLP reaches its maximal levels when oligodendrocytes are myelinating[545].

6.3 Conclusion

Thus far demyelinating conditions such as MS and neuromyelitis optica do not have any functional cures, although many pharmacological interventions have been attempted.

The work presented here addressed the response of MBP to myelin injury. This was achieved by the production of SFV vectors containing fluorescently tagged MBP chimera proteins. This was utilised to establish a model system for myelin injury, similar to the injury seen in demyelinating conditions such as MS. The response to this injury was compared to that of a known model for demyelination, LPC. The LPC injury was investigated using SMI methodologies, where MBP was found to change its behaviour in response to myelin injury, only when in mature cells. This suggested that the response of MBP to demyelinating stimuli relies on the interactions it makes with other molecules with myelin such as lipids and other

myelin proteins. These interactions are therefore important targets for future work aiming to understand how the early stages of demyelination progress, and identify new targets for myelin protection. The work presented provides several interesting avenues for progression of this work, most notably the exploration of MBP interactions with other myelin proteins, which may explain the behaviour discrepancies seen within different stages of differentiation of the cells investigated. The investigation of whether MBP behaviour varies with different types of injuries is also a key question for future work, the resolution of which may provide new directions for pharmacological interventions aiming to protect myelin from injury.

Chapter 7

References

“Science is not everything, but science is very beautiful.”

- Robert Oppenheimer

1. Bear, M. F., Connors, B. W. & Paradiso, M. A. *Exploring the brain*. *Brain* (Lippincott Williams & Wilkins, 2007). doi:10.1007/978-3-540-77829-5

2. Tuladhar, A., Mitrousis, N., Führmann, T. & Shoichet, M. S. Central Nervous System. *Transl. Regen. Med.* 415–435 (2015). doi:10.1016/B978-0-12-410396-2.00030-X

3. Wolburg, H., Wolburg-Buchholz, K., Mack, A. F. & Reichenbach, A. Ependymal cells. in *Encyclopedia of Neuroscience* 1133–1140 (Academic Press, 2010). doi:10.1016/B978-008045046-9.01001-9

4. Johns, P. Neurons and glial cells. in *Clinical Neuroscience* 61–69 (Churchill Livingstone, 2014). doi:10.1016/B978-0-443-10321-6.00005-9

5. Watson, C., Kirkcaldie, M. & Paxinos, G. Central nervous system basics–the brain and spinal cord. in *The Brain* 11–24 (Academic Press, 2010). doi:10.1016/B978-0-12-373889-9.50002-4

6. Shipp, S. Structure and function of the cerebral cortex. *Curr. Biol.* **17,** R443-9 (2007).

7. Zilles, K., Palomero-Gallagher, N. & Amunts, K. *Development of cortical folding during evolution and ontogeny*. *Trends in Neurosciences* **36,** 275–284 (2013).

8. Namkung, H., Kim, S.-H. & Sawa, A. The Insula: An Underestimated Brain Area in Clinical Neuroscience, Psychiatry, and Neurology. *Trends Neurosci.* **40,** 200–207 (2017).

9. Phillips, C. G., Zeki, S. & Barlow, H. B. Localization of function in the cerebral cortex. Past, present and future. *Brain* **107 (Pt 1,** 327–61 (1984).

10. Naqvi, N. H. & Bechara, A. The insula and drug addiction: an interoceptive view of pleasure, urges, and decision-making. *Brain structure & function* **214,** 435–450 (2010).

11. Purves, D. *et al. Neuroscience*. *Sunderland* **3,** (2004).

12. Cummings, B. Gross Anatomy of the Spinal Cord. *Neuroscience* 1–14 (2001). Available at: https://www.ncbi.nlm.nih.gov/books/NBK11160/. (Accessed: 2nd July 2018)

13. Puelles, E. & Martínez-de-la-Torre, M. Midbrain. *Mouse Nerv. Syst.* 337–359 (2012). doi:10.1016/B978-0-12-369497-3.10010-X

14. Zecca, L. *et al.* Substantia nigra neuromelanin: structure, synthesis, and molecular behaviour. *Mol. Pathol.* **54,** 414–8 (2001).

15. Miller, L. E. & Gibson, A. R. Red Nucleus. in *Encyclopedia of Neuroscience* 55–62 (Academic Press, 2010). doi:10.1016/B978-008045046-9.01334-6

16. Wurtz, R. H. Superior Colliculus. in *Encyclopedia of Neuroscience* 627–634 (Academic Press, 2010). doi:10.1016/B978-008045046-9.01103-7

17. Miall, R. C. Cerebellum: Anatomy and Function. in *Neuroscience in the 21st Century* 1149–1167 (Springer New York, 2013). doi:10.1007/978-1-4614-1997-6_38

18. O'Brien, J. W. & Hill, S. Y. Abnormalities of Cerebellar Structure and Function in Alcoholism and Other Substance Use Disorders. *Neuropathol. Drug Addict. Subst. Misuse* 575–586 (2016). doi:10.1016/B978-0-12-800213-1.00053-5

19. Bartanusz, V., Jezova, D., Alajajian, B. & Digicaylioglu, M. The blood-spinal cord barrier: Morphology and Clinical Implications. *Ann. Neurol.* **70,** 194–206 (2011).

20. Daneman, R. & Prat, A. The blood-brain barrier. *Cold Spring Harb. Perspect. Biol.* **7,** a020412 (2015).

21. Daneman, R. The blood-brain barrier in health and disease. *Ann. Neurol.* **72,** 648–672 (2012).

22. Zlokovic, B. V. The Blood-Brain Barrier in Health and Chronic Neurodegenerative Disorders. *Neuron* **57,** 178–201 (2008).

23. Ludwin, S. K., Rao, V. T., Moore, C. S. & Antel, J. P. Astrocytes in multiple sclerosis. *Mult. Scler. J.* **22,** 1114–1124 (2016).

24. Cramer, S. P., Simonsen, H., Frederiksen, J. L., Rostrup, E. & Larsson, H. B. W. Abnormal blood-brain barrier permeability in normal appearing white matter in multiple sclerosis investigated by MRI. *NeuroImage. Clin.* **4,** 182–9 (2014).

25. Bundgaard, M. & Abbott, N. J. All vertebrates started out with a glial blood-brain barrier 4-500 million years ago. *Glia* **56,** 699–708 (2008).

26. Coomber, B. L. & Stewart, P. A. Morphometric analysis of CNS microvascular endothelium. *Microvasc. Res.* **30,** 99–115 (1985).

27. Brightman, M. W. & Reese, T. S. Junctions between intimately apposed cell membranes in the vertebrate brain. *J. Cell Biol.* **40,** 648–77 (1969).

28. Reese, T. S. & Karnovsky, M. J. Fine structural localization of a blood-brain barrier to exogenous peroxidase. *J. Cell Biol.* **34,** 207–17 (1967).

29. Westergaard, E. & Brightman, M. W. Transport of proteins across normal cerebral arterioles. *J. Comp. Neurol.* **152,** 17–44 (1973).

30. Mittapalli, R. K., Manda, V. K., Adkins, C. E., Geldenhuys, W. J. & Lockman, P. R. Exploiting nutrient transporters at the blood-brain barrier to improve brain distribution of small molecules. *Ther. Deliv.* **1,** 775–84 (2010).

31. Löscher, W. & Potschka, H. Blood-brain barrier active efflux transporters: ATP-binding cassette gene family. *NeuroRX* **2,** 86–98 (2005).

32. Thiebaut, F. *et al.* Immunohistochemical localization in normal tissues of different epitopes in the multidrug transport protein P170: evidence for localization in brain capillaries and crossreactivity of one antibody with a muscle protein. *J. Histochem. Cytochem.* **37,** 159–164 (1989).

33. Cordon-Cardo, C. *et al.* Multidrug-resistance gene (P-glycoprotein) is expressed by endothelial cells at blood-brain barrier sites. *Proc. Natl. Acad. Sci. U. S. A.* **86,** 695–8 (1989).

34. Oldendorf, W. H., Cornford, M. E. & Brown, W. J. The large apparent work capability of the blood-brain barrier: A study of the mitochondrial content of capillary endothelial cells in brain and other tissues of the rat. *Ann. Neurol.* **1,** 409–417 (1977).

35. Sims, D. E. The pericyte--a review. *Tissue Cell* **18,** 153–74 (1986).

36. Peppiatt, C. M., Howarth, C., Mobbs, P. & Attwell, D. Bidirectional control of CNS capillary diameter by pericytes. *Nature* **443,** 700–4 (2006).

37. Hall, C. N. *et al.* Capillary pericytes regulate cerebral blood flow in health and disease. *Nature* **508,** 55–60 (2014).

38. Armulik, A. *et al.* Pericytes regulate the blood–brain barrier. *Nature* **468,** 557–561 (2010).

39. Daneman, R., Zhou, L., Kebede, A. A. & Barres, B. A. Pericytes are required for blood–brain barrier integrity during embryogenesis. *Nature* **468,** 562–566 (2010).

40. Abbott, N. J., Rönnbäck, L. & Hansson, E. Astrocyte–endothelial interactions at the blood–brain barrier. *Nat. Rev. Neurosci.* **7,** 41–53 (2006).

41. Janzer, R. C. & Raff, M. C. Astrocytes induce blood–brain barrier properties in endothelial cells. *Nature* **325,** 253–257 (1987).

42. del Zoppo, G. J. *et al.* Vascular matrix adhesion and the blood–brain barrier: Table 1. *Biochem. Soc. Trans.* **34,** 1261–1266 (2006).

43. Sorokin, L. The impact of the extracellular matrix on inflammation. *Nat. Rev. Immunol.* **10,** 712–723 (2010).

44. Butts, T., Green, M. J. & Wingate, R. J. T. Development of the cerebellum: simple steps to make a 'little brain'. *Development* **141,** 4031–4041 (2014).

45. Heck, D. & Sultan, F. Cerebellar structure and function: Making sense of parallel fibers. *Hum. Mov. Sci.* **21,** 99–109 (2002).

46. Redondo, J. *et al.* Purkinje Cell Pathology and Loss in Multiple Sclerosis Cerebellum. *Brain Pathol.* **25,** 692–700 (2015).

47. Damasceno, A., Damasceno, B. P. & Cendes, F. The clinical impact of cerebellar grey matter pathology in multiple sclerosis. *PLoS One* **9,** e96193 (2014).

48. Small, S. L., Hlustik, P., Noll, D. C., Genovese, C. & Solodkin, A. Cerebellar hemispheric activation ipsilateral to the paretic hand correlates with functional recovery after stroke. *Brain* **125,** 1544–1557 (2002).

49. Hoche, F., Guell, X., Vangel, M. G., Sherman, J. C. & Schmahmann, J. D. The cerebellar cognitive affective/Schmahmann syndrome scale. *Brain* **141,** 248–270 (2018).

50. Glaister, J., Carass, A., Pham, D. L., Butman, J. A. & Prince, J. L. Automatic falx cerebri and tentorium cerebelli segmentation from magnetic resonance images. in *Proceedings of SPIE--the International Society for Optical Engineering* **10137,** 101371D (NIH Public Access, 2017).

51. Hagan, C. E., Bolon, B. & Keene, C. D. Nervous System. in *Comparative Anatomy and Histology* 339–394 (Academic Press, 2012). doi:10.1016/B978-0-12-381361-9.00020-2

52. Love, B. B. & Biller, J. A. Neurovascular System. in *Textbook of Clinical Neurology: Third Edition* 405–434 (W.B. Saunders, 2007). doi:10.1016/B978-141603618-0.10022-0

53. Potts, M. B., Adwanikar, H. & Noble-Haeusslein, L. J. Models of traumatic cerebellar injury. *Cerebellum* **8,** 211–21 (2009).

54. Azevedo, F. A. C. *et al.* Equal numbers of neuronal and nonneuronal cells make the human brain an isometrically scaled-up primate brain. *J. Comp. Neurol.* **513,** 532–541 (2009).

55. Sillitoe, R. V., Fu, Y. & Watson, C. Cerebellum. in *The Mouse Nervous System* 360–397 (Academic Press, 2012). doi:10.1016/B978-0-12-369497-3.10011-1

56. Bagnall, M., du Lac, S. & Mauk, M. Cerebellum. The Basis of Cerebellar Microcircuits? in *Fundamental Neuroscience: Fourth Edition* 677–696 (Academic Press, 2012).

doi:10.1016/B978-0-12-385870-2.00031-7

57. Moulton, E. A., Schmahmann, J. D., Becerra, L. & Borsook, D. The cerebellum and pain: Passive integrator or active participator? *Brain Res. Rev.* **65,** 14–27 (2010).

58. Lodish, H. *et al.* Overview of Neuron Structure and Function. (2000).

59. Kettenmann, H. & Verkhratsky, A. Neuroglia: the 150 years after. *Trends Neurosci.* **31,** 653–9 (2008).

60. Jäkel, S. & Dimou, L. Glial Cells and Their Function in the Adult Brain: A Journey through the History of Their Ablation. *Front. Cell. Neurosci.* **11,** 24 (2017).

61. Herculano-Houzel, S. The human brain in numbers: a linearly scaled-up primate brain. *Front. Hum. Neurosci.* **3,** 31 (2009).

62. Williams, R. W. & Herrup, K. The control of neuron number. *Annu. Rev. Neurosci.* **11,** 423–453 (1988).

63. Cherry, T. J., Trimarchi, J. M., Stadler, M. B. & Cepko, C. L. Development and diversification of retinal amacrine interneurons at single cell resolution. *Proc. Natl. Acad. Sci. U. S. A.* **106,** 9495–500 (2009).

64. Feher, J. & Feher, J. Propagation of the Action Potential. in *Quantitative Human Physiology* 280–288 (Elsevier, 2017). doi:10.1016/B978-0-12-800883-6.00025-2

65. Morell, P. & Quarles, R. H. The Myelin Sheath. *Basic Neurochem. Mol. Cell. Med. Asp.* 1–5 (2015).

66. FRANKENHAEUSER, B. Saltatory conduction in myelinated nerve fibres. *J. Physiol.* **118,** 107–12 (1952).

67. Boullerne, A. I. The history of myelin. *Exp. Neurol.* **283,** 431–45 (2016).

68. Nave, K.-A. & Werner, H. B. Myelination of the Nervous System: Mechanisms and Functions. *Annu. Rev. Cell Dev. Biol.* **30,** 503–533 (2014).

69. Badura, S. Analysis for effective approaches towards generating of artificial neuron structures. in *IEEE International Symposium on Signal Processing and Information Technology, ISSPIT 2011* 130–133 (IEEE, 2011). doi:10.1109/ISSPIT.2011.6151546

70. Abraira, V. E. & Ginty, D. D. The sensory neurons of touch. *Neuron* **79,** 618–39 (2013).

71. Rolak, L. A., Loftus, B. D., Athni, S. S. & Cherches, I. M. Clinical Neuroanatomy. *Neurol. Secrets* 18–54 (2010). doi:10.1016/B978-0-323-05712-7.00002-7

72. Muffly, K. The neuron. in *xPharm: The Comprehensive Pharmacology Reference* 1–5 (Elsevier, 2011). doi:10.1016/B978-008055232-3.60010-8

73. Molnar, C. & Gair, J. Neurons. in *Concepts of BiologyThe American Biology Teacher* (Hewlett Foundation, 2012). doi:10.2307/4450113

74. Nixon, R. A. & Shea, T. B. Dynamics of neuronal intermediate filaments: A developmental perspective. *Cell Motil. Cytoskeleton* **22,** 81–91 (1992).

75. Lee, M. K., Xu, Z., Wong, P. C. & Cleveland, D. W. Neurofilaments are obligate heteropolymers in vivo. *J. Cell Biol.* **122,** 1337–50 (1993).

76. Ruangjaroon, T., Chokchaichamnankit, D., Srisomsap, C., Svasti, J. & Paricharttanakul, N. M. Involvement of vimentin in neurite outgrowth damage induced by fipronil in SH-SY5Y cells. *Biochem. Biophys. Res. Commun.* **486,** 652–658 (2017).

77. Schmidt, H. Three functional facets of calbindin D-28k. *Front. Mol. Neurosci.* **5,** 25 (2012).

78. Tord Berggård, ‡, Maria Silow, §, Eva Thulin, ‡ and & Sara Linse*, ‡. Ca2+- and H+-Dependent Conformational Changes of Calbindin D28k†. (2000). doi:10.1021/BI992394G

79. Berggård, T. *et al.* Calbindin D28k exhibits properties characteristic of a Ca2+ sensor. *J. Biol. Chem.* **277,** 16662–72 (2002).

80. Berggard, T., Szczepankiewicz, O., Thulin, E. & Linse, S. Myo-inositol monophosphatase is an activated target of calbindin D28k. *J. Biol. Chem.* **277,** 41954–9 (2002).

81. Schmidt, H., Kunerth, S., Wilms, C., Strotmann, R. & Eilers, J. Spino-dendritic cross-talk in rodent Purkinje neurons mediated by endogenous Ca2+-binding proteins. *J. Physiol.* **581,** 619–29 (2007).

82. Allen, N. J. & Barres, B. A. Neuroscience: Glia — more than just brain glue. **457,** 675–677 (2009).

83. Herculano-Houzel, S. The glia/neuron ratio: How it varies uniformly across brain structures and species and what that means for brain physiology and evolution. *Glia* **62,** 1377–1391 (2014).

84. Pakkenberg, B. & Gundersen, H. J. G. Total number of neurons and glial cells in human brain nuclei estimated by the disector and the fractionator. *J. Microsc.* **150,** 1–20 (1988).

85. von Bartheld, C. S., Bahney, J. & Herculano-Houzel, S. The search for true numbers of neurons and glial cells in the human brain: A review of 150 years of cell counting. *J. Comp. Neurol.* **524,** 3865–3895 (2016).

86. Kurosinski, P. & Götz, J. Glial Cells Under Physiologic and Pathologic Conditions. *Arch. Neurol.* **59,** 1524 (2002).

87. Nave, K.-A. & Trapp, B. D. Axon-Glial Signaling and the Glial Support of Axon Function. *Annu. Rev. Neurosci.* **31,** 535–561 (2008).

88. Baumann, N. & Pham-Dinh, D. Biology of oligodendrocyte and myelin in the mammalian central nervous system. *Physiol. Rev.* (2001).

89. Platt, S. R. The role of glutamate in central nervous system health and disease – A review. *Vet. J.* **173,** 278–286 (2007).

90. Simons, M. & Trajkovic, K. Neuron-glia communication in the control of oligodendrocyte function and myelin biogenesis. *J. Cell Sci.* **119,** 4381–9 (2006).

91. Soulet, D. & Rivest, S. Microglia. *Curr. Biol.* **18,** R506-8 (2008).

92. Giaume, C. & Venance, L. Gap junctions in brain glial cells and development. *Perspect. Dev. Neurobiol.* **2,** 335–45 (1995).

93. staff, B. co. & Staff, B. co. Medical gallery of Blausen Medical 2014. *WikiJournal Med.* **1,** 10 (2014).

94. Kettenmann, H., Hanisch, U.-K., Noda, M. & Verkhratsky, A. Physiology of Microglia. *Physiol.*

Rev. **91,** 461–553 (2011).

95. Kim, S. U. & de Vellis, J. Microglia in health and disease. *J. Neurosci. Res.* **81,** 302–313 (2005).

96. Wu, Y., Dissing-Olesen, L., MacVicar, B. A. & Stevens, B. Microglia: Dynamic Mediators of Synapse Development and Plasticity. *Trends Immunol.* **36,** 605–613 (2015).

97. Tierney, A. L., Nelson, C. A. & III. Brain Development and the Role of Experience in the Early Years. *Zero Three* **30,** 9–13 (2009).

98. Wiese, S., Karus, M. & Faissner, A. Astrocytes as a Source for Extracellular Matrix Molecules and Cytokines. *Front. Pharmacol.* **3,** 120 (2012).

99. Wujek, J. R. & Akeson, R. A. Extracellular matrix derived from astrocytes stimulates neuritic outgrowth from PC12 cells in vitro. *Brain Res.* **431,** 87–97 (1987).

100. Araque, A., Parpura, V., Sanzgiri, R. P. & Haydon, P. G. Tripartite synapses: glia, the unacknowledged partner. *Trends Neurosci.* **22,** 208–215 (1999).

101. Kettenmann, H., Backus, K. H. & Schachner, M. Aspartate, glutamate and γ-aminobutyric acid depolarize cultured astrocytes. *Neurosci. Lett.* **52,** 25–29 (1984).

102. Verkhratsky, A. & Steinhäuser, C. Ion channels in glial cells. *Brain Res. Rev.* **32,** 380–412 (2000).

103. Pankratov, Y., Lalo, U., Verkhratsky, A. & North, R. A. Vesicular release of ATP at central synapses. *Pflügers Arch. - Eur. J. Physiol.* **452,** 589–597 (2006).

104. Volterra, A. & Meldolesi, J. Astrocytes, from brain glue to communication elements: the revolution continues. *Nat. Rev. Neurosci.* **6,** 626–640 (2005).

105. Iram, T. *et al.* Astrocytes from old Alzheimer's disease mice are impaired in Aβ uptake and in neuroprotection. *Neurobiol. Dis.* **96,** 84–94 (2016).

106. Tsacopoulos, M. & Magistretti, P. J. Metabolic coupling between glia and neurons. *J. Neurosci.* **16,** 877–85 (1996).

107. Magistretti, P. J. & Pellerin, L. Astrocytes Couple Synaptic Activity to Glucose Utilization in the Brain. *News Physiol. Sci.* **14,** 177–182 (1999).

108. Bélanger, M. & Magistretti, P. J. The role of astroglia in neuroprotection. *Dialogues Clin. Neurosci.* **11,** 281–95 (2009).

109. Fontana, A., Fierz, W. & Wekerle, H. Astrocytes present myelin basic protein to encephalitogenic T-cell lines. *Nature* **307,** 273–276 (1984).

110. Constantinescu, C. S. *et al.* Astrocytes as antigen-presenting cells: expression of IL-12/IL-23. *J. Neurochem.* **95,** 331–340 (2005).

111. Alarcón, R., Fuenzalida, C., Santibáñez, M. & von Bernhardi, R. Expression of Scavenger Receptors in Glial Cells. *J. Biol. Chem.* **280,** 30406–30415 (2005).

112. Hüll, M. *et al.* Amyloid β peptide (25–35) activates protein kinase C leading to cyclooxygenase-2 induction and prostaglandin E2 release in primary midbrain astrocytes. *Neurochem. Int.* **48,** 663–672 (2006).

113. Walsh, J. G., Muruve, D. A. & Power, C. Inflammasomes in the CNS. *Nat. Rev. Neurosci.* **15,** 84–

97 (2014).

114. Fawcett, J. W. & Asher, R. A. The glial scar and central nervous system repair. *Brain Res. Bull.* **49,** 377–91 (1999).

115. Silver, J. & Miller, J. H. Regeneration beyond the glial scar. *Nat. Rev. Neurosci.* **5,** 146–156 (2004).

116. Nagy, B., Hovhannisyan, A., Barzan, R., Chen, T.-J. & Kukley, M. Different patterns of neuronal activity trigger distinct responses of oligodendrocyte precursor cells in the corpus callosum. *PLOS Biol.* **15,** e2001993 (2017).

117. Welsh, T. G. & Kucenas, S. Purinergic signaling in oligodendrocyte development and function. *J. Neurochem.* **145,** 6–18 (2018).

118. Kaplan, M. R. *et al.* Differential control of clustering of the sodium channels Na(v)1.2 and Na(v)1.6 at developing CNS nodes of Ranvier. *Neuron* **30,** 105–19 (2001).

119. Kaplan, M. R. *et al.* Induction of sodium channel clustering by oligodendrocytes. *Nature* **386,** 724–728 (1997).

120. Fannon, J., Tarmier, W. & Fulton, D. Neuronal activity and AMPA-type glutamate receptor activation regulates the morphological development of oligodendrocyte precursor cells. *Glia* (2015). doi:10.1002/glia.22799

121. Nave, K.-A. Myelination and the trophic support of long axons. *Nat. Rev. Neurosci.* **11,** 275–283 (2010).

122. Alizadeh, A., Dyck, S. M. & Karimi-Abdolrezaee, S. Myelin damage and repair in pathologic CNS: challenges and prospects. *Front. Mol. Neurosci.* **8,** 35 (2015).

123. Ehrenberg, C. G. Nothwendigkeit einer feineren mechanischen Zerlegung des Gehirns und der Nerven vor der chemischen, dargestellt aus Beobachtungen. *Ann. der Phys. und Chemie* **104,** 449–473 (1833).

124. Virchow, R. Ueber das ausgebreitete Vorkommen einer dem Nervenmark analogen Substanz in den thierischen Geweben. *Arch. für Pathol. Anat. und Physiol. und für Klin. Med.* **6,** 562–572 (1854).

125. Ranvier, P. L. Leçons sur l'Histologie du Système Nerveux. *J. Ment. Sci.* **24,** 118–122 (1878).

126. PENFIELD, W. OLIGODENDROGLIA AND ITS RELATION TO CLASSICAL NEUROGLIA. *Brain* **47,** 430–452 (1924).

127. BUNGE, M. B., BUNGE, R. P. & RIS, H. Ultrastructural study of remyelination in an experimental lesion in adult cat spinal cord. *J. Biophys. Biochem. Cytol.* **10,** 67–94 (1961).

128. BUNGE, M. B., BUNGE, R. P. & PAPPAS, G. D. Electron microscopic demonstration of connections between glia and myelin sheaths in the developing mammalian central nervous system. *J. Cell Biol.* **12,** 448–53 (1962).

129. Bunge, R. P. Glial cells and the central myelin sheath. *Physiol. Rev.* **48,** 197–251 (1968).

130. Norton, W. T. & Poduslo, S. E. Myelination in rat brain: method of myelin isolation. *J. Neurochem.* **21,** 749–57 (1973).

131. Lillie, R. S. FACTORS AFFECTING TRANSMISSION AND RECOVERY IN THE PASSIVE IRON NERVE

MODEL. *J. Gen. Physiol.* **7,** 473–507 (1925).

132. Huxley, A. F. & Stämpfli, R. Evidence for saltatory conduction in peripheral myelinated nerve fibres. *J. Physiol.* **108,** 315–39 (1949).

133. Tasaki, I. THE ELECTRO-SALTATORY TRANSMISSION OF THE NERVE IMPULSE AND THE EFFECT OF NARCOSIS UPON THE NERVE FIBER. *Am. J. Physiol. Content* **127,** 211–227 (1939).

134. Sajous, C. E. D. M. The Internal Secretions and the Principles of Medicine. *Am. J. Psychiatry* **60,** 174-NaN-175 (1914).

135. Fünfschilling, U. *et al.* Glycolytic oligodendrocytes maintain myelin and long-term axonal integrity. *Nature* **485,** 517–21 (2012).

136. Lee, Y. *et al.* Oligodendroglia metabolically support axons and contribute to neurodegeneration. *Nature* **487,** 443–8 (2012).

137. Boggs, J. M. Myelin basic protein: A multifunctional protein. *Cellular and Molecular Life Sciences* **63,** 1945–1961 (2006).

138. Greer, J. M. Autoimmune T-cell reactivity to myelin proteolipids and glycolipids in multiple sclerosis. *Mult. Scler. Int.* **2013,** 151427 (2013).

139. Olsen, J. A. & Akirav, E. M. Remyelination in multiple sclerosis: Cellular mechanisms and novel therapeutic approaches. *J. Neurosci. Res.* **93,** 687–96 (2015).

140. Zoupi, L., Markoullis, K., Kleopa, K. A. & Karagogeos, D. Alterations of juxtaparanodal domains in two rodent models of CNS demyelination. *Glia* **61,** 1236–49 (2013).

141. Bellander, B.-M. *et al.* Secondary insults following traumatic brain injury enhance complement activation in the human brain and release of the tissue damage marker S100B. *Acta Neurochir. (Wien).* **153,** 90–100 (2011).

142. Papastefanaki, F. & Matsas, R. From demyelination to remyelination : The road toward therapies for spinal cord injury. *Glia* (2015). doi:10.1002/glia.22809

143. Franklin, R. J. M. & ffrench-Constant, C. Remyelination in the CNS: from biology to therapy. *Nat. Rev. Neurosci.* **9,** 839–855 (2008).

144. Chang, A. *et al.* Cortical remyelination: a new target for repair therapies in multiple sclerosis. *Ann. Neurol.* **72,** 918–26 (2012).

145. Kidd, D. *et al.* Cortical lesions in multiple sclerosis. *Brain* **122 (Pt 1,** 17–26 (1999).

146. Larochelle, C., Alvarez, J. I. & Prat, A. How do immune cells overcome the blood-brain barrier in multiple sclerosis? *FEBS Lett.* **585,** 3770–80 (2011).

147. Lee, S. *et al.* A potential link between autoimmunity and neurodegeneration in immune-mediated neurological disease. *J. Neuroimmunol.* **235,** 56–69 (2011).

148. Hanafy, K. A. & Sloane, J. A. Regulation of remyelination in multiple sclerosis. *FEBS Lett.* **585,** 3821–8 (2011).

149. Coman, I. *et al.* Nodal, paranodal and juxtaparanodal axonal proteins during demyelination and remyelination in multiple sclerosis. *Brain* **129,** 3186–95 (2006).

150. Franklin, R. J. M. & ffrench-Constant, C. Regenerating CNS myelin — from mechanisms to

experimental medicines. *Nat. Rev. Neurosci.* **18,** 753–769 (2017).

151. Gravel, M. *et al.* Overexpression of 2',3'-cyclic nucleotide 3'-phosphodiesterase in transgenic mice alters oligodendrocyte development and produces aberrant myelination. *Mol. Cell. Neurosci.* **7,** 453–66 (1996).

152. Li, C. *et al.* Myelination in the absence of myelin-associated glycoprotein. *Nature* **369,** 747–50 (1994).

153. Filbin, M. The Muddle with MAG. *Mol. Cell. Neurosci.* **8,** 84–92 (1996).

154. Poltorak, M. *et al.* Myelin-associated glycoprotein, a member of the L2/HNK-1 family of neural cell adhesion molecules, is involved in neuron-oligodendrocyte and oligodendrocyte-oligodendrocyte interaction. *J. Cell Biol.* **105,** 1893–9 (1987).

155. Boison, D., Büssow, H., D'Urso, D., Müller, H. W. & Stoffel, W. Adhesive properties of proteolipid protein are responsible for the compaction of CNS myelin sheaths. *J. Neurosci.* **15,** 5502–13 (1995).

156. Simons, M. *et al.* Overexpression of the myelin proteolipid protein leads to accumulation of cholesterol and proteolipid protein in endosomes/lysosomes: implications for Pelizaeus-Merzbacher disease. *J. Cell Biol.* **157,** 327–36 (2002).

157. Karim, S. A. *et al.* PLP overexpression perturbs myelin protein composition and myelination in a mouse model of Pelizaeus-Merzbacher disease. *Glia* **55,** 341–51 (2007).

158. Peyron, F. *et al.* In situ expression of PLP/DM-20, MBP, and CNP during embryonic and postnatal development of the jimpy mutant and of transgenic mice overexpressing PLP. *J. Neurosci. Res.* **50,** 190–201 (1997).

159. Privat, A., Jacque, C., Bourre, J. M., Dupouey, P. & Baumann, N. Absence of the major dense line in myelin of the mutant mouse 'shiverer'. *Neurosci. Lett.* **12,** 107–12 (1979).

160. Campagnoni, A. T. & Macklin, W. B. Cellular and molecular aspects of myelin protein gene expression. *Mol. Neurobiol.* **2,** 41–89 (1988).

161. Aggarwal, S. *et al.* Myelin membrane assembly is driven by a phase transition of Myelin Basic Proteins into a cohesive protein meshwork. *PLoS Biol* **11,** e1001577 (2013).

162. Weil, M.-T. *et al.* Loss of Myelin Basic Protein Function Triggers Myelin Breakdown in Models of Demyelinating Diseases. *Cell Rep.* **16,** 314–322 (2016).

163. Jakovcevski, I. & Zecevic, N. Olig Transcription Factors Are Expressed in Oligodendrocyte and Neuronal Cells in Human Fetal CNS. *J. Neurosci.* **25,** 10064–10073 (2005).

164. Liu, Z. *et al.* Induction of oligodendrocyte differentiation by Olig2 and Sox10: Evidence for reciprocal interactions and dosage-dependent mechanisms. *Dev. Biol.* **302,** 683–693 (2007).

165. Kuroda, S. *et al.* Protein-protein interaction of zinc finger LIM domains with protein kinase C. *J. Biol. Chem.* **271,** 31029–32 (1996).

166. Yokoo, H. *et al.* Anti-human Olig2 antibody as a useful immunohistochemical marker of normal oligodendrocytes and gliomas. *Am. J. Pathol.* **164,** 1717–25 (2004).

167. McLellan, A. S., Langlands, K. & Kealey, T. Exhaustive identification of human class II basic helix-loop-helix proteins by virtual library screening. *Mech. Dev.* **119 Suppl 1,** S285-91 (2002).

168. Chakrabarti, L. *et al.* Olig1 and Olig2 triplication causes developmental brain defects in Down syndrome. *Nat. Neurosci.* **13,** 927–34 (2010).

169. Buffo, A. *et al.* Origin and progeny of reactive gliosis: A source of multipotent cells in the injured brain. *Proc. Natl. Acad. Sci. U. S. A.* **105,** 3581–6 (2008).

170. Buffo, A. *et al.* Expression pattern of the transcription factor Olig2 in response to brain injuries: implications for neuronal repair. *Proc. Natl. Acad. Sci. U. S. A.* **102,** 18183–8 (2005).

171. Arnett, H. A. *et al.* bHLH Transcription Factor Olig1 Is Required to Repair Demyelinated Lesions in the CNS. *Science (80-.).* **306,** 2111–2115 (2004).

172. Zhou, Q. & Anderson, D. J. The bHLH Transcription Factors OLIG2 and OLIG1 Couple Neuronal and Glial Subtype Specification. *Cell* **109,** 61–73 (2002).

173. Siebert, J. R., Conta Steencken, A. & Osterhout, D. J. Chondroitin sulfate proteoglycans in the nervous system: inhibitors to repair. *Biomed Res. Int.* **2014,** 845323 (2014).

174. Yuan, P. *et al.* Chondroitin sulfate proteoglycan 4 functions as the cellular receptor for Clostridium difficile toxin B. *Cell Res.* **25,** 157–168 (2015).

175. Iida, J., Skubitz, A. P., Furcht, L. T., Wayner, E. A. & McCarthy, J. B. Coordinate role for cell surface chondroitin sulfate proteoglycan and alpha 4 beta 1 integrin in mediating melanoma cell adhesion to fibronectin. *J. Cell Biol.* **118,** 431–44 (1992).

176. Niehaus, A., Stegmüller, J., Diers-Fenger, M. & Trotter, J. Cell-surface glycoprotein of oligodendrocyte progenitors involved in migration. *J. Neurosci.* **19,** 4948–61 (1999).

177. Karram, K., Chatterjee, N. & Trotter, J. NG2-expressing cells in the nervous system: role of the proteoglycan in migration and glial-neuron interaction. *J. Anat.* **207,** 735–44 (2005).

178. de Castro, R., Tajrishi, R., Claros, J. & Stallcup, W. B. Differential responses of spinal axons to transection: influence of the NG2 proteoglycan. *Exp. Neurol.* **192,** 299–309 (2005).

179. Rezajooi, K. *et al.* NG2 proteoglycan expression in the peripheral nervous system: upregulation following injury and comparison with CNS lesions. *Mol. Cell. Neurosci.* **25,** 572–584 (2004).

180. Lin, X. H., Grako, K. A., Burg, M. A. & Stallcup, W. B. NG2 proteoglycan and the actin-binding protein fascin define separate populations of actin-containing filopodia and lamellipodia during cell spreading and migration. *Mol. Biol. Cell* **7,** 1977–93 (1996).

181. Lin, X. H., Dahlin-Huppe, K. & Stallcup, W. B. Interaction of the NG2 proteoglycan with the actin cytoskeleton. *J. Cell. Biochem.* **63,** 463–77 (1996).

182. Fang, X. *et al.* Cytoskeletal reorganization induced by engagement of the NG2 proteoglycan leads to cell spreading and migration. *Mol. Biol. Cell* **10,** 3373–87 (1999).

183. Kantor, D. B. *et al.* Semaphorin 5A Is a Bifunctional Axon Guidance Cue Regulated by Heparan and Chondroitin Sulfate Proteoglycans. *Neuron* **44,** 961–975 (2004).

184. Bradbury, E. J. *et al.* Chondroitinase ABC promotes functional recovery after spinal cord injury. *Nature* **416,** 636–640 (2002).

185. Nishiyama, A., Lin, X. H., Giese, N., Heldin, C. H. & Stallcup, W. B. Co-localization of NG2 proteoglycan and PDGF alpha-receptor on O2A progenitor cells in the developing rat brain. *J.*

Neurosci. Res. **43,** 299–314 (1996).

186. Dawson, M. R. L., Levine, J. M. & Reynolds, R. NG2-expressing cells in the central nervous system: Are they oligodendroglial progenitors? *J. Neurosci. Res.* **61,** 471–479 (2000).

187. Bansal, R. & Pfeiffer, S. E. Novel stage in the oligodendrocyte lineage defined by reactivity of progenitors with R-mAb prior to O1 anti-galactocerebroside. *J. Neurosci. Res.* **32,** 309–316 (1992).

188. Sommer, I. & Schachner, M. Monoclonal antibodies (O1 to O4) to oligodendrocyte cell surfaces: an immunocytological study in the central nervous system. *Dev. Biol.* **83,** 311–27 (1981).

189. Bergers, G. & Song, S. The role of pericytes in blood-vessel formation and maintenance. *Neuro. Oncol.* **7,** 452–64 (2005).

190. Park, T. I.-H. *et al.* Cultured pericytes from human brain show phenotypic and functional differences associated with differential CD90 expression. *Sci. Rep.* **6,** 26587 (2016).

191. Robinson, A. P., Rodgers, J. M., Goings, G. E. & Miller, S. D. Characterization of oligodendroglial populations in mouse demyelinating disease using flow cytometry: clues for MS pathogenesis. *PLoS One* **9,** e107649 (2014).

192. He, Y., Cai, W., Wang, L. & Chen, P. A developmental study on the expression of PDGFαR immunoreactive cells in the brain of postnatal rats. *Neurosci. Res.* **65,** 272–279 (2009).

193. Andrae, J., Gallini, R. & Betsholtz, C. Role of platelet-derived growth factors in physiology and medicine. *Genes Dev.* **22,** 1276–1312 (2008).

194. Cabezas, R., Avila, M. & Vega-Vela, N. E. Growth Factors and Astrocytes Metabolism: Possible Roles for Platelet Derived Growth Factor Omic-driven Metabolic Reconstruction of the Human Astrocyte to Study the Response to the Synthetic Steroid Tibolone. View project PLA2 Inhibition View project. (2015). doi:10.2174/1573406411666151019120444

195. Svennerholm, L. & Fredman, P. A procedure for the quantitative isolation of brain gangliosides. *Biochim. Biophys. Acta* **617,** 97–109 (1980).

196. Holthuis, J. C. M., Pomorski, T., Raggers, R. J., Sprong, H. & Van Meer, G. The Organizing Potential of Sphingolipids in Intracellular Membrane Transport. *Physiol. Rev.* **81,** 1689–1723 (2001).

197. Yu, R. K., Bieberich, E., Xia, T. & Zeng, G. Regulation of ganglioside biosynthesis in the nervous system. *J. Lipid Res.* **45,** 783–793 (2004).

198. Xu, Y.-H., Barnes, S., Sun, Y. & Grabowski, G. A. Multi-system disorders of glycosphingolipid and ganglioside metabolism. *J. Lipid Res.* **51,** 1643–1675 (2010).

199. Baracskay, K. L., Kidd, G. J., Miller, R. H. & Trapp, B. D. NG2-positive cells generate A2B5-positive oligodendrocyte precursor cells. *Glia* **55,** 1001–1010 (2007).

200. Goldman, S. A. Neuronal development and migration in explant cultures of the adult canary forebrain. *J. Neurosci.* **10,** 2931–9 (1990).

201. Raff, M. C., Miller, R. H. & Noble, M. A glial progenitor cell that develops in vitro into an astrocyte or an oligodendrocyte depending on culture medium. *Nature* **303,** 390–396 (1983).

202. Barateiro, A. & Fernandes, A. Temporal oligodendrocyte lineage progression: In vitro models of proliferation, differentiation and myelination. *Biochim. Biophys. Acta - Mol. Cell Res.* **1843,** 1917–1929 (2014).

203. Reich, D. S., Lucchinetti, C. F. & Calabresi, P. A. Multiple Sclerosis. *N. Engl. J. Med.* **378,** 169–180 (2018).

204. Zhu, Y., He, Z.-Y. & Liu, H.-N. Meta-analysis of the relationship between homocysteine, vitamin B12, folate, and multiple sclerosis. *J. Clin. Neurosci.* **18,** 933–938 (2011).

205. Farez, M. F. & Correale, J. Immunizations and risk of multiple sclerosis: systematic review and meta-analysis. *J. Neurol.* **258,** 1197–1206 (2011).

206. Lunny, C., Knopp-Sihota, J. A. & Fraser, S. N. Surgery and risk for multiple sclerosis: a systematic review and meta-analysis of case–control studies. *BMC Neurol.* **13,** 41 (2013).

207. Warren, S. A. *et al.* Traumatic Injury and Multiple Sclerosis: A Systematic Review and Meta-Analysis. *Can. J. Neurol. Sci.* **40,** 168–176 (2013).

208. Barragán-Martínez, C. *et al.* Organic Solvents as Risk Factor for Autoimmune Diseases: A Systematic Review and Meta-Analysis. *PLoS One* **7,** e51506 (2012).

209. Lunny, C. A., Fraser, S. N. & Knopp-Sihota, J. A. Physical trauma and risk of multiple sclerosis: A systematic review and meta-analysis of observational studies. *J. Neurol. Sci.* **336,** 13–23 (2014).

210. Munger, K. L. *et al.* Vitamin D intake and incidence of multiple sclerosis. *Neurology* **62,** 60–5 (2004).

211. Smolders, J., Menheere, P., Kessels, A., Damoiseaux, J. & Hupperts, R. Association of vitamin D metabolite levels with relapse rate and disability in multiple sclerosis. *Mult. Scler. J.* **14,** 1220–1224 (2008).

212. Leray, E., Moreau, T., Fromont, A. & Edan, G. Epidemiology of multiple sclerosis. *Rev. Neurol. (Paris).* **172,** 3–13 (2016).

213. Pender, M. P. & Burrows, S. R. Epstein-Barr virus and multiple sclerosis: potential opportunities for immunotherapy. *Clin. Transl. Immunol.* **3,** e27 (2014).

214. Lünemann, J. D., Kamradt, T., Martin, R. & Münz, C. Epstein-barr virus: environmental trigger of multiple sclerosis? *J. Virol.* **81,** 6777–84 (2007).

215. Wandinger, K. *et al.* Association between clinical disease activity and Epstein-Barr virus reactivation in MS. *Neurology* **55,** 178–84 (2000).

216. Bray, P. F., Bloomer, L. C., Salmon, V. C., Bagley, M. H. & Larsen, P. D. Epstein-Barr virus infection and antibody synthesis in patients with multiple sclerosis. *Arch. Neurol.* **40,** 406–8 (1983).

217. Fraser, K. B., Haire, M., Millar, J. H. & McCrea, S. Increased tendency to spontaneous in-vitro lymphocyte transformation in clinically active multiple sclerosis. *Lancet (London, England)* **2,** 175–6 (1979).

218. Belbasis, L., Bellou, V., Evangelou, E., Ioannidis, J. P. A. & Tzoulaki, I. Environmental risk factors and multiple sclerosis: an umbrella review of systematic reviews and meta-analyses. (2015). doi:10.1016/S1474-4422(14)70267-4

219. Holmberg, M., Murtonen, A., Elovaara, I. & Sumelahti, M.-L. Increased Female MS Incidence and Differences in Gender-Specific Risk in Medium- and High-Risk Regions in Finland from 1981-2010. *Mult. Scler. Int.* **2013,** 182516 (2013).

220. Harbo, H. F., Gold, R. & Tintoré, M. Sex and gender issues in multiple sclerosis. *Ther. Adv. Neurol. Disord.* **6,** 237–48 (2013).

221. Orton, S.-M. *et al.* Sex ratio of multiple sclerosis in Canada: a longitudinal study. *Lancet Neurol.* **5,** 932–936 (2006).

222. Chitnis, T. The role of testosterone in MS risk and course. *Mult. Scler. J.* **24,** 36–41 (2018).

223. Compston, A. & Coles, A. Multiple sclerosis. *Lancet* **359,** 1221–1231 (2002).

224. Regan, J. C. & Partridge, L. Gender and longevity: Why do men die earlier than women? Comparative and experimental evidence. *Best Pract. Res. Clin. Endocrinol. Metab.* **27,** 467–479 (2013).

225. Sawcer, S., Franklin, R. J. M. & Ban, M. Multiple sclerosis genetics. *Lancet Neurol.* **13,** 700–709 (2014).

226. Hacohen, Y. *et al.* Disease Course and Treatment Responses in Children With Relapsing Myelin Oligodendrocyte Glycoprotein Antibody–Associated Disease. *JAMA Neurol.* **75,** 478 (2018).

227. Goldenberg, M. M. Multiple sclerosis review. *P T* **37,** 175–84 (2012).

228. Noseworthy, J. H. Progress in determining the causes and treatment of multiple sclerosis. *Nature* **399,** A40-7 (1999).

229. Hauser, S. L. & Oksenberg, J. R. The Neurobiology of Multiple Sclerosis: Genes, Inflammation, and Neurodegeneration. *Neuron* **52,** 61–76 (2006).

230. Weinshenker, B. G. Natural history of multiple sclerosis. *Ann. Neurol.* **36 Suppl,** S6-11 (1994).

231. Trapp, B. D. & Nave, K.-A. Multiple Sclerosis: An Immune or Neurodegenerative Disorder? *Annu. Rev. Neurosci.* **31,** 247–269 (2008).

232. Tullman, M., Oshinsky, R., Lublin, F. & Cutter, G. Clinical characteristics of progressive relapsing multiple sclerosis.

233. Sumelahti, M.-L., Hakama, M., Elovaara, I. & Pukkala, E. Causes of death among patients with multiple sclerosis. *Mult. Scler. J.* **16,** 1437–1442 (2010).

234. Smestad, C., Sandvik, L. & Celius, E. Excess mortality and cause of death in a cohort of Norwegian multiple sclerosis patients. *Mult. Scler. J.* **15,** 1263–1270 (2009).

235. Bronnum-Hansen, H., Koch-Henriksen, N. & Stenager, E. Trends in survival and cause of death in Danish patients with multiple sclerosis. *Brain* **127,** 844–850 (2004).

236. Leray, E. *et al.* Long-term survival of patients with multiple sclerosis in West France. *Mult. Scler. J.* **13,** 865–874 (2007).

237. Grytten Torkildsen, N., Lie, S., Aarseth, J., Nyland, H. & Myhr, K. Survival and cause of death in multiple sclerosis: results from a 50-year follow-up in Western Norway. *Mult. Scler. J.* **14,** 1191–1198 (2008).

238. Kingwell, E. *et al.* Relative mortality and survival in multiple sclerosis: findings from British

Columbia, Canada. *J. Neurol. Neurosurg. Psychiatry* **83,** 61–66 (2012).

239. Lalmohamed, A. *et al.* Causes of death in patients with multiple sclerosis and matched referent subjects: a population-based cohort study. *Eur. J. Neurol.* **19,** 1007–1014 (2012).

240. Phadke, J. G. Survival pattern and cause of death in patients with multiple sclerosis: results from an epidemiological survey in north east Scotland. *J. Neurol. Neurosurg. Psychiatry* **50,** 523–31 (1987).

241. Sadovnick, A. D., Ebers, G. C., Wilson, R. W. & Paty, D. W. Life expectancy in patients attending multiple sclerosis clinics. **42,** 991–994 (1992).

242. Wallin, M. T., Page, W. F. & Kurtzke, J. F. Epidemiology of multiple sclerosis in US veterans VIII. Long-term survival after onset of multiple sclerosis. *Brain* **123,** 1677–1687 (2000).

243. Ragonese, P., Aridon, P., Salemi, G., D'Amelio, M. & Savettieri, G. Mortality in multiple sclerosis: a review. *Eur. J. Neurol.* **15,** 123–127 (2008).

244. Scalfari, A. *et al.* Mortality in patients with multiple sclerosis. *Neurology* **81,** 184–92 (2013).

245. Gilmore, C. *et al.* Spinal cord grey matter lesions in multiple sclerosis detected by post-mortem high field MR imaging. *Mult. Scler. J.* **15,** 180–188 (2009).

246. Liu, W. *et al.* In vivo imaging of spinal cord atrophy in neuroinflammatory diseases. *Ann. Neurol.* **76,** 370–378 (2014).

247. Harrison, D. M. *et al.* Leptomeningeal Enhancement at 7T in Multiple Sclerosis: Frequency, Morphology, and Relationship to Cortical Volume. *J. Neuroimaging* **27,** 461–468 (2017).

248. Absinta, M. *et al.* Gadolinium-based MRI characterization of leptomeningeal inflammation in multiple sclerosis. *Neurology* **85,** 18–28 (2015).

249. Serafini, B., Rosicarelli, B., Magliozzi, R., Stigliano, E. & Aloisi, F. Detection of ectopic B-cell follicles with germinal centers in the meninges of patients with secondary progressive multiple sclerosis. *Brain Pathol.* **14,** 164–74 (2004).

250. Absinta, M. *et al.* Persistent 7-tesla phase rim predicts poor outcome in new multiple sclerosis patient lesions. *J. Clin. Invest.* **126,** 2597–2609 (2016).

251. Rawji, K. S., Mishra, M. K. & Yong, V. W. Regenerative Capacity of Macrophages for Remyelination. *Front. Cell Dev. Biol.* **4,** 47 (2016).

252. Ruckh, J. M. *et al.* Rejuvenation of Regeneration in the Aging Central Nervous System. *Cell Stem Cell* **10,** 96–103 (2012).

253. Prinz, M., Priller, J., Sisodia, S. S. & Ransohoff, R. M. Heterogeneity of CNS myeloid cells and their roles in neurodegeneration. *Nat. Neurosci.* **14,** 1227–1235 (2011).

254. van der Valk, P. & Amor, S. Preactive lesions in multiple sclerosis. *Curr. Opin. Neurol.* **22,** 1 (2009).

255. Mishra, M. K. & Yong, V. W. Myeloid cells — targets of medication in multiple sclerosis. *Nat. Rev. Neurol.* **12,** 539–551 (2016).

256. Strey, C. W. *et al.* The proinflammatory mediators C3a and C5a are essential for liver regeneration. *J. Exp. Med.* **198,** 913–23 (2003).

257. Linden, J. R. *et al. Clostridium perfringens* Epsilon Toxin Causes Selective Death of Mature Oligodendrocytes and Central Nervous System Demyelination. *MBio* **6,** e02513-14 (2015).

258. Gaitán, M. I. *et al.* Evolution of the blood-brain barrier in newly forming multiple sclerosis lesions. *Ann. Neurol.* **70,** 22–29 (2011).

259. Lassmann, H. Mechanisms of white matter damage in multiple sclerosis. *Glia* **62,** 1816–1830 (2014).

260. Michel, L. *et al.* B Cells in the Multiple Sclerosis Central Nervous System: Trafficking and Contribution to CNS-Compartmentalized Inflammation. *Front. Immunol.* **6,** 636 (2015).

261. Fisher, P. The Innate and Adaptive Immune Systems. *University of California San Francisco* (2016). Available at: https://www.ncbi.nlm.nih.gov/books/NBK279396/. (Accessed: 30th April 2018)

262. Wherry, E. J. & Masopust, D. Adaptive Immunity. in *Viral Pathogenesis* 57–69 (Elsevier, 2016). doi:10.1016/B978-0-12-800964-2.00005-7

263. Smithburn, K. C. & Haddow, A. J. Semliki Forest Virus: I. Isolation and Pathogenic Properties. *J. Immunol.* **49,** 141–157 (1944).

264. Bayly-Jones, C., Bubeck, D. & Dunstone, M. A. The mystery behind membrane insertion: a review of the complement membrane attack complex. *Philos. Trans. R. Soc. Lond. B. Biol. Sci.* **372,** 20160221 (2017).

265. Parkin, J. & Cohen, B. An overview of the immune system. *Lancet* **357,** 1777–1789 (2001).

266. Carroll, M. C. The complement system in regulation of adaptive immunity. *Nat. Immunol.* **5,** 981–986 (2004).

267. Elliott, D. E., Siddique, S. S. & Weinstock, J. V. Innate immunity in disease. *Clin. Gastroenterol. Hepatol.* **12,** 749–55 (2014).

268. Walport, M. J. Complement. First of two parts. *N. Engl. J. Med.* **344,** 1058–1066 (2001).

269. Sospedra, M. & Martin, R. Immunology of multiple sclerosis. *Annu Rev Immunol* **23,** 683–747 (2005).

270. Thompson, M. R., Kaminski, J. J., Kurt-Jones, E. A. & Fitzgerald, K. A. Pattern recognition receptors and the innate immune response to viral infection. *Viruses* **3,** 920–40 (2011).

271. Alberts, B. *et al. The Adaptive Immune System*. (Garland Science, 2002).

272. Carossino, M., Thiry, E., de la Grandière, A. & Barrandeguy, M. E. Novel vaccination approaches against equine alphavirus encephalitides. *Vaccine* **32,** 311–319 (2014).

273. Andre, F. E. *et al.* Vaccination greatly reduces disease, disability, death and inequity worldwide. *Bull. World Health Organ.* **86,** 140–6 (2008).

274. Ballanti, E. *et al.* Complement and autoimmunity. *Immunol. Res.* **56,** 477–491 (2013).

275. Sarma, J. V. & Ward, P. A. The complement system. *Cell Tissue Res.* **343,** 227–35 (2011).

276. Faisal, S. Liposome Adjuvants: Simultaneous Induction of Innate and Adaptive Immunity is Key to Success. *J Vaccines Immun* **1,** 011–013 (2015).

277. Del Rio-Tsonis, K. *et al.* Expression of the third component of complement, C3, in regenerating

limb blastema cells of urodeles. *J. Immunol.* **161,** 6819–24 (1998).

278. Kimura, Y. *et al.* Expression of complement 3 and complement 5 in newt limb and lens regeneration. *J. Immunol.* **170,** 2331–9 (2003).

279. Markiewski, M. M. *et al.* The regulation of liver cell survival by complement. *J. Immunol.* **182,** 5412–8 (2009).

280. Mastellos, D., Papadimitriou, J. C., Franchini, S., Tsonis, P. A. & Lambris, J. D. A novel role of complement: mice deficient in the fifth component of complement (C5) exhibit impaired liver regeneration. *J. Immunol.* **166,** 2479–86 (2001).

281. Pekny, M., Wilhelmsson, U., Bogestål, Y. R. & Pekna, M. The Role of Astrocytes and Complement System in Neural Plasticity. in *International review of neurobiology* **82,** 95–111 (2007).

282. Stevens, B. *et al.* The Classical Complement Cascade Mediates CNS Synapse Elimination. *Cell* **131,** 1164–1178 (2007).

283. Perry, V. H. & O'Connor, V. C1q: the perfect complement for a synaptic feast? *Nat. Rev. Neurosci.* **9,** 807–811 (2008).

284. Carroll, M. C. The complement system in B cell regulation. in *Molecular Immunology* **41,** 141–146 (2004).

285. Fleming, S. D. *et al.* Mice deficient in complement receptors 1 and 2 lack a tissue injury-inducing subset of the natural antibody repertoire. *J. Immunol.* **169,** 2126–33 (2002).

286. Pozdnyakova, O., Guttormsen, H.-K., Lalani, F. N., Carroll, M. C. & Kasper, D. L. Impaired antibody response to group B streptococcal type III capsular polysaccharide in C3- and complement receptor 2-deficient mice. *J. Immunol.* **170,** 84–90 (2003).

287. Thomas, A., Gasque, P., Vaudry, D., Gonzalez, B. & Fontaine, M. Expression of a complete and functional complement system by human neuronal cells in vitro. *Int. Immunol.* **12,** 1015–1023 (2000).

288. Gasque, P. *et al.* Expression of the complement classical pathway by human glioma in culture. A model for complement expression by nerve cells. *J. Biol. Chem.* **268,** 25068–25074 (1993).

289. Gasque, P. *et al.* Expression of complement components of the alternative pathway by glioma cell lines. *J. Immunol.* **149,** 1381–7 (1992).

290. Gasque, P., Fontaine, M. & Morgan, B. P. Complement expression in human brain. Biosynthesis of terminal pathway components and regulators in human glial cells and cell lines. *J. Immunol.* **154,** 4726–33 (1995).

291. D'Ambrosio, A. L., Pinsky, D. J. & Connolly, E. S. The role of the complement cascade in ischemia/reperfusion injury: implications for neuroprotection. *Mol Med* **7,** 367–382 (2001).

292. Morgan, B. P. & Gasque, P. Extrahepatic complement biosynthesis: Where, when and why? *Clinical and Experimental Immunology* **107,** 1–7 (1997).

293. Rutkowski, M. J. *et al.* Complement and the central nervous system: emerging roles in development, protection and regeneration. *Immunol. Cell Biol.* **88,** 781–786 (2010).

294. Rittirsch, D., Redl, H. & Huber-Lang, M. Role of complement in multiorgan failure. *Clin. Dev.*

Immunol. **2012,** 962927 (2012).

295. Walport, M. J. Complement and systemic lupus erythematosus. *Arthritis Res.* **4 Suppl 3,** S279-93 (2002).

296. Gandino, I. J. *et al.* Complement levels and risk of organ involvement in patients with systemic lupus erythematosus. *Lupus Sci. Med.* **4,** e000209 (2017).

297. Manderson, A. P., Botto, M. & Walport, M. J. The Role of Complement in the Development of Systemic Lupus Erythematosus. *Annu. Rev. Immunol.* **22,** 431–456 (2004).

298. Mackay, I. R., Rosen, F. S. & Walport, M. J. Complement. *N. Engl. J. Med.* **344,** 1058–1066 (2001).

299. Yang, D. Anaphylatoxins. in *Handbook of Biologically Active Peptides* 625–630 (Elsevier, 2013). doi:10.1016/B978-0-12-385095-9.00085-3

300. Kemper, C., Mitchell, L. M., Zhang, L. & Hourcade, D. E. The complement protein properdin binds apoptotic T cells and promotes complement activation and phagocytosis. *Proc. Natl. Acad. Sci. U. S. A.* **105,** 9023–8 (2008).

301. Bora, P. S. *et al.* Role of complement and complement membrane attack complex in laser-induced choroidal neovascularization. *J. Immunol.* **174,** 491–7 (2005).

302. Tohyama, Y. & Yamamura, H. Complement-mediated phagocytosis – the role of Syk. *IUBMB Life (International Union Biochem. Mol. Biol. Life)* **58,** 304–308 (2006).

303. Walport, M. J. Complement. Second of two parts. *N. Engl. J. Med.* **344,** 1140–1144 (2001).

304. Kemper, C., Gigli, I. & Zipfel, P. F. Conservation of Plasma Regulatory Proteins of the Complement System in Evolution: Humans and Fish. *Exp. Clin. Immunogenet.* **17,** 55–62 (2000).

305. Lindahl, G., Sjöbring, U. & Johnsson, E. Human complement regulators: a major target for pathogenic microorganisms. *Curr. Opin. Immunol.* **12,** 44–51 (2000).

306. Stoiber, H., Clivio, A. & Dierich, M. P. ROLE OF COMPLEMENT IN HIV INFECTION. *Annu. Rev. Immunol.* **15,** 649–674 (1997).

307. Pasinetti, G. M. *et al.* Hereditary Deficiencies in Complement C5 Are Associated with Intensified Neurodegenerative Responses That Implicate New Roles for the C-System in Neuronal and Astrocytic Functions. *Neurobiol. Dis.* **3,** 197–204 (1996).

308. Osaka, H., Mukherjee, P., Aisen, P. S. & Pasinetti, G. M. Complement-derived anaphylatoxin C5a protects against glutamate-mediated neurotoxicity. *J. Cell. Biochem.* **73,** 303–11 (1999).

309. Niculescu, T. *et al.* Effects of complement C5 on apoptosis in experimental autoimmune encephalomyelitis. *J. Immunol.* **172,** 5702–6 (2004).

310. Hila, S., Soane, L. & Koski, C. L. Sublytic C5b-9-stimulated Schwann cell survival through PI 3-kinase-mediated phosphorylation of BAD. *Glia* **36,** 58–67 (2001).

311. Soane, L., Rus, H., Niculescu, F. & Shin, M. L. Inhibition of oligodendrocyte apoptosis by sublytic C5b-9 is associated with enhanced synthesis of bcl-2 and mediated by inhibition of caspase-3 activation. *J. Immunol.* **163,** 6132–8 (1999).

312. Rahpeymai, Y. *et al.* Complement: a novel factor in basal and ischemia-induced neurogenesis.

EMBO J. **25,** 1364–1374 (2006).

313. Bénard, M. *et al.* Characterization of C3a and C5a Receptors in Rat Cerebellar Granule Neurons during Maturation. *J. Biol. Chem.* **279,** 43487–43496 (2004).

314. Nataf, S., Levison, S. W. & Barnum, S. R. Expression of the anaphylatoxin C5a receptor in the oligodendrocyte lineage. *Brain Res.* **894,** 321–6 (2001).

315. Hong, S. *et al.* Complement and microglia mediate early synapse loss in Alzheimer mouse models. *Science (80-.).* **352,** 712–716 (2016).

316. Kouser, L. *et al.* Emerging and novel functions of complement protein C1q. *Frontiers in Immunology* **6,** 317 (2015).

317. Ren, L. & Danias, J. A role for complement in glaucoma? *Advances in Experimental Medicine and Biology* **703,** 95–104 (2010).

318. Lobsiger, C. S. *et al.* C1q induction and global complement pathway activation do not contribute to ALS toxicity in mutant SOD1 mice. *Proc. Natl. Acad. Sci.* **110,** E4385–E4392 (2013).

319. Stokes, G. G. On the Change of Refrangibility of Light. *Philos. Trans. R. Soc. London* **142,** 463–562

320. Williams, R. T. & Bridges, J. W. Fluorescence of solutions: A review. *J. clin. Path* **17,** (1964).

321. Wolfbeis, O. S. An overview of nanoparticles commonly used in fluorescent bioimaging. *Chem. Soc. Rev.* **44,** 4743–4768 (2015).

322. Day, R. N. & Davidson, M. W. The fluorescent protein palette: tools for cellular imaging. *Chem. Soc. Rev.* **38,** 2887–921 (2009).

323. Langhans, M. & Meckel, T. Single-molecule detection and tracking in plants. *Protoplasma* (2014). doi:10.1007/s00709-013-0601-0

324. Shimomura, O., Johnson, F. H. & Saiga, Y. Extraction, Purification and Properties of Aequorin, a Bioluminescent Protein from the Luminous Hydromedusan,Aequorea. *J. Cell. Comp. Physiol.* **59,** 223–239 (1962).

325. Zimmer, M. GFP: from jellyfish to the Nobel prize and beyond. *Chem. Soc. Rev.* **38,** 2823 (2009).

326. Shimomura, O. Structure of the chromophore of *Aequorea* green fluorescent protein. *FEBS Lett.* **104,** 220–222 (1979).

327. Cody, C. W., Prasher, D. C., Westler, W. M., Prendergast, F. G. & Ward, W. W. Chemical structure of the hexapeptide chromophore of the Aequorea green-fluorescent protein. *Biochemistry* **32,** 1212–8 (1993).

328. Yang, F., Moss, L. G. & Phillips, G. N. The molecular structure of green fluorescent protein. *Nat. Biotechnol.* **14,** 1246–1251 (1996).

329. Heim, R., Prasher, D. C. & Tsien, R. Y. Wavelength mutations and posttranslational autoxidation of green fluorescent protein. *Proc. Natl. Acad. Sci.* **91,** 12501–12504 (1994).

330. Prasher, D. C., Eckenrode, V. K., Ward, W. W., Prendergast, F. G. & Cormier, M. J. Primary structure of the Aequorea victoria green-fluorescent protein. *Gene* **111,** 229–233 (1992).

331. Walthall, W., Chalfie, M., Euskirchen, G., Ward, W. & Prasher, D. Cell-cell interactions in the guidance of late-developing neurons in Caenorhabditis elegans. *Science (80-.).* **239,** 643–645 (1988).

332. Shaner, N. C. *et al.* Improved monomeric red, orange and yellow fluorescent proteins derived from Discosoma sp. red fluorescent protein. *Nat. Biotechnol.* **22,** 1567–1572 (2004).

333. Nagai, T. *et al.* A variant of yellow fluorescent protein with fast and efficient maturation for cell-biological applications. *Nat. Biotechnol.* **20,** 87–90 (2002).

334. Mason, S., Claridge, S. E., Blanch, R. & Styles, I. In vivo structural quantification of intraocular fibrosis from retinal Optical Coherence Tomography (OCT) images. *PSIBS Miniproject 1* 1–60 (2014).

335. Smith, R. The Basic Protein of CNS Myelin: Its Structure and Ligand Binding. *J. Neurochem.* **59,** 1589–1608 (1992).

336. Suzuki, N. *et al.* Differentiation of Oligodendrocyte Precursor Cells from Sox10-Venus Mice to Oligodendrocytes and Astrocytes. *Sci. Rep.* **7,** 14133 (2017).

337. Modesti, M. Fluorescent Labeling of Proteins. in *Single Molecule Analysis. Methods in Molecular Biology, vol 1665* (ed. Peterman, E. J. G.) 115–134 (Humana Press, New York, NY, 2018). doi:10.1007/978-1-4939-7271-5_6

338. Rassul, S. M., Neely, R. K. & Fulton, D. Live-imaging in the CNS: New insights on oligodendrocytes, myelination, and their responses to inflammation. *Neuropharmacology* **110,** 594–604 (2015).

339. Zhou, X. X. & Lin, M. Z. Photoswitchable fluorescent proteins: Ten years of colorful chemistry and exciting applications. *Curr. Opin. Chem. Biol.* **17,** 682–90 (2013).

340. Chudakov, D. M. *et al.* Kindling fluorescent proteins for precise in vivo photolabeling. *Nat. Biotechnol.* **21,** 191–194 (2003).

341. Ando, R., Mizuno, H. & Miyawaki, A. Regulated Fast Nucleocytoplasmic Shuttling Observed by Reversible Protein Highlighting. *Science (80-.).* **306,** 1370–1373 (2004).

342. Andresen, M. *et al.* Photoswitchable fluorescent proteins enable monochromatic multilabel imaging and dual color fluorescence nanoscopy. *Nat. Biotechnol.* **26,** 1035–1040 (2008).

343. Stiel, A. C. *et al.* Generation of Monomeric Reversibly Switchable Red Fluorescent Proteins for Far-Field Fluorescence Nanoscopy. *Biophys. J.* **95,** 2989–2997 (2008).

344. Ormö, M. *et al.* Crystal structure of the Aequorea victoria green fluorescent protein. *Science* **273,** 1392–5 (1996).

345. Wachter, R. Photoconvertible Fluorescent Proteins and the Role of Dynamics in Protein Evolution. *Int. J. Mol. Sci.* **18,** 1792 (2017).

346. Wachter, R. M., Watkins, J. L. & Kim, H. Mechanistic Diversity of Red Fluorescence Acquisition by GFP-like Proteins. *Biochemistry* **49,** 7417–7427 (2010).

347. Ando, R., Hama, H., Yamamoto-Hino, M., Mizuno, H. & Miyawaki, A. An optical marker based on the UV-induced green-to-red photoconversion of a fluorescent protein. *Proc. Natl. Acad. Sci. U. S. A.* (2002). doi:10.1073/pnas.202320599

348. Habuchi, S., Tsutsui, H., Kochaniak, A. B., Miyawaki, A. & van Oijen, A. M. mKikGR, a Monomeric Photoswitchable Fluorescent Protein. *PLoS One* **3,** e3944 (2008).

349. Gurskaya, N. G. *et al.* Engineering of a monomeric green-to-red photoactivatable fluorescent protein induced by blue light. *Nat. Biotechnol.* **24,** 461–465 (2006).

350. McKinney, S. A., Murphy, C. S., Hazelwood, K. L., Davidson, M. W. & Looger, L. L. A bright and photostable photoconvertible fluorescent protein. *Nat. Methods* **6,** 131–3 (2009).

351. Baker, S. M., Buckheit, R. W. & Falk, M. M. Green-to-red photoconvertible fluorescent proteins: tracking cell and protein dynamics on standard wide-field mercury arc-based microscopes. *BMC Cell Biol.* **11,** 15 (2010).

352. Adam, V. *et al.* Structural characterization of IrisFP, an optical highlighter undergoing multiple photo-induced transformations. *Proc. Natl. Acad. Sci. U. S. A.* **105,** 18343–8 (2008).

353. Adam, V. *et al.* Rational Design of Photoconvertible and Biphotochromic Fluorescent Proteins for Advanced Microscopy Applications. *Chem. Biol.* **18,** 1241–1251 (2011).

354. Ishitsuka, Y., Nienhaus, K. & Nienhaus, G. U. Photoactivatable Fluorescent Proteins for Super-resolution Microscopy. in 239–260 (2014). doi:10.1007/978-1-4939-0470-9_16

355. Wiedenmann, J. *et al.* From EosFP to mIrisFP: structure-based development of advanced photoactivatable marker proteins of the GFP-family. *J. Biophotonics* **4,** 377–390 (2011).

356. Deniz, A. A., Mukhopadhyay, S. & Lemke, E. A. Single-molecule biophysics: at the interface of biology, physics and chemistry. *J. R. Soc. Interface* **5,** 15–45 (2008).

357. van den Wildenberg, S. M. J. L., Prevo, B. & Peterman, E. J. G. A Brief Introduction to Single-Molecule Fluorescence Methods. in 93–113 (Humana Press, New York, NY, 2018). doi:10.1007/978-1-4939-7271-5_5

358. Zlatanova, J. & van Holde, K. Single-Molecule Biology: What Is It and How Does It Work? *Mol. Cell* **24,** 317–329 (2006).

359. Elsasser, W. M. Outline of a theory of cellular heterogeneity. *Proc. Natl. Acad. Sci. U. S. A.* **81,** 5126–9 (1984).

360. Rubin, H. The significance of biological heterogeneity. *CANCER METASTASIS Rev.* **9,** 1–20 (1990).

361. Hunting down heterogeneity. *Nature Chemical Biology* **6,** 691 (2010).

362. Schnell, U., Dijk, F., Sjollema, K. A. & Giepmans, B. N. G. Immunolabeling artifacts and the need for live-cell imaging. *Nat. Methods* **9,** 152–158 (2012).

363. Leake, M. C. Analytical tools for single-molecule fluorescence imaging in cellulo. *Phys. Chem. Chem. Phys. Phys. Chem. Chem. Phys* **16,** 12635–12647 (2014).

364. Shashkova, S. & Leake, M. C. Single-molecule fluorescence microscopy review: shedding new light on old problems. *Biosci. Rep.* **37,** (2017).

365. Ritter, J. G., Veith, R., Veenendaal, A., Siebrasse, J. P. & Kubitscheck, U. Light sheet microscopy for single molecule tracking in living tissue. *PLoS One* **5,** e11639 (2010).

366. Khaw, B. A., Beller, G. A., Haber, E. & Smith, T. W. Localization of cardiac myosin-specific antibody in myocardial infarction. *J. Clin. Invest.* **58,** 439–46 (1976).

367. MacDonald, L., Baldini, G. & Storrie, B. Does super-resolution fluorescence microscopy obsolete previous microscopic approaches to protein co-localization? *Methods Mol. Biol.* **1270,** 255–75 (2015).

368. Vrljic, M., Nishimura, S. Y. & Moerner, W. E. Single-Molecule Tracking. in 193–219 (Humana Press, 2007). doi:10.1007/978-1-59745-513-8_14

369. van Krugten, J. & Peterman, E. J. G. Single-Molecule Fluorescence Microscopy in Living Caenorhabditis elegans. in *Single Molecule Analysis. Methods in Molecular Biology, vol 1665* (ed. Peterman, E. J. G.) 145–154 (Humana Press, New York, NY, 2018). doi:10.1007/978-1-4939-7271-5_8

370. Huang, X. *et al.* Fast, long-term, super-resolution imaging with Hessian structured illumination microscopy. *Nat. Biotechnol.* **36,** 451–459 (2018).

371. Kuhl, C. K., Schild, H. H. & Morakkabati, N. Abbreviations: BI-RADS Breast Imaging Reporting and Data System 2D two-dimensional Dynamic Bilateral Contrast-enhanced MR Imaging of the Breast: Trade-off between Spatial and Temporal Resolution 1. *Radiology* **236,** 789–800 (2005).

372. Wolenski, J. S. & Julich, D. Fluorescence microscopy gets faster and clearer: roles of photochemistry and selective illumination. *Yale J. Biol. Med.* **87,** 21–32 (2014).

373. Boudreau, C. *et al.* Excitation Light Dose Engineering to Reduce Photo-bleaching and Photo-toxicity. *Sci. Rep.* **6,** 30892 (2016).

374. Combs, C. A. & Shroff, H. Fluorescence Microscopy: A Concise Guide to Current Imaging Methods. in *Current Protocols in Neuroscience* **79,** 2.1.1-2.1.25 (John Wiley & Sons, Inc., 2017).

375. Lord, S. J., Lee, H. L. & Moerner, W. E. Single-molecule spectroscopy and imaging of biomolecules in living cells. *Anal Chem* **82,** 2192–2203 (2010).

376. Santi, P. A. Light sheet fluorescence microscopy: a review. *J. Histochem. Cytochem.* **59,** 129–38 (2011).

377. Yuan, X., Martínez, J.-F., Eckert, M. & López-Santidrián, L. An Improved Otsu Threshold Segmentation Method for Underwater Simultaneous Localization and Mapping-Based Navigation. *Sensors (Basel).* **16,** (2016).

378. Marsh, B. P., Chada, N., Sanganna Gari, R. R., Sigdel, K. P. & King, G. M. The Hessian Blob Algorithm: Precise Particle Detection in Atomic Force Microscopy Imagery. *Sci. Rep.* **8,** 978 (2018).

379. H. Q. Sun & Y. Luo. Adaptive watershed segmentation of binary particle image. *J. Microsc.* **233,** 326–330 (2009).

380. Izeddin, I. *et al.* Wavelet analysis for single molecule localization microscopy. *Opt. Express* **20,** 2081 (2012).

381. Olivo-Marin, J.-C. Extraction of spots in biological images using multiscale products. *Pattern Recognit.* **35,** 1989–1996 (2002).

382. Shen, H. *et al.* Single Particle Tracking: From Theory to Biophysical Applications. *Chem. Rev.* **117,** 7331–7376 (2017).

383. Jaqaman, K. *et al.* Robust single-particle tracking in live-cell time-lapse sequences. *Nat.*

Methods **5,** 695–702 (2008).

384. Chenouard, N., Bloch, I. & Olivo-Marin, J.-C. Multiple Hypothesis Tracking for Cluttered Biological Image Sequences. *IEEE Trans. Pattern Anal. Mach. Intell.* (2013). doi:377077B0-C943-4376-B928-2872987BC8F1

385. Kim, Chanho; Li, Fuxin; Ciptadi, Arridhana; Rehg, J. M. Multiple Hypothesis Tracking Revisisted. *Iccv* **19,** (2015).

386. Teraguchi, S. & Kumagai, Y. Probabilistic Nearest Neighbor Estimation of Diffusion Constants from Single Molecular Measurement without Explicit Tracking.

387. Rasmussen, C. & Hager, G. D. Probabilistic data association methods for tracking complex visual objects. *IEEE Trans. Pattern Anal. Mach. Intell.* **23,** 560–576 (2001).

388. Vangindertael, J. *et al.* An introduction to optical super-resolution microscopy for the adventurous biologist. *Methods Appl. Fluoresc.* **6,** 22003 (2018).

389. Semwogerere, D. & Weeks, E. Confocal Microscopy. *Encyclopedia of Biomaterials and Biomedical Engineering, Second Edition - Four Volume Set* (2008). doi:10.1201/b18990-68

390. Segers-Nolten, G. M. J. *et al.* Scanning confocal fluorescence microscopy for single molecule analysis of nucleotide excision repair complexes. *Nucleic Acids Res.* **30,** 4720–7 (2002).

391. Witte, R., Andriasyan, V., Georgi, F., Yakimovich, A. & Greber, U. Concepts in Light Microscopy of Viruses. *Viruses* **10,** 202 (2018).

392. Wilson, T. Spinning-disk microscopy systems. *Cold Spring Harb. Protoc.* **2010,** pdb.top88 (2010).

393. Korobchevskaya, K., Lagerholm, B., Colin-York, H. & Fritzsche, M. Exploring the Potential of Airyscan Microscopy for Live Cell Imaging. *Photonics* **4,** 41 (2017).

394. Huff, J. The Airyscan detector from ZEISS: confocal imaging with improved signal-to-noise ratio and super-resolution. *Nat. Methods* **12,** i–ii (2015).

395. Gramatikov, B. I. Modern technologies for retinal scanning and imaging: An introduction for the biomedical engineer. *BioMedical Engineering Online* **13,** 52 (2014).

396. Mattheyses, A. L., Simon, S. M. & Rappoport, J. Z. Imaging with total internal reflection fluorescence microscopy for the cell biologist. *J. Cell Sci.* **123,** 3621–8 (2010).

397. Boulanger, J. *et al.* Fast high-resolution 3D total internal reflection fluorescence microscopy by incidence angle scanning and azimuthal averaging. *Proc. Natl. Acad. Sci. U. S. A.* **111,** 17164–9 (2014).

398. Hosny, N. A. *et al.* Super-Resolution Imaging Strategies for Cell Biologists Using a Spinning Disk Microscope. *PLoS One* **8,** e74604 (2013).

399. Lauterbach, M. A., Ronzitti, E., Sternberg, J. R., Wyart, C. & Emiliani, V. Fast Calcium Imaging with Optical Sectioning via HiLo Microscopy. *PLoS One* **10,** e0143681 (2015).

400. Endesfelder, U. & Heilemann, M. Direct Stochastic Optical Reconstruction Microscopy (dSTORM). in *Methods in molecular biology (Clifton, N.J.)* **1251,** 263–276 (2015).

401. van de Linde, S. & Sauer, M. How to switch a fluorophore: from undesired blinking to controlled photoswitching. *Chem. Soc. Rev.* **43,** 1076–1087 (2014).

402. Rust, M. J., Bates, M. & Zhuang, X. Sub-diffraction-limit imaging by stochastic optical reconstruction microscopy (STORM). *Nat. Methods* **3,** 793–796 (2006).

403. Dani, A., Huang, B., Bergan, J., Dulac, C. & Zhuang, X. Super-resolution Imaging of Chemical Synapses in the Brain.

404. Henriques, R., Griffiths, C., Hesper Rego, E. & Mhlanga, M. M. PALM and STORM: Unlocking live-cell super-resolution. *Biopolymers* **95,** 322–331 (2011).

405. Lundstrom, K. Alphaviruses in gene therapy. *Viruses* **7,** 2321–2333 (2015).

406. Liljeström, P. & Garoff, H. Expression of proteins using Semliki Forest virus vectors. *Curr. Protoc. Mol. Biol.* **Chapter 16,** Unit16.20 (2001).

407. Mukhopadhyay, S. *et al.* Mapping the structure and function of the E1 and E2 glycoproteins in alphaviruses. *Structure* **14,** 63–73 (2006).

408. Akhrymuk, I., Kulemzin, S. V. & Frolova, E. I. Evasion of the Innate Immune Response: the Old World Alphavirus nsP2 Protein Induces Rapid Degradation of Rpb1, a Catalytic Subunit of RNA Polymerase II. *J. Virol.* **86,** 7180–7191 (2012).

409. GLANVILLE, N., MORSER, J., UOMALA, P. & KAARIAINEN, L. Simultaneous Translation of Structural and Nonstructural Proteins from Semliki-Forest-Virus RNA in Two Eukaryotic Systems in vitro. *Eur. J. Biochem.* **64,** 167–175 (1976).

410. Atkins, G. J., Sheahan, B. J. & Dimmock, N. J. Semliki Forest Virus Infection of Mice: A Model for Genetic and Molecular Analysis of Viral Pathogenicity. *J. Gen. Virol.* **66,** 395–408 (1985).

411. Ehrengruber, M. U. *et al.* Semliki Forest virus A7(74) transduces hippocampal neurons and glial cells in a temperature-dependent dual manner. *J Neurovirol* **9,** 16–28 (2003).

412. Ehrengruber, M. U., Schlesinger, S. & Lundstrom, K. Alphaviruses: Semliki Forest Virus and Sindbis Virus Vectors for Gene Transfer into Neurons. in *Current Protocols in Neuroscience* **Chapter 4,** Unit 4.22 (John Wiley & Sons, Inc., 2011).

413. Vähä-Koskela, M. J. *et al.* A novel neurotropic expression vector based on the avirulent A7(74) strain of Semliki Forest virus. *J. Neurovirol.* **9,** 1–15 (2003).

414. Glasgow, G. M. *et al.* Two mutations in the envelope glycoprotein E2 of semliki forest virus affecting the maturation and entry patterns of the virus alter pathogenicity for mice. *Virology* **185,** 741–748 (1991).

415. Bradish, C. J., Allner, K. & Maber, H. B. The Virulence of Original and Derived Strains of Semliki Forest Virus for Mice, Guinea-pigs and Rabbits. *J. gen. Virol* 4–6

416. RIKKONEN, M. Functional Significance of the Nuclear-Targeting and NTP-Binding Motifs of Semliki Forest Virus Nonstructural Protein nsP2. *Virology* **218,** 352–361 (1996).

417. Santagati, M. G., Määttä, J. A., Röyttä, M., Salmi, A. A. & Hinkkanen, A. E. The Significance of the 3'-Nontranslated Region and E2 Amino Acid Mutations in the Virulence of Semliki Forest Virus in Mice. *Virology* **243,** 66–77 (1998).

418. Mathiot, C. C. *et al.* An outbreak of human Semliki Forest virus infections in Central African Republic. *Am. J. Trop. Med. Hyg.* **42,** 386–93 (1990).

419. Boere, W. A. M., Benaissa-Trouw, B. J., Harmsen, T., Erich, T. & Kraaijeveld, C. A. *Mechanisms*

of Monoclonal Antibody-Mediated Protection Against Virulent Semliki Forest Virus Downloaded from. *JOURNAL OF VIROLOGY* **54,** (1985).

420. Ingram, G., Hakobyan, S., Robertson, N. P. & Morgan, B. P. Complement in multiple sclerosis: its role in disease and potential as a biomarker. *Clin. Exp. Immunol.* **155,** 128–39 (2009).

421. Fulton, D., Paez, P. M. & Campagnoni, A. T. The Multiple Roles of Myelin Protein Genes During the Development of the Oligodendrocyte. *ASN Neuro* **2,** AN20090051 (2010).

422. Golds, E. & Braun, P. Protein Associations and Basic Protein Conformation in the Myelin Membrane THE USE OF DIFLUORODINITROBENZENE AS A CROSS-LINKING REAGENT. *J. Biol. Chem.* **253,** 8162–8170 (1978).

423. Trotter, J., Bitter-Suermann, D., Schachner, M., Bitter-Suermann, D. & Schachner, M. Differentiation-regulated loss of the polysialylated embryonic form and expression of the different polypeptides of the neural cell adhesion molecule by cultured oligodendrocytes and myelin. *J. Neurosci. Res.* **22,** 369–383 (1989).

424. Raju, S. R., Suma, M. ., Nalina, M. & Chandrashekara, K. . Animal Biotechnology. in *Basic Concept of Biotechnology* (ed. Chandrashekara, K. N.; Yakkaldevi, A.) 239–321 (Laxmi Book Publication, 2015).

425. Eisenstein, M. New fluorescent protein includes handy on-off switch. *Nat. Methods* **2,** 8–9 (2005).

426. Rosenbluth, J., Nave, K.-A., Mierzwa, A. & Schiff, R. Subtle myelin defects in PLP-null mice. *Glia* **54,** 172–182 (2006).

427. Griffiths, I. R., Schneider, A., Anderson, J. & Nave, K. A. Transgenic and natural mouse models of proteolipid protein (PLP)-related dysmyelination and demyelination. *Brain Pathol.* **5,** 275–81 (1995).

428. Saugier-Veber, P. *et al.* X–linked spastic paraplegia and Pelizaeus–Merzbacher disease are allelic disorders at the proteolipid protein locus. *Nat. Genet.* **6,** 257–262 (1994).

429. Readhead, C. & Hood, L. The dysmyelinating mouse mutations shiverer (shi) and myelin deficient (shimld). *Behav. Genet.* **20,** 213–234 (1990).

430. Chernoff, G. F. Shiverer: an autosomal recessive mutant mouse with myelin deficiency. *J. Hered.* **72,** 128 (1981).

431. Jacobs, E. C. *et al.* Targeted Overexpression of a Golli-Myelin Basic Protein Isoform to Oligodendrocytes Results in Aberrant Oligodendrocyte Maturation and Myelination. *ASN Neuro* **1,** AN20090029 (2009).

432. Nawaz, S. *et al.* Phosphatidylinositol 4,5-bisphosphate-dependent interaction of myelin basic protein with the plasma membrane in oligodendroglial cells and its rapid perturbation by elevated calcium. *J. Neurosci.* **29,** 4794–807 (2009).

433. Braun, S. M. G. *et al.* Programming Hippocampal Neural Stem/Progenitor Cells into Oligodendrocytes Enhances Remyelination in the Adult Brain after Injury. *Cell Rep.* **11,** 1679–1685 (2015).

434. Feeney, M., Murphy, K. & Lopilato, J. Designing PCR primers painlessly. *J. Microbiol. Biol. Educ.* **15,** 28–9 (2014).

435. Lorenz, T. C. Polymerase chain reaction: basic protocol plus troubleshooting and optimization strategies. *J. Vis. Exp.* e3998 (2012). doi:10.3791/3998

436. Dieffenbach, C. W., Lowe, T. M. & Dveksler, G. S. General concepts for PCR primer design. *Genome Res.* **3,** S30–S37 (1993).

437. New England Biosciences. Cleavage Close to the End of DNA Fragments | NEB. Available at: https://www.neb.com/tools-and-resources/usage-guidelines/cleavage-close-to-the-end-of-dna-fragments#.UEecadBWrDY. (Accessed: 26th May 2016)

438. Waterhouse, A. M., Procter, J. B., Martin, D. M. A., Clamp, M. & Barton, G. J. Jalview Version 2--a multiple sequence alignment editor and analysis workbench. *Bioinformatics* **25,** 1189–1191 (2009).

439. Buermans, H. P. J. & den Dunnen, J. T. Next generation sequencing technology: Advances and applications. *Biochim. Biophys. Acta - Mol. Basis Dis.* **1842,** 1932–1941 (2014).

440. Michael Gertz, E. BLAST Scoring Parameters. (2005).

441. Kelley, L. A., Mezulis, S., Yates, C. M., Wass, M. N. & Sternberg, M. J. E. The Phyre2 web portal for protein modeling, prediction and analysis. *Nat. Protoc.* **10,** 845–58 (2015).

442. Harauz, G. *et al.* Myelin basic protein—diverse conformational states of an intrinsically unstructured protein and its roles in myelin assembly and multiple sclerosis. *Micron* **35,** 503–542 (2004).

443. Ehrengruber, M. U. Alphaviral Vectors for Gene Transfer into Neurons Alphaviral Vectors : The. **26,** 183–201 (2002).

444. Desjardins, P. & Conklin, D. NanoDrop microvolume quantitation of nucleic acids. *J. Vis. Exp.* (2010). doi:10.3791/2565

445. Lonza. Amaxa Cell Line Nucleofection Kit L. 4–7 (2009).

446. Berglund, P. *et al.* Semliki Forest Virus Expression System: Production of Conditionally Infectious Recombinant Particles. *Bio/Technology* **11,** 916–920 (1993).

447. Lundstrom, K., Abenavoli, A., Malgaroli, A. & Ehrengruber, M. U. Novel Semliki Forest virus vectors with reduced cytotoxicity and temperature sensitivity for long-term enhancement of transgene expression. *Mol. Ther.* **7,** 202–9 (2003).

448. Begum, G. *et al.* NF-Y-dependent regulation of glutamate receptor 4 expression and cell survival in cells of the oligodendrocyte lineage. *Glia* (2018). doi:10.1002/glia.23446

449. Söhl, G., Hombach, S., Degen, J. & Odermatt, B. The oligodendroglial precursor cell line Oli-neu represents a cell culture system to examine functional expression of the mouse gap junction gene connexin29 (Cx29). *Front. Pharmacol.* **4,** 83 (2013).

450. Pereira, G. B., Dobretsova, A., Hamdan, H. & Wight, P. A. Expression of myelin genes: Comparative analysis of Oli-neu and N20.1 oligodendroglial cell lines. *J. Neurosci. Res.* **89,** 1070–1078 (2011).

451. Ehrengruber, M. U. *et al.* Gene Transfer into Neurons from Hippocampal Slices: Comparison of Recombinant Semliki Forest Virus, Adenovirus, Adeno-Associated Virus, Lentivirus, and Measles Virus. *Mol. Cell. Neurosci.* **17,** 855–871 (2001).

452. Ainger, K. *et al.* Transport and localization of exogenous myelin basic protein mRNA microinjected into oligodendrocytes. *J Cell Biol* **123,** 431–441 (1993).

453. Colman, D. R., Kreibich, G., Frey, A. B. & Sabatini, D. D. Synthesis and incorporation of myelin polypeptides into CNS myelin. *J. Cell Biol.* **95,** 598–608 (1982).

454. Amur-Umarjee, S., Schonmann, V. & Campagnoni, A. T. Neuronal Regulation of Myelin Basic Protein mRNA Translocation in Oligodendrocytes Is Mediated by Platelet-Derived Growth Factor. *Dev. Neurosci.* **19,** 143–151 (1997).

455. Paez, P. M. *et al.* Golli myelin basic proteins regulate oligodendroglial progenitor cell migration through voltage-operated Ca++ influx. *J Neurosci* **20,** 6663–6676 (2009).

456. Archibald, C. J. *et al.* Pain prevalence, severity and impact in a clinic sample of multiple sclerosis patients. *Pain* **58,** 89–93 (1994).

457. Ben-Zacharia, A. B. Therapeutics for multiple sclerosis symptoms. *Mt. Sinai J. Med.* **78,** 176–191 (2011).

458. Kister, I. *et al.* Natural history of multiple sclerosis symptoms. *Int. J. MS Care* **15,** 146–158 (2013).

459. Kopper, T. J. & Gensel, J. C. Myelin as an inflammatory mediator: Myelin interactions with complement, macrophages, and microglia in spinal cord injury. *J. Neurosci. Res.* **96,** 969–977 (2018).

460. Tatomir, A. *et al.* The complement system as a biomarker of disease activity and response to treatment in multiple sclerosis. *Immunol. Res.* **65,** 1103–1109 (2017).

461. Prineas, J. W. *et al.* Immunopathology of secondary-progressive multiple sclerosis. *Ann. Neurol.* **50,** 646–57 (2001).

462. Lumsden, C. E. The immunogenesis of the multiple sclerosis plaque. *Brain Res.* **28,** 365–90 (1971).

463. Linington, C. *et al.* The role of complement in the pathogenesis of experimental allergic encephalomyelitis. *Brain* **112 (Pt 4),** 895–911 (1989).

464. Abrahamson, H. A. Prevention of experimental allergic encephalomyelitis with cobra venom factor. *J. Asthma Res.* **8,** 151–2 (1971).

465. Pabst, H., Day, N. K., Gewurz, H. & Good, R. A. Prevention of experimental allergic encephalomyelitis with cobra venom factor. *Proc. Soc. Exp. Biol. Med.* **136,** 555–60 (1971).

466. Hinman, C. L., Stevens-Truss, R., Schwarz, C. & Hudson, R. A. Sequence Determinants of Modified Cobra Venom Neurotoxin Which Induce Immune Resistance to Experimental Allergic Encephalomyelitis: Molecular Mechans for Immunologic Action. *Immunopharmacol. Immunotoxicol.* **21,** 483–506 (1999).

467. Winter, M. *et al.* Dose-dependent inhibition of demyelination and microglia activation by IVIG. *Ann. Clin. Transl. Neurol.* **3,** 828–843 (2016).

468. Harrer, M. D. *et al.* Live imaging of remyelination after antibody-mediated demyelination in an ex-vivo model for immune mediated CNS damage. *Exp Neurol* **216,** 431–438 (2009).

469. Möbius, W., Nave, K.-A. & Werner, H. B. Electron microscopy of myelin: Structure

preservation by high-pressure freezing. *Brain Res.* **1641,** 92–100 (2016).

470. Gärtner, U., Härtig, W., Brauer, K., Brückner, G. & Arendt, T. Immunofluorescence and immunoelectron microscopic evidence for differences in myelination of GABAergic and cholinergic septohippocampal fibres. *Int. J. Dev. Neurosci.* **19,** 347–52 (2001).

471. Piddlesden, S. J., Lassmann, H., Zimprich, F., Morgan, B. P. & Linington, C. The demyelinating potential of antibodies to myelin oligodendrocyte glycoprotein is related to their ability to fix complement. *Am. J. Pathol.* **143,** 555–64 (1993).

472. Woodruff, R. H. & Franklin, R. J. Demyelination and remyelination of the caudal cerebellar peduncle of adult rats following stereotaxic injections of lysolecithin, ethidium bromide, and complement/anti-galactocerebroside: a comparative study. *Glia* **25,** 216–28 (1999).

473. Diemel, L. T., Wolswijk, G., Jackson, S. J. & Cuzner, M. L. Remyelination of cytokine- or antibody-demyelinated CNS aggregate cultures is inhibited by macrophage supplementation. *Glia* **45,** 278–286 (2004).

474. Körtvélyessy, P. *et al.* ADEM-like presentation, anti-MOG antibodies, and MS pathology: TWO case reports. *Neurol. - Neuroimmunol. Neuroinflammation* **4,** e335 (2017).

475. Jarius, S. *et al.* Screening for MOG-IgG and 27 other anti-glial and anti-neuronal autoantibodies in 'pattern II multiple sclerosis' and brain biopsy findings in a MOG-IgG-positive case. *Mult. Scler. J.* **22,** 1541–1549 (2016).

476. Di Pauli, F. *et al.* Fulminant demyelinating encephalomyelitis. *Neurol. - Neuroimmunol. Neuroinflammation* **2,** e175 (2015).

477. Spadaro, M. *et al.* Histopathology and clinical course of MOG-antibody-associated encephalomyelitis. *Ann. Clin. Transl. Neurol.* **2,** 295–301 (2015).

478. von Büdingen, H. C. *et al.* Frontline: Epitope recognition on the myelin/oligodendrocyte glycoprotein differentially influences disease phenotype and antibody effector functions in autoimmune demyelination. *Eur. J. Immunol.* **34,** 2072–2083 (2004).

479. Zhang, H., Jarjour, A. A., Boyd, A. & Williams, A. Central nervous system remyelination in culture — A tool for multiple sclerosis research. *Exp. Neurol.* **230,** 138–148 (2011).

480. Sebti, S. M. Protein farnesylation: Implications for normal physiology, malignant transformation, and cancer therapy. *Cancer Cell* **7,** 297–300 (2005).

481. Goudarzi, M. *et al.* Bleb Expansion in Migrating Cells Depends on Supply of Membrane from Cell Surface Invaginations. *Dev. Cell* **43,** 577–587.e5 (2017).

482. Monie, T. P. & Monie, T. P. A Snapshot of the Innate Immune System. *Innate Immune Syst.* 1–40 (2017). doi:10.1016/B978-0-12-804464-3.00001-6

483. Du Clos, T. W. & Mold, C. Complement in host deficiencies and diseases. *Clin. Immunol.* 252–269 (2013). doi:10.1016/B978-0-7234-3691-1.00041-6

484. Rus, H., Cudrici, C., David, S. & Niculescu, F. The complement system in central nervous system diseases. *Autoimmunity* **39,** 395–402 (2006).

485. Matute, C. *et al.* Excitotoxic damage to white matter. *J. Anat.* **210,** 693–702 (2007).

486. Peterson, S. L. & Anderson, A. J. Complement and spinal cord injury: Traditional and non-

traditional aspects of complement cascade function in the injured spinal cord microenvironment. *Exp. Neurol.* **258,** 35–47 (2014).

487. Cen, H., Mao, F., Aronchik, I., Fuentes, R. J. & Firestone, G. L. DEVD-NucView488: a novel class of enzyme substrates for real-time detection of caspase-3 activity in live cells. doi:10.1096/fj.07-099234

488. Dyer, C. A. Novel oligodendrocyte transmembrane signaling systems. *Mol. Neurobiol.* **7,** 1–22 (1993).

489. Jeltsch, M. *et al.* Hyperplasia of lymphatic vessels in VEGF-C transgenic mice. *Science* **276,** 1423–5 (1997).

490. Zhuo, L. *et al.* Live Astrocytes Visualized by Green Fluorescent Protein in Transgenic Mice. *Dev. Biol.* **187,** 36–42 (1997).

491. Cardarelli, F. *et al.* The intracellular trafficking mechanism of Lipofectamine-based transfection reagents and its implication for gene delivery. *Sci. Rep.* **6,** 25879 (2016).

492. Escobar, N. M. *et al.* High-throughput viral expression of cDNA-green fluorescent protein fusions reveals novel subcellular addresses and identifies unique proteins that interact with plasmodesmata. *Plant Cell* **15,** 1507–23 (2003).

493. Kaschula, C., Lang, D. & Parker, M. I. Live In-Cell Visualization of Proteins Using Super Resolution Imaging. in *Protein Interactions* (ed. Cai, J.) 311–326 (IntechOpen, 2012). doi:10.5772/37948

494. Walter, N. G. & Bustamante, C. Introduction to single molecule imaging and mechanics: Seeing and touching molecules one at a time. *Chemical Reviews* (2014). doi:10.1021/cr500059w

495. Chéreau, R., Tønnesen, J. & Nägerl, U. V. STED microscopy for nanoscale imaging in living brain slices. **88,** 57–66 (2015).

496. Cognet, L., Groc, L., Varela, J. A., Dupuis, J. P. & Etchepare, L. tracking in acute brain slices. 1–10 (2016). doi:10.1038/ncomms10947

497. Coelho, M., Maghelli, N. & Tolic-Norrelykke, I. M. Single-molecule imaging in vivo: the dancing building blocks of the cell. *Integr Biol* **5,** 748–758 (2013).

498. Giner-Casares, J. J., Henriksen-Lacey, M., Coronado-Puchau, M. & Liz-Marzán, L. M. Inorganic nanoparticles for biomedicine: where materials scientists meet medical research. *Mater. Today* **19,** 19–28 (2016).

499. Kremers, G.-J., Gilbert, S. G., Cranfill, P. J., Davidson, M. W. & Piston, D. W. Fluorescent proteins at a glance. *J. Cell Sci.* **124,** 157–60 (2011).

500. Nishiyama, A., Suzuki, R. & Zhu, X. NG2 cells (polydendrocytes) in brain physiology and repair. *Front. Neurosci.* **8,** 133 (2014).

501. Pringle, N. *et al.* Origins and early development of oligodendrocyte precursor cells. in *Molecular Signaling and Regulation in Glial Cells* 3–10 (Springer Berlin Heidelberg, 1997). doi:10.1007/978-3-642-60669-4_1

502. Emery, B. & Dugas, J. C. Purification of Oligodendrocyte Lineage Cells from Mouse Cortices by Immunopanning. *Cold Spring Harb. Protoc.* **2013,** pdb.prot073973 (2013).

503. Huang, W. *et al.* Novel NG2-CreERT2 knock-in mice demonstrate heterogeneous differentiation potential of NG2 glia during development. *Glia* **62,** 896–913 (2014).

504. Raff, M. C., Abney, E. R., Cohen, J., Lindsay, R. & Noble, M. Two types of astrocytes in cultures of developing rat white matter: differences in morphology, surface gangliosides, and growth characteristics. *J. Neurosci.* **3,** 1289–1300 (1983).

505. Lillien, L. E., Sendtner, M., Rohrer, H., Hughes, S. M. & Raff, M. C. Type-2 astrocyte development in rat brain cultures is initiated by a CNTF like protein produced by type-1 astrocytes. *Neuron* **1,** 485–494 (1988).

506. Fumagalli, M. *et al.* Phenotypic changes, signaling pathway, and functional correlates of GPR17-expressing neural precursor cells during oligodendrocyte differentiation. *J. Biol. Chem.* **286,** 10593–10604 (2011).

507. Bonfanti, E. *et al.* The role of oligodendrocyte precursor cells expressing the GPR17 receptor in brain remodeling after stroke. *Cell Death Dis.* **8,** e2871 (2017).

508. Osterhout, D. J., Wolven, A., Wolf, R. M., Resh, M. D. & Chao, M. V. Morphological differentiation of oligodendrocytes requires activation of Fyn tyrosine kinase. *J. Cell Biol.* **145,** 1209–18 (1999).

509. Yamashita, T. *et al.* Differentiation of oligodendrocyte progenitor cells from dissociated monolayer and feeder-free cultured pluripotent stem cells. *PLoS One* **12,** e0171947 (2017).

510. Gard, A. L. & Pfeiffer, S. E. Oligodendrocyte progenitors isolated directly from developing telencephalon at a specific phenotypic stage: myelinogenic potential in a defined environment. *Development* **106,** 119–32 (1989).

511. Sakry, D., Yigit, H., Dimou, L. & Trotter, J. Oligodendrocyte Precursor Cells Synthesize Neuromodulatory Factors. *PLoS One* **10,** e0127222 (2015).

512. Fratangeli, A. *et al.* The regulated expression, intracellular trafficking, and membrane recycling of the P2Y-like receptor GPR17 in Oli-neu oligodendroglial cells. *J. Biol. Chem.* **288,** 5241–56 (2013).

513. Kippert, A., Trajkovic, K., Rajendran, L., Ries, J. & Simons, M. Rho Regulates Membrane Transport in the Endocytic Pathway to Control Plasma Membrane Specialization in Oligodendroglial Cells. *J. Neurosci.* **27,** 3560–3570 (2007).

514. Dyer, C. A. The Structure and Function of Myelin: From Inert Membrane to Perfusion Pump. *Neurochem. Res.* **27,** 1279–1292 (2002).

515. Schumacher, M. *et al.* Progesterone synthesis in the nervous system: implications for myelination and myelin repair. *Front. Neurosci.* **6,** 10 (2012).

516. de Chaumont, F. *et al.* Icy: an open bioimage informatics platform for extended reproducible research. *Nat. Methods* **9,** 690–696 (2012).

517. Meijering, E., Dzyubachyk, O. & Smal, I. Methods for cell and particle tracking. *Imaging Spectrosc. Anal. Living Cells Opt. Spectrosc. Tech.* **504,** 183–200 (2012).

518. Chenouard, N. *et al.* Objective comparison of particle tracking methods. *Nat. Methods* **11,** 281–289 (2014).

519. Murooka, T. T. & Mempel, T. R. Multiphoton Intravital Microscopy to Study Lymphocyte

Motility in Lymph Nodes. in 247–257 (2011). doi:10.1007/978-1-61779-166-6_16

520. Garcia, Z. *et al.* Competition for antigen determines the stability of T cell-dendritic cell interactions during clonal expansion. *Proc. Natl. Acad. Sci. U. S. A.* **104,** 4553–8 (2007).

521. Textor, J., Sinn, M. & de Boer, R. J. Analytical results on the Beauchemin model of lymphocyte migration. *BMC Bioinformatics* **14,** S10 (2013).

522. Beltman, J. B., Marée, A. F. M. & de Boer, R. J. Analysing immune cell migration. *Nat. Rev. Immunol.* **9,** 789–798 (2009).

523. Krouglova, T., Vercammen, J. & Engelborghs, Y. Correct Diffusion Coefficients of Proteins in Fluorescence Correlation Spectroscopy. Application to Tubulin Oligomers Induced by Mg2+ and Paclitaxel. *Biophys. J.* **87,** 2635–2646 (2004).

524. Hasnain, S., McClendon, C. L., Hsu, M. T., Jacobson, M. P. & Bandyopadhyay, P. A New Coarse-Grained Model for E. coli Cytoplasm: Accurate Calculation of the Diffusion Coefficient of Proteins and Observation of Anomalous Diffusion. *PLoS One* **9,** e106466 (2014).

525. Weiß, K. *et al.* Quantifying the diffusion of membrane proteins and peptides in black lipid membranes with 2-focus fluorescence correlation spectroscopy. *Biophys. J.* **105,** 455–462 (2013).

526. Lyon, W. A. & Nie, S. Confinement and Detection of Single Molecules in Submicrometer Channels. *Anal. Chem.* **69,** 3400–3405 (1997).

527. Chan, K.-F. J., Robb, N. D. & Chen, W. H. Myelin basic protein: Interaction with calmodulin and gangliosides. *J. Neurosci. Res.* **25,** 535–544 (1990).

528. Boggs, J. M. & Rangaraj, G. Interaction of lipid-bound myelin basic protein with actin filaments and calmodulin. *Biochemistry* **39,** 7799–7806 (2000).

529. Frid, K. *et al.* Aggregation of MBP in chronic demyelination. *Ann. Clin. Transl. Neurol.* **2,** 711–21 (2015).

530. Setton-Avruj, C. P., Aquino, J. B., Goedelman, C. J., Soto, E. F. & Villar, M. J. P0 and Myelin Basic Protein-Like Immunoreactivities Following Ligation of the Sciatic Nerve in the Rat. *Neurochem. Res.* **27,** 1293–1303 (2002).

531. Ozgen, H. *et al.* The Lateral Membrane Organization and Dynamics of Myelin Proteins PLP and MBP Are Dictated by Distinct Galactolipids and the Extracellular Matrix. *PLoS One* **9,** e101834 (2014).

532. Zambrano, F., Aguila, | L, Arias, | Me, Sanchez, | R & Felmer, | R. Effect of sperm pretreatment with glutathione and membrane destabilizing agents lysolecithin and Triton X-100, on the efficiency of bovine intracytoplasmic sperm injection. (2017). doi:10.1111/rda.12906

533. Gonsette, R. E. Neurodegeneration in multiple sclerosis: The role of oxidative stress and excitotoxicity. *J. Neurol. Sci.* **274,** 48–53 (2008).

534. Kostic, M., Zivkovic, N. & Stojanovic, I. Multiple sclerosis and glutamate excitotoxicity. *Rev. Neurosci.* **24,** 71–88 (2013).

535. Pitt, D., Werner, P. & Raine, C. S. Glutamate excitotoxicity in a model of multiple sclerosis. *Nat. Med.* **6,** 67–70 (2000).

536. Matute, C. *et al.* The link between excitotoxic oligodendroglial death and demyelinating diseases. *Trends Neurosci.* **24,** 224–30 (2001).

537. Werner, P., Pitt, D. & Raine, C. S. Glutamate excitotoxicity--a mechanism for axonal damage and oligodendrocyte death in Multiple Sclerosis? *J. Neural Transm. Suppl.* 375–85 (2000).

538. Smith, T., Groom, A., Zhu, B. & Turski, L. Autoimmune encephalomyelitis ameliorated by AMPA antagonists. *Nat. Med.* **6,** 62–66 (2000).

539. Follett, P. L., Rosenberg, P. A., Volpe, J. J. & Jensen, F. E. NBQX attenuates excitotoxic injury in developing white matter. *J. Neurosci.* **20,** 9235–41 (2000).

540. Li, S. & Stys, P. K. Mechanisms of ionotropic glutamate receptor-mediated excitotoxicity in isolated spinal cord white matter. *J. Neurosci.* **20,** 1190–8 (2000).

541. DeSilva, T. M., Kabakov, A. Y., Goldhoff, P. E., Volpe, J. J. & Rosenberg, P. A. Regulation of Glutamate Transport in Developing Rat Oligodendrocytes. *J. Neurosci.* **29,** 7898–7908 (2009).

542. Pitt, D., Nagelmeier, I. E., Wilson, H. C. & Raine, C. S. Glutamate uptake by oligodendrocytes: Implications for excitotoxicity in multiple sclerosis. *Neurology* **61,** 1113–20 (2003).

543. Newcombe, J. *et al.* Glutamate Receptor Expression in Multiple Sclerosis Lesions. *Brain Pathol.* **18,** 52–61 (2008).

544. Edwards, A. M., Ross, N. W., Ulmer, J. B. & Braun, P. E. Interaction of myelin basic protein and proteolipid protein. *J. Neurosci. Res.* **22,** 97–102 (1989).

545. Wight, P. A. & Dobretsova, A. Where, when and how much: regulation of myelin proteolipid protein gene expression. *Cell. Mol. Life Sci.* **61,** 810–21 (2004).

Appendix

“People keep saying ‘science doesn't know everything!’ Well, science ‘knows’ it doesn't know everything; otherwise it would stop.”

- Dara Ó Briain

7.1 Image randomising code

```
str = input('What is the file type?','s');                    % User input of file type
path=uigetdir('C:\','Where are your files?')                  % User defines the location of the files
fls=dir(fullfile(path,strcat('*.',str)));                     % produces a list of files with defined type in the directory
flnm={fls.name}';                                             % extracts the filenames of all files
imgcbe=[];                                                    % Make empty matrix for data
filename = 'Rankings.xlsx';                                   % defines the name of the excel file
ltrs='acegik'                                                 % Every second letter of the alphabet for matrix allocation later
for j=1:numel(flnm)                                           % Loop to open all defined files in directory
   imgcbe{j}=imread(strcat(path,'\',char(flnm(j))));          % Saves images as an element in cell array
end
for g=1:4                                                     % Loop for the number of repeats for the ranking to be performed
rp = randperm(size(flnm,1),size(flnm,1));                     % Makes random numbers
finalfilertng=[];                                             % New matrix for storing rankings and file information
for i=1:numel(rp)                                             % Loop of all files
   imshow(imadjust(imgcbe{rp(i)}))                            % Opens random file determined by random number matrix
   rtng=input('Rating of Injury from 1 to 4 is ');            % User defines the Ranking for image
   close all                                                  % Closes image
   finalfilertng=[finalfilertng;flnm(i),strcat('File N',num2str(rp(i))),rtng];   % adds file information to matrix with ranking
end
srtflrnt=sortrows(finalfilertng,3);                           % Sorts the files in filename order
writetable(,filename,'Sheet',1,'Range',strcat(ltrs(g),'1'))   % Outputs the matrix to excel
x = input('Are you ready to continue?')                       % Break point till user decides to continue
end
```

7.2 Image J Image Processing Macro

```
dir1 = getDirectory("Choose Source Directory ");  % User defines the location of the files
dir2 = getDirectory("Choose Destination Channel Directory ");  % User defines the destination of the split channels
dir3 = getDirectory("Choose Destination Directory ");  % User defines the destination of the z projected files
list = getFileList(dir1);  % Makes list of files in directory
setBatchMode(true);  % Runs the loop in batch mode
for (i=0; i<list.length; i++) {  % Loop of all the files in the directory
showProgress(i+1, list.length);  % Has an output for user to see in console
run("Bio-Formats Importer", "open=["+dir1+list[i]+"] autoscale color_mode=Default split_channels view=Hyperstack stack_order=XYCZT");
% Opens files in Bioformat plugin
for (h=0;h<nImages;h++) {  % Loop of all the images open
selectImage(h+1);  % Selects image
title = getTitle;  % extracts the filename from the image
saveAs("tiff", dir2+title);  % saves file as tiff
 print(title);  % outputs filename
 selectImage(h+1);  % selects image which has been saved
  close();  % closes image
}
}
list2 = getFileList(dir2);  % makes list of all files in split channel directory
setBatchMode(true);  % runs in batch mode
for (i=0; i<list2.length; i++) {  % Loops all files in directory
showProgress(i+1, list2.length);  % Has an output for user to see in console
open(dir2+list2[i]);  % Opens file
run("Z Project...", "projection=[Max Intensity]");  % Z projects the file using maximum intensity
run("Enhance Contrast", "saturated=0.35");  % contrasts file
run("Apply LUT");  % applies contrast
saveAs("TIFF", dir2+list[i]);  % Saves file as tiff
close();  % Closes file
}
```

7.3 Supplementary figures

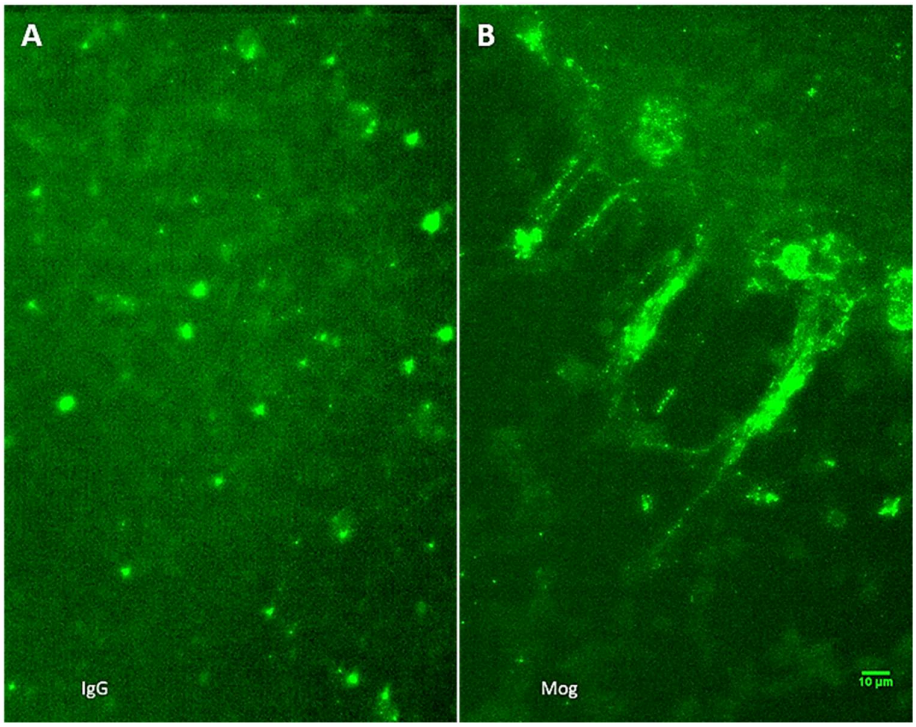

Supplementary Figure S4.1: IgG stain on brain slices, and MOG stain on brain slices. A) IgG Staining shows no structural localisation with majority being confined to cell bodies. B) MOG staining shows localisation to cell processes and confinement to mainly the white matter.